GEOMORPHIC-GEOLOGIC INDICATORS OF ZONES OF HYDROLOGIC FLUX IN DRYLANDS ON EARTH AND MARS

by

RACHEL ROSE ROTZ

(Under the Direction of Adam Milewski)

ABSTRACT

Drylands are water-scarce regions but home to increasing human populations and diverse wildlife. This is possible in part by groundwater supplied during a wetter climatic period of the past. While groundwater is hidden beneath the surface, hints of water are left behind on the surface in the form of geomorphic and geologic indicators. This study explores a series of indicators at three sites to answer questions about the timing and flow of surface and subsurface water in drylands. The relationship between fluvial and aeolian processes is investigated at a small playa in the northern Simpson Desert of Australia to understand the relationship between flooding and linear dune formation using field, laboratory, and remote sensing methods. A topographically induced inland freshwater lens in the desert of northern Kuwait is explored to calculate the timing and flow of freshwater resources in a saline aquifer using physical and numerical modeling methods, and a proposal for a study of a thrust fault and fluvial channel in Arabia Terra Mars is presented to estimate the timing and flow of surface water on Mars using remote sensing and fluvial geomorphological techniques. An interdisciplinary and integrated approach is used to answer these questions over varying temporal and spatial scales. Studies of this nature are important to answer questions of geomorphological and hydrological significance at zones of

hydrologic flux not only on Earth where water resources are paramount in the face of population growth and climate change but also as we search for water within extraterrestrial settings.

INDEX WORDS: drylands; zones of hydrologic flux, water; deserts; Mars; hydrology of Mars; arid environments; interdisciplinary studies

GEOMORPHIC-GEOLOGIC INDICATORS OF ZONES OF HYDROLOGIC FLUX IN DRYLANDS ON EARTH AND MARS

by

RACHEL ROSE ROTZ

BA, University of Central Florida, 1997

BS, University of Georgia, 2014

MS, University of Georgia, 2016

A Dissertation Submitted to the Graduate Faculty of The University of Georgia in Partial Fulfillment of the Requirements for the Degree

DOCTOR OF PHILOSOPHY

ATHENS, GEORGIA

2020

GEOMORPHIC-GEOLOGIC INDICATORS OF ZONES OF HYDROLOGIC FLUX IN DRYLANDS ON EARTH AND MARS

by

RACHEL ROSE ROTZ

Major Professor: Adam Milewski

Committee: Robert Craddock
David Leigh
Christian Klimczak
Todd Rasmussen

Electronic Version Approved:

Ron Walcott
Interim Dean of the Graduate School
The University of Georgia
August 2020

DEDICATION

I dedicate this to the children of my dear friends Ashley and Angela. For Stella, Liam, and Finn. May the universe inspire you as it did for us: to explore, discover, and protect our precious home – planet Earth.

ACKNOWLEDGEMENTS

Thank you to my advisor Dr. Adam Milewski and my committee. Each of you supported me in unique ways that resulted in some very exciting and meaningful research! Thank you to Dr. Milewski for your open-mind to my vision for this work and the freedom to explore my interests, as well as the guidance to complete my studies. Thank you to Dr. Craddock for providing the proverbial vehicle by which I could explore these interests, as well as making me a part of your world on both Earth and Mars. Thank you to Dr. Leigh for listening to my ideas, your sage advice, and being a patient, sounding board. Thank you to Dr. Klimczak for introducing me to something novel and unexpected within my research oeuvre, as well as reminding me that I am the custodian of my ideas. Thank you to Dr. Rasmussen for teaching me concepts in hydrogeology that I never thought I could learn and inspiring me to embrace the complexities of science.

I would also like to acknowledge Dr. Marta Patiño Douce and the sisters of Delta Kappa Gamma whose kindness and support will forever guide me as an educator in the geosciences.

There are a few other professors and colleagues I would like to acknowledge for their personal and professional support. They are Dr. John Dowd, Dr. Patricia Yager, Dr. Doug Crowe, Dr. Mike Roden, Dr. Paul Schroeder, and Dr. Steve Holland for your mentorship on research and career matters. Thank you to Dr. Stephanie Fulton and Laura Fackrell for being my friend and including me in your research. Thank you to Rachel Ashton and Ashley Arnold for always including and helping me. Lastly, I would like to acknowledge the Water Resources and Remote Sensing Laboratory and all my lab mates for being there for me and each other. Keep it up!

TABLE OF CONTENTS

LIST OF TABLES

LIST OF FIGURES

CHAPTER 1

INTRODUCTION

Despite their reputation as dry wastelands, deserts on Earth are home to thriving human populations and diverse wildlife. Most of the water is hidden in the subsurface as groundwater, but traces are left on the surface as distinct geological and geomorphological features that point to stored groundwater or past hydrologic movement. As scientists, how can we investigate these features to understand the timing and flow of water at these locations across scales? How can the geologic and geomorphic indicators of zones of hydrologic flux on Earth explain processes of groundwater accumulation on other planetary surfaces? To answer these questions, this document characterizes the common geomorphic and geologic indicators of zones of hydrologic flux and presents three case studies to demonstrate how this broad, yet effective, approach improves our understanding of surface and subsurface processes in deserts on Earth and extraterrestrial settings.

WHAT ARE DRYLANDS?

Life in present-day drylands is possible only by the occasional rainstorm and ancient reserves of water hidden in the subsurface as groundwater. On the surface, the shapes of rivers and lakes remain in dry form. This is the result of the extreme environmental conditions (e.g., low rainfall, high temperature) by which the term dryland is defined. Drylands are also referred to as deserts or arid environments, and their terms are used interchangeably for the scope of this work. Deserts are most known for their dryness and sparse vegetation. In some cases, a desert is defined as receiving less than 250 mm of precipitation per year. The Food and Agricultural Organization (FAO) defined drylands as those with a growing period of 1 – 179 days. However, using only

precipitation, growing periods, or temperature to determine aridity may be misleading. For example, Antarctica (Earth's largest desert) is a cold desert even with abundant water in the form of ice. The work presented on Earth here primarily deals with hot deserts. Therefore, cold deserts will not be discussed in detail other than when they pertain to the current environmental conditions of Mars.

One must consider the moisture deficit to determine aridity. This is because the water taken from an environment is just as important as the amount of water gained. For example, if the wet season of a region occurs during summer when temperatures are high, rainfall will quickly evaporate, and the climate will be drier. Conversely, if precipitation is more pronounced in the winter months, less water is taken from the system and the region is relatively less arid. Therefore, most classification systems consider the basic relationship between precipitation and evaporative losses, which are driven by temperature and humidity (Thornthwaite, 1948; Meigs, 1953; Howe et al., 1968). These factors help to characterize deserts by varying degrees of aridity. The use of an aridity index (*AI*) is often used to quantitatively classify aridity. An extensive summary of *AI*s are presented in Stephen (2005).

A common approach to determine the *AI* of a region of interest is shown in Equation 1:

$$AI = \frac{\sum_{i-1}^{n} \frac{P_i}{PE_i}}{n} \quad (1)$$

where n is the number of years, i denotes the year, P is precipitation (L), and PE is potential evaporation (L). Here, aridity is quantified by the comparison between the long-term precipitation and atmospheric water demand, or potential evaporation, on the region of interest. Potential evaporation may overestimate the total amount of water taken from the system, as it assumes an infinite amount of water is available. Also, plant transpiration is not mentioned in this example or

other factors (e.g., humidity, latent heat) that could also be considered. *AIs* are also used for other planets such as Mars (e.g., (Horvath and Andrews-Hanna, 2017)).

From the approach in Eq. 1, a desert sub-type ($AI < 0.65$) can be derived from this index as shown in Table 1. A global map of aridity by CGIAR-CSI (2009) is presented in Figure 1 and shows that nearly 40% of the Earth is covered in an arid zone.

Table 1. Desert sub-types by Aridity Index (*AI*)

Desert Sub-type	AI
Hyper-arid	$AI < 0.05$
Arid	$0.05 \leq AI < 0.2$
Semi-arid	$0.2 \leq AI < 0.5$
Dry Sub-humid	$0.5 \leq AI < 0.65$

Deserts are also defined by meteorological influences. The three general types of meteorological deserts are trade-wind deserts, monsoon deserts, and polar deserts. Trade-wind deserts are arid regions such as North Africa and Arabia where warm, trade-winds blow over the desert further desiccating rainless regions. Monsoon deserts experience occasional storms generated in higher altitudes that blow over the desert delivering moist air. Polar deserts are subjected to cold and dry descending air that is constantly pushed west from the higher rotational velocity of the lower latitudes.

Plant growth is restricted in drylands due to hot temperatures and scant rainfall. However, deserts support biodiverse populations of plants and animals. Desert flora such as wildflowers, succulents, trees, shrubs, and grasses have adapted to extreme environmental conditions. For example, the sandhill canegrass (Zygochloa paradoxa) of the Simpson Desert, lines the flanks and crests of the dunes (Buckley, 1981). The spinifex dune grass (Triodia basedowii) also grows on

the dune and interdune areas and has adapted waxy leaves to hold in water (Wiedemann, 1971). The grass stabilizes the dunes and provides shelter to animals (Figure 2).

Arid lands are currently home to 2 billion people (Koohafkan and Stewart, 2008), but supported indigenous humans long before the dawn of modern civilization. The Bedouin, an Arabic word meaning "desert dweller," are believed to have migrated out of Africa to the drylands of the Arabian Peninsula 60,000-125,000 years ago, and the Aboriginal people in the arid regions of Australia as long as 40,000 years (Davidson, 1999; Rodriguez-Flores et al., 2016). Humans have flourished in drylands because of improved water management practices and desalinization technologies. Currently, arid lands are faced with the challenges of water scarcity and land degradation due to a growing human population and climate change.

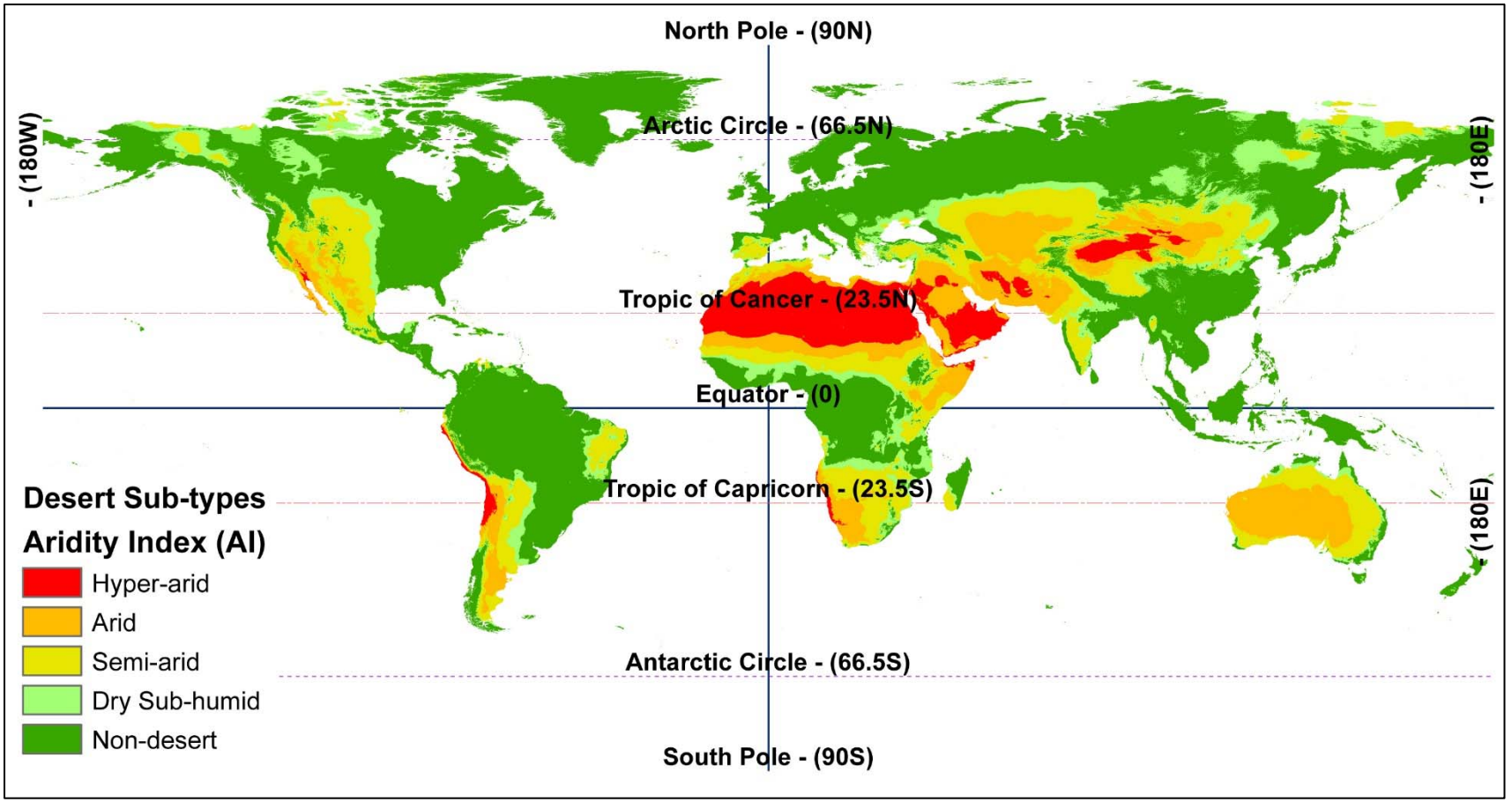

Figure 1. Global Aridity Index map of present-day Earth with world georeferenced lines. Data source (CGIAR-CSI, 2009).

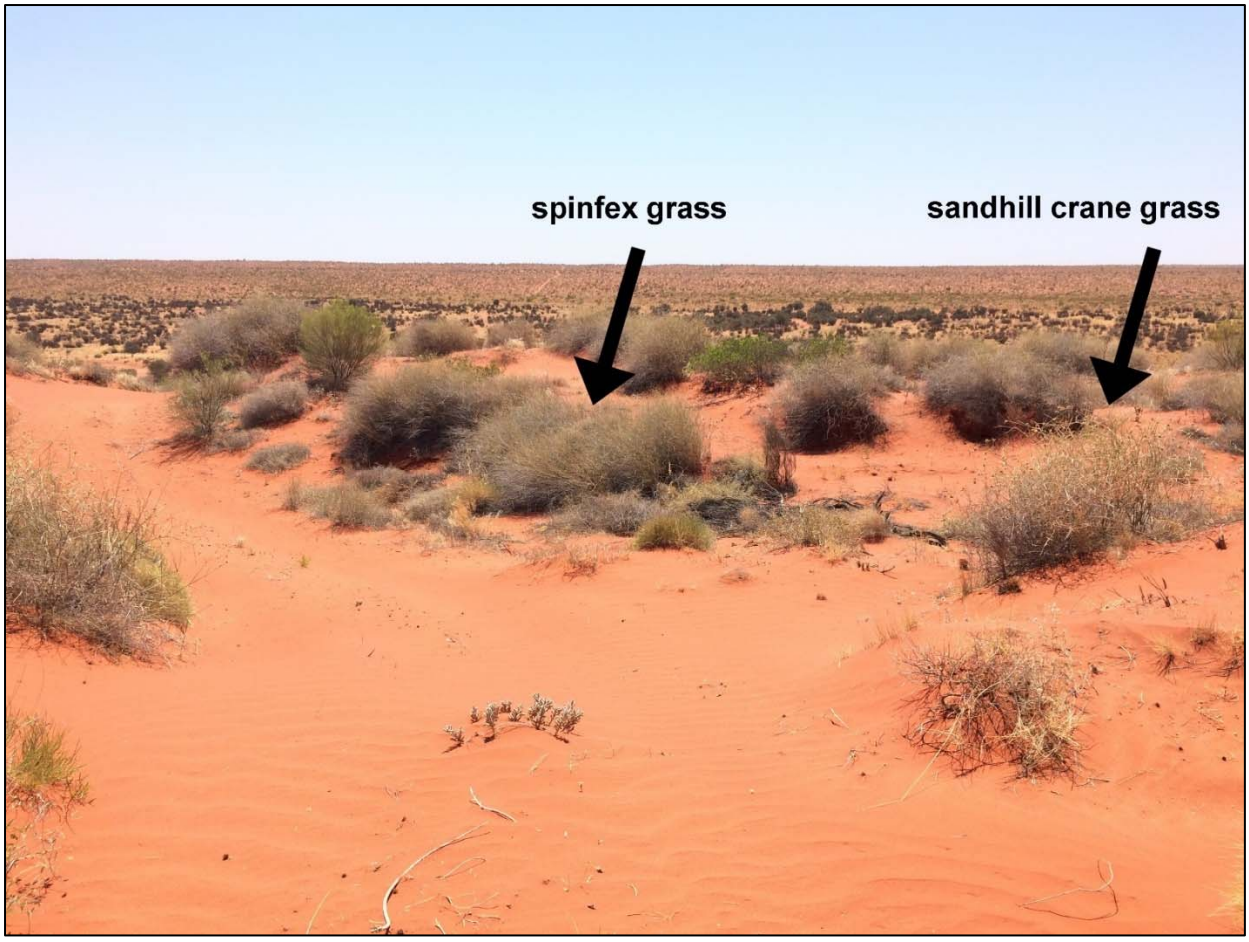

Figure 2. Spinifex grass and sandhill canegrass on a dune crest in the Simpson Desert of Australia.

THE CLIMATES OF DRYLANDS PRESENT AND PAST

Present Climate and Drylands

The climates of drylands vary by location by most have cool/dry and hot/dry seasons with a punctuated wet season and extreme diurnal temperature fluctuations. Most of the drylands on the Earth are situated at latitudes of 23.5° above and below the equator, such as the Arabian Desert of Asia and the Simpson Desert of Australia. These latitudes are referred to as the Tropic of Cancer and Tropic of Capricorn (Figure 1). The factor responsible for the position of arid environments is the global atmospheric circulation (Randall, 2015). The distribution of ice, land, and oceans around the planet combined with the tilt of the Earth's axis causes variable heating of the Earth's surface. At the higher latitudes, radiation from the sun spreads over a large surface area. At the equator, radiation is more concentrated. At the poles, radiation is less concentrated. The difference in heating creates a thermal gradient between the equator and poles.

Rising air around the equator and higher latitudes produce low-pressure systems and rainfall resulting in a relatively wet climate. Sinking air, at the mid-latitudes and poles, produces high-pressure systems resulting in a relatively dry climate. Atmospheric cells (i.e., Hadley, Ferrel, Polar) redistribute the rising hot, moist air from the equator as sinking dry, cold air to the poles. As the Earth rotates, the Coriolis Effect causes the rising and sinking air to move in a curved direction, creating the Earth's major global winds. The Hadley (at the equator), Ferrel (at mid-latitudes), and Polar (at poles) cells circulate the rising and sinking air relative to their position. Ferrel cells, which are situated in between Hadley and Polar cells, act as a gear to circulate air in the opposite direction. Due to their distinct position within the global circulation system, Ferrel cells produce a semi-permanent area of high- and low-pressure systems. These regions are called the Horse latitudes where high-pressure systems deliver relatively warm, dry winds. Winds diverge

at these latitudes and flow toward the poles, known as the prevailing westerlies, or toward the equator as the prevailing trade winds. Not all deserts are situated near the Horse latitudes but instead occur within continental interiors far from an ocean (e.g., Gobi Desert) or in the rain shadow of a large mountain range (e.g., Ordos Desert). Other climate drivers such as the El Niño–Southern Oscillation (ENSO), La Niña, and seasonal monsoons also affect oceanic and atmospheric conditions, which changes the pressure systems around the globe (Webster and Yang, 1992). These changes subject drylands to even more extreme conditions including prolonged periods of drought and episodic rainfall.

Past Climate and Drylands

Although deserts are dry today, their features (e.g., dry river channels, playas, dunes) hint to a past climate that was much warmer and wetter (or cooler and moderately wet (Brakenridge, 1978)). Earth's climate has changed repeatedly throughout geologic time, and the most pronounced periods are referred to as glacial (cold) and interglacial (warm). Cyclical variations in the Earth's climate are driven by incoming solar radiation related to Earth's orbit, Earth's axial rotation, solar activity, and tectonics (e.g., volcanism, continental drift). These drive the feedback mechanisms of Earth's biogeochemical cycles, which amplify the warming and cooling effects. The interplay between these cycles and feedback mechanisms result in climatic variations that occur over millennia, centuries, and decades and expressed in the geological record (Knauth and Lowe, 1978; Hoffman et al., 1998; Petit et al., 1999; Royer et al., 2001; Hansen et al., 2013).

As the Earth's climate fluctuated between glacial and interglacial cycles over geologic time, deserts expanded and contracted. The deserts we know today started to form during the Cenozoic Era (65.5 Ma to present) (Williams, 2014). The climate during this period continually cooled after the Late Paleocene Thermal Maximum (55 Ma) to form the Antarctic ice sheet. As

the ocean temperature gradient between the equators and poles increased, winds mobilized and transported large amounts of sediment to the Saharan, Kalahari, and Australian Deserts. During the Pliocene Epoch (5.5-2.5 Ma), the inland rivers and lakes of these deserts began to dry out while wind covered them with sand (Servant, 1973). A general trend of cooling and glaciation continued until the Pleistocene Epoch (2.3 Ma-12 ka). Afterward, the Quaternary had numerous glacial and interglacial intervals with widely different climate conditions for present-day drylands. This shift, linked to solar activity, brought rapid environmental changes from the Quaternary Period (2.6 Ma-present) to Holocene Epoch (12 ka) (Bond et al., 2001). Evidence of more than twenty-four cycles of glacial and interglacial periods ranging from 2,000 to 500 years throughout the Pleistocene and Holocene Epochs is documented from the Greenland ice core oxygen isotope records (Johnsen et al., 2001). During the times of interglaciation, increased ocean temperatures and rainfall restored fluvial networks and vegetation in deserts. During maximum glaciation, lower ocean temperatures and precipitation resulted in the expansion of deserts in Africa, Arabia, Australia, and India.

As Australia progressively shifted northward from Antarctica, it increasingly became more arid. Remnants of the fluvial networks once very active in present-day deserts are observed in the form of sporadic, localized ephemeral lakes and channels (El-Baz et al., 2000; Magee, 2009; Craddock et al., 2010). The drainage systems of these features are poorly integrated because much of the channels and playas are covered with sand from the dominant aeolian processes in the current climatic regime. They periodically fill with water after heavy rainfall and drain infiltrating water through invisible, subsurface paleodrainage systems. The remaining features on the surface are a reminder of a time when large volumes of water once flowed across the surface in drylands not only on Earth but also on in extraterrestrial settings such as Mars.

EXTRATERRESTRIAL DESERTS

Charles Lyell's central argument in *Principles of Geology* was that the "present is key to the past." This dictum may be applied to find evidence of past water from present-day features in extraterrestrial deserts or drylands in other locales than Earth. Satellite images show landforms on the surface of Venus, Mars, and Titan like landforms created by aeolian processes in drylands on Earth (Lancaster, 2006; Bourke et al., 2010; Craddock, 2011). Linear streaks, yardangs, and dune fields occur on Venus, and a variety of dunes like those on Earth (e.g., linear, barchan), dust storms, and dust devils occur on Mars. Large, linear dunes occur on Titan. Observations of dunes on all planets with an appreciable atmosphere motivates questions regarding the generation and transport of sediment in these environments. On Earth, the interaction between fluvial and aeolian processes are responsible for the formation of deserts. Craddock (2011) proposes that sediment generation and transport are basic geologic processes on planetary surfaces, and (for Mars) were initiated by large volumes of surface runoff generated by rainfall.

Although the entire planet of Mars is an extraterrestrial desert today, most scientists agree that liquid water once flowed on its surface in the ancient past. The Mariner and Viking missions in the 1960s and 1970s returned images of dry fluvial landforms on the surface of Mars resembling the ephemeral river channels in deserts on Earth (Figure 3). High-resolution imagery from Mars is increasing with each new generation of satellite and rover missions (McEwen et al., 2007). This allows us to apply our geomorphological and geological expertise to the landscapes of the red planet.

Features that indicate the presence of long-standing surface water are more diverse than just valley networks. To name just a few, they include terraces, gullies, deltas, shorelines, layered sedimentary rocks, evaporites, and clays, of which all attest to flowing liquid water ranging from

tiny seepages to catastrophic flows. Implications of these observations include that Mars may have once been much wetter and warmer in its ancient past like the deserts on Earth today (Craddock and Howard, 2002). Groundwater in the form of ground ice may remain in the subsurface of Mars in the same manner that paleowater remains in the deep aquifers of deserts on Earth today. Investigations into the timing, flow, and location of water on Mars have informed agencies like National Aeronautics and Space Administration (NASA) on where to land for the search for life and access to water for future manned missions. In this way, the search for water on Mars and other extraterrestrial deserts is not unlike the search for water in deserts on Earth.

The Climate of Early Mars

Mars is presently cold and dry, and early studies worked off the assumption that the climate on Mars was always cold because of astronomical observations and climate models. Mars receives less than half of the amount sunlight (43%) compared to the Earth, which suggests that global temperatures rarely, if ever, exceeded freezing on Mars. It is suggested that the luminosity of the Sun is not what it currently is (70% of present-day) and that a "faint, young Sun" prevented a warm, early Mars (Gough, 1981). Therefore, it is surmised by some that precipitation on Mars could only have occurred as snow (at best) and not rain (Wordsworth et al., 2015; Palumbo et al., 2018). These studies purport that flowing water and subsequent fluvial features on Mars were driven by volcanic activity and geothermal heating (Greeley and Spudis, 1981; Gulick, 1998). However, considerable uncertainty exists regarding the nature of the young Sun and climate models in general (Craddock and Howard, 2002). It is proposed that the determination of an early climate on Mars requires an all-inclusive examination of the geology and geomorphic features.

Craddock and Howard (2002) point out that large valleys that formed by groundwater sapping on Earth have developed in layered sedimentary rocks, and therefore required previous

erosional and depositional processes to be in-play long before conditions were favorable for valley development. Also, the question of the origin of ground ice remains unanswered, specifically for a cold and dry early Mars. How did the ground ice initially accumulate on Mars without rainfall? Lines of evidence also exist in climate models. Generally, it is agreed that the early Martian atmosphere was thicker than the atmosphere of today, but a warm and wet early Mars would need a dense, persistent atmosphere. Pollack et al. (1987) presented a model where a CO_2 enriched atmosphere could have sustained a hydrologic cycle and weathering for 10^9 years under warm conditions despite a reduction in solar luminosity and high orbital eccentricity. The problem was also addressed in this study and deemed that decomposing carbonate by volcanic activity provided a persistent source of CO_2 to maintain the thick, greenhouse atmosphere. Other models suggest a climatic shift to warming during the Noachian/Hesperian boundary (the two earliest time and stratigraphic systems on Mars) caused by volcanic emissions, which implies a fluctuating cold/dry and warm/wet early Mars (Ramirez and Craddock, 2018). Instead of invoking either a warm/wet and cold/dry early Martian climate, evidence has been presented that the climate oscillated throughout the Noachian and early Hesperian Periods. This is supported by the late-stage breaching of enclosed basins, delta, and alluvial fan deposition, and widespread erosion (Howard et al., 2005; Irwin et al., 2005).

Fluvial features on Mars have been determined to form before, during, and long after Tharsis, which is considered a major source of heat for the floods (Fairén et al., 2003). However, a network of dendritic valleys east of the Syrtis Major volcanic complex called the Zarga Vallis exhibit fluvial features appear to have formed by both rainfall/runoff process (Noachian) and volcanic induced ground ice-melting (middle-Hesperian) (Baker et al., 2015). Further, the observation of higher drainage densities using the Mars Orbiter Laser Altimeter (MOLA) and

higher resolution images from the Mars Global Surveyor (MGS) showed drainage densities akin to those formed by rainfall/runoff processes on Earth albeit of much larger scale (Craddock and Howard, 2002; Ansan et al., 2008; Hynek et al., 2010).

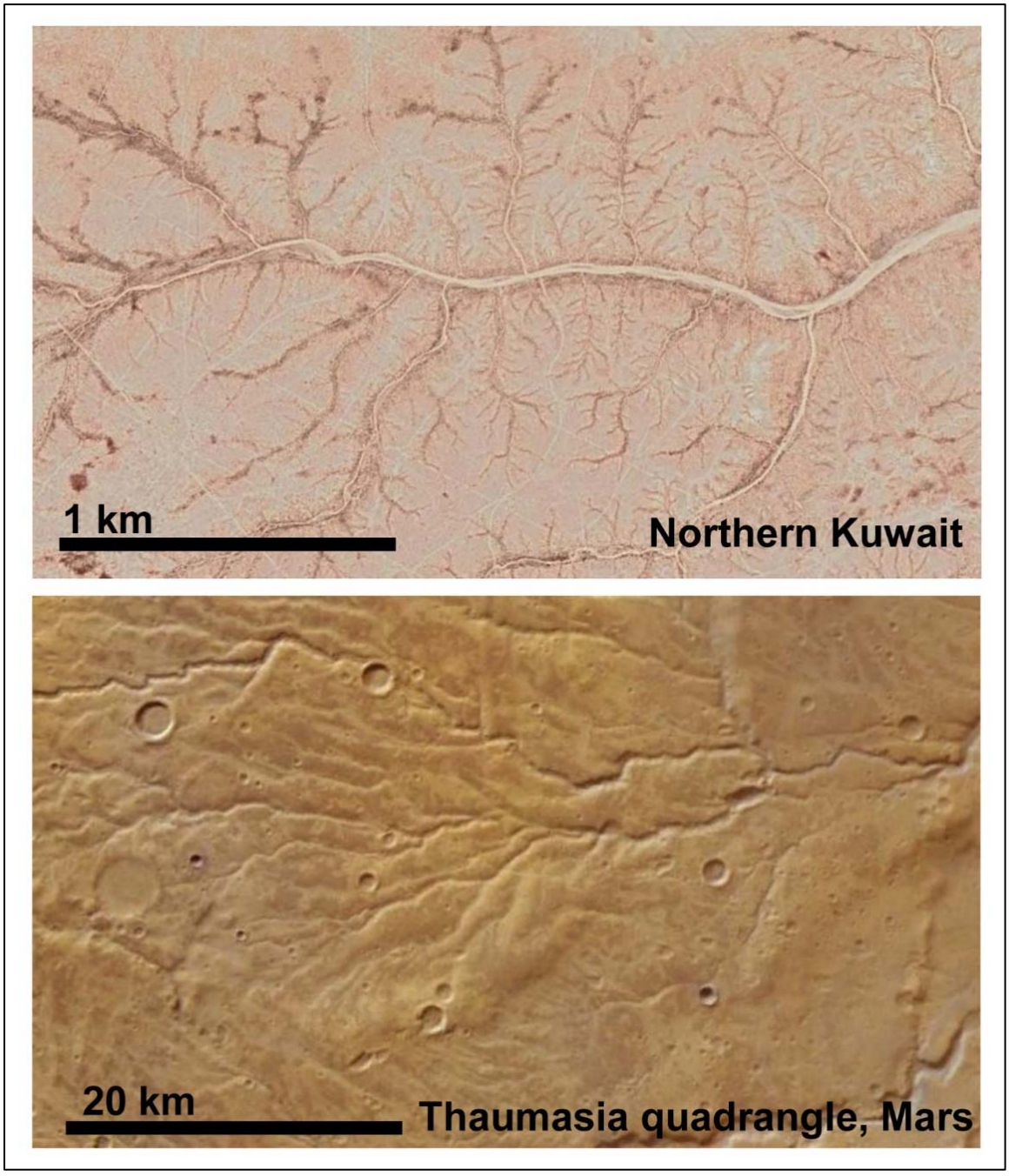

Figure 3. The dendritic drainage pattern of an ephemeral creek in Kuwait (top), and a dendritic pattern from a valley network on Mars (bottom).

HYDROLOGY OF DESERTS

The Water Cycle

Investigating water in deserts seems somewhat counterintuitive, but water is a very active force in arid regions at both the surface and subsurface. As discussed earlier in this paper, deserts are subjected to extreme environmental conditions. Rainfall is sparse, highly variable, and sometimes episodic. Depending on the intensity of rainfall, temperature, wind, and humidity of a location, precipitation may evaporate soon after it condenses or collects on the surface. Rainfall that intercepts the surface can seep through cracks in rocks and sediments as infiltration. If the rainfall rate exceeds the infiltration rate, or the infiltration capacity of a material is exceeded, rainfall will run off and accumulate in topographic low areas. Runoff may accumulate in river channels and basins, sometimes so much so that temporary flooding will occur. The surface water is eventually evaporated back into the atmosphere, taken in by plants, or infiltrated into the subsurface to replenish the groundwater. This is referred to as the ephemeral nature of surface water bodies and an essential part of the water cycle in drylands. Hydrologists quantify the water cycle by constructing a water budget. Due to the paucity of surface water bodies in deserts, a basic form of the water budget is presented:

$$P = ET + R + \Delta S \tag{2}$$

where P is precipitation (L^3), ET is evapotranspiration (L^3), R is runoff (L^3), and ΔS is the change in groundwater storage (L^3) (Fetter, 1988). The next sections will describe the most common parts of the water budget and their unique properties in deserts.

Precipitation

One of the most known characteristics of a desert is its lack of precipitation. Atmospheric precipitation also takes the form of fog, snow, hail, and sleet. For the scope of this paper, all precipitation will be referred to as rainfall unless otherwise specified. Precipitation as rainfall in deserts is delivered in a very irregular manner due to highly variable atmospheric conditions (e.g., ENSO). For example, the eastern side of the Namib desert receives most of its rainfall from intense, short-duration bursts of rainfall in the east (85 - 200 mm/yr) but as little as 2 mm/yr by fog from cold, upwelling oceanic air in the west (Sharon, 1981; Lancaster et al., 1984).

Kalma and Franks (2003) classify this variability by characterizing rainfall regimes as (1) a short rainy season followed by a long dry period, (2) several short rainy periods (< 48 hours) unevenly scattered, (3) extreme, high-intensity showers delivered over small areas (10 km^2), and (4) highly irregular rainfall across scales that cannot be statistically rendered. While this characterization attempts to capture the highly variable conditions of drylands, the recurring theme for these regimes is rainfall intensity, duration, and frequency. The next section will focus on rainfall intensity, or the amount of rainfall precipitated over a period.

Once rainfall exceeds a certain threshold or is above a rainfall intensity value, it may overcome evaporative processes. Soil may not be able to absorb all the water. This creates runoff, sometimes very high volumes that lead to flash floods, particularly in drylands. The consensus is that a rainfall intensity of 20 mm/hr or greater in arid environments is enough to trigger surface runoff and potentially flash floods (Koohafkan and Stewart, 2008). This is oversimplified because it disregards the temperature, soil properties, and other characteristics (e.g., slope, infiltration capacity) that also contributes to runoff. Even so, rainfall intensity is tightly coupled with runoff processes as well as groundwater replenishment in drylands.

Evaporation & Transpiration

Evaporation for the scope of this paper is defined as the conversion of water in its liquid phase to vapor by atmospheric conditions. In all environments, evaporation is driven by temperature, humidity, and wind. If the air is warm and humidity is low, evaporative processes are more likely to remove moisture from the air and ground. Evaporation can be measured directly (e.g., evaporation pans, lysimeters) and indirectly (e.g., temperature) (Penman, 1948; Thornthwaite, 1948). Both approaches provide insight into evaporation rates of a region of interest. However indirect measurement of potential evaporation, or the atmospheric demand for moisture in the air and ground, is commonly used for deserts. Potential evaporation rates in drylands often far exceed rainfall rates in deserts due to their high temperatures. For example, the Negev Desert of the northern Arabian Peninsula typically receives 50 to 200 mm of rainfall each year. Potential evaporation rates range from 1400 mm/yr to greater than 2600 mm/yr (Nativ, 2004). This results not only in the drying of the air but also in the drying of the surface and subsurface by capillary processes. Humidity, or the paucity of, also plays a role in evaporation for deserts. The lack of humidity in deserts creates a positive feedback loop for evaporation. Dry air does not reflect incoming solar radiation as it does in solar regions. Therefore, the arid lands can receive twice as much as solar radiation as humid regions. Wind also plays a role in evaporation as it removes moist air around plants and soil. Evaporation increases with high temperatures, low humidity, and strong winds.

Transpiration is the process by which water is taken up and evaporated from the roots, leaves, stems, and flowers of plants. In hyper-arid regions where vegetation is not prolific, transpiration may not be a factor considered for the water budget. However, in arid and semi-arid regions, perennial and ephemeral vegetation may have a significant impact on the

evapotranspiration (the combined removal of water by evaporation and transpiration) and the water budget, including the amount of surface runoff and interception of subsurface infiltrating water (Kacimov and Obnosov, 2019). The common types of vegetation and their responses to rainfall and runoff in arid lands are summarized in El-Ghani et al. (2017).

Runoff & Infiltration

Runoff is the term in hydrology used to describe water within the water cycle that flows over the surface and not into the subsurface. Due to the episodic nature of rainfall in deserts, storms can quickly generate large volumes of surface runoff (Figure 4). This may result in the rapid transport of surface runoff to ephemeral channels and playas. Climate (e.g., rainfall, temperature, humidity) is a factor that controls runoff, but vegetation, geomorphology, and geology also play a role. The lack of vegetation in deserts intensifies runoff along with hard, steeply sloped surfaces (i.e., desert pavement). For example, the Jal-az-Zor escarpment (elevation = 145 m) in eastern Kuwait disrupts the gentle slope and relatively lower elevations (< 50 m) of the surrounding area. The high-point is surrounded by low hills and shallow depressions. Several ephemeral channels, referred to as wadis, carry water after rainfall to this area, which accumulates in the depressions. While the area has experienced significant damage to private property due to flash flooding, the natural functionality of the basins to accommodate the runoff is considered a suitable site to harvest stormwater (Al-Rukaibi et al., 2017). Some of the accumulated runoff is susceptible to evapotranspiration, while the remaining infiltrates into the subsurface to replenish groundwater.

Infiltration is a term applied in hydrology when water intercepts the surface and is absorbed by the subsurface. The infiltration capacity in deserts is highly variable due to the characteristics of the soils, sediments, and rocks on the surface (Beutner et al., 1940; USDA-NRCS, 2007). Dry, highly permeable, porous sediments and rocks (i.e., gravel, sandstone) typically have a high

infiltration capacity. Dry sediments and rocks in deserts with low permeability (e.g., desert pavement) do not have a high infiltration capacity due to an inability to easily transmit fluid through the pores, referred to as permeability. Desert pavement is a surface covered with closely interlocking fragments of pebbles and cobbles, from which fine material is stabilized underneath. This reduces infiltration and increases runoff. One local name of desert pavement is "gibber" in Australia. Clay, which is common on both the surface of deserts as claypans as well as in the subsurface as impervious stratigraphic layers, dramatically reduces infiltration and increases runoff on the surface.

The amount of moisture in the pore spaces of material also affects the infiltration capacity to absorb water. As the water content of the sediment increases, the infiltration capacity decreases. Early studies by Horton (1933) showed that an equilibrium infiltration capacity is reached during the absorption of rainfall. This depends not only on the porosity and initial saturation of the sediment but also on the presence of colloidal particles (i.e., clay) that swell when wet. The infiltration capacity is negatively correlated with both the water content of the sediment and precipitation rate. When the sediments become completely saturated, the surface can no longer absorb the water which runs off. This is referred to as excess runoff. When the precipitation rate exceeds the equilibrium infiltration capacity, water cannot be absorbed quickly enough and runs off the surface. This is referred to as Horton overland flow. The interplay between infiltration and runoff in deserts is significant because these processes not only promote the movement of water on the surface but also help determine how much of it infiltrates to replenish the groundwater reserves.

Groundwater & Recharge

Water that infiltrates into the subsurface through the pores of sediment and rock is called groundwater (Figure 5). Surprisingly, most deserts contain large volumes of groundwater despite the paucity of rainfall and surface water bodies. This is made possible by past, wetter climatic conditions that supplied water presently stored in the subsurface. The age of groundwater, or the amount of time elapsed since a water molecule entered the subsurface, can span hundreds of thousands of years or longer. As a result, most of the freshwater in deserts are considered fossil water. For example, the Nubian Sandstone Aquifer System currently contains 14,460,000 Mm^3 of exploitable, non-renewable groundwater. Isotopic dating techniques have measured the groundwater age in this aquifer to range from 21,000 years at depths of 300 m and 800 m to more than 50,000 years at depths of 750 m below the surface (Foster and Loucks, 2006; Abouelmagd et al., 2014).

Fresh groundwater in deserts is considered non-renewable because the aquifers are not replenished. Groundwater recharge is a term used when referring to the downward infiltration of water through the unsaturated zone to the water table. Infiltration contributes to the storage of the groundwater system (Meinzer, 1923; Freeze, 1969). Like runoff and infiltration, the factors that control recharge are climate, topography, geology, vegetation, as well as land use. In deserts, recharge to the groundwater system occurs from runoff after episodic rainfall that infiltrates into the surface from a channel or low elevation area like a playa, or by water infiltrating directly into the pore space of an outcropped hydrogeologic unit. Arid zones are already vulnerable to a lack of recharge simply because of the relatively low rainfall and high evaporation in these regions. Like infiltration, recharge is promoted in highly-permeable media (e.g. sandstone). In drylands, these include but are not limited to sandstones, limestones, evaporites, unconsolidated depositional

landforms, and desert pavements. Understanding the geology of any environment is requisite to understanding and quantifying recharge. Other important geologic features are the relative position of geologic units in the subsurface referred to as stratigraphy, and structural features (e.g. faults, ridges). Overall, groundwater receives very small, if any, freshwater recharge to the existing groundwater system (Alsharhan et al., 2001b).

Other than non-renewable fossil freshwater, groundwater in drylands of often brackish to saline. This is due in part to the water age and geology of the subsurface. As groundwater flows through the pore spaces of sediment and rocks over long residence times or the period water travels from the recharge area to the discharge area, the water reacts with the rock and becomes mineralized. Residence time is like water age in that water can persist in the subsurface from tens to millions of years. As a result, the chemistry of groundwater in deserts is highly variable. The water classification summary is listed in Table 2. According to the International Groundwater Resources Assessment Center (IGRAC), the world-wide total area with brackish to saline groundwater at shallow and intermediate depths is approximately 24 million km^2 (Figure 6).

Table 2. Classification of water salinity.

Class Name	TDS range (mg/l)
Freshwater	0 – 1,000
Brackish water	1,000 – 10,000
Saline water	10,000 – 100,000
Brine	100,000

Brackish to saline groundwater poses serious problems in arid environments for humans. It is expensive to desalinate and cannot be directly used for most agricultural applications. However, in some cases, the occurrence of brackish to saline groundwater at shallow depths promotes the accumulation of meteoric freshwater in the subsurface as inland freshwater lenses (IFLs). These

sporadic, localized freshwater resources are often the only form of renewable freshwater resources in drylands (Kuldzhayev, 1974; Barrett et al., 2002; Houben et al., 2014; Milewski et al., 2014b; Kacimov and Obnosov, 2019).

The exploration of new water resources in arid lands includes the identification and improved understanding of IFLs, as well as the geomorphic and geologic systems that favor the past and present accumulation of groundwater on Earth and extraterrestrial settings. The next section will discuss those geomorphic and geologic systems in arid lands that promote the accumulation of groundwater on planetary surfaces.

Figure 4. Example of surface runoff in central Kuwait after episodic rainfall: (a) Al-Liyah, 2010, (b) Al-Salyyel, 2009, (c) Al-Jarfan, 2010, and (d) Jal Al-Zor, 2012. Photographs courtesy of Barq Albraq photos ©.

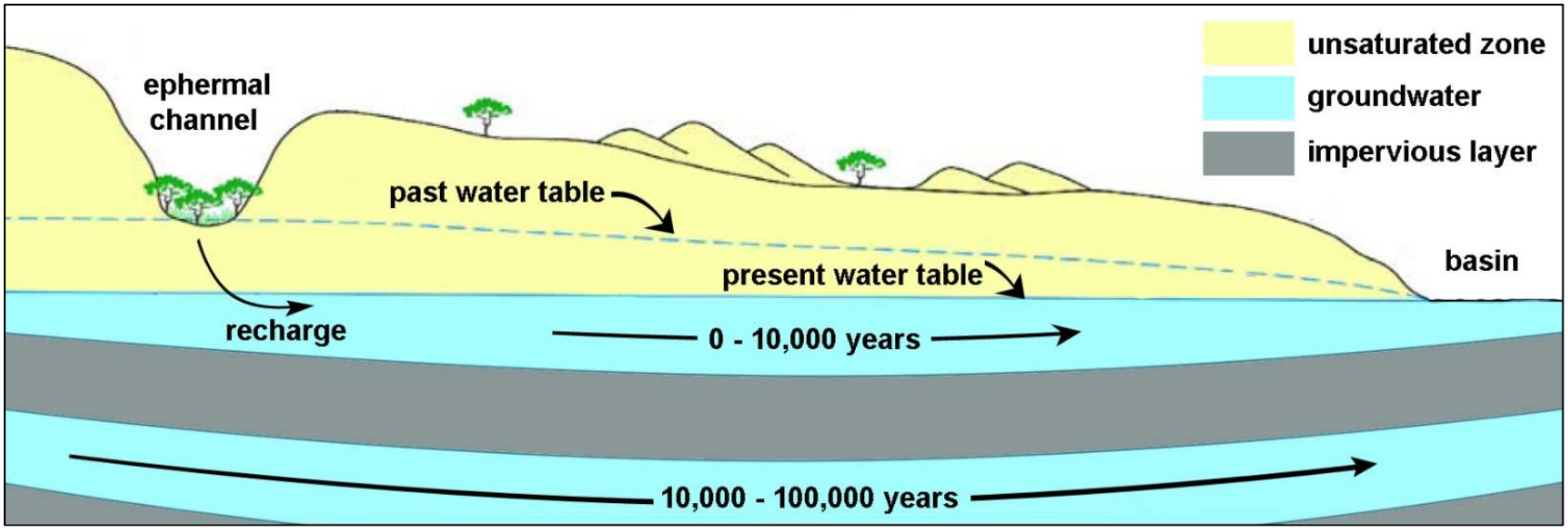

Figure 5. Conceptual diagram of a groundwater system and water age in deserts modified from Foster and Loucks (2006).

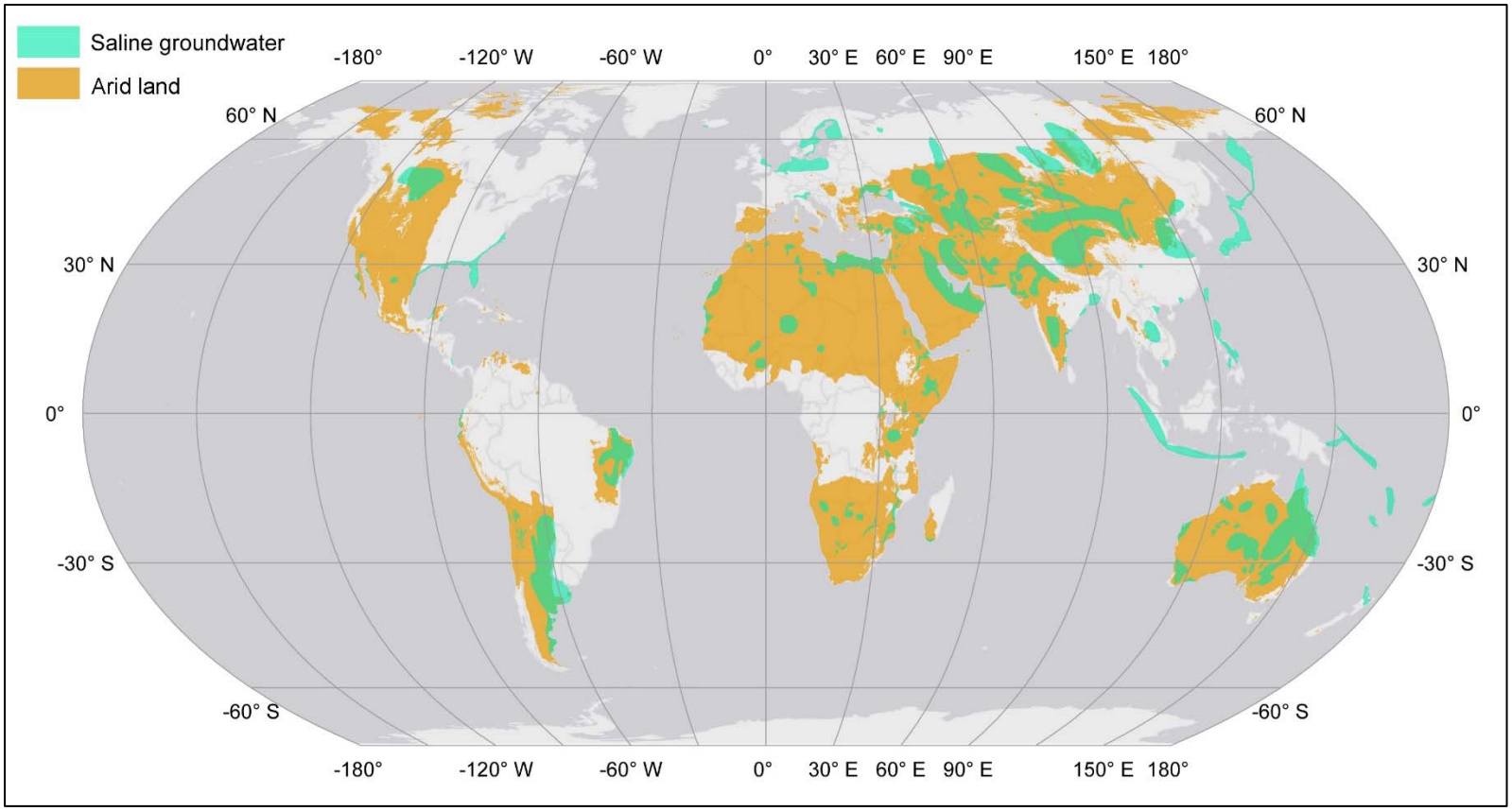

Figure 6. The global occurrence of saline groundwater and arid land. Data source from Van Weert and van der Gun (2012) and CGIAR-CSI (2009).

Geomorphic & Geologic Indicators

The geologic and geomorphic features at zones of hydrologic flux in drylands are not mutually exclusive. The processes responsible for their formation work in tandem across scales. For example, a basin is defined as a low area in the Earth's crust of tectonic origin. This is a geological process. However, basins evolve by fluvial processes and contain smaller geomorphic features such as playas, shallow lakes that fill periodically. Common geological features of playas are evaporite minerals, such as halite and gypsum, that precipitate from the wetting and drying of the lake. Therefore, the interplay between the geomorphology and geology are tightly coupled and useful for identifying zones of hydrologic flux. These features are referred to as the geomorphic and geologic indicators of zones of hydrologic flux and are summarized in Table 3 and visual examples provided in Figure 7.

Table 3. Summary of relevant geomorphic indicators of zones of hydrologic flux.

Indicator	Definition	Formation Process
Basin	A regional-scale term for a low area in the Earth's crust of tectonic origin. Includes impact craters.	Geologic
Depression	A general small-scale term for a low sunken area.	Geomorphic
Playa	Flat-floor depression within a basin that temporarily becomes a shallow lake.	Geomorphic
Interdune swale	The flat or gently sloping depression between dunes.	Geomorphic
Claypan	A small depression with a slowly permeable, sub-soil layer of clay.	Geomorphic
Ephemeral channel	A general term for a dry river or stream bed eroded into the surface by water, may or may not temporarily fill with water.	Geomorphic
Alluvial Fan	Fan-shaped mass of alluvium deposited by water that terminates in a low elevation area such as a basin.	Geomorphic
Evaporite mineral	Precipitated mineral resulting from evaporative processes or fluctuations of the water table. Common in playas.	Geologic
Fault	Thrust or normal faults systems that influence drainage of the basin; often intersects with channels and basins.	Geologic

Basins & Depressions

The terms basin and depression are often used interchangeably, but there are specific differences between these landforms. Basins are regional, low elevation valleys formed by tectonic origin. A classification system of modern basins of known plate tectonic settings is found in Ingersoll (1988). The Arabian Gulf, home to one of the world's largest petroleum basins, formed by a large asymmetric syncline located between the Arabian Peninsula and Iran. Within the basin, there are several geomorphic structures including the Basra-Kuwait and Rub-El-Khail Depressions (Li, 2011). An exoreic basin drains to the ocean, and an endorheic basin drains internally.

The term depression is defined as a low elevation area on a local scale that has no downslope flow paths. Depressions can form as a result of tectonics but also aeolian processes such as deflation by wind (Neal, 1975). In Kuwait, the Raudhatain and Umm-Al-Aish depressions formed by wind erosion that led to the lowering of the land (Al-Sulaimi and Mukhopadhyay, 2000). Depression is a general term used for most low-lying sunken areas.

Playas

The term playa in the context of arid environments is specific in that they occur in the lower portions of endorheic, internally draining basins. Playas are dry lakes that periodically flood. A playa lake refers to a playa that is filled with water. Lake Eyre, a playa in the lowest point of the Great Artesian Basin of Australia, periodically floods as seen in Figure 7. Playas are archives of climate as they can show the frequency and magnitude of flooding over long temporal scales (Ely et al., 1993). This not only an important indicator of zones of hydrologic flux in drylands at present but also to understand past climates that may have been wetter including Mars (Grotzinger et al., 2005).

Interdune Swales

An interdune swale is a flat or gently sloping depression between dunes. Interdune swales experience the periodic flooding from surface runoff or groundwater discharge by a temporarily elevated water table after rainfall. Interdune swales often serve as desert refugia to vegetation, small animals, and bacteria (Li et al., 2015).

Claypans

Claypans are topographic low areas that contain a slowly permeable, sub-layer of clay carried by ephemeral streams from local and distal sources. The formation of clay in the layer may continue by weathering of in situ minerals, as well as illuviation (Jenny and Smith, 1935). Claypans occur at the terminus of rivers in flood-out plains, playas, and interdune swales. A continuous flat or gently sloping surface between dunes is referred to as an interdune swale. The morphology and scale of interdune swales differ by dune type.

Ephemeral Channels

The term ephemeral channel is used to describe a low elevation area that has been eroded into the surface by the intermittent flow of water. The term gully is sometimes interchanged with the term channel but for smaller, steeper sided, incisions with a low width-to-depth ratio (Knighton, 1998). In Arabic-speaking countries, the term wadi is used for an ephemeral channel. On Mars, many of the dry channels are described as valley networks because of their relatively large size compared to the fluvial networks on Earth (Baker et al., 1992). Although no periodic filling of valley networks on channels on Mars has been observed, liquid water is believed to have flowed intermittently on the surface over millennia in Mars ancient past (Craddock and Howard, 2002; Howard et al., 2005; Irwin et al., 2008).

Alluvial Fans

An alluvial fan is defined as a fan-shaped mass of alluvium deposited by water that terminates in a low elevation area such as a basin. This feature is a strong indicator of a zone of hydrologic flux for two reasons. The first is that the material deposited in fans grade from large, poorly-sorted, unconsolidated boulders and gravels at the higher elevations to small, well-sorted sand, silt, and clay alluvium along the bottom (Hooke, 1967). The highly permeable sediments towards the top of the fan make efficient storage reservoirs for infiltrating water. Some alluvial fans are called megafans and extend in length for as much as 100 km and make excellent aquifers (Caldwel, 1969). Alluvial fans occur in locations where the hydraulic gradient significantly increases. Figure 7 shows an example of an alluvial fan emptying into the Lake Eyre Basin where water can infiltrate into the subsurface of the basin to recharge the underlying surficial aquifer.

Mineral Deposits

In arid environments, the growth of a mineral precipitate implies past ponding of water. Runoff transported to a basin often contains dissolved ions from the rocks of the surrounding area or upstream. As the water evaporates or infiltrates into the surface, evaporite minerals (i.e., gypsum, halite) precipitate on the surface of the dried depression. Thinly laminated layers of silcrete also precipitate in zones of hydrologic flux from the seasonal fluctuation of the water table on the surface (Twidale and Milnes, 1983).

Faults

Faulting on the surface is an important geologic indicator of zones of hydrologic flux because of their ability to channel water through the cracks, as well as act as barriers or conduits to groundwater flow (Maclay and Small, 1983; Babiker and Gudmundsson, 2004). Faults coupled with other indicators of zones of hydrologic flux such as channels or alluvial fans strengthen the

possibility of groundwater accumulation in the area. For example, the Sardar river, and ephemeral channel that incises an uplifted region of the Shotori mountains in Iran terminates with an alluvial fan (Walker et al., 2003). The intersection of two or more faults and other features (i.e. dykes, shear zones) were also deemed favorable for groundwater accumulation in the Najd shear system of the Arabian Nubian Shield (Sultan et al., 2008b).

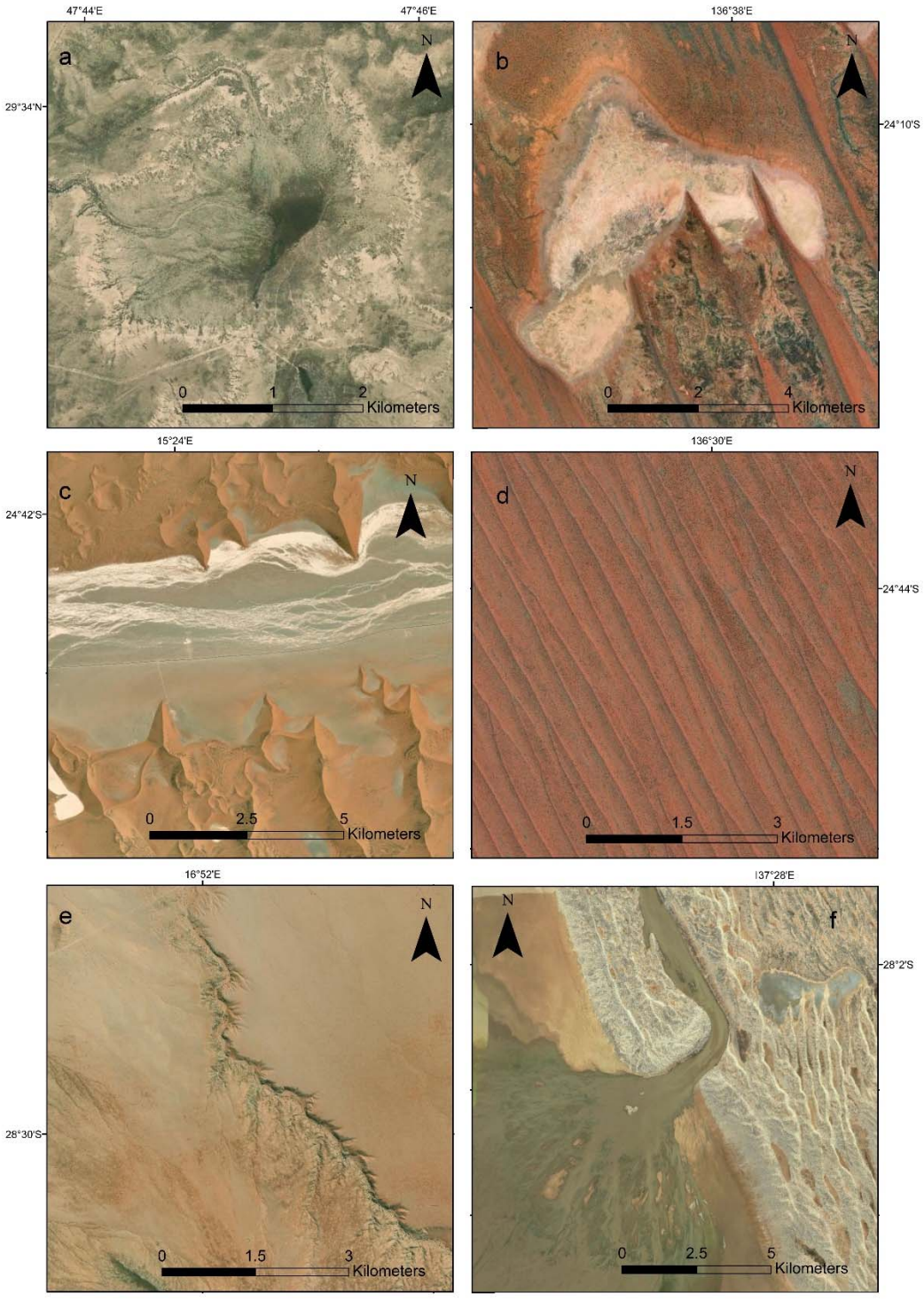

Figure 7. Geomorphic indicators of zones of hydrologic flux including (a) Rimmam depression in northern Kuwait, (b) playa in Plenty Lakes region of the Simpson Desert in Australia, (c) Deadvlei clay pan in the Namib Desert of southern Africa, (d) interdune swales within linear dunes in the Simpson Desert of Australia, (e), an ephemeral channel of the Kookrivier in South Africa, and (f) alluvial fan of Lake Eyre in Australia.

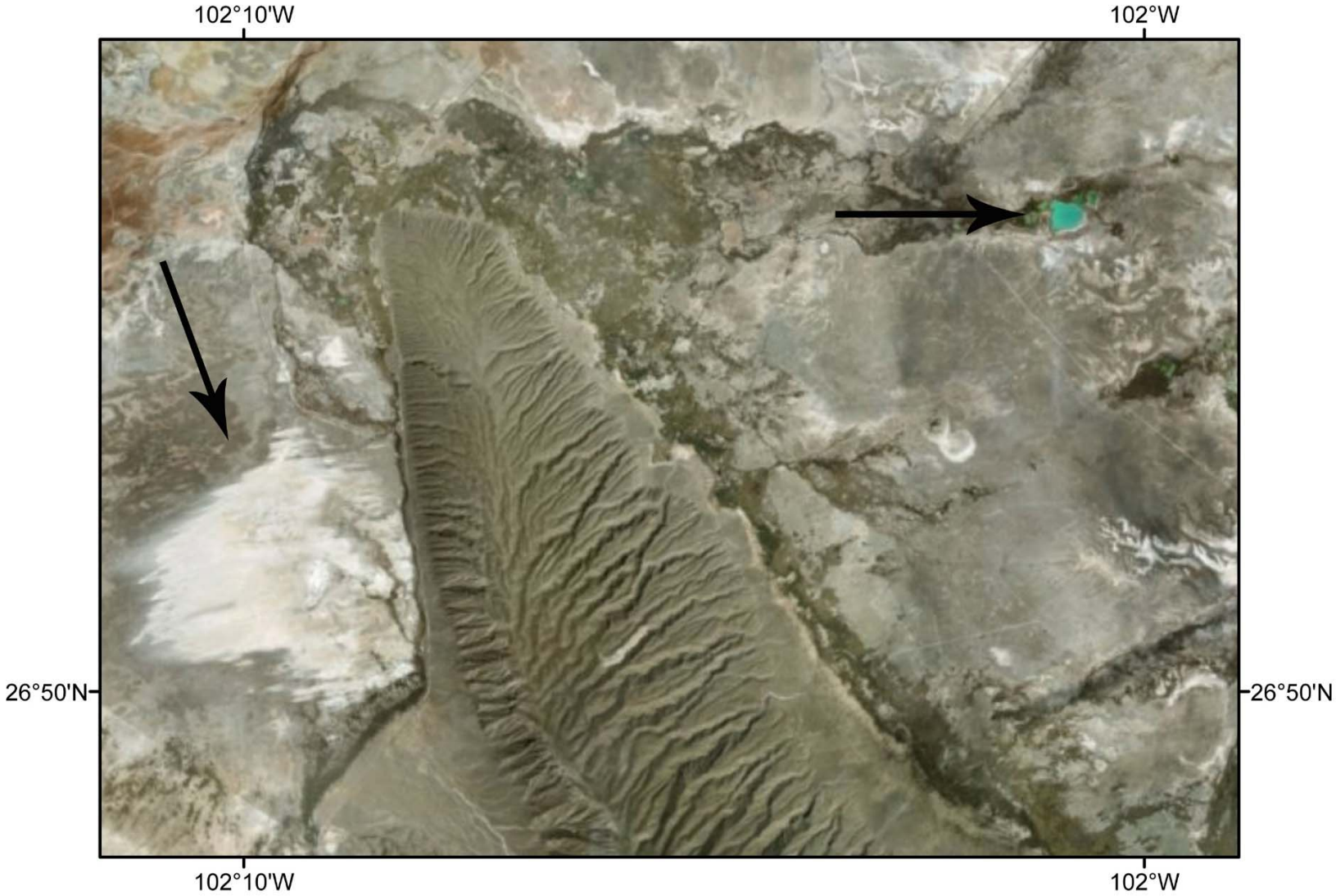

Figure 8. Evaporite formations (white-colored region) and springs of Cuatro Cinegas Basin of Mexico. The arrow on the right points to ponding water in a smaller depression of the area.

ZONES OF HYDROLOGIC FLUX

Whether it is in the deserts on Earth or extraterrestrial settings, “chasing the water” is likely one of the desert dweller’s earliest activities. Locations of interest are depressions, pans, playas, channels, and have playful and colloquial names (e.g. dayas, pang-yangs, spring pots, wadis) (Stone, 1967). The Aboriginal people in the traditional drylands of Australia used waterholes for migration paths, religious rituals, social gatherings, and to gather food. The relationship between water and land was a fundamental aspect of their survival and a recurring theme in Aboriginal Art (Figure 9) (Toussaint et al., 2005).

Understanding how landforms relate to water is essential to the locations of groundwater accumulation in the past and present. In this way, landforms are linked to the hydrologic system on Earth, particularly at locations where fluxes to and from groundwater reservoirs occur. These locations are referred to as recharge and discharge zones and serve as important nodes in hydrological networks across scales (Covino, 2017). Under natural conditions, recharge is defined as an influx of water to the subsurface that replenishes the groundwater reservoir. Conversely, discharge is the efflux of groundwater to the surface (Freeze, 1969). Zones of hydrologic flux (i.e. recharge, discharge) each exhibit distinct geomorphic and hydrogeologic characteristics. While recharge and discharge zones may occur in the same locations, discharge zones occur where the topography intersects the water table and recharge zones where the water table elevation is lower than the surface of a catchment. Thus, the distinction between a recharge and discharge zone is often driven by the elevation of the water table relative to the surface. This relationship is highly variable and depends greatly on climatic, geomorphic, and geologic factors. Integrated studies of zones of hydrologic flux on Earth and other planetary environments broaden our understanding of the hydrologic cycle, groundwater accumulation, and evolution over large temporal scales. The

next section will identify and discuss the geomorphic and geologic indicators of zones of hydrologic flux.

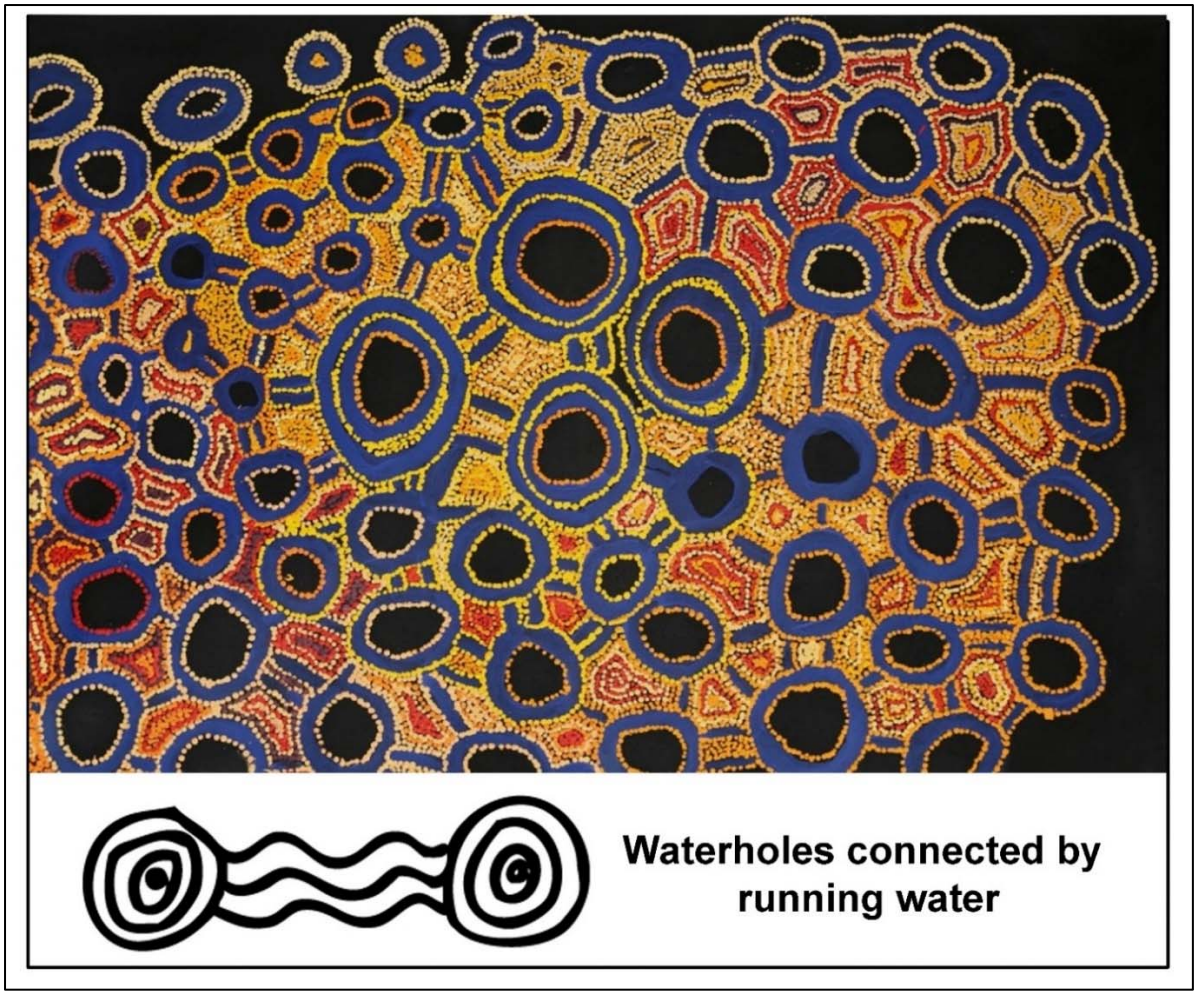

Figure 9. Aboriginal painting by Kathleen Jap, no. 011050 (top), and aboriginal symbol of waterholes connected by ephemeral channels (Plunkett, 2020).

Geomorphological Similarities on Mars

Geomorphic features on Earth have been used to explain the relationship between water and the Martian landscape for more than half a century (Pieri, 1979; Baker, 1982). The Martian surface is covered with many dry valley networks, channels, depressions, and impact basins, as well as extensive fault systems, clays, and evaporite minerals. These features along with infilled craters, debris flows, spillover channels, and shoreline indicators promote the idea of liquid water once flowing on the surface (Carr, 1986). Further, it is suggested that groundwater and ground ice reservoirs continue to exist within the Martian subsurface today (Squyres and Carr, 1986).

Aeolian depositional landforms, which require fluvial activity for sediment supply, have been observed on multiple planetary surfaces (Lee and Thomas, 1995; Lancaster, 2006; Craddock, 2012). Linear dunes occur on Venus, Earth, Mars, and Titan, all of which possess appreciable atmospheres and therefore support the idea that aeolian processes are not exclusive to Earth. The relationship between playas and other landforms on other planetary surfaces is an emerging topic. Landforms (i.e. mounds) have been identified to impact the morphology of linear dunes on Titan (Cisneros, 2014). While Hayes et al. (2017) analyzed the morphometry of lacustrine depressions in Titan's polar terrain to suggest past connectivity between regional lakes and seas.

Mineralogical evidence that supports the presence of water on Mars in the past was not available until after 1997 when the Thermal Emission Spectrometer (TES) identified hematite deposits in the Terra Meridiani (Christensen et al., 2000). They include oxides, phyllosilicates, hydrated silicates, carbonates, and sulfates (Ehlmann and Edwards, 2014). The presence of these minerals in conjunction with their respective sedimentary structures reveals information about the environment of which they formed (e.g. springs, playa lakes).

Large fault systems including and tectonic evolution has been recognized on Mars including the occurrence of Tharsis and a global collection of wrinkle ridges that surround the planet (Carr, 1974). Thrust faults have been identified in several regions including the Thaumasia and Arabia Terra regions where extensive fluvial networks occur (Grott et al., 2007; Klimczak et al., 2018). In some cases, channels are observed intersecting the fault systems. Implications of these observations include opportunities to constrain the timing and flow of surface water relative to the faulting, as well as zones of hydrologic flux where surface water infiltrated the brecciated rock of the faults to recharge the groundwater system. Other faults systems (i.e., polygonal, trace ridges) have also been associated with past water on Mars. (Treiman, 2008; Moscardelli et al., 2012).

CHAPTER 2

LITERATURE REVIEW

Research into the geomorphic and geologic indicators at zones of hydrologic flux in drylands from an interdisciplinary, planetary perspective is uncommon. In this context, geomorphological studies focus on the landforms and processes responsible for their formation across scales. Hydrogeological studies focus on the quantity and quality of recharge and discharge at zones of flux, and planetary studies focus on the identification of recharge and discharge zones as evidence to liquid water in extraterrestrial settings. Studies focusing specifically on recharge and/or discharge zones in semi-arid and arid environments are ever-present within the literature (Gee and Hillel, 1988; Allison et al., 1994; Scanlon et al., 2006; Chowdhury et al., 2010). Investigations primarily deal with (1) field and laboratory approaches to understanding the changes in climate and dominant processes over long temporal scales, (2) modeling groundwater proximal to recharge and discharge zones, and (3) the geospatial analysis of regional and global data sets for the identification and recharge and discharge zones. The following section highlights the significant studies within the literature that lay the framework for approaching questions of geomorphological and hydrological significance through the lens of geomorphic and geologic indicators in drylands on Earth and extraterrestrial settings.

Field & Laboratory Studies

Field and laboratory studies into geomorphic and geologic landforms and their relationship to zones of hydrologic flux in drylands begin with early, scientific explorations into deserts. Charles Sturt (1844), Ted Colson (1936), and Cecil Madigan (1939) were the first to cross the

Simpson Desert for exploratory and scientific purposes (Sturt, 1849; Madigan, 1946). Sturt was the first to identify the Strzelecki, Cooper, and Eyre Creeks, while Madigan documented their 19-day trek across the "dead heart" of the Simpson Desert with a botanist, biological collector, geologist, photographer, wireless operator, cook, camel man, and an Aboriginal guide. Madigan also performed an aerial survey highlighting the ubiquity of linear dunes throughout the region (Royal Geographical Society, 1929). Charles Montagu Doughty, also a British explorer, explored the Arabian Deserts for almost two years creating geologic maps including lava floods, ancient irrigation systems (e.g., qanats), and Captain William Shakespear (1914) documented geographical and geological features between Kuwait and Riyadh (Vincent, 2008).

Fieldwork has progressed considerably since the days of camels, and most deserts today have been explored and are relatively more accessible compared to the past. Extensive fieldwork on the lithological, mineralogical, and chronological characteristics of linear dunes is well-documented. Folk (1976) created a classification system for the colored sediments of the Simpson, of which the oldest and darkest red dune sand are of Pleistocene, orange sands are Holocene, and dull yellow-green are Paleozoic. Further, he identified the sediment as quartz with hematite and limonite coatings depending on the amount of weathering. Lancaster (1986) investigated the grain size and sorting of sediments from linear dunes and interdune swales in the southwestern Kalahari and determined that grains of dunes coarsen up towards the crest. Magee et al. (1995) identified the deflation of deep and shallow water lacustrine environments through the variations of gypsum and halite evaporites in the Madigan Gulf section of Lake Eyre. The study also compiled a summary of chronological dating literature (i.e. radiocarbon, uranium/thorium, and thermoluminescence (TL)) obtained to reconstruct the paleohydrology of the area. Craddock et al. (2015) combined sampling and in-situ measurements with data collection by the Global

Positioning System (GPS) and unmanned aerial systems (UASs) over a series of visits to track dune activity in the Simpson Desert.

Fitzsimmons et al. (2007) pointed out that the lack of organic material in dunes, along with high levels of uncertainty in TL studies are problematic for accurately dating desert landforms. Instead, optically stimulated luminescence (OSL) techniques were used to precisely date the linear and transverse dunes new the ephemeral Lake Frome in the Strzelecki Desert of Australia. OSL is the current standard for measuring the chronology of landforms composed of quartz grains in deserts (Huntley et al., 1985; Lian, 2007). The age since the time of burial of the mineral grain can be obtained from samples as small as tens of microns in diameter to as large as boulders on a time scale to roughly 100-200 ka (Smedley, 2018). Other laboratory methods such as X-ray diffraction (XRD) are used to obtain the bulk-composition of desert sediments which reflect the local and upland geology (Wasson et al., 1984; Goudie et al., 1993; El-Sayed, 1999; Cohen et al., 2010).

Field and laboratory studies on Mars fall into two groups. This first group encompasses Earth analog sites where studies are conducted in terrestrial settings with environmental conditions like Mars (Wharton Jr et al., 1989; Golombek and Rapp, 1997). The second group encompasses in-situ studies currently conducted on Mars by rover missions. One of the most popular studies for Earth analog sites for Mars is by Wierzchos et al. (2006) in the Atacama Desert where thick layers of halite evaporite rocks contain cyanobacteria colonies. However, many analog sites have been investigated for their geomorphological and geological similarities and relationship with past and present accumulation of groundwater (Heggy, 2018). Precipitated silica formations and discharging brine groundwater in Manitoba, Canada have been investigated for their astrobiological significance (Grasby et al., 2009). While the search for life is certainly a goal for many investigations related to water on Mars, many shield and platform deserts make excellent

terrestrial analogs for aeolian landform investigations in the Saharan, Kalahari, and Australian Deserts (El-Baz et al., 1979; Livingstone et al., 2010; Craddock, 2012).

Modeling Zones of Hydrologic Flux

The mathematical framework to calculate groundwater recharge was developed in classical studies based on the Dupuit-Forchheimer assumption in one and two-dimensional numerical solutions (Jacob, 1943; Maasland, 1959), using a resistance network (Bouwer, 1962), and analytical expressions (Dagan, 1967; Hantush, 1967). Visual and physical models of groundwater flow processes have been developed for groundwater investigations and are described in detail by Shanafield et al. (2019). Groundwater hydrology numerical studies continued with the integration of soil physics (e.g. evaporation, infiltration) to explain the mechanisms of groundwater recharge and discharge from a saturated-unsaturated perspective (Freeze, 1969). Three-dimensional, transient flow, numerical solutions including infiltration, groundwater recharge, water table depth, and stream base flow were created to simulate the hydrologic response of groundwater basins to rainfall and support new water resources management initiatives (Freeze, 1971, 1979). McDonald and Harbaugh (1988) developed a modular, three-dimensional, finite-difference groundwater model (MODFLOW) to simulate groundwater flow associated with external processes such as recharge. MODFLOW as well as a suite of multi-dimensional numerical modeling software. continues to evolve and is applied to many current studies (Ehtiat et al., 2018). For example, the Great Artesian Basin has been modeled as an entire basin and part-basin with MODFLOW. A summary of the Great Artesian Basin numerical models can be found in Welsh and Doherty (2005).

Guo and Langevin (2002) incorporated the variable-density programming code of MODFLOW with SEAWAT, to investigate the flow and transport of groundwater when multiple species of varying solute concentrations are present. Numerical, analytical, and physical modeling

of variable-density groundwater studies are primarily limited to saltwater intrusion problems in coastal settings (Qahman and Larabi, 2006; Dose et al., 2014). These studies include the investigation of a freshwater lens or wedge atop saline groundwater from the ocean. Few studies specifically consider indicators of hydrologic flux and variable-density environments. Szymkiewicz et al. (2018) investigated recharge and water table fluctuations of groundwater beneath an interdune area in coastal Brazil, and Chang et al. (2018) simulated seawater intrusion to coastal aquifers in the south coast of Laizhou Bay, China. Most arid regions, except for places like the Atacama Desert, are located a considerable distance from the ocean and are vulnerable to saltwater intrusion into local freshwater aquifers (e.g., inland freshwater lenses) by groundwater that has become highly mineralized over long residence times. Hantush (1967), Fetter (1972), and Van Der Veer (1977) presented analytical solutions to solve water table elevation as a function of density differences and recharge zone area. Numerical models of dryland variable-density environments are scant within the literature but offer an improved approximation of water table elevation over multiple time steps (Al-Weshah and Yihdego, 2016; Alrashidi and Bailey, 2020). These numerical models include the groundwater flow equation coupled with variable-density principles by Baydon-Ghyben (1898) that approximate the thickness of the freshwater lens. However, heterogeneities of media in the subsurface coupled with the lateral movement of inland freshwater lenses presented challenges in estimating the lens volume. This means that even when the water table elevation is modeled within acceptable parameters, the estimate of the freshwater volume may not be accurate. Advanced numerical modeling and calibration techniques are required to accurately estimate freshwater lens geometry for desert inland freshwater lens systems.

Modeling groundwater systems on Mars is limited to conceptual and statistical models due to our lack of knowledge on the subsurface. Inferences made from geomorphic and geologic

indicators such as impact basins and sedimentary rocks suggest that a planet-wide, liquid groundwater system once existed on Mars (Clifford, 1993; Salese et al., 2019). Numerical models in the literature mostly focus on paleoclimatic reconstructions or geochemical models to build a case for past water on Mars. For example, Turbet et al. (2017) suggest with a three-dimensional, global climate model that groundwater sourced flooding from large outflow channels on Mars induced significant rainfall responsible for the large valley networks.

Geospatial Analysis & Remote Sensing

Studies regarding geomorphic and geologic indicators of zones of hydrologic flux include a detailed analysis of the local and regional topography to determine recharge and discharge zones. In particular, the occurrence of topographic depressions in select drylands (Reeves Jr, 1966; Lancaster, 1978; Goudie, 1991; Al-Sulaimi and El-Rabaa, 1994). Topographic information once measured in-situ, is now derived by stereograms and digital elevation models (DEMs) from high-resolution satellite sensors (e.g., passive, active) including shuttle radar and light imaging and ranging (LiDAR) (Le and Kumar, 2014). This data informs studies dedicated to understanding the relationship between the topography and water for past, present, and future.

In Kuwait, Al-Sulaimi et al. (1997) used detailed morphometric data to delineate subsurface drainage network through the gravel and sand deposits, which later informed the integrated study by (Milewski et al., 2014b) using climatic, topographic, geologic, and hydrogeologic data to identify recharge zones and quantify recharge volumes. The latter study quantified recharge with a computational model called the Surface Water Assessment Tool (SWAT). Meteoric recharge was thought to be negligible for the region, and this study demonstrated how arid regions can accumulate appreciable volumes of renewable freshwater when conditions are favorable for groundwater accumulation.

In southeastern Australia, Tweed et al. (2007) combined remote sensing and GIS techniques to identify a series of surface-subsurface recharge and discharge areas in salinity prone catchments in Australia. Geospatial information systems and remote sensing methods are also used for paleohydrology studies, such as Craddock et al. (2010) who identified a buried fluvial landscape in Australia using topographic data. As new remote sensing technologies (e.g., Advanced Land Observing Satellite (ALOS) Phased Array Type L-band Synthetic Aperture Radar (PALSAR)) become publicly available, more paleohydrologic features in drylands will be identified. Abdelkareem et al. (2020) showed advancements in the observation of paleodrainage systems that underlay a dune system and terminate a depression in Saudi Arabia.

Geologic features such as basement uplifts and faults have also been investigated as zones of groundwater accumulation using integrated applications with remote sensing. Dailey et al. (2015) combined LiDAR and Geo-Eye 1 remote sensing images, geophysical, and isotopic data to show how fault zones redirect groundwater flow along a fault system in the Mojave Desert. The intersection of two or more faults and other features (i.e., dykes, shear zones) were also deemed favorable for groundwater accumulation in the Najd shear system of the Arabian Nubian shield using field data and Landsat-based methodologies (Sultan et al., 2008b). Discharge zones containing deep-seated faults and overlaying alluvium in the Saharan were identified using remote sensing, geochemical, and isotopic data sets (Sultan et al., 2007). These studies demonstrate how remote sensing and GIS mapping applications can use structural elements in arid regions on Earth to identify zones of hydrologic flux and groundwater accumulation.

Except for rover missions, most of the data collected for studies on Mars is from remotely sensed orbital or fly-by spacecraft observations. A complete chronology of Mars exploration can be found at Williams (2020). Of note is the Mars Reconnaissance Orbiter (MRO). The payload

includes a high-resolution visible imaging stereo camera (HiRISE), the Compact Reconnaissance Imaging Spectrometer for Mars (CRISM), the wide-area Context Camera (CTX), a shallow subsurface sounding radar (SHARAD), and other sensors to monitor atmospheric activities. Global geological and geomorphological maps have been created from the data collected by this and other missions (Christensen et al., 2001; Hynek et al., 2010; Tanaka et al., 2014). Morphometric and statistical analyses of data from Mars missions provide evidence for fluvial activity, an active hydrologic cycle, and a warm/wet Mars (Craddock and Howard, 2002; Howard et al., 2005; Matsubara et al., 2013). DEMs from the Mars Orbiter Laser Altimeter (MOLA) sensor and other regional data sets are now used with machine learning algorithms to map the groundwater recharge potential zones on Mars (Pourghasemi et al., 2020). Investigations regarding water in Mars include a combination of remote sensing and field data to investigate a variety of Saharan landforms (i.e. theater-headed valleys, depressions, escarpments, playas, tufa deposits) to better understand their relationship to groundwater processes to extrapolate to Mars (Abotalib et al., 2016). Novel analyses of structural features (i.e., thrust faults) and fluvial features (i.e., outflow channels) on Mars are required to advance our knowledge of zones of groundwater accumulation.

RESEARCH AIMS AND OBJECTIVES

Studies attempting to answer questions of geomorphological and hydrological significance through the lens of geomorphic and geologic indicators at zones of hydrologic flux are uncommon. Integrated disciplines and techniques provide researchers with unique opportunities to approach these questions and provide a holistic understanding of the timing and flow of surface and subsurface waters in drylands across scales.

FOCUS OF STUDY

This research provides a detailed examination of two dryland areas on Earth and an exploratory analysis for one on Mars. The first example is of a playa lake and linear dune field located at Lake Caroline in the northern Simpson Desert of Australia. The second example is at a topographic depression in the desert of northern Kuwait, and the last example is located at the intersection between a thrust fault and a fluvial channel in the northern Arabia Terra region of Mars. The objectives for these examples are listed below:

RESEARCH AIMS AND OBJECTIVES

1. **Playa Lake and Linear Dune Study**: Examine the relationship between playa sediments and linear dune formation in the northern Simpson Desert of Australia using lithological, mineralogical, and chronological techniques.

2. **Inland Freshwater Lens Study:** Investigate the accumulation of fresh groundwater beneath a topographic depression and atop a saline groundwater system in northern Kuwait using physical, analytical, and numerical modeling techniques.

3. **Thrust Fault on Mars Study:** Propose a future study to investigate the intersection of a thrust fault and fluvial channel on Mars using remote sensing and fluvial geomorphological techniques.

VALUE OF RESEARCH

This research draws from the fields of geomorphology, geology, hydrogeology, and planetary science to evaluate the timing, source, and flow of surface and subsurface waters over varying spatial and temporal scales on Earth and other planetary surfaces. Studies like this are important to further our understanding of groundwater accumulation not only on Earth, where water resources are paramount in the face of population growth and climate change but also as we search for water within extraterrestrial settings.

This work explores the relationship between landforms and water resources in the deserts of Australia and Kuwait at present and the past during a wetter climate that provided the groundwater hidden in the subsurface. Global climate models predict an increase in the frequency and severity of extreme climatic events in drylands, including floods and droughts. Research into playa lake fluctuations and their effect on linear dunes in Australia is important for predictions regarding groundwater recharge to the Great Artesian Basin, as well as sediment supply for aeolian processes such as dune formation and dust storms. This is not only important for human populations in the region but also wildlife and vegetation which are highly sensitive to abrupt environmental changes (Greenville et al., 2012).

In Kuwait, renewable freshwater resources have been considered negligible until recently (Milewski et al., 2014b; Alrashidi and Bailey, 2020). Our knowledge regarding their formation and long-term plausibility is limited. Research into topographically induced inland freshwater

lenses is needed for the accurate estimate of water resources and their long-term sustainability. Further, naturally occurring saline groundwater environments, which occur throughout deserts on Earth and possibly Mars, provide opportunities for water resource discovery, artificial recharge, and stormwater management (Omar, 1982; Van Weert and van der Gun, 2012).

On Mars, this work supports future missions in the context of water resources and the search for life. The Mars 2020 Rover, Perseverance, is the next in-situ mission scheduled to launch in the summer of 2020. It will land in Jezero Crater in February 2021 to look for life. The rover has a ground-penetrating radar instrument specifically designed to look in the subsurface for ice. Research into geomorphic and geologic indicators on Mars, as well as analog sites on Earth like the Simpson Desert of Australia, inform stakeholders where future rover and human missions explore (Williford et al., 2018). In summary, integrated studies of zones of hydrologic flux on Earth and other planetary environments broaden our understanding of the hydrologic cycle and groundwater accumulation across scales on planetary surfaces.

CHAPTER 3

METHODOLOGY

Deserts are remote and often inaccessible. They contain few monitoring stations which lead to a paucity of continuous, long-term data. As scientists, how can we investigate the geomorphic and geologic indicators of zones of hydrologic flux to understand the timing and flow of water at these locations across scales? How can we use these investigations to better understand the processes of groundwater accumulation on other planetary surfaces? To answer these questions, an integrated, interdisciplinary research approach is needed. This includes the use of field and laboratory techniques, modeling, geospatial analysis, and remote sensing within the disciplines of geomorphology, geology, hydrogeology, and planetary science. A summary of the methods associated with each objective is presented in Table 4.

Table 4. Summary of geomorphic and geologic indicators, methods used, and related disciplines for each site location of research.

Study & Location	Indicator	Approach	Analysis	Discipline
Playa Lake and Linear Dune Australia (Lake Caroline)	Playa Linear Dune	Field methods Laboratory analyses Remote sensing techniques	-Lithological, Wind -XRD - -OSL -Rainfall/Flood	Geomorphology Hydrology Planetary Science
Inland Freshwater Lens Kuwait (Raudhatain Depression)	Depression Saline groundwater	Physical modeling Numerical modeling	Physical tank SEAWAT/MODFLOW	Hydrogeology
Thrust Fault on Mars Mars (Arabia Terra)	Thrust fault Channel	Remote sensing Quantitative methods	DEM derivation Fluvial mechanics	Geomorphology Geology Planetary Science

Design Method & Rationale

The process for gathering and analyzing data was unique for each of the objectives. Detailed methodologies for each example can be found in the following chapters dedicated specifically to the individual study. This section will summarize the process for gathering and analyzing the data for each objective, as well as a rationale for the design choice.

The Playa Lake and Linear Dune study in the northern Simpson Desert was selected because of the prominence of Lake Caroline among many smaller claypans in the area. The approach to meet the objectives included field methods, laboratory analyses, and remote sensing techniques. In the field, we made general observations and collected sediment samples. Those samples were analyzed at the University of Georgia Clay (UGA) Mineralogy Laboratory by a lithological analysis (i.e., grain size, composition) and mineralogical analysis by XRD techniques. Samples were also sent off for OSL testing to obtain the age of sediments. Weather station data was collected from publicly available sources, and remote sensing data were obtained in the UGA Water Resources and Remote Sensing (WRRS) Laboratory to understand the frequency of flooding at Lake Caroline.

The Inland Freshwater Lens study used a physical laboratory and numerical model to gather data and answer questions regarding the flow of subsurface groundwater in Kuwait. The previously built physical model in the Water Resources and Remote Sensing Laboratory was used to conduct additional simulations to finalize the data for the numerical analysis. The numerical model SEAWAT was used to solve the groundwater flow equation with MODFLOW and the solute transport equation with a Modular Three-Dimensional Multispecies Transport Model (MT3DMS).

The proposed Thrust Fault study on Mars focused on a site where a thrust fault intersected with a fluvial channel providing a unique opportunity to employ methods from geomorphology and structural geology to answer questions about the timing and flow of surface water in Arabia Terra on Mars. Newly available, high-resolution visual data (6 m) from CTX on Mars is available to create DEMs for topographic analysis.

The location for each study and the methodology was selected for their diverse combination of geomorphic and geologic indicators. The Playa Lake and Linear Dune study allows us to answer questions about the timing and flow of water on the surface of a desert that is an important hydrological location for human and wildlife populations on Earth but also can be used as an analog location for aeolian-fluvial interaction studies on Mars. The Inland Freshwater Lens study allows us to answer questions regarding the flow and timing of water in the subsurface beneath a topographic depression and saline groundwater using physical, analytical, and numerical models. Lastly, the proposed Thrust Fault on Mars study allows us to approach a question regarding the flow and timing of water on the surface of Mars and apply it to the identification of a potential zone of groundwater accumulation.

An important benefit of the collection of locations, indicators, and methods chosen for this approach is that research can be conducted over varying spatial and temporal scales. Field methods are useful for smaller spatial scales, but also answer questions over longer temporal scales when combined with laboratory analyses such as OSL. Remote sensing data is useful to answer questions over larger spatial scales for the Thrust Fault on Mars study but is limited on the temporal scale due to the novelty of the data source. However, when combined with the principles of structural geology, fluvial mechanics, and other methods (e.g., crater counting), questions of the timing and flow of water on the surface of Mars can be answered. This study could have been just as impactful

if three separate studies were performed at one site and directly translated to a similar site on Mars. However, the selected studies provide scholars interested in interdisciplinary studies an approach to answer questions of geomorphological and hydrological significance at zones of hydrologic flux in drylands on Earth and Mars.

CHAPTER 4

PRESENT-DAY FLUVIAL INFLUENCES ON LINEAR DUNE FORMATION AT LAKE CAROLINE IN THE SIMPSON DESERT OF AUSTRALIA[1]

[1]Rachel Rotz, Adam M. Milewski, Robert Craddock, Alex Morgan, David Leigh. To be submitted to *Journal of Arid Environments*.

ABSTRACT

In present-day drylands, fluvial activity is typically not considered a dominant process for the supply of sediment and dune activity because of scant rainfall and its effect on dune stabilization by vegetation. However, intense episodes of moisture can tip the scale between aeolian and fluvial processes in terms of weathering, erosion, and landform development. This study considered the interaction between aeolian and fluvial processes and how they relate to the sand uptake of linear dunes. Lake Caroline, a prominent playa located in the northern Simpson Desert, was investigated as a case study to observe present-day aeolian-fluvial-lacustrine interaction. An integrated approach of field methods, laboratory analyses, and remote sensing techniques were employed. We observed that the playa has flooded at least 58 times over 19 years and the sediments are a combination of eroded dunes, weathered basement rock from the local area, clay, and evaporite minerals. Wind speeds at Lake Caroline have surpassed the threshold for transporting fine sand more than 20% of the time over a six-year analysis. Implications suggest that present-day hydrologic activity is sufficient to erode linear dunes and generate new sediment to be used by aeolian processes for linear dune accretion. Refining our understanding of the relationship between fluvial-aeolian interaction and linear dune development is useful to investigate how linear dunes form and evolve across scales.

INTRODUCTION

Fluvial processes triggered by occasional storms and episodic rainfall events, influence the sand uptake of active dunes even in present-day arid environments (Langford, 1989; Field et al., 2009). The surface runoff generated from these torrential rains removes sediment from landforms, transports it downslope, and deposits it in low lying areas (e.g., swales, drainage paths, claypans, and playas). In playas, fluvial erosion occurs alongside the base of adjacent dunes as water flows

through drainage paths along interdune swales and into the basin. Once the water has evaporated or infiltrated into the subsurface, the newly deposited sediment (i.e., sand, clay) and precipitated minerals (i.e., evaporites) become available for aeolian transport (Twidale, 1972). The newly deposited sediment is made available to aeolian processes to rework and modify dunes, particularly in present-day arid to semi-arid deserts that experience an abrupt change in moisture (Bullard and Livingstone, 2002). However, research into the role of fluvial activity on modern dryland landscapes is not common within the literature (Reid and Frostick, 1997). Instead, much of the research that focuses on fluvial processes occur within time scales before aridity under wetter paleoenvironmental conditions. Bullard and Livingstone (2002) attribute this problem to a "reductionist perspective," by which aeolian processes have been center-stage since the publication of Bagnold (1941). This inequity is further galvanized by sediment mobility indices that scale any precipitation towards vegetation growth rather than sediment entrainment (Yizhaq et al., 2009). For example, the linear dunes of Australia are designated as stable by vegetation (Tsoar et al., 1986). Yet, crestal sand movement and dune accretion have been observed (Craddock et al., 2015; Hesse et al., 2017). To understand the source of this sediment in the context of linear dune activity, the coupled processes of aeolian and fluvial interaction must be explored with a focus on hydrologic activity. Our goal was to assess the temporal interaction between the aeolian systems (i.e., wind) and fluvial systems (i.e., precipitation, flooding) at Lake Caroline within the northern Simpson Desert of Australia as a case study to relate present-day fluvial activity to the supply of sediment for active, vegetated, linear dunes. To achieve this goal, we focused on the following objectives:

1) Investigate the sediments of Lake Caroline to determine their composition and mineralogy and understand their relationship with adjacent linear dunes.

2) Identify the frequency and magnitude of present-day flooding at Lake Caroline.
3) Characterize the relationship between present-day wind speed and wind direction at Lake Caroline with fluvial activity (i.e., rainfall, flooding) to determine the potential for sediment transport.

This study begins by summarizing the current models of linear dune formation to lay the framework for sediment uptake into the dunes. Here, we use the terms linear dune formation and activity synonymously from the perspective that dune maintenance encompasses both. This is followed by the main modes by which fluvial systems have been observed to interact with linear dunes, particularly but not limited to the deserts of Australia. The study site of Lake Caroline is described next and includes climatic, hydrological, and geological information pertinent to analyses put forth in the results and discussion part of this paper. This is followed by a description of the methods used to achieve the objectives and the results. The discussion section presents the implications of this study not only for climate change, but also for investigations in other locations with linear dunes and fluvial features, including extraterrestrial settings such as Titan where large linear dune sands are of interest regarding the search for liquid organics (Lorenz et al., 2008).

Linear Dune Formation and Sediment Uptake

Linear dunes are the most prevalent and large-scale dune type on Earth (Lancaster, 1982). They occur in the major sand seas of Australia (e.g. Simpson and Strzelecki Deserts), Africa (e.g., Sahara, Namib, Kalahari Deserts), China (e.g., Thar Desert), and the Arabian Peninsula (e.g., Rub' al Khali), as well as on all planets in the solar system with an appreciable atmosphere (i.e., Mars, Venus, Titan) (Greeley and Iversen, 1987; Craddock, 2011). Linear dunes are known for their characteristic ridge-like structure, parallelism, and great length. They extend hundreds of kilometers in length and more than 30 m in height. Despite their prevalence, many questions

remain regarding their formation and development. These discussions have spanned for more than a century and converged into three primary formation models: (1) vertical accretion (wind rift) (King, 1960; Pell et al., 2000), (2) linear or downwind extension (Wopfner and Twidale, 2001), and (3) lateral migration (Hesp et al., 1989; Rubin, 1990). The model of formation is associated with sediment characteristics, as well as the linear dune morphology (Folk, 1971).

The vertical accretion or wind rift model proposes upward growth of a linear dune by wind denudation or scouring of the sand sheet, dune flanks, or interdune swales (Pell et al., 1999). This is achieved either by helical roll vortices or a bimodal wind direction intercepting the dune obliquely from each side. Sand is eroded by wind and transported onto the adjacent dunes (King, 1960; Folk, 1971). In this model, sand accumulates on the dune crest and upper flanks, and the dune increases in height and develops vertically.

The linear or downwind extension model proposes sand deposition on the downwind end or snout of the dune in the resultant wind direction. (Tsoar, 1989). Wopfner and Twidale (2001) refuted evidence from Pell et al. (1999) for vertical accretion from local sources in the Simpson Desert and suggested that the dunes formed by downwind extension from sediment located hundreds of kilometers upwind. However, they acknowledged that the incorporation of materials from local flood-out basins and playas should not be precluded in limited cases.

The lateral migration model proposes net deposition of sand on one flank of the dune and erosion on the other despite the dune orientation trending parallel to the present-day, prevailing wind direction (Rubin and Hunter, 1985; Hesp et al., 1989; Hollands et al., 2006). This results in the sideways propagation of the dune.

Fluvial-Linear Dune Interactions

It is no surprise that discussions surrounding linear dune formation focus on aeolian processes. After all, wind is the dominant process where water resources are limited, and fluvial processes dominate in wetter climates. However, abrupt increases in the moisture of drylands can balance the share of work between the processes. The resultant fluvial activity takes place in the leftover ephemeral channels and lakes of the past. The channels and playas that remain are disconnected, drain internally, and are often superimposed by aeolian landforms (e.g., sand sheets, dunes) as is the case for Australia, the Sahara, and other major deserts on Earth (El-Baz et al., 2000; Abdelkareem et al., 2020). The location of channels and playas are where this runoff and groundwater discharge and erode the dunes. This occurs alongside the dune flanks where sediment is entrained and slumps into the river and carried to a playa or depression. The sediments generated by these events replenish the supply for dune building, albeit to a lesser degree than the previous, wetter climatic optimum (Langford, 1989). The interactions between these fluvial features and linear dunes can express themselves by the large-scale erosion of dunes, the encroachment of fluvial features by the dunes, or the creation of new dunes from the cannibalization of older ones.

Investigations into the influence of present-day fluvial activity on sediment supply for active dunes are not common especially where vegetated linear dunes are regarded as stabilized (Hesse and Simpson, 2006). This may be in part due to the difficulties in observing the slow rate of erosion and deposition on small time scales. Bristow et al. (2007) constrained the downwind extension of linear dunes to 3000 m over the last 10 ka using GPR and TL dates from the literature at Camel Flat Basin and Copper Creek. However, Craddock et al. (2015) observed the vertical accretion of a vegetated linear dune in the Simpson Desert exceeding a meter in some places over eight years under present-day climatic conditions. Both studies suggest that linear dunes within

these regions are activity taking-up sediment on shorter time scales, despite the relatively wetter climate of central Australia at-present compared to the onset of aridity as much as 1 Ma ago (Fujioka et al., 2009).

Fluvial Erosion of Linear Dunes

An added complexity for observing dune growth over small time scales is ongoing erosion, particularly in semi-arid and arid zones where dunes subjected to intermittent, albeit extreme, fluvial events. In these cases, water from surface runoff or discharging groundwater temporarily floods channels, playas, and interdune swales where sediment is mostly eroded at the bases and exposed snouts of the dunes. Langford (1989) documented the widespread disruption of a vegetated linear dune field by Lake Lewis to the north of the Simpson Desert, and English et al. (2001) observed the erosion of non-vegetated dunes by Medano Creek in the Great Sand Dunes National Park. Further, Teller and Lancaster (1986) recorded the erosion of linear dunes by fluvial activity in interdune pans in the Namib Desert, and conversely, the disruption of the Tsondab River by encroaching linear dunes.

Encroachment of Dunes on Fluvial Systems

The encroachment of linear dunes on fluvial systems is observed using the principle of superposition combined with advanced lithological and chronological dating methods (e.g., TL, OSL) In this case, the linear dune is observed to overlay a paleo floodplain or appear to be extending across a playa lake. Encroaching dunes have been observed to overlay a paleo floodplain from the Todd River and Camel Flat Basin (Hollands et al., 2006; Liu and Coulthard, 2015), and Bristow et al. (2007) observed vegetated linear dunes of the Strzelecki Desert overlaying the paleo floodplain of Copper Creek. The latter study characterized the dune building model as linear

extension over 9,000 years and cited that the sediment was derived from a local, source bordering dune.

Fluvial Systems and Source Bordering Dunes

One way by which fluvial activity is linked to linear dunes is by transverse or source bordering dunes (Twidale, 1972; Fitzsimmons et al., 2007). Source bordering dunes occur at the downwind edge of a playa and are oriented perpendicular to the linear dunes and dominant wind. Sediment that is deposited into floodplains and playa lakes is blown downwind during drier periods to form parabolic dunes, and sometimes transverse dunes - also referred to as lunettes when crescent-shaped. The sediment on the source bordering dune is believed to blow downwind to form new linear dunes. Twidale (1972) presents an extensive analysis of the relationship between fluvial systems, source bordering dunes, and linear dunes in South Australia and south-western Queensland, whereby he identified mounds of eolian debris on the downwind end of playas. In these cases, the linear dunes downwind of the transverse dunes are younger, smaller in height and dune spacing, and differing in mineralogy than the older, larger dunes upwind. Cohen et al. (2011) identified linear dunes that accreted vertically from underlying transverse, or source bordering dunes atop an array of paleochannels in the Copper Creek region. Fitzsimmons et al. (2007) noted that the initiation of dune activity from the reworking of a transverse dune was controlled not only by periods of aridity but also local hydrology (i.e., surface runoff, groundwater discharge) at Lake Frome in Australia. The formation of linear dunes by the downwind extension of source-bordering dune sediments is one possibility depending on the climatic and topographic conditions of a region.

Al-Masrahy and Mountney (2015) developed an aeolian-fluvial interaction classification system showing that most linear dunes, except for in hyper-arid zones, exist in environments where both fluvial and aeolian processes operate together without interruption. These observations

demonstrate the complexity in characterizing the dominant mode of dune formation over varying scales but also highlight the value of investigating linear dunes at the margins of fluvial features to improve understanding of their formation, development, and degradation across scales (Liu and Coulthard, 2015).

Study Site

The Simpson Desert covers more than 300,000 km^2 in an arid and semi-arid region of central Australia (Figure 10). The desert overlaps four of the six states of Australia (i.e., New South Wales, South Australia, Queensland, and the Northern Territory (NT)). The MacDonnell mountain ranges bound the desert by the north, while fluvial systems bound the desert on the other sides, including Lake Eyre to the south. The Simpson Desert is known for its remoteness, large linear dune fields, playa lakes, and its location within the Great Artesian Basin (GAB). The region of interest for this study is Lake Caroline (137°11' 9" E, 23° 46' 42" S) and the surrounding area. Lake Caroline is a shallow playa (< 5 m) located on the northern margins of the Simpson Desert within the Northern Territory (Figure 10). It covers an area of 4.2 km^2 and belongs to a series of several shallow playas and interdune pans that are partially drained by the ephemeral Hay River. The landscape surrounding the playa series is composed of a bright red-colored vegetated linear dune field extending from the northern edge of the Simpson Desert for more than 300 kilometers southward to Lake Eyre. The dunes are oriented at SSE-NNW, with the prevailing wind from the SSE, and run relatively parallel to one another, although dune-spacing and height vary. The interdune swales are vegetated with small playa lakes or claypans. West of Lake Caroline is the Plenty Lakes region, which is drained by the Plenty River and contains several smaller playas and pans.

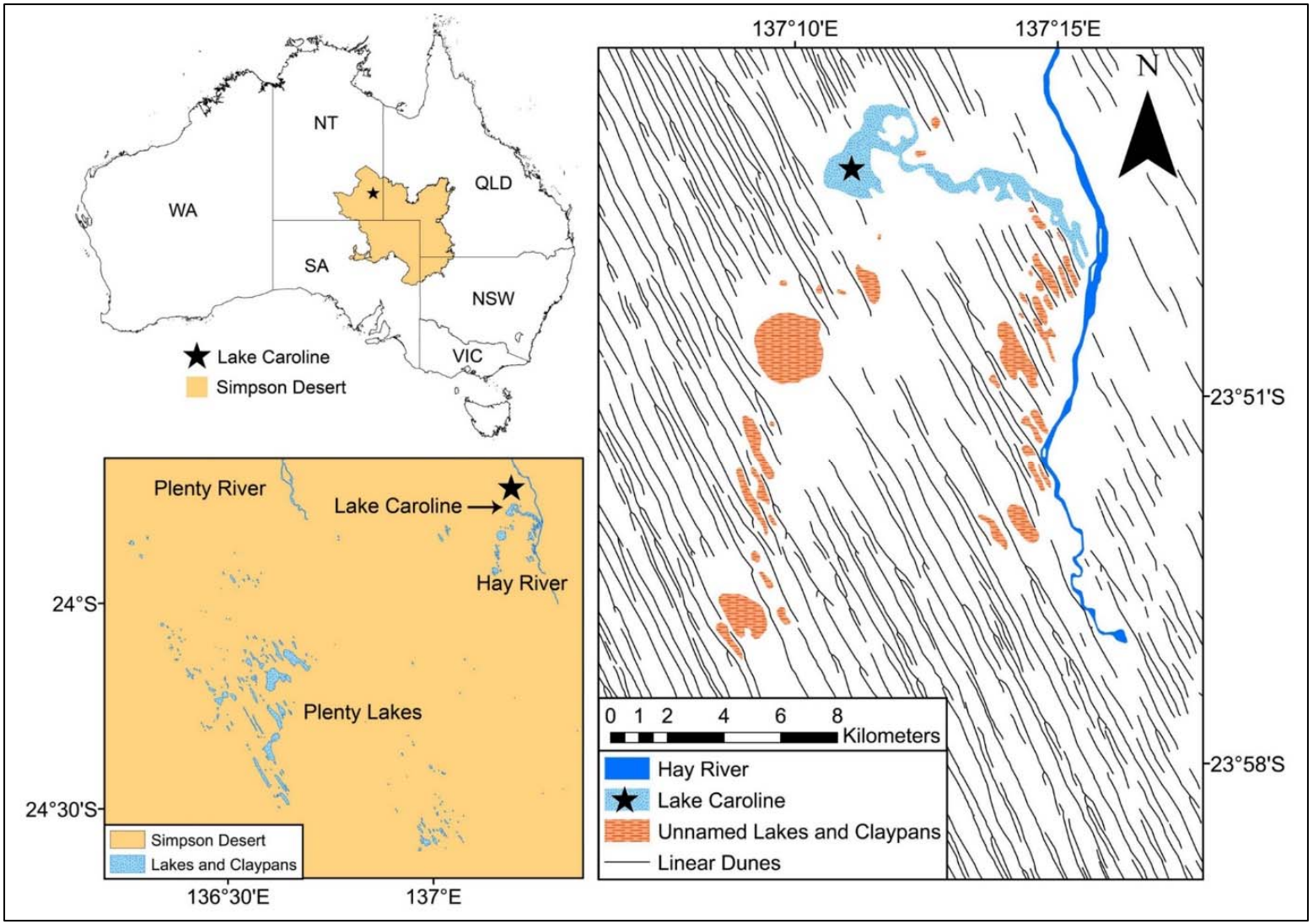

Figure 10. The Simson Desert, Lake Caroline, and the Plenty Lakes region located in the Northern Territory (NT) of Australia.

Climate

Climatic conditions in the northern Simpson Desert are arid to semi-arid and classified as a hot desert climate (BWh) by the Köppen climate classification (Kottek et al., 2006). Although hot deserts are some of the hottest and driest lands, the region experiences seasonal rainfall with 61% generated during the monsoonal summer phase (December – March). Lake Caroline and the southern region of the NT experience heavy monsoonal rains when low westerly winds force the northern trough over central Australia. The Jervois Station (22.95° S, 136.14° E), a weather station approximately 136 km northeast of Lake Caroline, reported a mean annual rainfall of 292 mm/year between the years of 1966 and 2020 (Australian Bureau of Meteorology, 2020). The mean maximum temperature is reported as 31°C with mean highs to 38°C in December and January. The mean minimum temperature is 14.7°C with mean lows to 5°C in July. The Australian Bureau of Meteorology reports an average annual evaporation rate west of Alice Springs at 2800 – 3200 mm/year (Australian Bureau of Meteorology, 2020).

Monsoons also drive the prevailing winds, particularly during the summer season as the continent heats up faster than the surrounding oceans. The resultant difference in pressure draws in moisture and creates a whorl-like, anticlockwise wind circulation pattern over Australia (Suppiah, 1992). The prevailing winds of the Simpson Desert in the NT and Lake Caroline originate from the southeast and east and are strongest during the summer season. At Jervois Station, more than 30% of the winds originating from the southeast are between 11 and 16 knots. The mean 9 AM wind speed (6.9 knots) is positively correlated with rainfall and temperature, whereby the spring and summer months (September – March) experience the highest rainfall, temperature, and wind speed. The 3 PM mean wind speed (7.1 knots) is relatively consistent throughout the year despite other climatic changes (Australian Bureau of Meteorology, 2020).

Hydrology and Groundwater

Lake Caroline is positioned in the Western Eromanga sub-basin of the GAB, one of the largest basins (1.7×10^6 km^2) on Earth (Figure 11). Lake Caroline and the other ephemeral playas, rivers, and pans of the region are remnants of an extensive paleodrainage system of the GAB from the Tertiary period (Brown et al., 1968). Many of the ancient rivers and lakes in these systems would have greatly exceeded the size of the water bodies present today (Magee, 2009; Craddock et al., 2010). In the northern Simpson Desert of the NT, the Hale, Plenty, and Hay Rivers drain southward towards Lake Eyre but terminate shortly after flowing into the desert largely due to transmission losses. The Plenty and Hale Rivers run parallel to the dune fields. Lake Caroline and the Plenty Lakes water bodies are the only sizable ephemerals lakes and pans remaining. The elevation of the northwestern edge of the GAB at the Hay River starts at 211 m above mean sea level (AMSL) and gently slopes southward to 157 m AMSL over 63 km at Lake Caroline and onto 140 m AMSL over 28 km at the terminus of the Hay River. The lowest elevation of the GAB is -16 AMSL at Lake Eyre in South Australia.

Throughout the GAB, groundwater naturally discharges through springs and rivers where the water table is closest to the surface. Groundwater recharge in the Western Eromanga basin is presently considered negligible and only marginally occurs under episodic flow events. Lake Caroline is located 16 kilometers south of a recharge zone along the periphery of the GAB (Figure 11). The water table is reported at Lake Caroline to be 0-5 m from the surface (Bioregional Assessment Program, 2019). Although the water table is closer to the surface at Lake Caroline than much of the surrounding area, the lake only floods from surface runoff or groundwater when the water table sharply rises after heavy floods (Duguid, 2011). Observed floods in the region were reported in 1967, 1971, 1974, 1993, and 2000 (Northern Territory Government of Australia, 2018).

The connection between discharging groundwater and the inundation of the playas and claypans is not documented, nor is the frequency of flooding likely due to the remoteness and inaccessibility of the area.

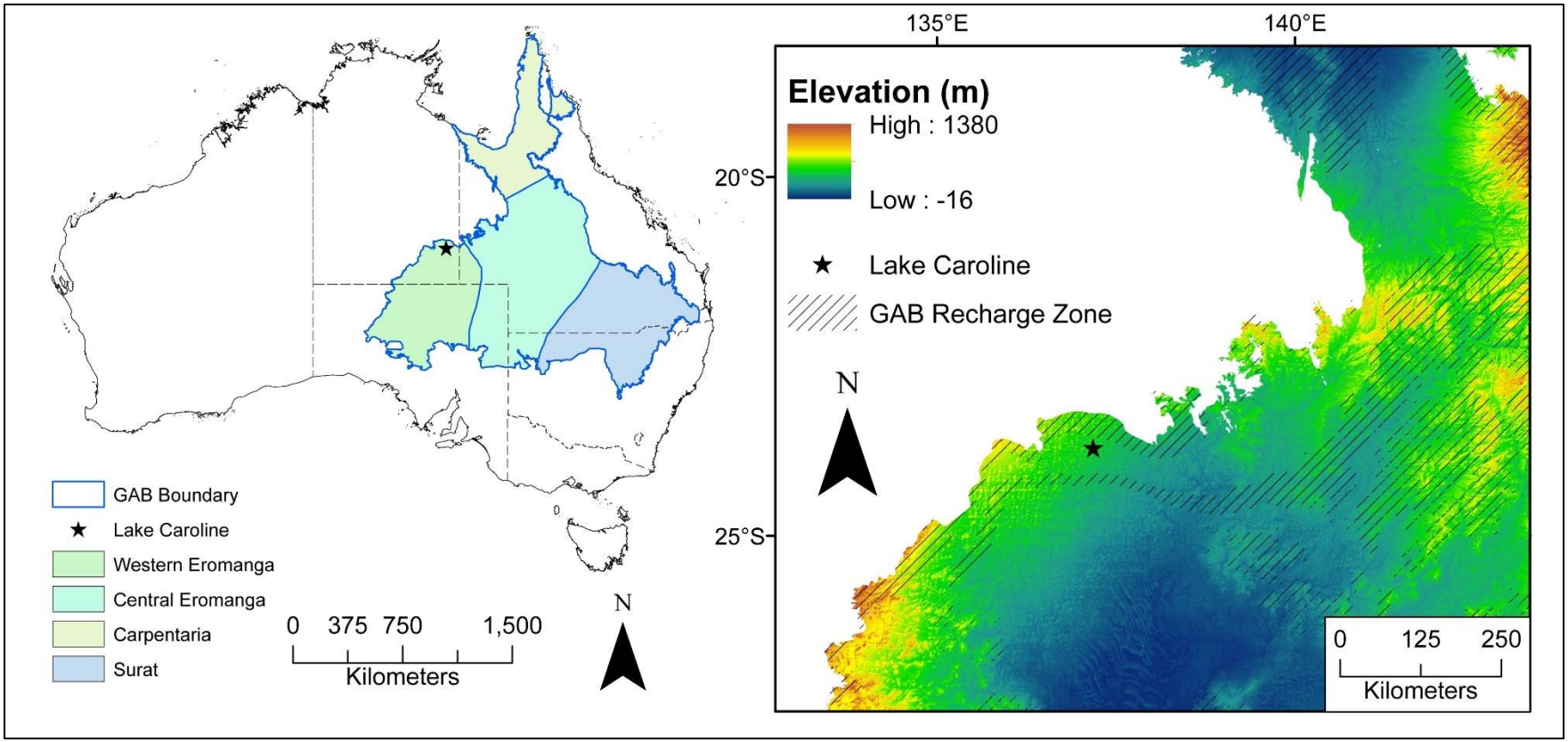

Figure 11. Map of the GAB boundary and sub-basins in eastern Australia (left), and regional location of Lake Caroline relative to the GAB recharge zones and topographic elevation (right).

Geology

The Simpson Desert in the Lake Caroline region is composed of linear dunes of red aeolian quartz sand and clay pellets of Quaternary age. In some regions along the Hay River, the aeolian sand is underlain by interbedded fluvial quartz sand (Northern Territory Government of Australia, 2018). Stony plains and rises called gibber landscapes are associated with the lakes and pans of Lake Caroline and the Plenty Lakes (Duguid, 2011). Gibbers are sometimes coated with dark desert varnish. These deposits are underlain by Cretaceous rocks of the Rolling Downs Group (Mond and Yeates, 1973; Exon and Senior, 1976). The depositional environments of the Rolling Downs Group range from freshwater to shallow marine. Bore samples from the Hay River and Plenty River exhibited salmon pink and yellow to cream shale claystone with a thickness to 55m (Crespin and Evans, 1962). Mica was also identified within these deposits. These rocks are underlain by the Allaru Mudstone and Wallumbilla Formation, respectively, which is reported to outcrop on the edges of Lake Caroline. The Allaru Mudstone is a light to medium grey, silty shale, and the Wallumbilla Formation is dark-grey, silicified mudstone colored by iron staining. This formation is also glauconite-bearing. The thicknesses of these units in the Lake Caroline area are not documented.

METHODOLOGY

Reconnaissance

The attempt to characterize aeolian-fluvial interactions in the context of linear dune dynamics was initiated by observations of Lake Caroline appearing to cannibalize several linear dunes in satellite imagery (Figure 12). The observation of the linear dune "melting" into the playa challenges the basic paradigm that fluvial activity only drives dune activity towards stability and the present-day, wetter conditions stabilize and don't erode the vegetated linear dunes of the

Simpson Deseret (Ash and Wasson, 1983; Tsoar et al., 1986). Questions arose regarding the sensitivity of linear dunes located along the margins of fluvial systems and the dominant role of present-day fluvial processes on linear dunes.

The initial observations for reconnaissance of the Lake Caroline area were performed using Esri's World Imagery map, which provides 1 meter or better (e.g., 30 cm, 60 cm) satellite imagery and aerial photography (Figure 12). Temporal observations and time stamps are not available with this product, but the high-resolution was very useful for initial analyses.

Reconnaissance was followed by a methodology aided by (1) fieldwork conducted at Lake Caroline and laboratory analyses (i.e., lithology, mineralogy) to understand the relationship between the playa sediments, linear dunes, and surrounding area, (2) the data acquisition and analyses of radar data and multispectral remote-sensing satellite images for precipitation and flood frequency analysis, and (3) analyses of present-day precipitation and wind data collected by satellite remote sensors and weather stations.

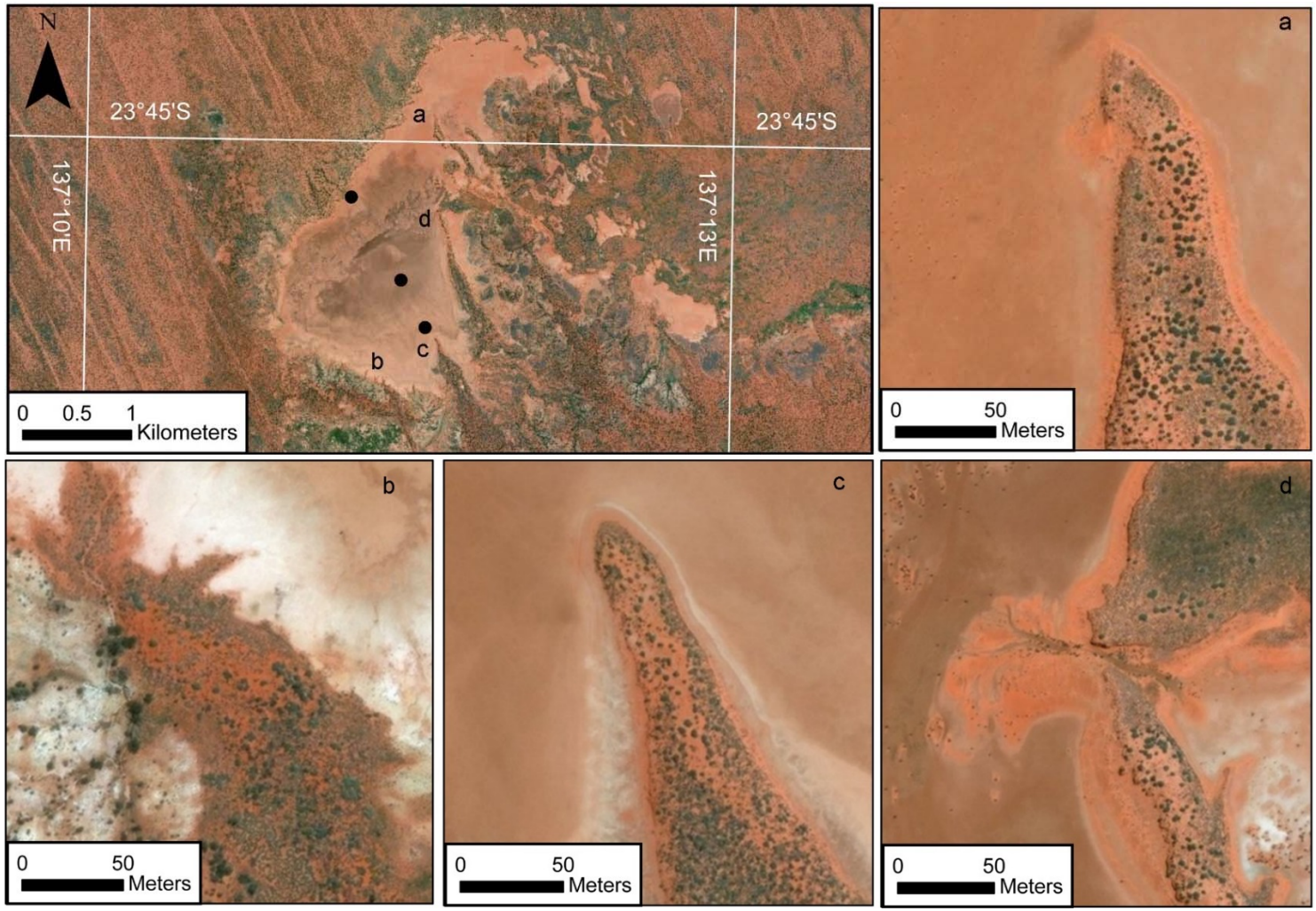

Figure 12. Study area and sample sites indicated by the black dots at Lake Caroline (top-left), and linear dune extending from the southern edge of the playa. Note: the dunes appear to be eroding into the playa. Images courtesy of Esri, DigitalGlobe, GeoEye, Earthstar, Geographics, CNES/Airbus DS, USDA, USGS, AeroGRID, IGN, and the GIS User Community.

Field Methods and Analyses

The research team sampled multiple areas of Lake Caroline and the surrounding area as part of an ongoing, larger study led by the Smithsonian Institution investigation of linear dune formation (Craddock et al., 2015). For this study, we collected three cores in the playa using a hand auger to a depth of 2.25 m along a 1.7 km transect extending from the north side to the south side of the playa. Grab-samples from linear dune C, a linear dune adjacent to the playa was also collected (Figure 12). Sediments from select depths of each core (n = 18) underwent a particle size analysis using a Keck Sieve Shake Kit (Poppe et al., 2000), a color analysis using a Munsell Color System, and a powdered bulk composition analysis by XRD techniques (Brown and Brindley, 1980) in the Clay Mineralogy Laboratory at the University of Georgia.

Remote Sensing Satellite Data Acquisition and Observations

Precipitation data were collected specifically for Lake Caroline using the gridded data generated by the Global Precipitation Measurement Mission (GPM) from NASA (Huffman et al., 2015). Daily rainfall was collected for Lake Caroline between 01/01/2001 and 12/31/2019 from the GPM IMERG Final Precipitation L3 product (GPM_3IMERGDF 06).

Daily rainfall data was filtered to highlight daily rainfall values greater than 5mm, defined as a wet day. Subsequently, multispectral satellite images were inspected on and after the days that experienced a wet day to identify flooding. True color Landsat 7 images (bands 3, 2, 1) from NASA were inspected between the dates of 1/1/2001 and 12/31/2019. True color Rapid Eye Satellite Sensor (bands 3, 2, 1) from the Satellite Imaging Corporation between the dates of 8/29/2008 and 12/31/2019, and true color Sentinel-2 images (bands 4, 3, 2) from the European Space Agency (ESA) between the dates of 6/23/2015 and 12/31/2019 were also examined. The

satellite, temporal, and spatial resolution, as well as the number of scenes inspected for wet days and playa floods.

Table 5. Satellite products used for data acquisition and inspection.

Satellite Mission	Spatial Resolution	Date Range Inspected	Number of Scenes Inspected
GPM	11 km	1/1/2001-12/31/2019	6936
Landsat 7	30 m	1/1/2001-12/31/2019	392
RapidEye	5 m	08/29/2008-12/31/2019	6
Sentinel 2	10 m	06/23/2015-12/31/2019	162

Precipitation and Wind Analyses

Precipitation data acquired from the GPM satellite mission were analyzed using the R programming environment and the hydroTSM package. Free, publicly available, continuous, and 5-minute wind speed and wind direction data with the dates of 1/1/2009-12/31/2015 were downloaded from the NT Solar Resource Group Meteorological Station in Alice Springs, Australia. Monthly-averaged wind speed and wind direction were computed to determine the prevailing wind direction and identify the percentage of counts when the wind speed exceeded 12 knots, the threshold velocity for dry, fine sand (d=0.30 mm) at 10 m above the surface (Bagnold, 1941), defined as a windy period. Statistical analyses of the wind data were analyzed using the openair R package, a tool written with the R programming code to analyze meteorological data.

Summarized meteorological data is available from the Australian Bureau of Meteorology, but historical data is not publicly available. Further, no currently operating meteorological station is within a distance smaller than 100 km from Lake Caroline. Access to real-time, continuous meteorological data in the Simpson Desert is virtually non-existent, which underpins the importance of projects like the NT Solar Resource Meteorological Station for linear dune formation studies.

RESULTS

Fieldwork

Site Observations

Observations were made of the linear dunes adjacent to the playa, as well as the sediment and rocks of the surrounding area. The entire playa floor was completely dry during the visit and primarily covered in fine red sand and clay. We observed a silver mirage on the desert floor as we entered the playa and headed west (Figure 13). Desiccation cracks were observed in various places and to varying degrees throughout (Figure 14). A shiny coating on the polygonal cracks was observed on the south edge of the playa near Linear dune C. A fine coating of fine sand covered the cracks to the north, where a thin layer of an evaporite was observed.

Three vegetated linear dunes, oriented NNW-SSE, superimposed the playa extending from the southern edge (Figure 15). These dunes appeared "to melt" into the playa, as well as five, vegetated islands of sand, oriented approximately NNW-SSE, in the playa. These features appeared to be linear dunes that once extended across the entire length of the playa. These former dunes are now being cannibalized during flooding and the "melting" reflects linear creep that is driven by heavy rainfall events. The northern edge of the playa is bordered at either end by several linear dunes or several transverse, source bordering dunes. These dunes are lithified with exposed crossbedding, which was visible while facing north, as well as longitudinally along the channel cuts (Figure 16). Several small ephemeral channels were observed cutting through the exposed dunes to the north, and a thin layer of reddish-brown dust covered the playa at the mouth of the channel at the northern sample site. The surficial playa sediments ranged from Red (2.5 YR 4/8) at the north sample site to Yellowish Red (5YR 4/6) at the central sample site and Dark Reddish Brown (2.5YR 5/4) at the south sample site. The color of the linear dune sand was Red (2.5YR

5/8) at the southern sample site at linear dune C. The channels on the northern side appeared to be responsible for the fine red sand covering the playa. Sporadic and widely spaced, long grasses were observed to be growing in the playa on the northern side.

Outcrops of white, yellow, and pink claystone were exposed on the western and northwestern edge of the playa, and some were cut by ephemeral channels from the west and northwest (Figure 17). These outcrops were highly weathered and mound-shaped. Weathered clasts of the claystone washed out onto the playa floor at the channel mouths on the northwest and western edges of the playa.

Beds of black gibbers were observed on the southeastern edges of the playa floor along the ephemeral channel leading into the playa (Figure 17). The outcrops of gibbers were most prominent in the eastern end of the tributary closest to the Hay River. No gypsum or halite evaporite minerals were observed in or around the playa other than a thin layer (thickness < 1 mm) precipitating in a small crack on the northern edge as previously shown.

Figure 13. Desert mirage reflecting off the surface of Lake Caroline. The photograph is taken at the mouth of the tributary leading into the playa at 23° 46' 10.29" S, 137° 11' 22.64" E facing north.

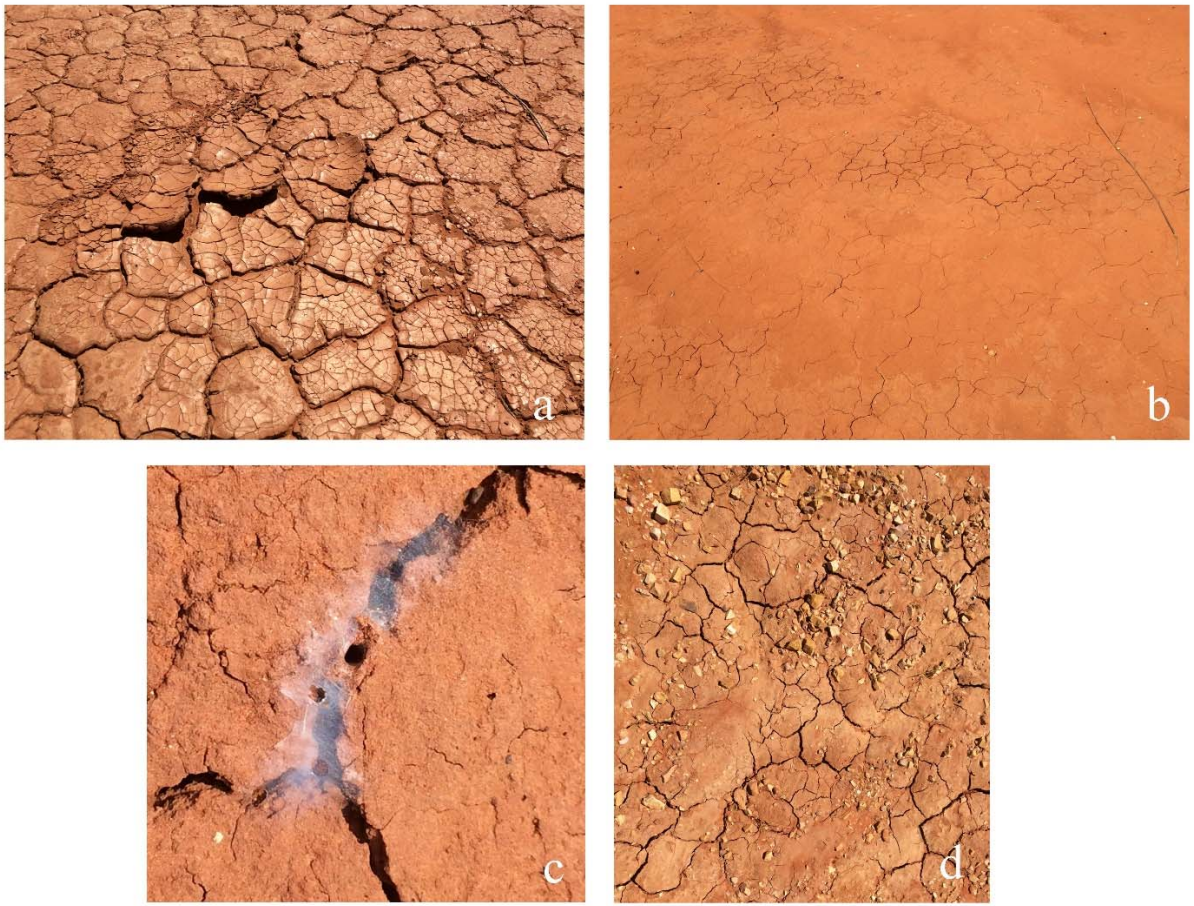

Figure 14 Desiccation cracks observed at Lake Caroline. Polygon sizes are approximately the size of a human hand or smaller and were photographed at (a) northeast end of Linear Dune C, (b & c) northeast edge of Lake Caroline, and (d) western edge of Lake Caroline. A think evaporite was observed precipitating within a crack on the north edge of the playa.

Figure 15. (Left) Linear dune C "melts" into Lake Caroline. The photo was taken from the northeast end of the snout and facing west, (right) a continuation of linear dune C from the northeastern side of the dune facing south (23° 46' 58.27" S, 137° 11' 24.61" E).

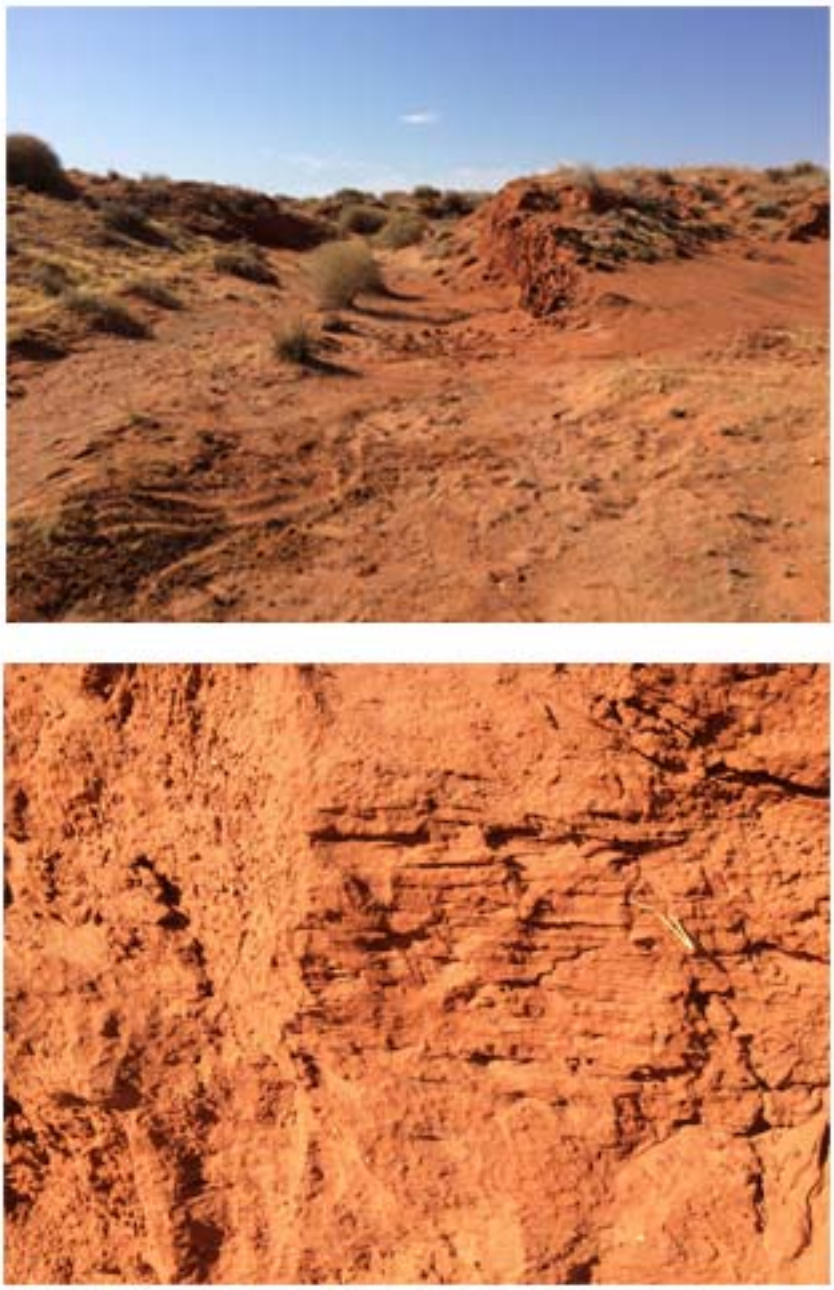

Figure 16. (Top) a channel cutting through a remnant dune on the northern edge of the playa 23° 46' 7.40" S, 137° 10' 58.69" E) facing north into the channel, and (bottom) cross-bedding on the side of the remnant dune facing east. The bed thicknesses in the center of the photo are approximately 10 mm.

Figure 17. (Top) colored silcrete exposed by the downcutting of a fluvial channel into the on the western edge of the playa (23° 47' 10.59" S, 137° 11' 0.77" E) facing north. The arrow points to a hiking boot for scale. (Bottom), exposed layer of dark-coated gibber in the main tributary leading to the playa (23° 47' 0.74" S, 137° 13' 0.08" E) facing northwest.

Particle Analysis

The particle analysis of the playa determined the composition of samples from the northern, central, and southern sample sites at select depths to as much as 2.25 m (Figure 18). The sediments consisted of a high percentage of sand (> 95.9 %) at all three sites, except for a small percentage of silt and clay (0.4-5.7 %) and gravel identified at the center and southern site (16.0-18.0 %). The sand is characterized as fine to coarse sand with D_{60} values ranging from fine (0.15 mm) to coarse (0.83 mm). The linear dune sand, which was sampled at the crest, consisted of 100%, fine sand (0.20 mm). Gravel sized sediments (> 4 mm) were identified at depths of 200 cm in the center of the playa and 151 cm at the southern site.

The gravel identified at the center of the playa was white and yellow that resembled the claystone outcrops and washed-out clasts observed 1 km away on the western edge of the playa. The gravel identified at the southern site was a dark grey or black coated, weathered, siltstone (Figure 5). The linear dune and playa sediments at shallow depths were moderately sorted and sub-rounded. However, sediments at depth became increasingly poorly sorted and included small crystals of salt, clay, and gravel. The roundedness of the playa sediment at depth was difficult to determine due to clumping and the presence of cement on the grains.

Bulk-Composition

The bulk-composition of the linear dune and playa sediments varied by location along the sample transect and by depth (n=10) (Figure 19). The sediments from the linear dune consisted primarily of quartz and feldspar reflecting sediment maturity. The sediments from the northern sample site resembled dune sand at the shallow depth (14 cm) and exhibited gypsum in the middle (89 cm) and lower (173 cm) depths. The sediments from the central sample site included quartz, feldspar, halloysite, and kaolinite at the shallow depth (14 cm), as well as gypsum and halite at the

middle (83 cm) and lower (160 cm) depths. The sediments from the southern sample site include quartz, feldspar, gypsum, kaolinite, halloysite, and halite at the shallow depth (16 cm), as well as bassanite in the middle layer (69 cm), and goethite at the lower layer (151 cm).

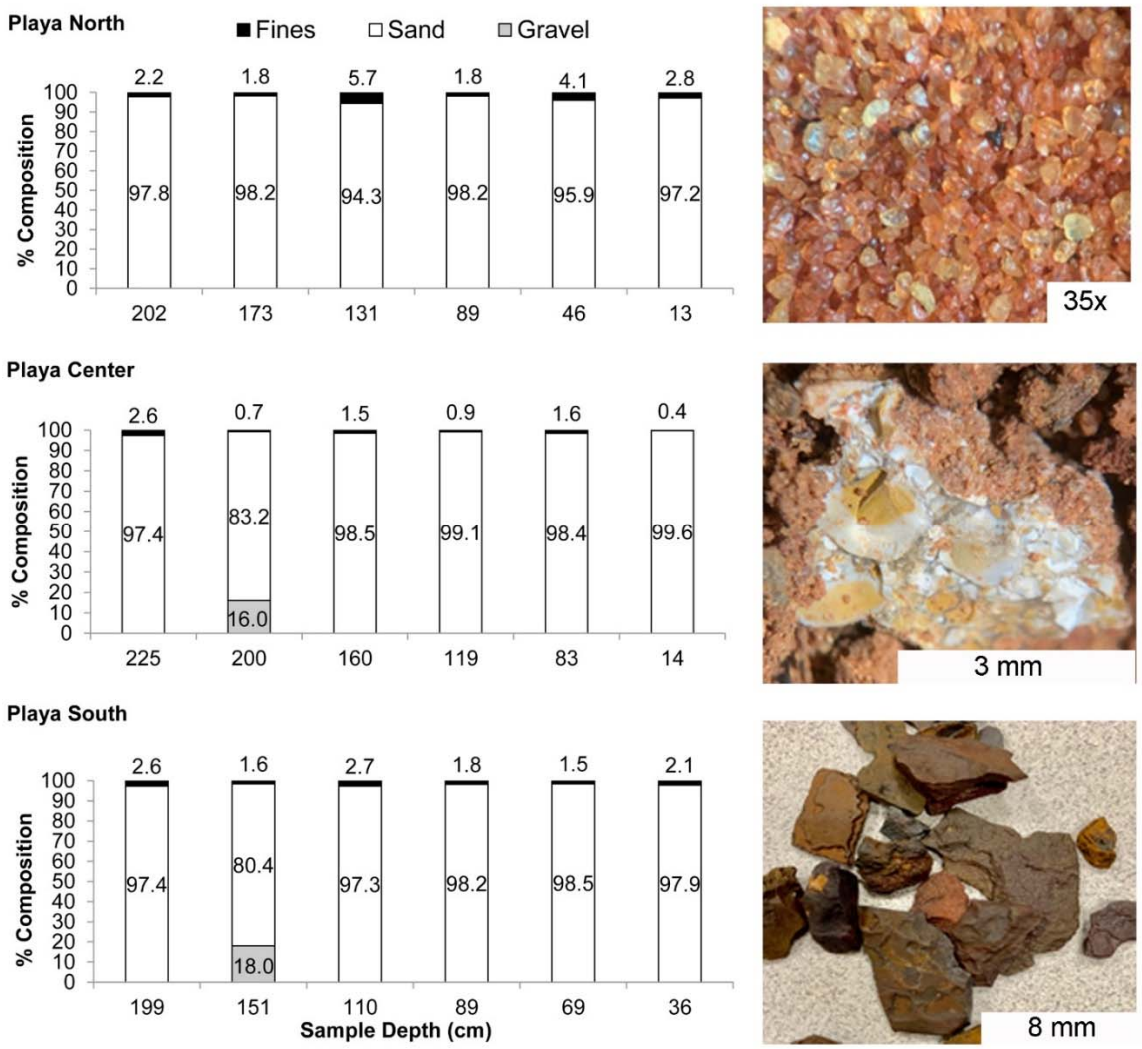

Figure 18. Particle analysis of playa sediments (left) and examples of sediment including linear dune sand (top-right), claystone clasts (middle-right), and weathered siltstone clasts (bottom-right).

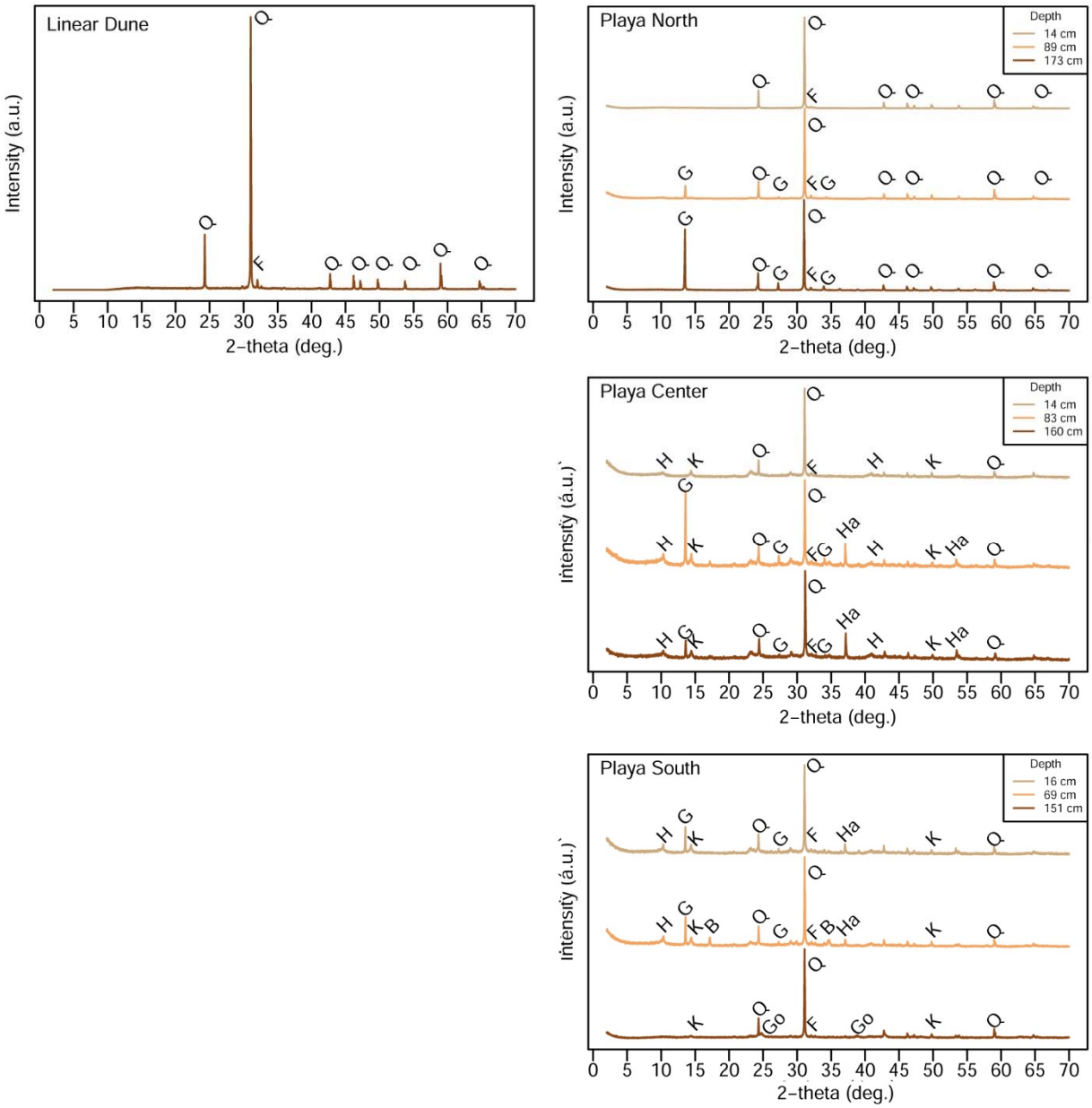

Figure 19. The bulk composition of linear dune and playa sediments by XRD. Some, but not all of the major peaks of the minerals are labeled and include halloysite (H), gypsum (G), kaolinite (K), quartz (Q), feldspar (F), halite (Ha), bassanite (B), and goethite (Go).

Water and Wind Analyses

Rainfall and Flood Frequency

Daily rainfall amounts between 1/1/2001 and 12/31/2019 directly above Lake Caroline were analyzed using the GPM satellite mission. A mean annual rainfall of 252 mm was computed specifically for Lake Caroline over 19 years. The maximum annual rainfall was computed to 763 mm for 2010, and the maximum daily rainfall was identified as 125.2 mm on 2/28/2010. The area experienced 237 wet days, defined as more than 5 mm of daily rainfall, during the 6936 days. A summary of wet days and the percentile distribution of those days are summarized in Table 6.

Table 6. The number of wet days.

Rainfall (mm)	Number of Days
> 5.2	226
> 8.0	159
> 14.4	81
> 41.7	12

The inspection of satellite images on or after an identified wet day returned a total of 58 images where runoff from a wet day accumulated within Lake Caroline (Figure 20). An example of an observed flood by satellite images in between dry periods is shown in Figure 21. The minimum daily rainfall amount from an observed flood at Lake Caroline was 5 mm. The 25th empirical quartile included daily rainfall values of 12 mm or less, and more than half of observed floods occurred after daily rainfall values of 27 mm (Figure 22).

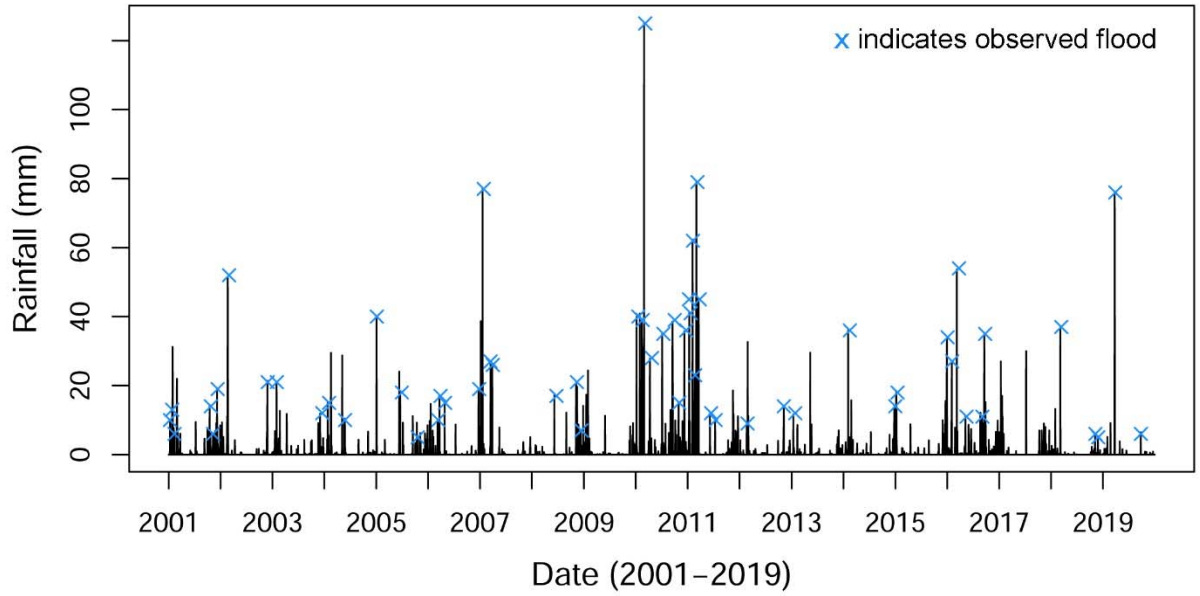

Figure 20. A time series of daily rainfall at Lake Caroline from 1/1/2001 to 12/31/2019. The blue X indicates observed floods at Lake Caroline in satellite images.

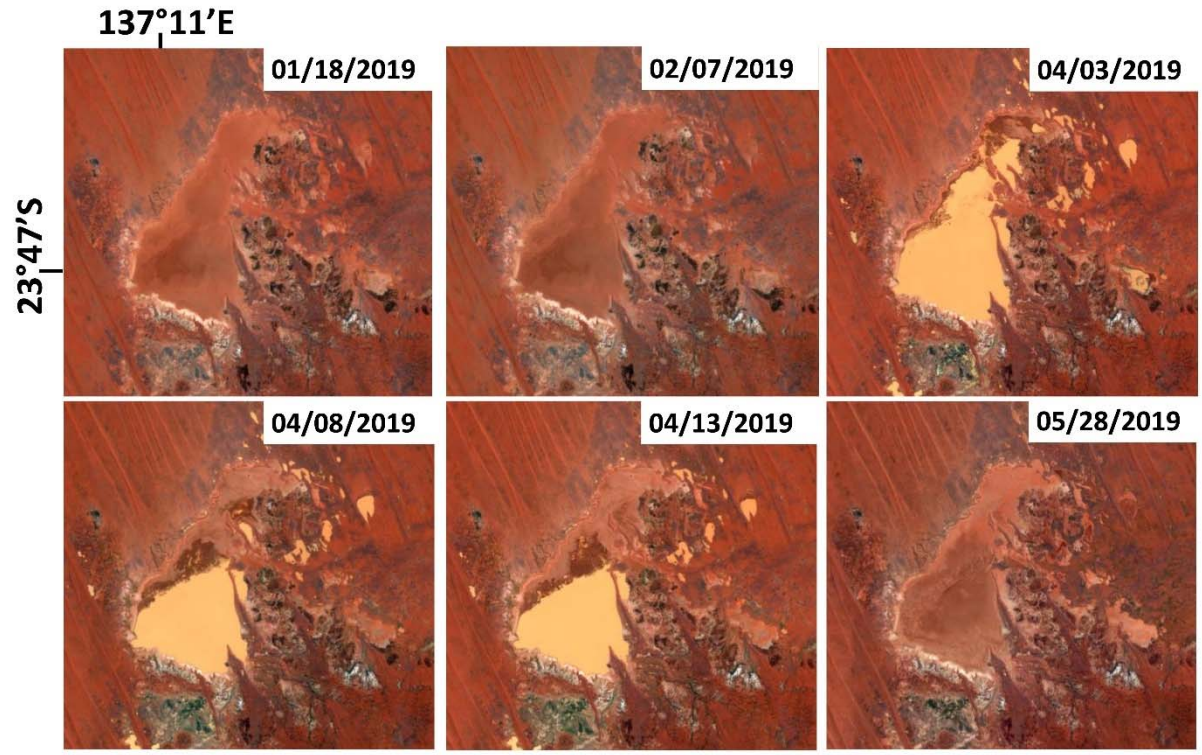

Figure 21. Sentinel-2 satellite images of Lake Caroline dry and wet before and after an identified rainstorm on 03/24/2019 (76 mm) and 03-25-2019 (64 mm).

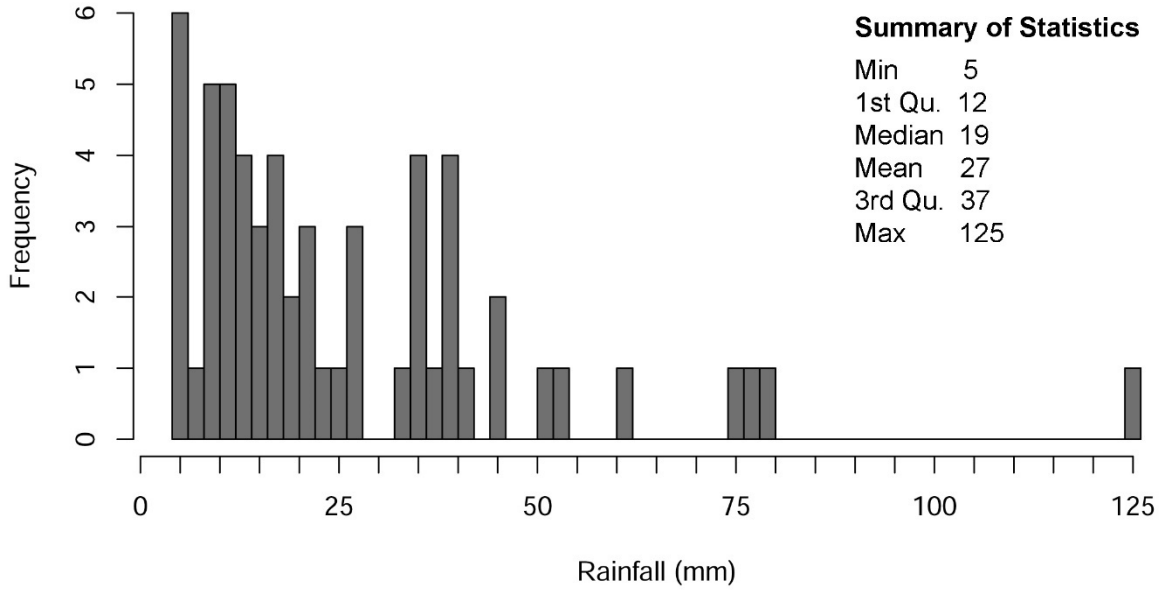

Figure 22. Frequency of observed floods by daily rainfall amount and statistical summary.

Seasonal rainfall was calculated for Lake Caroline (Figure 22). The late spring and summer months (November – March) are the wettest months over the 19 years. The maximum mean monthly rainfall was calculated as 33.51 mm for January. The minimum mean monthly rainfall was calculated at 0.01 for August.

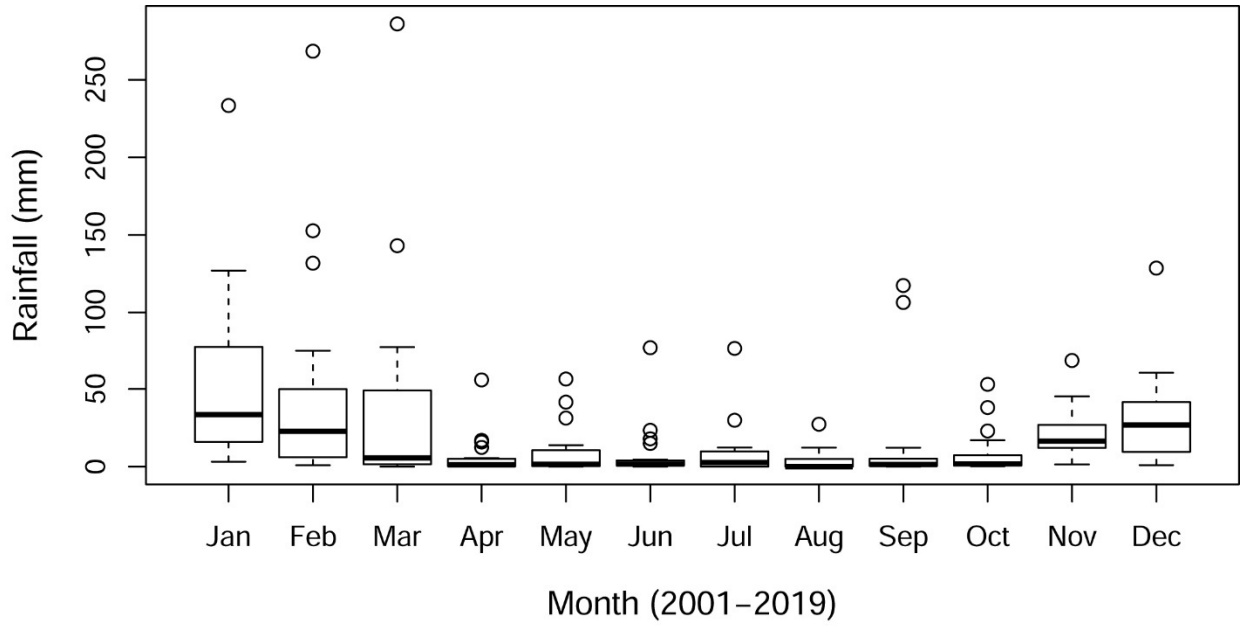

Figure 23. Box plot and whisker diagram of mean monthly rainfall for Lake Caroline between the years of 2001-2019. The boxes represent the interquartile range (25th – 75th percentile). The "T" lines represent the minimum and maximum values, and the circles represent outliers.

Wind Speed and Direction

Five-minute wind speed and wind direction data between the dates of 1/1/2009 and 12/31/2015 from the NT Solar Resource Group Meteorological Station were analyzed. A mean wind speed of 5.04 knots was computed over 9 years. The prevailing wind direction originates from the southeast and is strongest during the summer months (December – January) with a mean wind speed of 5.63 knots. The maximum wind speed was identified as 85 knots on 7/30/2015. The weather station recorded 20,322 5-minute intervals of wind speeds greater than 12 knots. Time-averaged wind speed periods to 1-hour and 24-hours result in 1,500 hours where the average sustained winds were greater than 12 knots, and 10 days where average sustained winds were greater than 12 knots.

Windrose diagrams in Figure 24 show time-averaged wind speeds and directions by month for the Alice Springs region, which is located ~330 km to the west from Lake Caroline. The

maximum mean monthly wind speed occurred during January at 5.8 knots, exceeded 12 knots for 20% of the counts, and prevailed from the southeast. The minimum mean monthly wind speed occurred in June at 4.1 knots, exceeded 12 knots 19% of the counts, and prevailed from the southeast. Overall, the prevailing wind direction was from the southeast more than 50% of the time during the 9 years. These observations agree with the general seasonal winds for the entire area surrounding the Simpson Desert, which is multimodal with a net sediment flux to the NNW oblique to the orientation of the linear dunes in the area (Craddock et al., 2015). Additional hourly, seasonally, and yearly windrose diagrams are presented in

Appendix B and

Appendix C respectively.

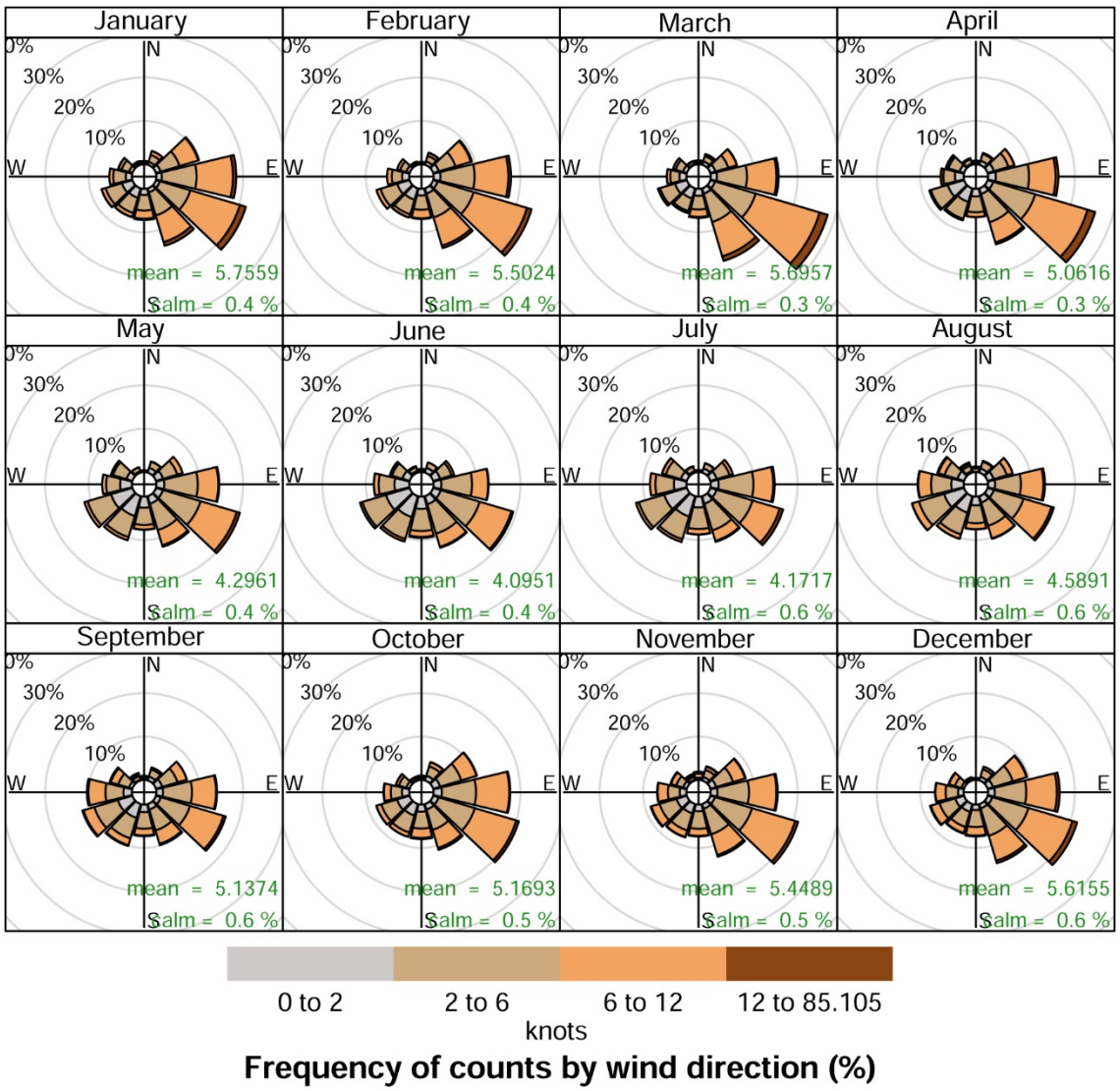

Figure 24. Windrose diagrams for Alice Springs by month between 1/1/2006 to 12/31/2015.

DISCUSSION

This study demonstrates present-day fluvial-aeolian processes and how they relate to linear dune formation and evolution. Observations made at the field site, as well as lithological and mineralogical similarities between playa and dune sediments, indicate that present-day fluvial processes are eroding the dunes into the playa. This was the most obvious on the surface and shallow depths (< 16 cm) of the playa, and particularly at the northern sample site where a fluvial channel draining into the playa incises a dune. Clay (e.g., halloysite, kaolinite) and evaporite minerals (e.g., gypsum, halite) were present in the surface, middle, and lower layers at the central and southern sites, but not at the surface of the northern site. The presence of kaolinite and halloysite in the Simpson Desert are likely a result of weathered feldspars and phyllosilicates (i.e., muscovite) from the north (Anand and De Broekert, 2005). The presence of goethite in the lower layers of the southern sample site indicates advanced weathering of bedrock and saprolite. These minerals were not present in the linear dune at the southern sample site, which superimposed the playa.

The regional topography indicates that water drains from north to south in the playa, and many of the flood observations from the satellite data showed only the southern end of the playa filled with water. This may explain why clay and evaporite minerals are more pronounced towards the center and the southern end of the playa, as well as greater depths. Conversely, these sediments may simply be covered up by a thicker layer of eroded dune sediment at the northern edge of the playa.

To properly address the question of sediment from the playa being reworked downwind into the linear dunes to the north of the playa, lithological and mineralogical analyses of the downwind dune sediments are required. Also, the application of OSL dating techniques of the

playa and dunes located at both the southern and northern edges would be useful to determine if the linear dunes are actively accreting downwind, as well as understand the relative ages of the linear dunes superimposed on the playa surface, the cut-off dune in the eastern central part of the playa, the lithified dunes on the northern edge of the playa, and the linear dunes just north of the playa border as in Fitzsimmons et al. (2007). Nonetheless, the wind analyses showed that wind speeds reached at least 12 knots more than 20% of the counts during the wet season. Any mobilized sediment deposited into the playa by a flood is susceptible to remobilization by aeolian processes in the direction of but not limited to the prevailing wind (i.e., from SE to the NW) once the playa was dry.

Floods in the playa were observed after daily rainfall amounts of 5 mm, and 237 wet days occurred after only 8 mm of rainfall during the 19 years. In all, Lake Caroline experienced 478 wet days. The flooding after only a 5mm rainstorm is likely a result of throughflow groundwater discharging into playa from upland precipitation not accounted for in this study. Since there are linear dunes that superimpose the playa, improved DEMs of the Lake Caroline area would allow for a volumetric measurement of playa lake water to be obtained with satellite images after storms. This calculation combined with a watershed analysis of precipitation at Lake Caroline would support a water balance study. The elevated position of the water table at Lake Caroline may also significantly impact deflation during drier periods and aggradation during wetter, which ultimately affects the sediment supply for the surrounding dunes.

Currently, the consensus in the scientific community regarding this threshold is 20 mm/hr whereby volumes of runoff are enough to temporarily overwhelm evaporative processes (Critchley et al., 2013). Additional analyses of rainfall intensity over shorter durations, such as 30-minute intervals and over a larger area would be useful for understanding the correlations between rainfall

and flooding frequencies not just in the Simpson Desert of Australia but all drylands. Rigorously calibrated gridded-data, such as that from NASA's GPM, provides this information but also struggles with underestimating rainfall in arid environments (Milewski et al., 2015).

CONCLUSION

Investigations into the models of linear dune formation are typically relegated to aeolian processes or only consider the fluvial activity that occurred preceding the aridity. This study considered how present-day aeolian, fluvial, and lacustrine processes relate to linear dune dynamics. Field observations combined with lithological and mineralogical analyses demonstrate that the playa sediments are a combination of eroded dunes, fluvial deposits, and weathered basement rock from the local area. Clay and evaporite minerals identified at the shallow layers on at the southern sample site were not detected in linear dunes that superimposed the playa at the same location. Although it was undetermined if the playa sediment is being reworked into the dunes downwind of the playa, the present-day wind and hydrologic activity (i.e., rainfall, flooding) are adequate to generate and transport sediment into the playa under present-day conditions. Possibly, the superimposed linear dunes of Lake Caroline have been disrupted by episodic floodwaters but are continuing to accrete, encroach, and erode simultaneously by present-day fluvial-aeolian interaction. Refining our understanding of the relationship between fluvial-aeolian interaction and linear dune development is useful to investigate not only how linear dunes form and evolve across scales, but also how global warming will drive changes in the frequency and severity of flooding, sediment supply, and dust storms (Greenville et al., 2012). The prevalence of linear dunes in the deserts on Earth, as well as other planets such as Titan, have important implications for studies related to fluvial and aeolian processes within a planetary science context and water resources research in arid regions with similar settings.

ACKNOWLEDGEMENTS

The authors would like to acknowledge Paul Schroeder and the University of Georgia Clay Mineralogy Lab providing space and equipment for the lithological and mineralogical analyses.

FUNDING

Funding for this project was provided by the William and Valerie Anders Foundation Endowment at the Smithsonian Institution's Center for Earth and Planetary Studies, the Geological Society of America's Farouk El-Baz Student Desert Award, and the University of Georgia Watts Wheeler Research Grant.

CHAPTER 5

PHYSICAL MODELING OF INLAND FRESHWATER LENS FORMATION AND EVOLUTION IN DRYLANDS[1]

[1]Rachel Rotz[1], Adam M. Milewski. 2019. *Hydrogeology Journal.* 27:1597–1610.
Reprinted here with permission of the publisher.

ABSTRACT

Dryland inland freshwater lenses (IFLs) that have been topographically induced are represented using physically modeled laboratory simulations, to characterize the stages of IFL evolution (i.e. formation, migration, degradation) as a function of recharge rate. Arid regions with shallow brackish to saline groundwater possess IFLs. The position and geometry (i.e. thickness, length) of IFLs over varying temporal and spatial scales is poorly understood due to their transient nature. The physically modeled IFLs in this study formed from an initial recharge pulse, after which IFL geometry was measured over time as it flowed in the direction of simulated groundwater flow. The time required for an IFL to reach the maximum thickness exhibited a negative exponential correlation to recharge rate. At IFL formation, thickness and length were positively correlated, and the ratio of IFL thickness to length exhibited a positive exponential correlation to recharge rate. After IFL formation, the central position of the simulated IFLs migrated laterally in the direction of groundwater flow at a velocity less than the range of applied recharge rates and greater than the groundwater flow velocities. The time required for the IFL to reach a minimum thickness or IFL degradation exhibited a positive exponential correlation to recharge rate. The Dupuit-Ghyben-Herzberg solution used to model coastal freshwater lens thickness was tested against the physically modeled IFLs and deemed invalid. A correction factor and modified solution are provided to predict IFL thickness, motivating future analytical and numerical studies on inland variable-density groundwater systems in arid regions globally.

INTRODUCTION

Other than fossil groundwater (e.g. Nubian sandstone aquifer) in arid and semi-arid regions, groundwater throughout the Arabian Peninsula and other drylands is often brackish to saline (Milton, 1968; Saleh et al., 1999; Van Weert and van der Gun, 2012). In regions like the

Arabian Peninsula, mineralization processes over long residence times at great and shallow depths have changed fresh groundwater to brackish or saline, a condition generally considered a widespread problem. However, the occurrence of shallow brackish to saline groundwater encourages the development and sustainability of sporadic, shallow-subsurface accumulations (thickness > 30 m) of meteoric freshwater, some of which supply limited drinking water to Kuwait, Oman, Libya, Namibia, and Egypt (Christellis et al., 2001; Hadi and Al-Ruwaih, 2008; Anderson, 2013; UN-ESCWA, 2013). Recharge is focused and generated by infrequent, high intensity, short duration, rainfall events, typical in regions with low rainfall rates (< 120 mm/yr), and lack of permanent surface water bodies. (Hoekstra and Shachak, 1999; Kwarteng et al., 2000; Lewis and Walker, 2002). The runoff from storms is drained to topographically low areas (i.e. depressions) and vertically infiltrates through permeable desert sediments along preferential pathways towards the water table (Gee and Hillel, 1988). The resultant variable-density condition encourages freshwater accumulation on top of the saline groundwater to form a horizontally oriented, biconvex-shaped lens configuration directly beneath the overlying topographic depression (Bergstrom and Aten, 1965a; Kwarteng et al., 2000). These accumulations of water are referred to as inland freshwater lenses (IFLs), which are considered renewable freshwater resources in arid environments. Recent studies in Kuwait have identified over 20 locations with favorable conditions for IFL occurrence and more than 100 potential locations throughout the Arabian Peninsula. Potential recharge estimates up to 8,000,000 m^3/yr in Kuwait draw attention to the potential of IFLs for sustainable water resource development in dryland regions which comprise more than 40% of the land surface on Earth (Milewski et al., 2014b).

The IFLs of Kuwait were discovered during an exploratory mission in 1961 beneath the Raudhatain and Umm Al-Aish catchments, of which an exploitable IFL occurs below the

Raudhatain depression (Parson's Corporation, 1961). Freshwater in the lens was measured to contain less than 1,000 mg/l total dissolved solids (TDS) in contrast to the saline regional groundwater (TDS > 35,000 mg/l). Long-term pumping tests from 1963 – 1967 were conducted to provide sustainable yield estimates for drinking water (Senay, 1977; Fadlelmawla et al., 2008). Groundwater extraction commenced in 1963 at a rate of 9,000 m^3/d and then increased to 11,000 m^3/d in 1969. During this period, an increase from 550 to 1150 mg/l TDS prompted the State of Kuwait Ministry of Electricity and Water to reduce the extraction rate to 6,500 m^3/d. Over the next twenty years, pumping was systematically decreased and halted in 1990 to protect the resource. IFL water quality improvements were observed during the adjustment period of pumping rates. Kwarteng et al. (2000) noted that decreased pumping rates between 1969 and 1977 combined with above-average precipitation led to improved IFL water quality and decreased concentrations of dissolved solids from 1150 mg/l to 750 mg/l TDS. In particular, two storms (72 and 105 mm) in Kuwait City on November 2 and 11 of 1977 corresponded to a one-meter rise in the water table (Al-Rashed and Sherif, 2000). Some studies have investigated the IFLs of Kuwait focusing on water quality and water age using hydrological and lithological information. Recharge and salinity evolution processes were presented using chemical and isotopic analyses, as well as geochemical modeling (Bergstrom and Aten, 1965a; Himida, 1981; Robinson and Al Ruwaih, 1985; Al-Ruwaih et al., 1998; Al-Ruwaih and Hadi, 2005; Fadlelmawla et al., 2008). The water age in the Raudhatain IFL was characterized as “young” ranging from one to eight years in the northern part of the Raudhatain depression in the recharge zone. In the southern part of the freshwater lens, the spatial distribution of groundwater age correlates with the regional groundwater flow direction where ages ranged from 30 to 500 years. However, IFLs in Kuwait have been speculated to have originally formed from a wetter climate during the Pleistocene epoch (Alsharhan et al., 2001a; Hadi and Al-

Ruwaih, 2008). The formation and proposed age of IFLs suggest that recharge has continued over thousands of years from meteoric precipitation to sustain the lens and prevent the IFL from dissolving or degrading into the saline aquifer. Other studies focused on the climatic and geomorphological conditions necessary for IFL occurrence. Such factors that have been evaluated include cyclonic rainfall, desert sediments, centripetal drainage, topographic depressions, and low gradients (Al-Sulaimi and El-Rabaa, 1994; Al-Sarawi, 1995; Al-Ruwaih et al., 1998; Al-Sulaimi and Mukhopadhyay, 2000; Din et al., 2007; Milewski et al., 2014a). Based on this research, IFLs can occur in various locations, are recharged episodically, and degrade over time as the IFL is exploited or flows away from the recharge area.

The majority of freshwater lens studies that examine the geometry (i.e. thickness) are located in coastal settings (e.g. islands, peninsulas) in contrast to low-lying, terrestrial inland environments particularly in drylands with negligible precipitation (Figure 25). Freshwater lenses are commonplace in coastal settings, and like the inland form, float on top of denser saline water. Early coastal freshwater lens research focused on variable-density relationships and their influence on the depth to the saltwater/freshwater interface from sea level (Baydon-Ghyben, 1898; Herzberg, 1901; Hubbert, 1940). Coastal variable-density systems are governed by recharge rate, geometry, hydraulic conductivity, as well as boundary conditions and spatial variations. Coastal freshwater lens geometry (i.e. thickness, length) is estimated using analytical models in isotropic and anisotropic conditions (Fetter, 1972; Van Der Veer, 1977; Vacher, 1988; Stuyfzand and Bruggeman, 1994; Chesnaux and Allen, 2008), as well as for coastal freshwater wedges (Glover, 1959; Henry, 1964; Carol et al., 2010; Eeman et al., 2011). Physical and numerical models to simulate the dynamics of coastal freshwater lenses are also found in the literature (Zhao et al., 2009; Stoeckl and Houben, 2012; Dose et al., 2014; Stoeckl et al., 2016; Cellone et al., 2018).

Studies regarding IFLs located in non-coastal settings are documented and have led to increased awareness of their importance as a water resource and supply (Laattoe et al., 2017). Rain-fed freshwater lenses bound by a river have been studied utilizing physical and analytical models in drylands (Werner et al., 2016; Werner and Laattoe, 2016a). Inland lenses have also been studied using numerical and geophysical models (Phelps and Rohrer, 1987; Barrett et al., 2002; Houben et al., 2014). Houben et al. (2014) delineated the geometry of a rain-fed IFL in Paraguay located 900 km from the nearest coast using geophysical and analytical methods. The study identified basal freshwater layers older than a thousand years and demonstrated that IFL recharge continues under current climatic conditions. In this case, the IFL exhibited characteristics similar to an island lens because it formed beneath a hill and was bounded by the surrounding Saline groundwater of the Chaco lowlands. Barrett et al. (2002) investigated saltwater intrusion in an IFL beneath a sinkhole using geophysical techniques to measure IFL geometry near Waikerie, South Australia. These studies, including an IFL beneath a coastal interdune depression in Brazil by Szymkiewicz et al. (2018) and an IFL beneath a remnant dune complex in central Australia by Cendón et al. (2010), bring attention to the various configurations and longevity of IFLs, as well as their sensitivity to recharge through time. However, investigations into the formation and transience of a topographically induced focused recharge driven, dryland IFL are rare in the literature.

A conceptual model of the formation and transient evolution of drylands IFLs is shown in Figure 26 and is described as (a) freshwater infiltrates from an episodic recharge event directly beneath the central area of a topographic depression, (b) freshwater accumulates atop the saltwater layer directly beneath the depression until time of maximum thickness or IFL formation, (c) lateral

flow of the IFL ensues in the direction of the regional gradient and saline groundwater flow, and (d) IFL thickness decreases and length increases until IFL degradation occurs at a time of minimum thickness. Observations of the formation and transient evolution of IFLs are challenging because they require long-term, continuous data sets that are generally not available. Therefore, models that investigate the development and transient evolution provide an understanding of this water resource over varying temporal and spatial scales. The primary objectives of this study were to (1) use a physical hydrologic model to support direct observations of topographically induced, focused recharge driven, dryland IFLs, (2) examine the transient evolution of IFLs in regards to the formation, position, and degradation through time, and (3) test the validity of an analytical solution (Vacher, 1988) used to predict coastal freshwater lens geometry on the simulated IFLs.

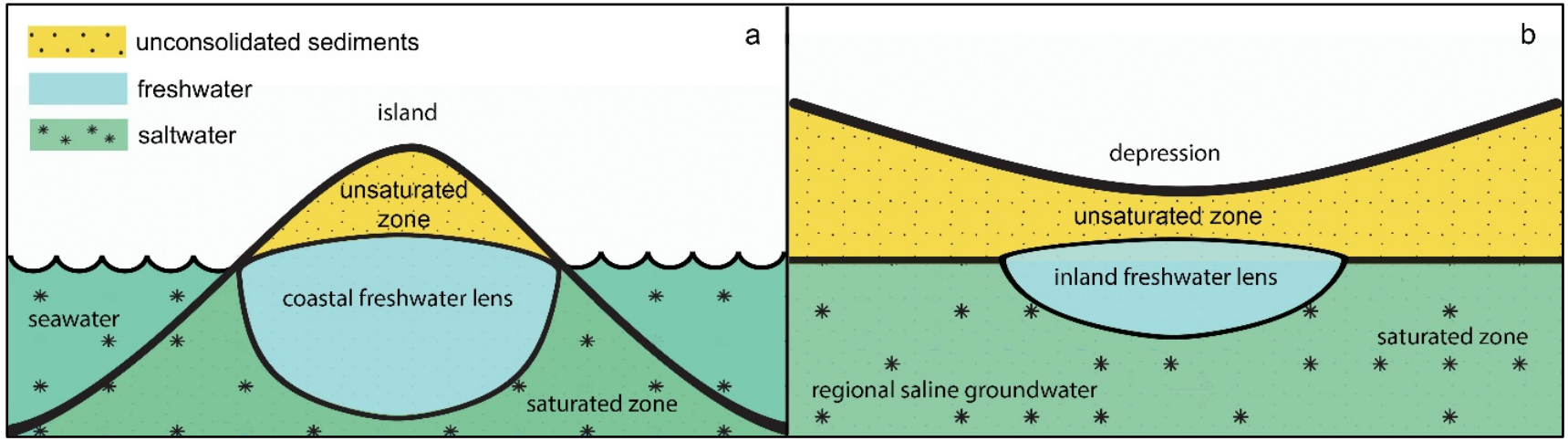

Figure 25. Conceptual diagrams of a coastal freshwater lens (a) and an IFL (b).

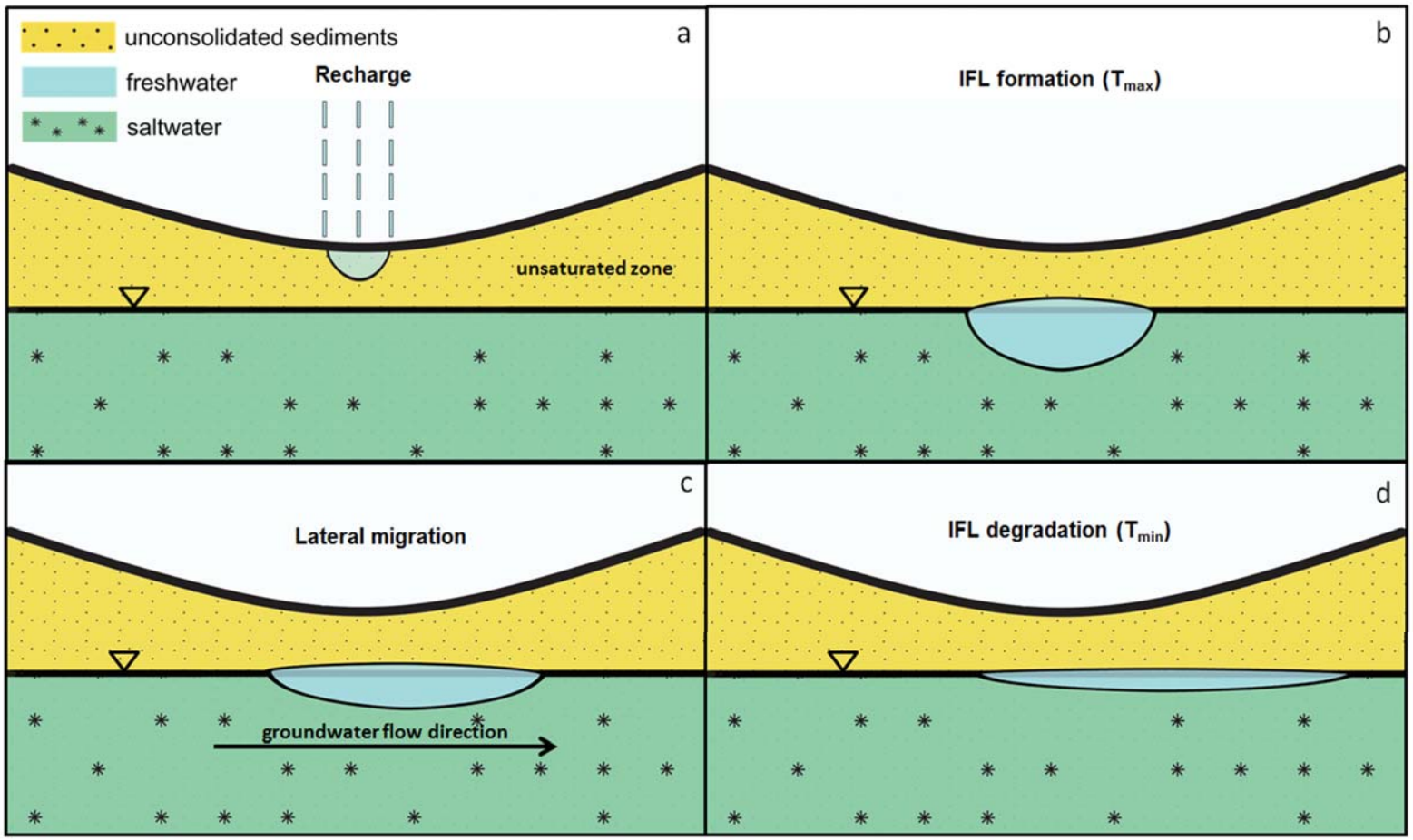

Figure 26. The formation and transient evolution of a dryland IFL. A recharge event occurs (a), at which time an IFL develops to a maximum thickness (T_{max}) (b), followed by the lateral migration (c) until time of minimum thickness (T_{min}), or IFL degradation (d).

METHODOLOGY

Physical model

Previous studies have utilized physical models to investigate rain-fed freshwater lenses on the coast and bounded by a river (Pennink, 1915; Zhao et al., 2009; Stoeckl and Houben, 2012; Dose et al., 2014; Werner et al., 2016). The approach for this study was inspired by a physical model by Stoeckl and Houben (2012) utilized to simulate an infinite strip island freshwater lens. For this study, an acrylic tank (2.00 m L x 0.10 m W x 1.0 m H) and an experimental system were designed to perform simulations of an IFL (Figure 27). The physical model represents a two-dimensional, cross-section of a topographic depression with features similar to the Raudhatain watershed of northern Kuwait, This included (1) an elongated depression (0.45 m L x 0.15 m W) with a length to width ratio of three to represent the interior Raudhatain depression (16,000 m L x 4800 m W), (2) highly permeable sand to represent the coarse sand and gravel which encourages vertical infiltration at the recharge zone in northern Kuwait, and (3) a variable-density groundwater environment (IFL = 649 ppm TDS, groundwater = 35,700 ppm TDS) similar to the fresh and brackish to saline water beneath the Raudhatain depression (IFL = 600 – 1000 ppm, groundwater water = 7,000 – 50,000 (Bergstrom and Aten, 1965b; Kwarteng et al., 2000).

The top of the tank was outfitted with a lid and included a central slit (0.01 m x 1.80 m) that served as a mounting guide for the freshwater recharge tubes. The bottom and right lower side of the tank was outfitted with drainage holes (12 basal, 3 lateral) spaced 15 cm apart, which channeled water into catchment containers by polyurethane tubing and control valves. The inside-left side of the tank was fitted with a PVC pipe (1.00 m H x 0.04 m D), which was vertically and horizontally perforated (5 mm holes, 15 mm spacing) from the bottom to a height of 0.41 m and used to inject saline water, maintain a hydraulic gradient, and sustain a constant flow through the

tank. A low-flow, APT branded peristaltic pump was used to impel the saltwater, and Adafruit branded 12V DC peristaltic pumps with tubing (3 mm ID, 5 mm OD) were used to impel the freshwater into the tank during simulations. Power was supplied to the pumps with a Philmore branded multi-voltage regulated DC power supply. The sand utilized inside the tank was naturally occurring, unfiltered sand, semi-dry (2% moisture content), well-sorted, well-rounded, and medium to fine-grained (d_{50} = 0.55 mm) as determined by a particle size analysis using a sieve kit. Grain size distribution results characterized the sand as 5.2% gravel, 93.8% sand, and 1% fines. Total porosity was calculated to 39% using the sum of solid and pore volumes. The saturated hydraulic conductivity was measured before the simulations using a constant head permeameter at a value of 1.5×10^{-3} m/s, a value typical of coarse sand and gravel rather than medium to fine sand due to the loosely packed particles.

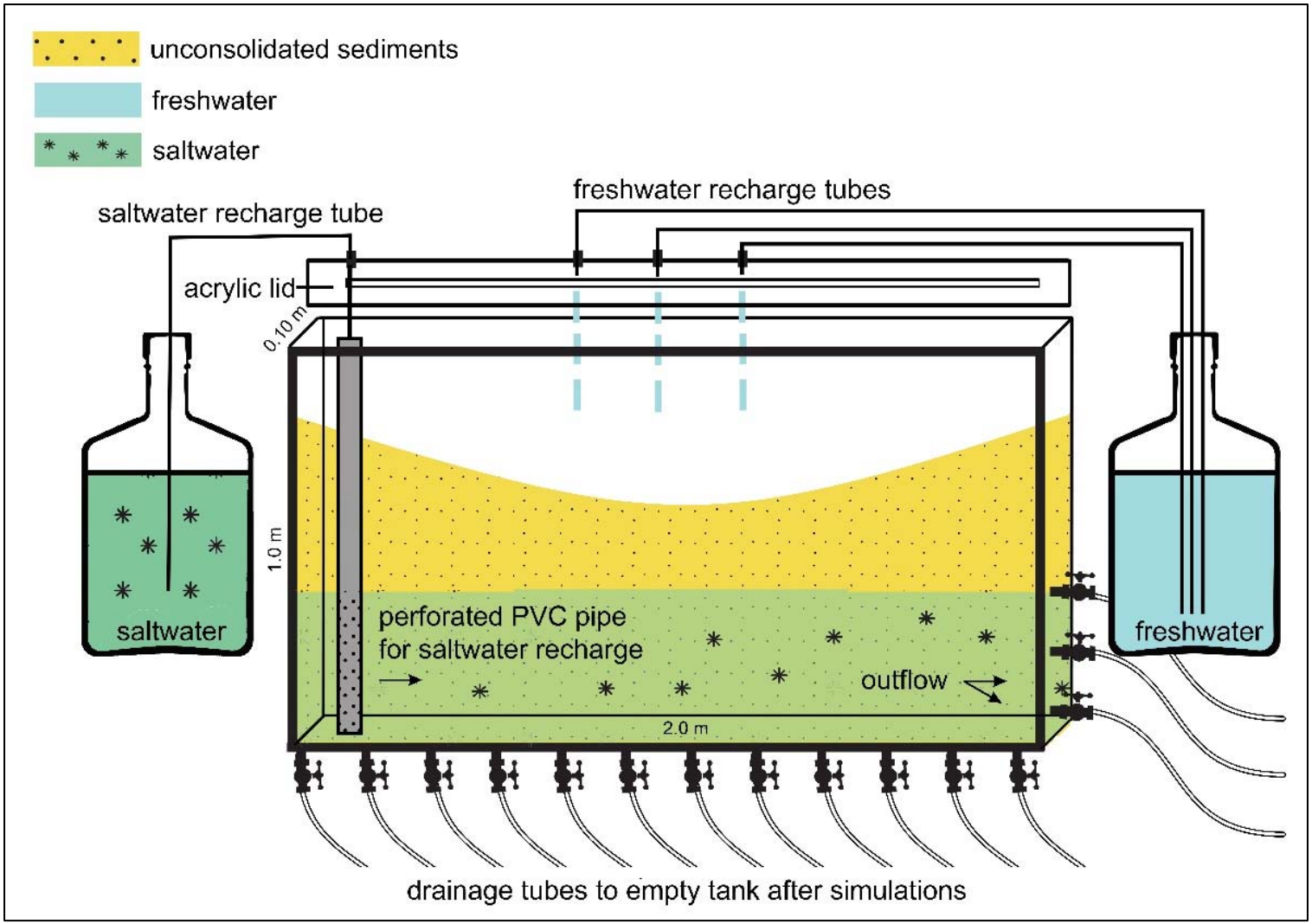

Figure 27. Physical model schematic and configuration.

Experimental simulations and analysis

Twelve freshwater lens simulations were generated with varying recharge rates, saltwater flow rates, and recharge widths. For all simulations, the recharge application was stopped after 3600 seconds. Vertical infiltration velocities of the freshwater recharge ranged between 1.85 x 10^{-5} m/s and 1.50 x 10^{-4} m/s, or volumetric flow rates between 8.33 x 10^{-7} m^3/s and 7.13 x 10^{-6} m^3/s, respectively. Simulations A1 to A8 (A-series) included saline groundwater flow, of which volumetric flow rates of 8.90 x 10^{-9} m^3/s and 9.55 x 10^{-9} m^3/s were pumped to achieve lateral infiltration velocities between 2.17 x 10^{-7} m/s and 2.33 x 10^{-7} m/s, respectively (Table 7). Simulations B1 to B4 (B-series) did not include saline groundwater flow, assumed a static saline water body, and the recharge width of two simulations (B2, B3) were greater than 0.50 m (0.60 m, 1.04 m). IFLs that formed during simulations B3 and B4 became too large, due to high recharge rates, such that they extended to the edges of the tank before the freshwater application was finished. Therefore, maximum thickness and the subsequent increase in length were not observed for these two simulations.

Table 7. Simulation variable values: recharge rate I, recharge volumetric flow rate (Q_R), recharge length (w_R), saltwater flow rate (q_s), and saltwater volumetric flow rate (Q_s).

Simulation	R (m/s)	Q_R (m^3/s)	W_r (m)	q_s (m/s)	Q_s (m^3/s)
A1	1.85×10^{-5}	8.33×10^{-7}	0.45	2.17×10^{-7}	8.90×10^{-9}
A2	2.00×10^{-5}	1.00×10^{-6}	0.50	2.17×10^{-7}	8.90×10^{-9}
A3	2.33×10^{-5}	1.05×10^{-6}	0.45	2.33×10^{-7}	9.55×10^{-9}
A4	3.27×10^{-5}	1.63×10^{-6}	0.50	2.33×10^{-7}	9.55×10^{-9}
A5	3.97×10^{-5}	1.67×10^{-6}	0.42	2.33×10^{-7}	9.55×10^{-9}
A6	4.72×10^{-5}	1.98×10^{-6}	0.42	2.33×10^{-7}	9.55×10^{-9}
A7	6.48×10^{-5}	2.92×10^{-6}	0.45	2.33×10^{-7}	9.55×10^{-9}
A8	7.86×10^{-5}	3.30×10^{-6}	0.42	2.33×10^{-7}	9.55×10^{-9}
B1	2.22×10^{-5}	9.33×10^{-07}	0.42	0	0
B2	2.56×10^{-5}	1.54×10^{-6}	0.60	0	0
B3	5.61×10^{-5}	5.83×10^{-6}	1.04	0	0
B4	1.50×10^{-4}	7.13×10^{-6}	0.48	0	0

For each simulation, sand was systematically added and packed to replicate the lower layer of the topographic depression comprised of unconsolidated sediment. After the sand was added to a height of 0.41 m, saltwater was slowly poured into the left side of the tank until the sand was saturated. Saturated sand was gently repacked and left for twenty-four hours to allow air to escape from the pore spaces. Synthetic marine salt was utilized to create the saltwater. The salinity levels and densities of saltwater (35,700 ppm TDS, 1028 kg/m^3) and freshwater (649 ppm TDS, 1000 kg/m^3) were measured using a Magnum Media branded refractometer using specific gravity and salinity percentage measurements. After the saltwater layer was created, "dry" sand was packed atop the saturated sand on alternating left and right sides of the tank, and a depression was formed in the center. To simulate the saline groundwater flow, saltwater was pumped into a perforated PVC pipe to achieve lateral infiltration rates of 2.17×10^{-7} m/s-2.33×10^{-7} m/s and flowed from the left to right side of the tank. The bottom drainage valves were primarily utilized to flush the tank between simulations except for two drainage valves on the bottom and right side of the tank, which controlled lateral outflow rates of 2.17×10^{-7} m/s and 2.33×10^{-7} m/s. To initiate the IFL simulations, freshwater was pumped through the polyurethane tubing of three to five pumps depending on the recharge rate. The ends of the tubes were positioned directly above the depression center to simulate the accumulation of runoff within a depression and focused recharge in a dryland environment. The freshwater application length also referred to as the recharge length, ranged from 0.42 m to 1.04 m. To distinguish freshwater from saltwater, a water-soluble form of Uranine fluorescein tracer dye was added at a concentration of 475 mg/l of freshwater to ensure the coloring was bright enough to be photographed. The specific gravity of the freshwater and tracer dye mixture was measured with a Magma Media branded refractometer to be 1.00 and determined negligible. Simulations were digitally photographed at 30-second intervals from the onset of

recharge application with a Brinno TLC200 time-lapse camera at 720 dpi resolution. Recordings continued for an average duration of 15 hours. Time-lapse images were then compiled into a video recording of each simulation. Each video was reviewed, and the capturing of still images began when the simulated IFL was observed to reach a maximum thickness. Subsequent still images were captured every 3600 seconds until the IFL was observed to distort proximal to the tank wall (Figure 28).

Still-images were imported into WebPlotDigitizer software and calibrated by two, meter-long measuring sticks placed on the outside of the tank. Images were enhanced to improve the visual interpretation of freshwater accumulation, which was represented by areas of maximum tracer dye saturation. The freshwater table was interpolated between the left and right edges of the lenses through the capillary rise, and the freshwater-saltwater interface was visually interpreted. IFL geometry (i.e. thickness, length) was measured throughout the simulations (Figure 29). Statistical analyses were performed to analyze IFL formation, geometry, position, and degradation as a function of recharge rate. Lastly, IFL volume and specific retention above the IFL was calculated for each simulation eleven hours after the recharge event, when all the lenses reached a maximum measurable length before appearing to deform by the tank wall.

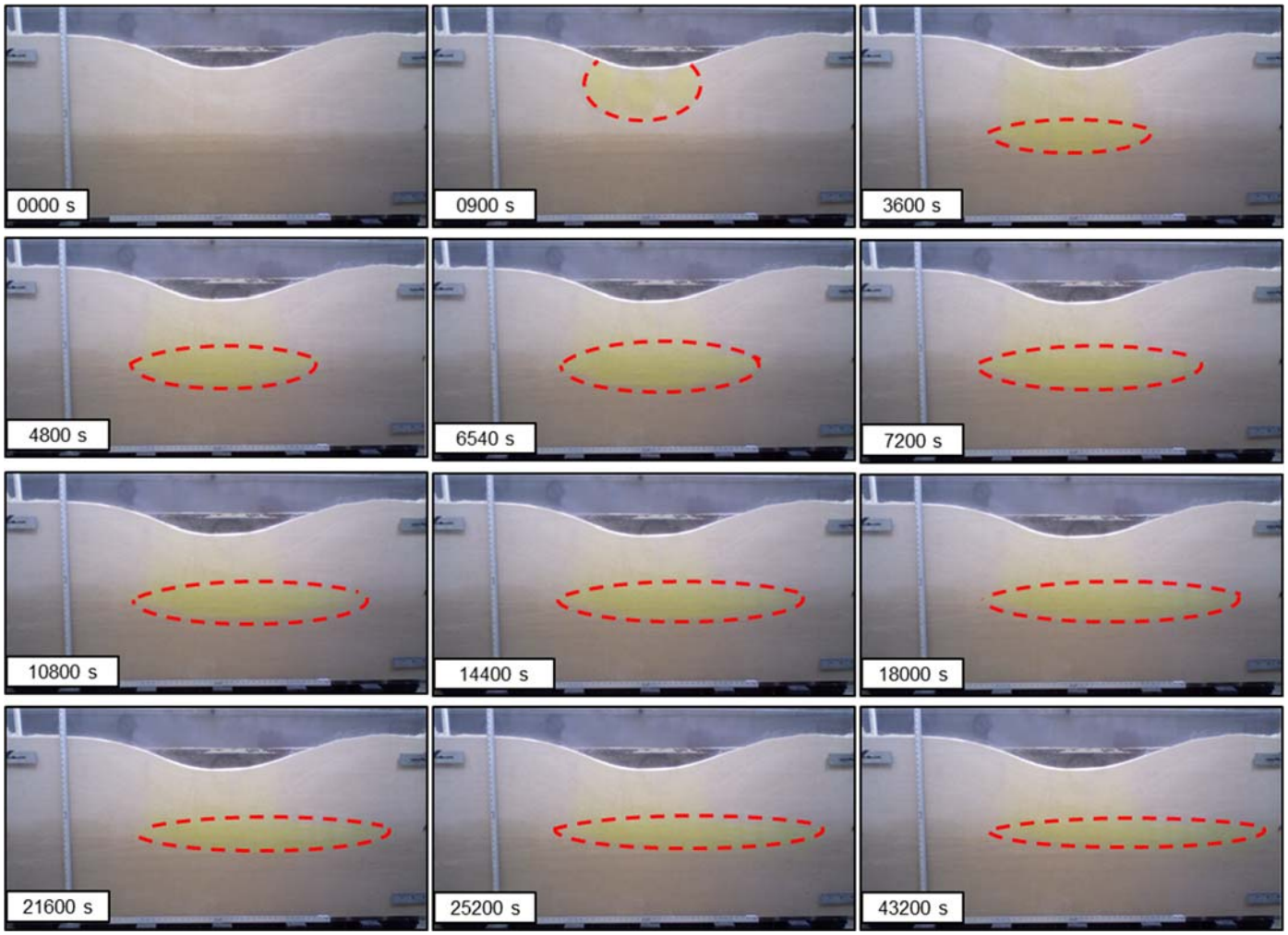

Figure 28. Captured still photographs for the A6 IFL simulation shown by the dashed line for 43200 seconds are shown. The timestamp of the photograph is displayed in the bottom left corner. The maximum thickness occurs at 6540 seconds. The residual yellow area above-defined lens indicates infiltrating or retained freshwater.

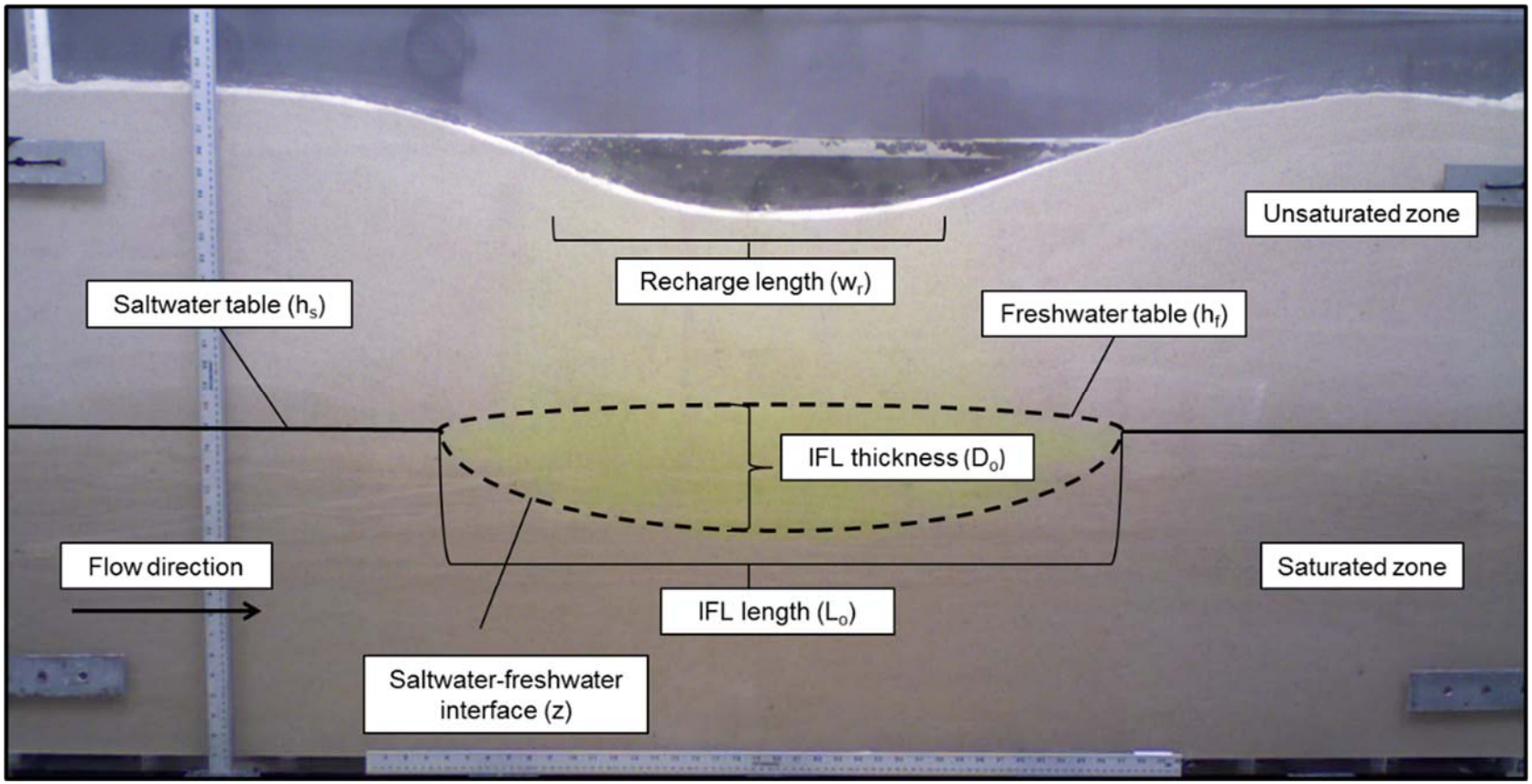

Figure 29. Simulated IFL system including experimental conditions (e.g. unsaturated, zone saturated zone), measured variables (i.e. D_o, L_o, w_r), and meter sticks for calibration.

Analytical solution

This study tested the Dupuit-Ghyben-Herzberg solution by Vacher (1988) and Hubbert (1940) as seen in Eqns. 1-3 to calculate the geometry of a coastal freshwater lens with observed IFL geometry. The analytical solution assumes steady-state conditions of a coastal lens as opposed to the transient state of the IFL system. Therefore, the analytical solution was tested against the IFL geometry only at the time of maximum thickness, or the moment when the rate of IFL development in the vertical direction was zero and before lateral migration was observed. Additional assumptions include homogenous, isotropic conditions, and a sharp freshwater-saltwater interface with horizontal groundwater flow (Dupuit, 1863).

$$h_f^2 = \frac{R}{K(\alpha+1)}(w_R x - x^2) \quad (3)$$

$$\alpha = \frac{\rho_f}{\rho_s - \rho_f} \quad (4)$$

$$z = \alpha h_f \quad (5)$$

Eqn. 3 defines the elevation of the freshwater table (h_f) from a datum at sea level, as a function of the ratio between recharge rate (R), the product of hydraulic conductivity (K), and the Ghyben-Herzberg factor (α) (Baydon-Ghyben, 1898; Herzberg, 1901), when $h_f = 0$ at $x = w_R$, and $x = 0$, where w_R is the full width of the island and x is any position along a horizontal axis. The depth of the freshwater-saltwater interface (z) from sea level can then be calculated. For each experiment, a coastal freshwater lens was modeled using analytical methods in Microsoft Excel using the same variable values (w, R, K, α) selected to simulate an IFL with the physical laboratory model. Total thickness and length were calculated:

$$D_a = h_f + z \quad (6)$$

$$L_a = w_R \quad (7)$$

where D_a is defined as the thickness of the modeled lens, and L_a is defined as the length of the modeled lens. Thickness and length values of the modeled lenses were compared to the measured thickness (D_o) and length values (L_o) of the observed IFLs at their time of maximum thickness. Statistical analyses were performed to examine the differences in the response of geometry to varying recharge rates between the two types of lenses. Also, the effect of recharge rate on coastal lens formation and geometry was measured and characterized using statistical analyses.

RESULTS & DISCUSSION

Recharge Rate IFL Formation, Geometry, Position

A log-log regression was performed on the A-series simulations to determine the effect of recharge rate on IFL formation or at the time of maximum thickness (T_{max}) (Figure 30). Results show that recharge rate has a significant, positive relationship with the time required for IFL formation. As the recharge rate increased, IFLs formed more quickly [R^2=0.90, n=8, p=0.0003]. B-series simulations were not included in this analysis because they did not include saline groundwater flow. To analyze the effect of recharge rate on IFL geometry for the A-series simulations, a log-log regression was performed on the IFL thickness to length ratio (D_o/L_o) as a function of the recharge rate (Figure 31). As the recharge rate increased for each simulation, the IFL thickness to length ratio also increased [R^2=0.92, n=8, p=0.00006].

A Pearson correlation coefficient was computed for the combined A and B-series datasets to examine IFL geometry at the time of IFL formation and to demonstrate the relationship between IFL thickness and length. Although a positive correlation was determined between the two variables [r=0.87, n=12, p=0.0002], a second Pearson correlation coefficient for only the A-series simulations revealed a more significant correlation [r=0.97, n=8, p=0.00004] (Figure 32). Larger recharge widths for the B-series simulations likely explain the difference in correlation, which

suggests that recharge widths also affect IFL geometry. Additional studies are required to determine this effect.

The center position of the IFL was measured every 3600 seconds after IFL formation to determine a lateral migration rate. Velocities of the A-series simulations ranged from 5.1 x 10^{-6} m/s to 6.7 x 10^{-6} m/s with an average freshwater velocity of 6.3 x 10^{-6} m/s or 2.0 cm/hr in the direction of the saline groundwater flow. A small amount of freshwater was observed to flow in the opposite direction of the saline groundwater flow, likely in response to the hydraulic gradient induced by mounding and preferential flow paths, but this localized condition did not affect the overall flow direction of the IFL. The rates of lateral migration intercede between the lower rates of saline groundwater flow (2.17 x 10^{-7} -2.3 x 10^{-7} m/s) and recharge rates (1.4 x–10^{-4} - 1.8 x 10^{-5} m/s) (Figure 33). In all cases, IFLs were observed to flow at a slower rate than the applied vertical recharge rate, but faster than the saline groundwater flow rate. These observations align with the natural conditions in the Kuwait Group Aquifer, where vertical infiltration rates were measured as high as 1.6 x 10^{-4} m/s (Fadlelmawla et al., 2008), freshwater flow rates up to as much as 7.8 x 10^{-6} m/s (Bhandary et al., 2015; Al-Weshah and Yihdego, 2016), and saline groundwater down to as much 3.5 x 10^{-7} m/s.

Recharge Rate and IFL Degradation

Based on the observations of IFL lateral migration, it was assumed that the simulated IFL would continue to smear atop the saltwater surface until indiscernible. A minimum thickness of 0.01 m was selected to predict the time required for each simulated IFL to reach a minimum thickness (T_{min}), referred to as IFL degradation. A positive, significant relationship was determined between recharge rate and IFL degradation [R^2=0.88, n=8, p=0.0006] (Figure 34). As

the recharge rate increased for each simulation, the IFL longevity increased. A summary of the results is provided in Table 8.

The volume of recharge applied to each simulation was reconciled to the volume freshwater observed to be contained within the simulated IFL twelve hours after the start time. Due to the transient nature of the IFL and capillary fringe, IFL volume was calculated using the area of an ellipse and then multiplied by the width of the tank. Calculations overestimated freshwater volume by 10% ± 1% on average for the eight simulations. Several factors may attribute to the overestimation. These include differences in geometries between the IFL and the ellipse shape, as well as the mixing of tracer-dyed freshwater with the saline water and / or the moisture content of the pore spaces above the IFL, which was measured to be between at 2% at the beginning of the simulations and 3.8% twenty-four hours after recharge was applied.

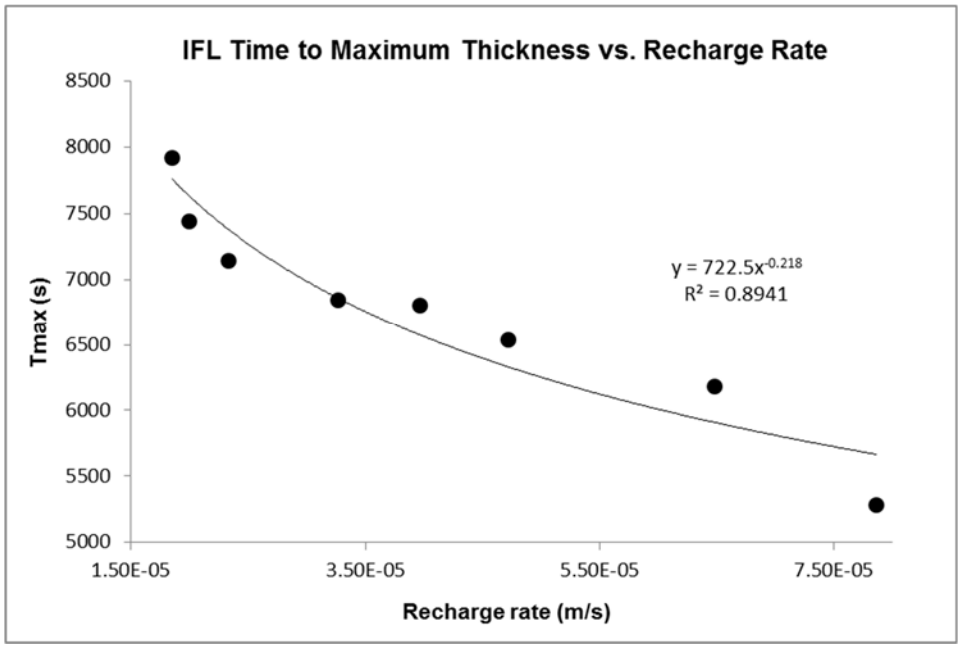

Figure 30. Recharge rate as a function of the time required for a simulated IFL to reach a maximum thickness (T_{max}), also referred to as IFL formation.

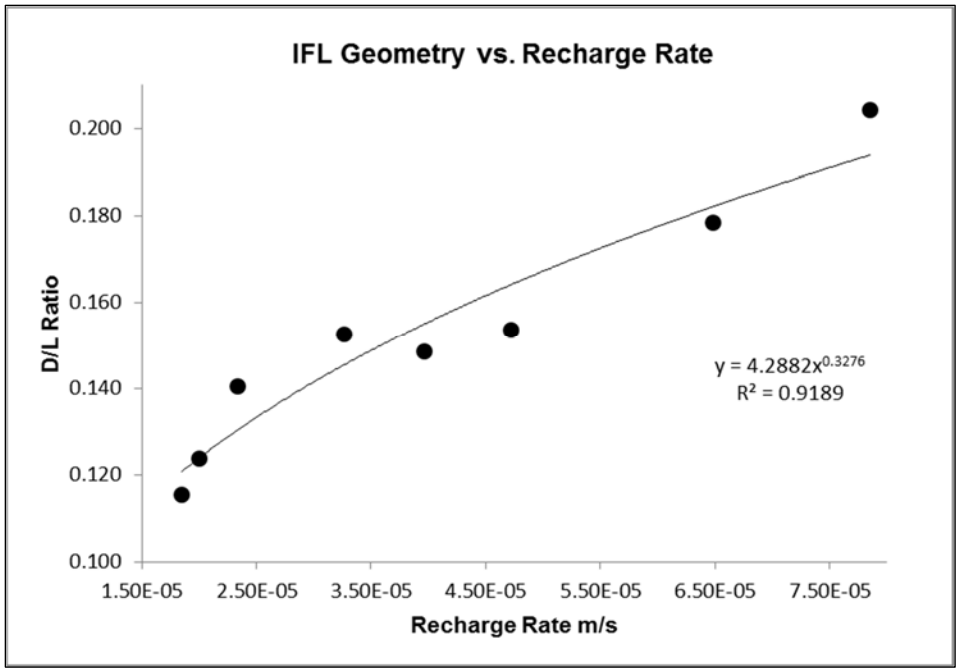

Figure 31. IFL thickness/length (D/L) ratio as a function of recharge rate.

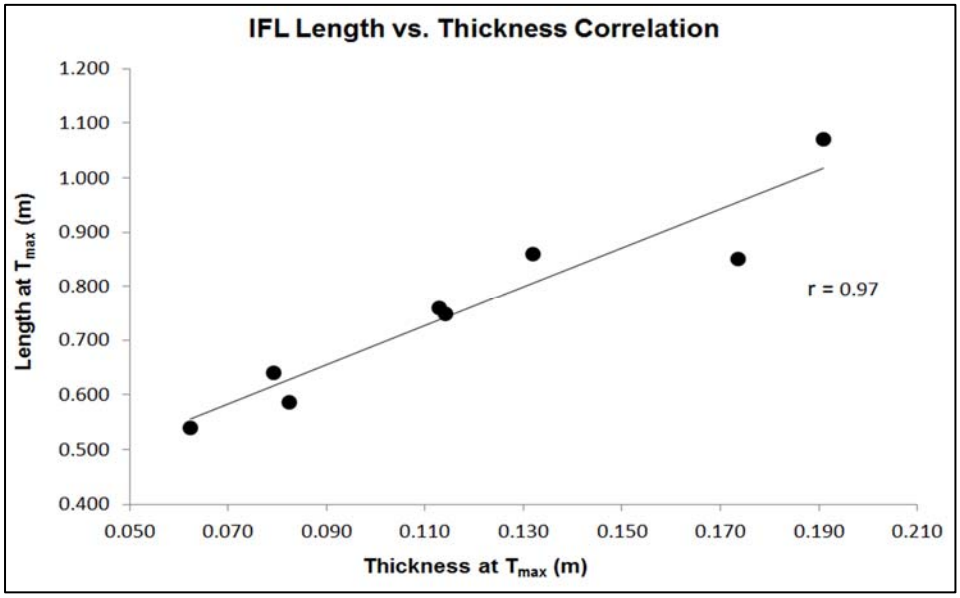

Figure 32. Correlation between IFL thickness and length at the time of maximum thickness (T_{max}) for A-series simulations.

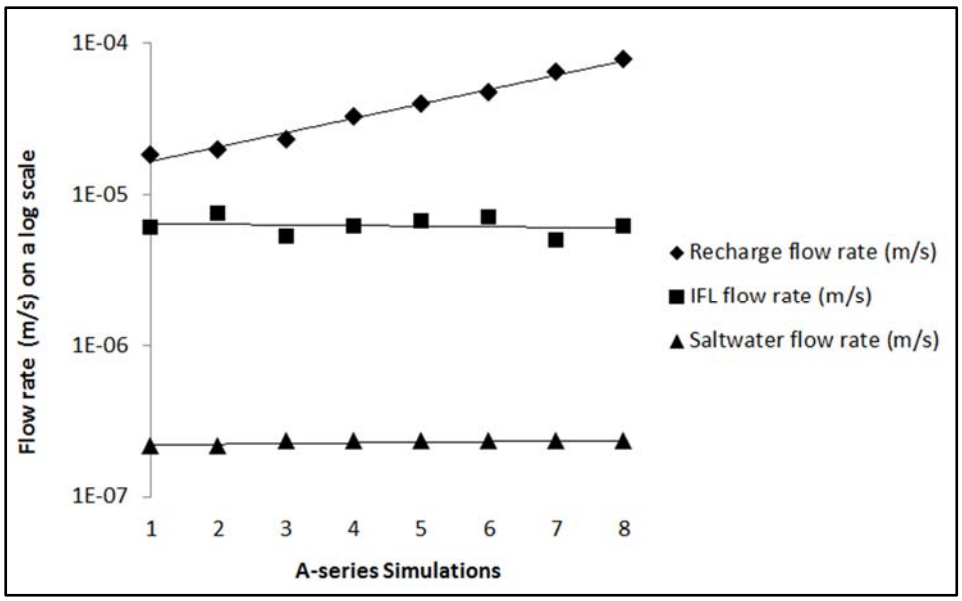

Figure 33. Comparison between recharge, IFL, and saltwater flow rates for simulations A1–A8 shown on a log scale.

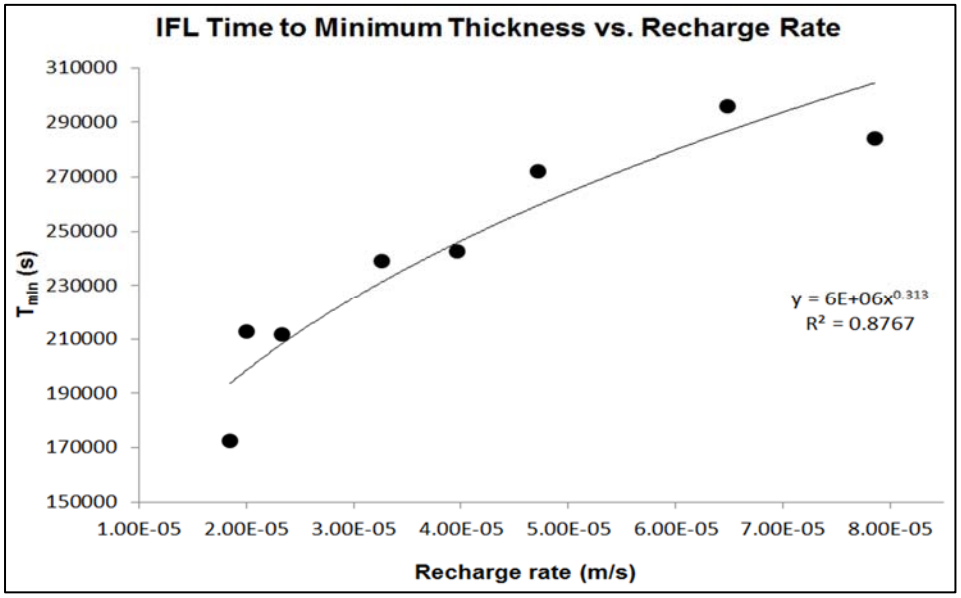

Figure 34. The predicted time required for IFL to reach a minimum thickness (T_{min}) or degradation as a function of recharge rate shown in seconds.

Validity test of an analytical solution to observed IFLs

In all cases, the modeled thicknesses were greater than observed thicknesses (Figure 35). A log-log regression between modeled thicknesses and observed IFL thicknesses as a function of recharge showed a significant positive correlation between both freshwater lens types and recharge [R^2=0.93, n=8 p=9.3 x 10^{-5}] and [R^2=0.93, n=8, p=1.2 x 10^{-4}] respectively (Figure 36). Although not within the scope of this study, the lens thicknesses of both analytical and laboratory models respond to the variation of recharge widths as shown by the scatter of data points along the trend line of both models. However, the recharge rate only had a significant effect on the IFL lengths [R^2=0.82, n=8, p=0.00140]; whereas, the modeled lens lengths were equal to the full width of the island as defined by the boundary conditions of the analytical solution (Figure 37).

The lengths of freshwater lenses modeled using the Dupuit-Ghyben-Herzberg solutions were subtracted from the lengths of the simulated IFLs. A log-log regression of the subtracted lengths as a function of recharge shows a significant relationship between the variables [R^2=0.77, n=8, p=0.004] (Figure 38). The differences in the lengths of the observed and analytically modeled lenses increase as recharge rates increase, demonstrating how the IFL lengths continue to increase and extend as recharge rate increases. However, a log-log regression to examine differences in thicknesses as a function of recharge showed no significant relationship [R^2=0.34, n=8, p=0.1304]. The differences between the thicknesses of modeled and observed lenses in this study maintained an average thickness of 0.10 m ± 0.003 m despite increased recharge rates (Figure 38).

The regression model (Eqn. 8) demonstrating the differences in thicknesses between the analytical and modeled lenses (ΔD) was subtracted from the regression model (Eqn. 9) demonstrating analytical lens thickness (D_a) to predict the thickness of an IFL (D_i) at a given recharge rate (Eqn. 10).

$$\Delta D = 278.57R + 0.0872 \quad (8)$$

$$D_a = 16.485\, R^{0.4234} \quad (9)$$

$$D_i = 16.485\, R^{0.4234} - 278.57R + 0.0872 \quad (10)$$

Further, the correction factor can be applied to the Ghyben-Herzberg principle (Eqn–. 11 - 14) to predict the IFL water table elevation (h_i) and depth to the saltwater interface (z_i).

$$D_i = \sqrt{h^2} + z - 278.57R + 0.0872 \quad (11)$$

$$h_i = \frac{Di}{\alpha+1} \quad (12)$$

$$D_i = h_i + z_i \quad (13)$$

$$z_i = \alpha h_i \quad (14)$$

A modified form of the Dupuit-Ghyben-Herzberg solution (Eqn. 15) was used to model IFL thicknesses. An independent t-test did not provide a statistically significant difference between the modeled and observed IFL thicknesses (t = -0.016496, df = 13.998, p-value = 0.9871). Figure 39 shows the modeled and observed thicknesses as a function of recharge using the modified solution.

$$h_i = \frac{\sqrt{\frac{R}{K(\alpha+1)}(w_R x - x^2)} + \alpha\sqrt{\frac{R}{K(\alpha+1)}(w_R x - x^2)} - 278.57R + 0.0872}{\alpha+1} \quad (15)$$

The correction factor and modified equation were only tested on the modeled lenses and therefore are not directly transferable outside laboratory experiments due to scaling and complexity challenges. Further, this study examines the formation and transient evolution of an

IFL after one recharge pulse, but IFLs that occur in nature have been recharged over varying spatial and temporal scales. The development of analytical and numerical methods will provide improved approaches to understanding IFLs like the one beneath the Raudhatain depression.

Results from this investigation are consistent when compared to a previously published study that modeled coastal freshwater lenses using a physical model and successfully fit the coastal freshwater lens to the same analytical solution used in this study. A physical model of similar materials and scale (2.0 m x 0.5 m x 0.05 m) created by (Dose et al., 2014) was utilized to simulate a coastal lens with a recharge rate of 1.152 m/d. The coastal lens reached a maximum thickness of 15 cm after 200 minutes. The most comparable IFL simulation was one with a recharge rate of 1.598 m/d, during which an IFL reached a maximum thickness of 6 cm in 132 minutes. These differences in thicknesses, despite a much higher recharge rate for the IFL simulation, suggest the comparisons made between modeled coastal freshwater lenses and IFLs in this study are applicable. However, additional variables (i.e. Ghyben-Herzberg factor, saline groundwater flow, recharge width) certainly influence freshwater lens dynamics, and therefore require additional investigation to thoroughly compare the models.

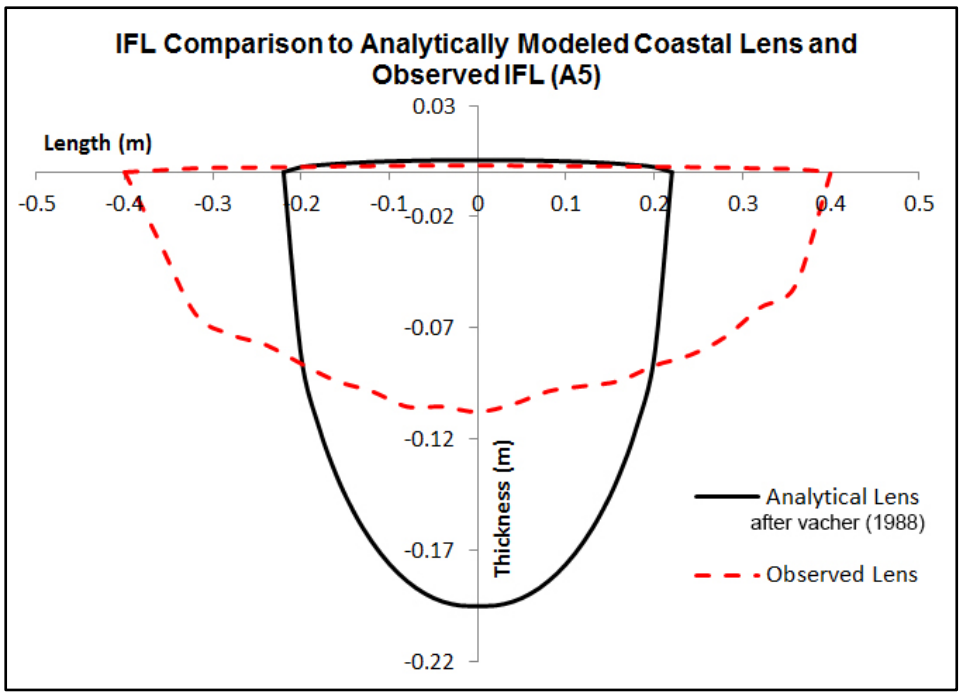

Figure 35. Lens comparison between simulation A5 (dashed line) at T_{max} = 6800 seconds and an analytically modeled (solid line) coastal freshwater lens using the same variable values demonstrate the differences in thicknesses and lengths of lens types.

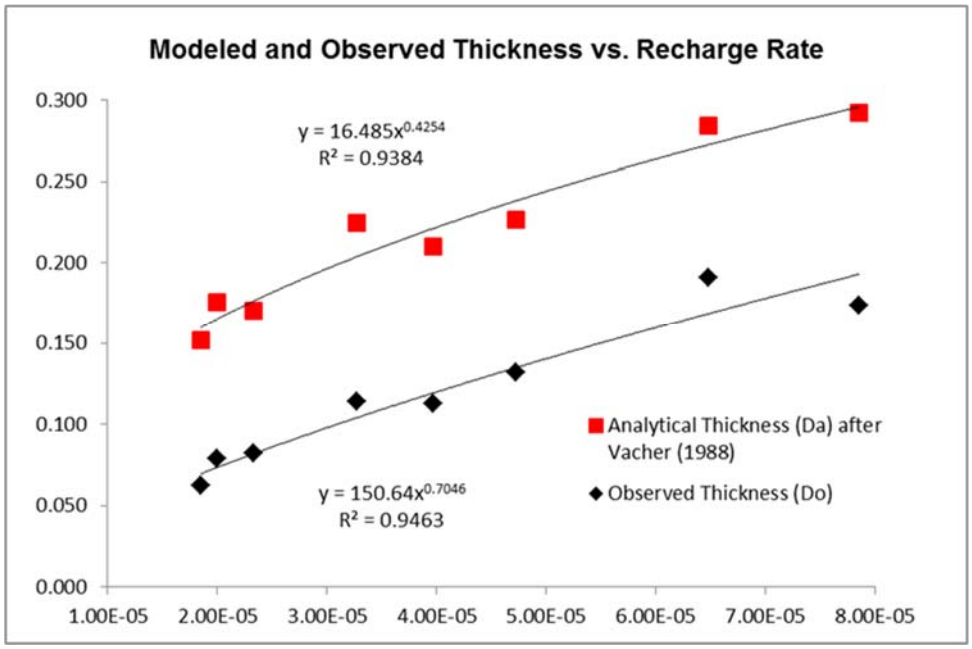

Figure 36. Analytically modeled lens thicknesses and observed IFL thickness as a function of recharge rate. Systematic scatter along with the analytical solution and observed trend lines indicate recharge width affects thickness.

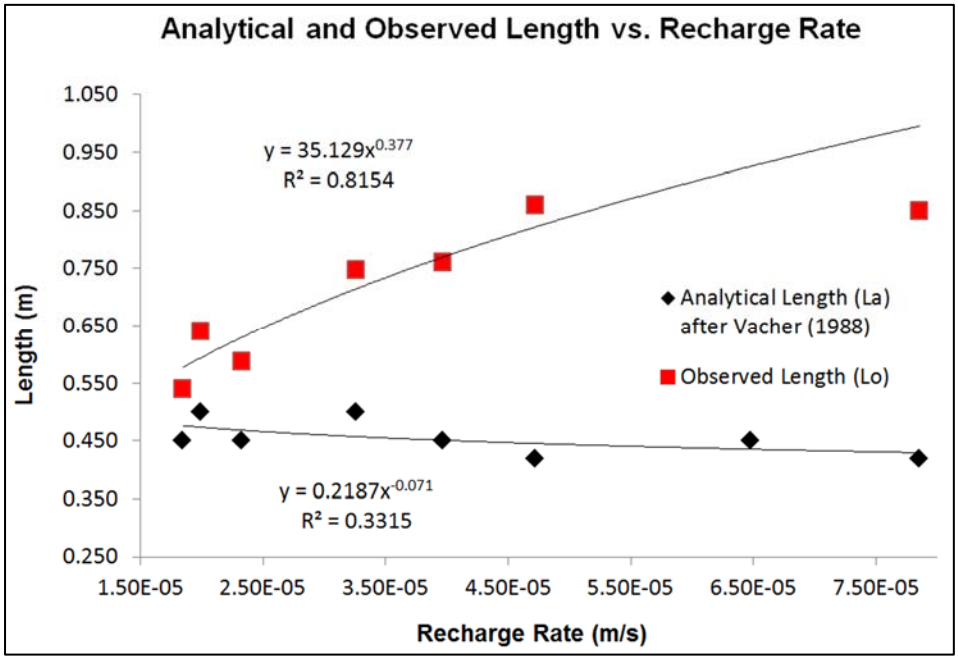

Figure 37. Analytically modeled lengths and observed IFL lengths as a function of recharge rate. Analytically modeled lens lengths have no relationship with recharge rate; whereas, observed lengths increase as the recharge rate increases.

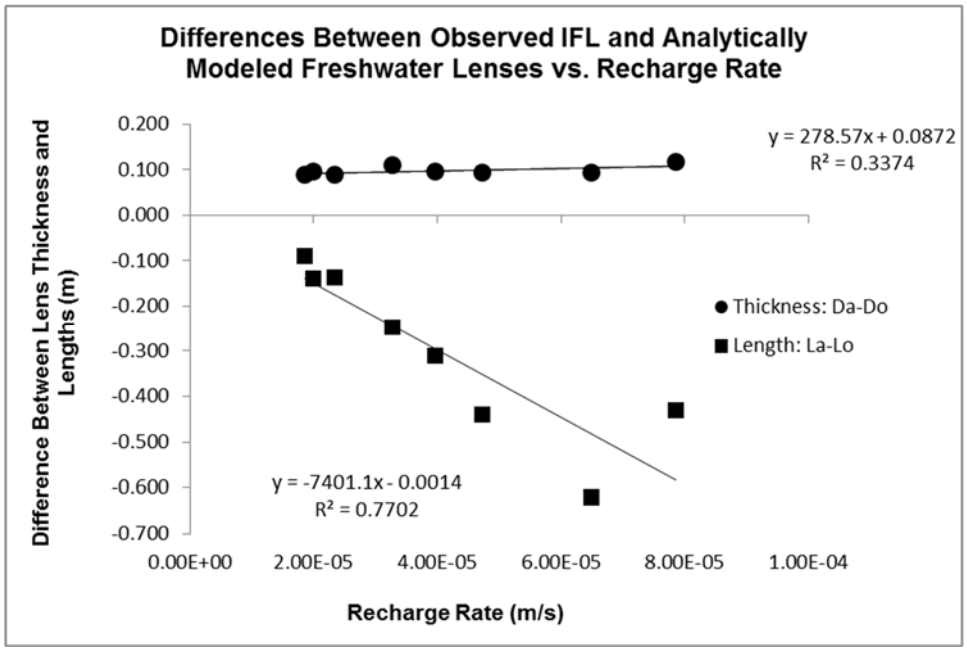

Figure 38. Subtracted values between the lengths and thicknesses of analytically modeled lenses and observed IFLs.

Table 8. Summary of results including the time to maximum thickness (Tmax), recharge rate (R), observed thickness (Do), observed length (Lo), time to minimum thickness (Tmin), modeled thickness (Da), modeled length (La), differences in thicknesses (ΔD), and differences in lengths (ΔL).

Analyses	Statistical Model	Reported Values	p-value	Interpretation
IFL Formation	$T_{max} = 722.5R^{-0.218}$	$R^2 = 0.90$	p =0.0003	IFL T_{max} thickness decreases as R increases.
IFL Geometry (A Series)	$D_o/L_o = 4.2882R^{0.3276}$	$R^2 = 0.92$	p = 0.00006	IFL D_o/L_o increases as R increases.
IFL Geometry (All Series)	n/a	r = 0.87	p = 0.0002	IFL D_o and L_o exhibit a strong linear relationship for all series.
Geometry (A Series)	n/a	r = 0.97	p = 0.00004	IFL D_o and L_o exhibit a stronger linear relationship for A Series.
IFL Degradation	$T_{min} = 6 \times 10^6 R^{0.313}$	$R^2 = 0.88$	p = 0.0006	IFL T_{min} D_o increases as R increases.
IFL Thickness vs. Recharge Rate	$D_o = 150.64R^{0.7046}$	$R^2 = 0.93$	p = 1.2 x 10-4	IFL D_o positively correlated with R.
IFL Length vs. Recharge Rate	$L_o = 35.129R^{0.377}$	$R^2 = 0.82$	p = 0.0014	IFL L_o positively correlated with R.
Modeled Thickness vs. Recharge Rate	$D_a = 16.485R$	$R^2 = 0.93$	p = 9.3 x 10-5	Modeled lens D_a increases with R.
Modeled Length vs. Recharge Rate	$L_a = 0.2187R^{-0.071}$	$R^2 = 0.33$	p = 0.1593	Modeled lens L_a is not correlated with R.

Thickness Differences between Observed and Modeled Lenses	$\Delta D = 278.57R + 0.0872$	$R^2 = 0.34$	$p = 0.1304$	Differences in thickness between IFLs and modeled lenses are not correlated with R
Length Differences between Observed and Modeled Lenses	$\Delta L = -7401.1R - 0.0014$	$R^2 = 0.77$	$p = 0.004$	Differences in lengths between IFLS and modeled lenses are correlated with R.

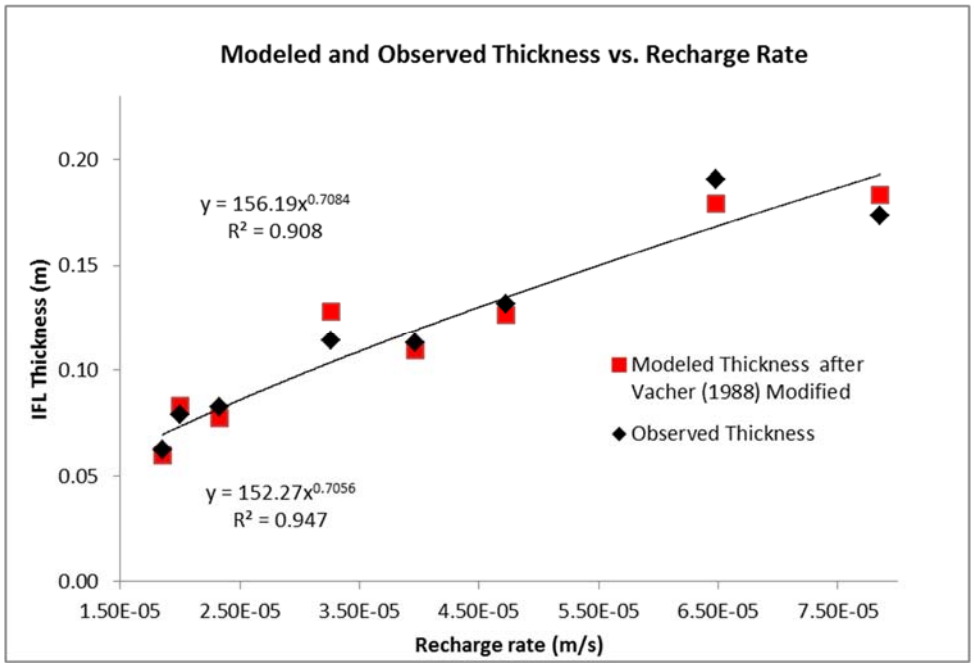

Figure 39. A comparison between modeled IFL water table elevations using a corrected form of the Dupuit-Ghyben-Herzberg solution and observed IFL water table elevations.

CONCLUSIONS

IFLs are subsurface freshwater accumulations that form beneath inland topographic depressions and mound on top of regional brackish to saline groundwater. The Raudhatain depression of northern Kuwait is one such IFL of regional importance, and other IFLs have been documented across the globe including the Arabian Peninsula (Rizk and Alsharhan, 2003; Young et al., 2004), Australia (Barrett et al., 2002; Cendón et al., 2010) Central Asia (Shevchenko, 1963; Ostrovsky, 2007), South America (Jayawickreme et al., 2011; Cellone et al., 2018), and the United States (Phelps and Rohrer, 1987; James et al., 1996; Jayawickreme et al., 2011; Cellone et al., 2018). While brackish and saline groundwater is often viewed as a problem, the presence of it, along with other specific environmental conditions, promotes the development of IFLs in regions where renewable freshwater resources are limited. Drylands are estimated to comprise more than 40% of the Earth's land surface, and saline groundwater at shallow to intermediate depths is estimated to occupy the equivalent of 16% of the total land area on Earth (Van Weert and van der Gun, 2012). Enhanced understanding of the scope, distribution, and dynamics of IFLs and saline groundwater is requisite to effectively manage water resources in arid regions and optimize fresh groundwater resources. This study presented direct observations on the formation and transient evolution of an IFL tested the Dupuit-Ghyben-Herzberg solution typically used to predict coastal freshwater lenses and provided a corrected solution to predict IFL thickness as a function of recharge rate.

IFL simulations provide insight into the effect of recharge on formation, geometry, degradation) Increased recharge rates quicken IFL formation and increase the maximum IFL thicknesses and lengths, respectively. IFL geometry also expressed as a ratio of IFL thickness to length is directly proportional to recharge rate. After IFL formation, length increases, and thickness

decreases over time. IFLs change position through time atop the saltwater along the wetting front in homogenous and isotropic conditions, primarily flow in the same direction of the regional saline groundwater and extend beyond the recharge area. The location of an IFL saltwater/freshwater interface, as well as its thickness and length, were not accurately predicted using the selected analytical model; however, a corrected solution was provided.

Although a physical laboratory model is a useful tool for generating qualitative insights, potential caveats exist regarding the operation and interpretation of these simulations such as scaling limitations, homogeneity, anisotropy, and other environmental differences. This research provides interpretive information concerning IFL occurrence and longevity as a function of recharge rate. Additional studies should include testing precipitation dynamics (e.g. frequency, duration), and how these variables influence flow, geometry, and extent. Lastly, the transient behavior of IFLs lends itself to a comparison of analyses regarding Light Non-Aqueous Phase Liquid (LNAPL) flow, geometry, and volume in porous media (Farr et al., 1990; Schroth et al., 1995).

New approaches to calculating IFL thickness and length through time and space are required for the accurate estimation of available freshwater volume directly beneath the center of the depression where extraction is most ideal. Further, these models provide support for the identification of favorable IFL artificial recharge sites that can exploit saline groundwater systems as “impermeable boundaries” for a specified time. Improved understanding of IFL dynamics in combination with newly verified IFL locations (Milewski et al., 2014b) provides water resource development opportunities in every major dryland region with brackish to saline groundwater ant shallow depths.

FUNDING

The authors would like to thank the Society of Exploration Geophysics and the University of Georgia, Department of Geology for the financial support of this research, particularly the Gary and Lorene Groundwater Exploration Scholarship and the Watts Wheeler Award

ACKNOWLEDGMENTS

The authors would like to thank the Society of Exploration Geophysics and the University of Georgia Department of Geology for the financial support of this research, particularly the Gary and Lorene Groundwater Exploration Scholarship and the Watts Wheeler Award. Further, the authors thank the anonymous reviews who provided valuable and appreciated feedback.

CHAPTER 6

TRANSIENT EVOLUTION OF INLAND FRESHWATER LENSES: COMPARISON OF NUMERICAL AND PHYSICAL EXPERIMENTS[1]

[1]Rachel Rotz, Adam Milewski, and Todd Rasmussen. 2020. *Water*. 12(4): 1154.
Reprinted here with permission of the publisher.

ABSTRACT

Brackish to saline groundwater in arid environments encourages the development and sustainability of inland freshwater lenses (IFLs). These freshwater resources supply much-needed drinking water throughout the Arabian Peninsula and other drylands, but little is understood about their sustainability. This study presents a numerical model using the SEAWAT programming code (i.e., MODFLOW and the Modular Three-Dimensional Multispecies Transport Model (MT3DMS)) to simulate IFL transient evolution. The numerical model was designed from a physical laboratory model and calibrated by results from simulations conducted in a previous study of the Raudhatain IFL in northern Kuwait. Data from three previously conducted physical model simulations were evaluated against the corresponding numerical model simulations. The hydraulic conductivities in the horizontal and vertical directions were successfully optimized to minimize the objective function of the numerical model simulations. The numerical model matched observed IFL water levels at four static locations through time, as well as IFL thicknesses and lengths (R2 = 0.89, 0.94, 0.85). The predicted lens degradation times corresponded to the observed lenses, which demonstrated the utility of numerical models and physical models to assess IFL geometry and position. Improved understanding of IFL dynamics provides water resource exploration and development opportunities in drylands throughout the Arabian Peninsula and elsewhere with similar environmental settings.

INTRODUCTION

While saline groundwater systems in semi-arid and arid environments are generally considered a problem for water resource managers, the occurrence of shallow (<100 m) brackish to saline groundwater promotes the development of localized accumulations of subsurface freshwater referred to as inland freshwater lenses (IFLs) (Bergstrom and Aten, 1965b; Kunin,

1968; Rotz and Milewski, 2019). IFLs serve as alternative freshwater resources for drinking water, livestock management, and micro-oasis agriculture in several arid and semi-arid regions including the Middle East (e.g., Kuwait, Oman, United Arab Emirates (UAE), Saudi Arabia), Australia (e.g., Murray Basin, Queensland), Central South America (e.g., Paraguay), Central Asia (e.g., Turkmenistan), Africa (e.g., Zambia, Namibia), and elsewhere with similar environmental settings (Shevchenko, 1963; Bergstrom and Aten, 1965b; Kunin, 1968; Barrett et al., 2002; Macumber, 2003; Young et al., 2004; Houben et al., 2014; Werner and Laattoe, 2016b; Laattoe et al., 2017). IFLs form and are sustained by runoff from infrequent, high-intensity rainfall events (>20 mm/h), which occur between every one to three years based on a correlation between the El Niño-Southern Oscillation and rainfall anomalies (Cluff, 1990; Marcella and Eltahir, 2008). Runoff collects in low elevation geomorphic features (e.g., depressions, gullies, interdune swales) and infiltrates vertically and laterally through highly permeable sediments towards the saline groundwater (Hantush, 1967; Kwarteng et al., 2000). The resultant variable-density condition forms a boundary surface or freshwater-saltwater interface, above which a freshwater lens forms (Henry, 1959) (Figure 40). Unlike coastal and oceanic island freshwater lenses, which are stabilized by bounding seawater on one or more sides, IFLs migrate atop the saline groundwater in the direction of the regional gradient changing in geometry and position through time (Fadlelmawla et al., 2008; Rotz and Milewski, 2019)

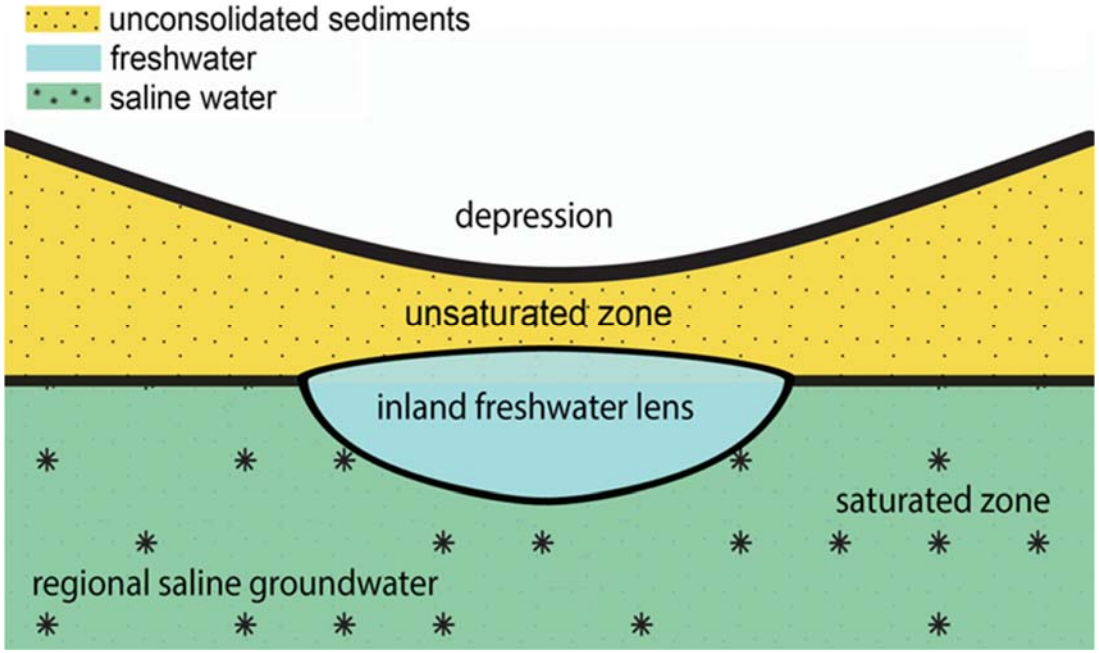

Figure 40. Conceptual diagram of an inland freshwater lens (IFL). Modified from Rotz and Milewski (2019).

Investigations into IFLs are limited likely due to their sporadic nature and smaller scale relative to the larger-scale freshwater aquifers commonly exploited in populous regions. However, Bedouin communities likely once utilized these resources along with other ancient irrigation techniques (i.e., runoff harvesting), but abandoned these systems due to changes in the governing authority, modern agricultural practices, and inadequate drainage (Shanan, 2000). Recent studies have identified more than 100 potential locations throughout the Arabian Peninsula with conditions favorable (e.g., climatic, geomorphic, hydrogeologic) for the development and sustainability of IFLs (Milewski et al., 2014b). Investigations into the formation and transient evolution of IFLs offer freshwater resources sustainability and development opportunities throughout the Arabian Peninsula and elsewhere with similar environmental settings. Novel solutions for the management of freshwater resources in these regions are critical as the overreliance on desalinization and non-renewable fossil water has created risks for environmental, political, economic, and social conditions (Sultan et al., 2008a; Sultan et al., 2013; Lezzaik and Milewski, 2018; Lezzaik et al., 2018).

Freshwater lens studies typically occur in coastal settings where the lenses are surrounded by seawater (Fetter, 1972; Vacher, 1988; Stuyfzand and Bruggeman, 1994; Chesnaux and Allen, 2008). Physical models (Dose et al., 2014), analytical solutions (Fetter, 1972; Van Der Veer, 1977; Vacher, 1988), and numerical models have demonstrated the relationships between recharge rate, hydraulic conductivity, differences in fluid densities, and coastal freshwater lens geometry. IFL investigations using geophysical techniques (Barrett et al., 2002; Houben et al., 2014), analytical methods (Hantush, 1967; Werner and Laattoe, 2016b; Kacimov and Obnosov, 2019), and physical laboratory models (Rotz and Milewski, 2019) highlight IFL relationships between the physical and chemical properties (i.e., salinity, age) and geometry. However, none of these studies address the

transient nature of IFLs over varying temporal and spatial scales. A three-dimensional, numerical model of the Raudhatain and Umm Al-Aish IFLs in Kuwait by Al-Weshah and Yihdego (2016) used MODLFOW-SURFACT code to predict water table elevations over 22 years but does not account for the freshwater extent in the vertical or horizontal direction as it migrates laterally through space and time. Research into the geometry of IFLs is needed to adequately predict the position and sustainability of exploitable freshwater resources. The purpose of this research is to presents a variable-density, finite-difference numerical model that considers geometry (i.e., thickness, length) calibrated by and compared with shared results from physical model observations by Rotz and Milewski (2019).

METHODOLOGY

This study compares three simulations from a newly developed numerical model with three simulations from a previously conducted physical model in Rotz and Milewski (2019) to investigate the development and transient evolution of a topographically induced IFL over varying recharge rates. The physical model simulations conducted in Rotz and Milewski (2019) represent the formation, migration, and degradation of IFLs using an acrylic sandbox model inspired by the Raudhatain IFL in northern Kuwait (Figure 41). The previous study investigated the effect of recharge on IFL development and compared results to the Dupuit–Ghyben–Herzberg analytical solution by Vacher (1988). The statistical analyses in Rotz and Milewski (2019) showed the analytical solution overestimated IFL thickness (D) and had no correlation with the recharge rate (R) ($\Delta D = 278.57R + 0.0872$, $R2 = 0.34$, $p = 0.1304$). The study concluded that the differences in lens geometry between the physically modeled lenses and the analytical solution were due to the transient nature of IFLs, subsequently motivating the need for numerical studies that could address IFL changes in geometry through time.

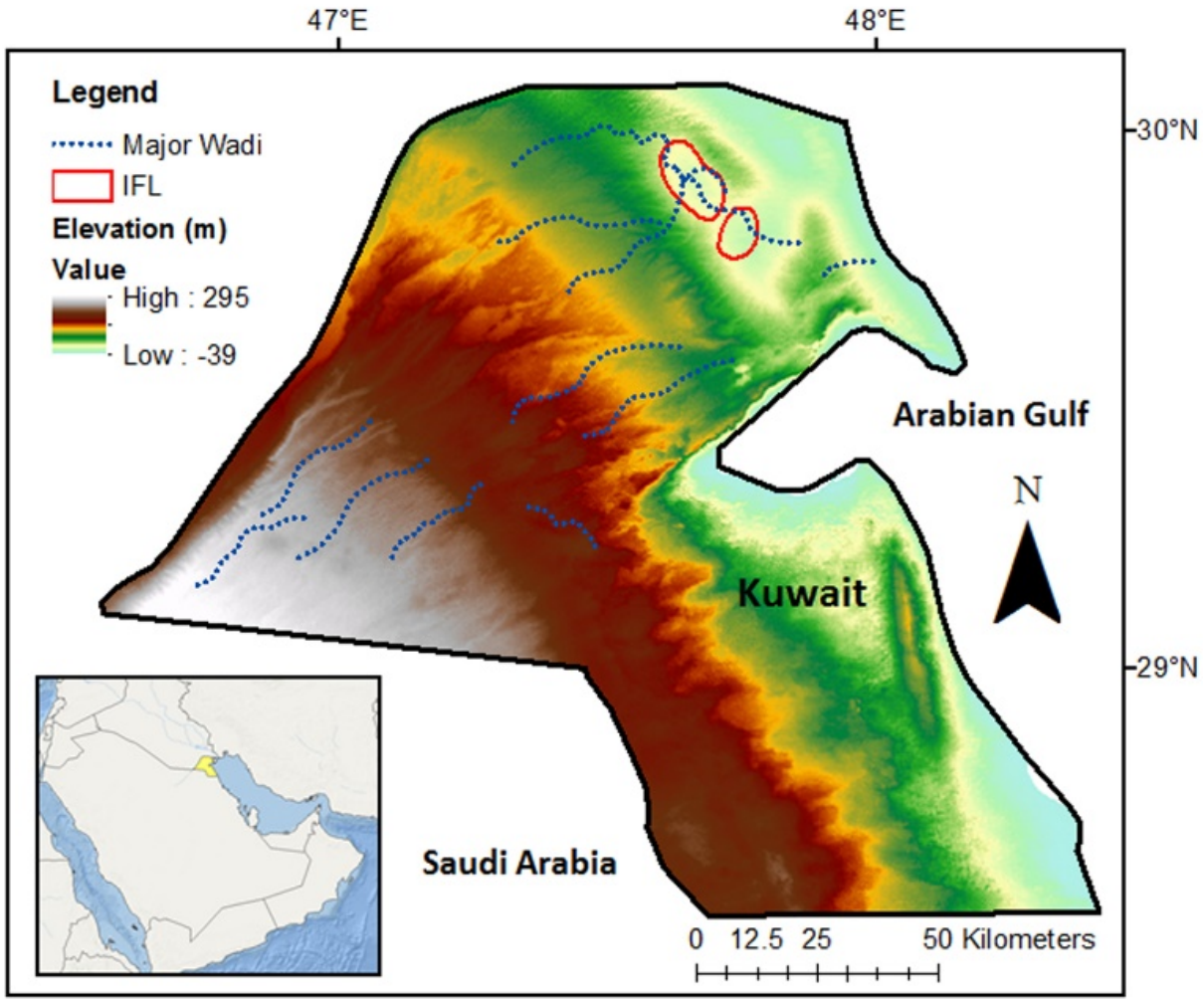

Figure 41. Map of Kuwait showing the location of the Raudhatain (top) and Umm Al-Aish (bottom) IFLs highlighted in red.

For this study, the numerical model was designed by using the physical model dimensions, porous medium, boundary conditions, and initial conditions from Rotz and Milewski (2019). Also, numerical model calibration and comparative analyses used the observational data from three physical model simulations. The observational data (i.e., water table elevation, thickness, length) was obtained from still photographic images generated during the previous study (Figure 42). Uranine tracer-dye added to the freshwater during the physical model simulations allowed for the digital measurement of IFL geometry (i.e., thickness, length) using ImageJ software. Results from the numerical model were then compared to the results from the previously conducted physical model simulations to determine if the numerical model adequately simulated the observed IFLs.

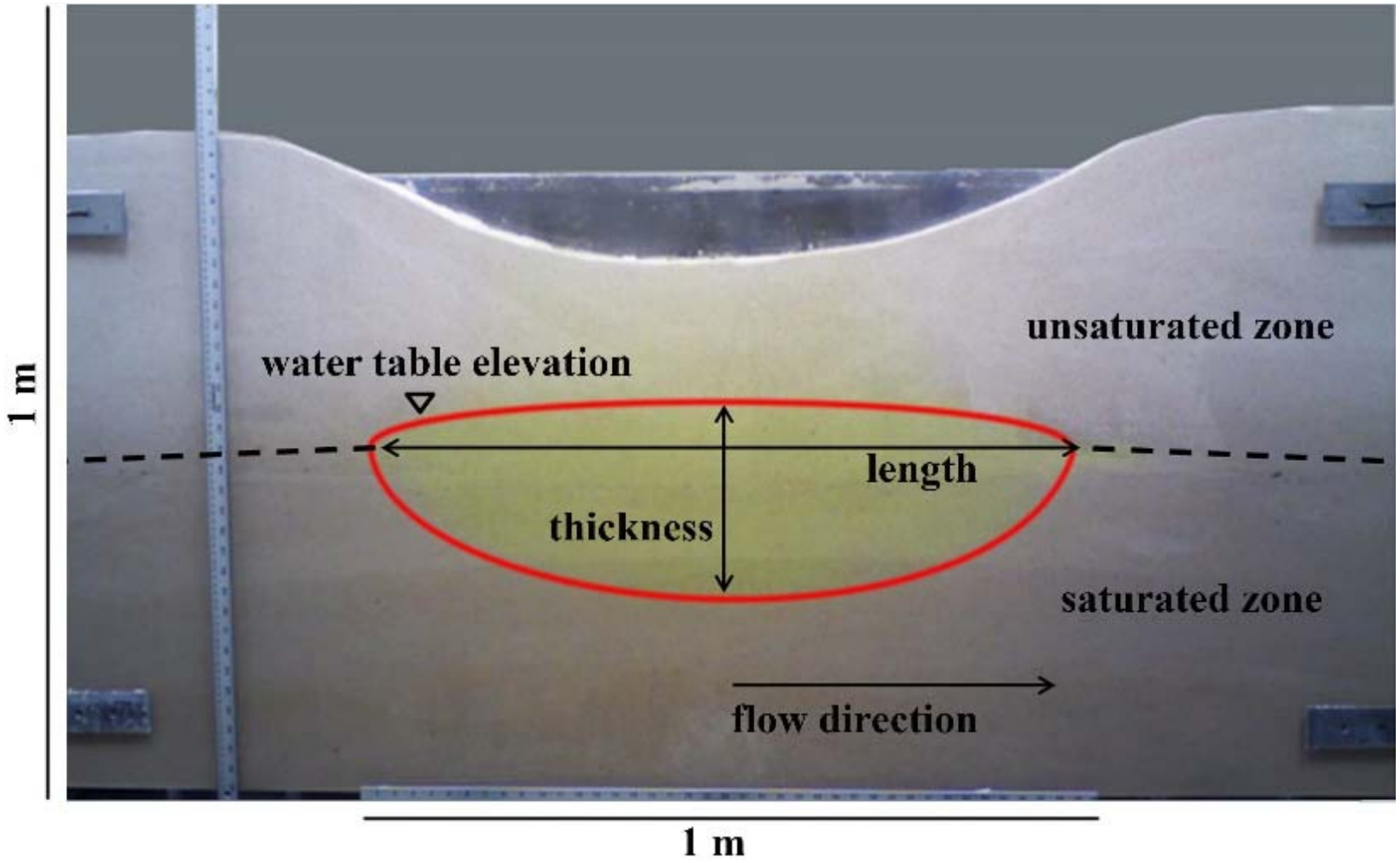

Figure 42. Diagram of observational data collected including water table elevation and IFL geometry (i.e., thickness, length) from previously conducted physical laboratory simulation.

The numerical model was developed using the SEAWAT programming code to simulate saturated, variable-density groundwater flow, and solute transport. The SEAWAT program is a density-dependent groundwater flow model utilized for the modeling of groundwater in aquifers with fresh and saline groundwater interaction (Guo and Langevin, 2002). SEAWAT couples MODFLOW-2000 (Harbaugh et al., 2000) and the Modular Three-Dimensional Multispecies Transport Model (MT3DMS) to solve the three-dimensional groundwater flow and solute transport numerically with finite difference approximations (Zheng and Wang, 1999; Harbaugh et al., 2000; Langevin et al., 2003; Langevin et al., 2008). The shell program is Visual Modflow. The numerical model was designed in a two-dimensional manner to represent a cross-sectional slice of the hydrogeological system of a topographically induced IFL simulated with the physical model.

SEAWAT solves the fluid flow equation in terms of the hydraulic head by combining a general form of Darcy's law for variable density conditions (Bear, 1979) with a hydraulic conductivity tensor (Senger and Fogg, 1990), and vertical flow components (Oberlander, 1989; Holzbecher, 1998) (Equation (16)):

$$\nabla \cdot \left[\rho K \left(\nabla h + \frac{\rho - \rho_{\mathrm{f}}}{\rho_{\mathrm{f}}} \nabla z\right)\right] = \rho S_{\mathrm{s}} \frac{\partial h}{\partial t} + \theta \frac{\partial \rho}{\partial t} - \rho_{\mathrm{s}} q_{\mathrm{s}} \tag{16}$$

where ∇ is the del operator, ρ is fluid density (ML^{-3}), K is hydraulic conductivity tensor (LT^{-1}), h is the freshwater head (L), ρ_f is the freshwater density (ML^{-3}), z is elevation, S_s is the freshwater specific storage (L^{-1}), θ is porosity (1), and q_s is a source or sink (T^{-1}) of fluid with density ρ_s.

SEAWAT uses the MT3DMS model to solve the general form of the solute transport equation (Zheng and Wang, 1999) (Equation (17)):

$$\frac{\partial C}{\partial t} = \nabla \cdot (D \nabla C - vC) - \frac{q_s}{\theta} C_s \tag{17}$$

where C is the solute concentration (ML^{-3}), D is the solute dispersion tensor, v is the advective velocity (LT^{-1}), and C_s is the source or sink concentration (ML^{-3}). The linking of Equations (16) and (17) requires a function to relate concentration and fluid density.

Numerical Model Design and Parameters

A transient flow model was developed with SEAWAT to assess IFL geometry and transience for 200 h. The domain of the numerical model encompasses a space of 2.0 m (L) × 0.5 m (H) × 0.10 m (W) (Figure 43). The numerical model did not include the upper 0.5 m of the unsaturated zone of the physical model, as these were considered inactive cells within SEAWAT. The bottom left side elevation of the domain is at 0 m. The grid consists of 100 columns to represent the length (x-axis), 25 rows to represent the height (z-axis), and one layer to represent the width (y-axis). The parameters of hydraulic conductivity (K_x, K_y, K_z), were used from measurements taken during the previously conducted physical laboratory model study with a constant head permeameter during the laboratory experiments from sediments comprised of medium to fine sand (d_{50} = 0.55 mm) to represent the highly permeable gravel sediments in the upper layer of the Kuwait Group Aquifer (Bear, 1979). The porosity (θ) was calculated during the previous study using the sum of solid and pore volumes. Additional representative properties of variable-density values through porous media were selected after Konikow et al. (2013) and others, as shown in Table 9.

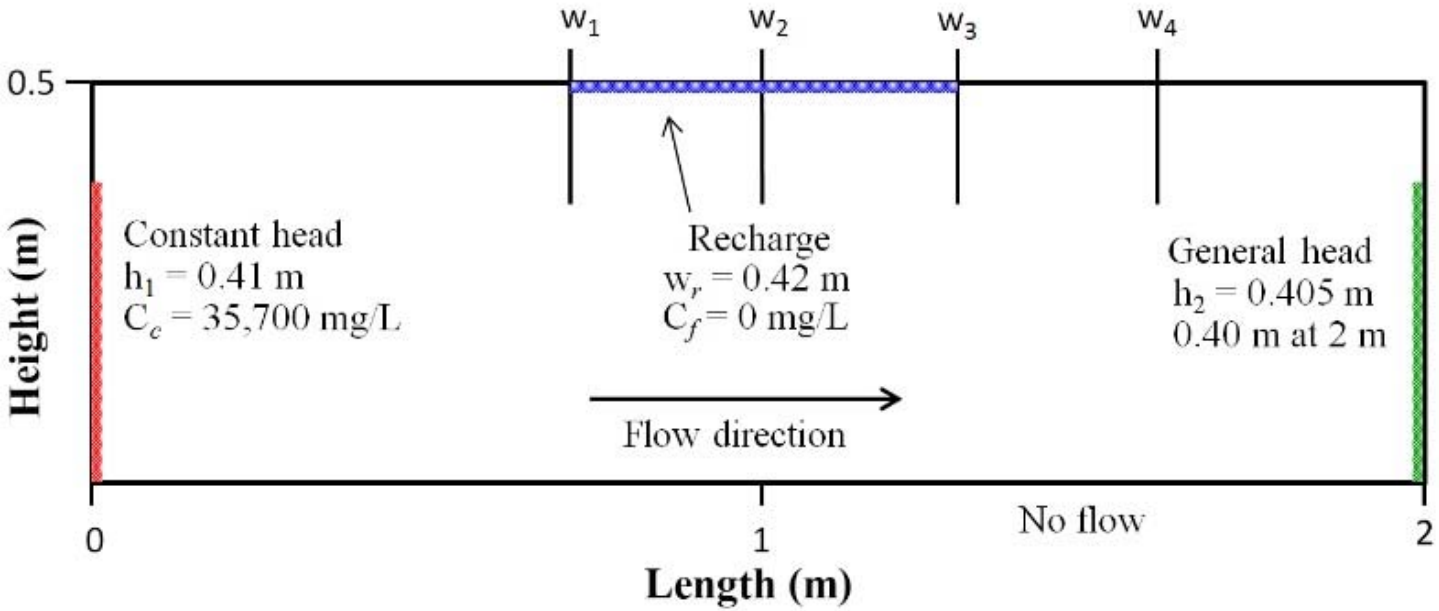

Figure 43. Conceptual diagram of the numerical model with domain dimensions, boundary conditions, and observation well locations.

Table 9. Initial model parameters.

Input Parameter	Value	Description
K_x, K_y, K_z	0.0015 m/s	Hydraulic conductivity
θ	0.39	Porosity
S_s	1 × 10−5	Specific storage
S_y	0.34	Specific yield
D_m	1 × 10−10 m2/s	Molecular diffusion coefficient
$\Delta\rho/\Delta C$	0.7143	Slope of fluid density to solute concentration
δL	1 × 10−5 m	Longitudinal dispersivity
$\delta v/\Delta l$	0.02	Vertical/longitudinal dispersivity

Boundary and Initial Conditions

The boundary conditions of the numerical model corresponded to the physical laboratory model conditions (Figure 43). The base of the domain included a no-flux boundary. The left side of the domain included a constant head boundary of 0.41 m (h_1) with a constant concentration of 35,700 mg/L for the full duration of the model (200 h). The right side of the domain included a general-head boundary with a general-head elevation at 0.405 m (h_2) and boundary-head elevation at 0.40 m for a distance of 2 m, which generated a slope of 0.25% to represent the gentle gradient. The top layer of the domain included a recharge boundary with a width (w_r) of 0.42 m. The initial condition of the freshwater head (h_f) was calculated to 0.4075 m based on the change in water table elevation between the left and right boundaries of the domain. The initial saltwater concentration (C_s) of 35,700 mg/L was selected for the brackish to saline water from the Raudhatain Depression (7000–50,000 mg/L) and used with the physical model simulations. Evaporation, like the previously conducted physical laboratory simulations, was considered negligible. A summary of the boundary conditions is shown in Table 10.

Table 10. Boundary condition and concentration values.

Boundary Condition	Position (x,y)	Values
Constant head	0, 0.41	35,700 mg/L
General head	2, 0.405	calculated
Recharge	0.79, 1.21	0 mg/L
Evaporation	Entire domain	0 m/s

Observation Wells and Geometry Data

Observation wells for water table elevations were used within the numerical model. Measurements from the physical model simulations at four static locations along the cross-section provided data for the wells. Water table elevation measurements were obtained from the physical laboratory model simulations from the previous study when the lens reached a maximum thickness and then every hour until ten hours, which was the time observed for the physical simulations where the tank wall did not interfere with the lens geometry. Wells 1–3 were located beneath the recharge zone, and Well 4 was assigned on the right side or down gradient end of the model (Figure 4). The elevation of the well screens within the numerical model was set directly below the initial water table elevation of 0.40 m. IFL thickness and length measurements from the physical model were taken to compare with the numerical model.

Numerical Settings

The simulation scenario selections for the SEAWAT numerical engine are described here. The explicitly coupled or "one-time step lag" option was selected where the flow equation is calculated using the fluid density from the previous transport time step, as solute concentrations are not expected to change rapidly. Due to the transient nature of IFLs, the upstream-weighting algorithm was selected to calculate the density value based on the flow direction of an iteration. For the viscosity calculations, a single species was used with no temperature dependence.

The Preconditioned Conjugate Gradient (PCG2) solver package was selected for the flow calculations with the maximum inner and outer iterations set to 100 each. The head change criterion was set to 1×10^{-5} m because of the small range of measurement values from the physical laboratory model. The flow solver used the incomplete Cholesky preconditioning method.

The implicit finite-difference method was used with the Generalized Conjugate Gradient (GCG) package to solve the transport equation. An upstream finite difference method was used to solve the advection term. The maximum number of outer and inner iterations was set to 1 and 50, respectively. A modified incomplete Cholesky preconditioner was also used for the transport solver. The relative convergence criterion was set to 1×10^{-8}. The lengths of transport time steps were calculated using a Courant number of 0.75. The time steps for the flow calculations for stress periods 1, 2, and 3 are 10, 50, and 50, respectively. The maximum number of transport steps was set at 3000 with a maximum step size set at 0.125 h. Simulation results were saved at every time step for both flow and transport calculations to use for analyses.

Simulations

Three physical laboratory simulations at varying recharge rates were selected to reproduce three numerical simulations (Table 11). An example of Simulation 2 from the previously conducted physical laboratory simulations is shown in Figure 44. For the physical model simulations, recharge was applied at varying rates for 1 hour. For the numerical model, the recharge rates were adjusted to account for the infiltration travel time through the unsaturated zone (Table 11). Observations made of the time passed for the freshwater to initially flux across the water table (T_q) were recorded and subtracted from the time observed for each simulated lens to reach a maximum thickness (T_{max}). The initial recharge rates (R_i) used in physical experiments were divided by the calculated time differences to equal the adjusted recharge rates (R_a). The beginning of the second stress period was set to the observed time of initial flux, and the end of the second stress period was set at the time of the observed maximum thickness to match the maximum thickness times of the physical model to the numerical model. Three stress periods were assigned to each simulation to apply the recharge and represent (1) a period of no recharge, (2) a

period of freshwater recharge applied across the recharge boundary, and (3) a period of no recharge for a total duration of 200 h. The duration of each stress period was set accordingly (Table 11). Freshwater was infused with a tracer dye, which allowed for the measurements of IFL thicknesses and lengths for 10 hours for each simulation before the tank wall interfered with the lens geometry, which was compared to the numerical model using concentration data exported from the software. Statistical model evaluation techniques were used to determine the accuracy of the simulated data (Moriasi et al., 2007).

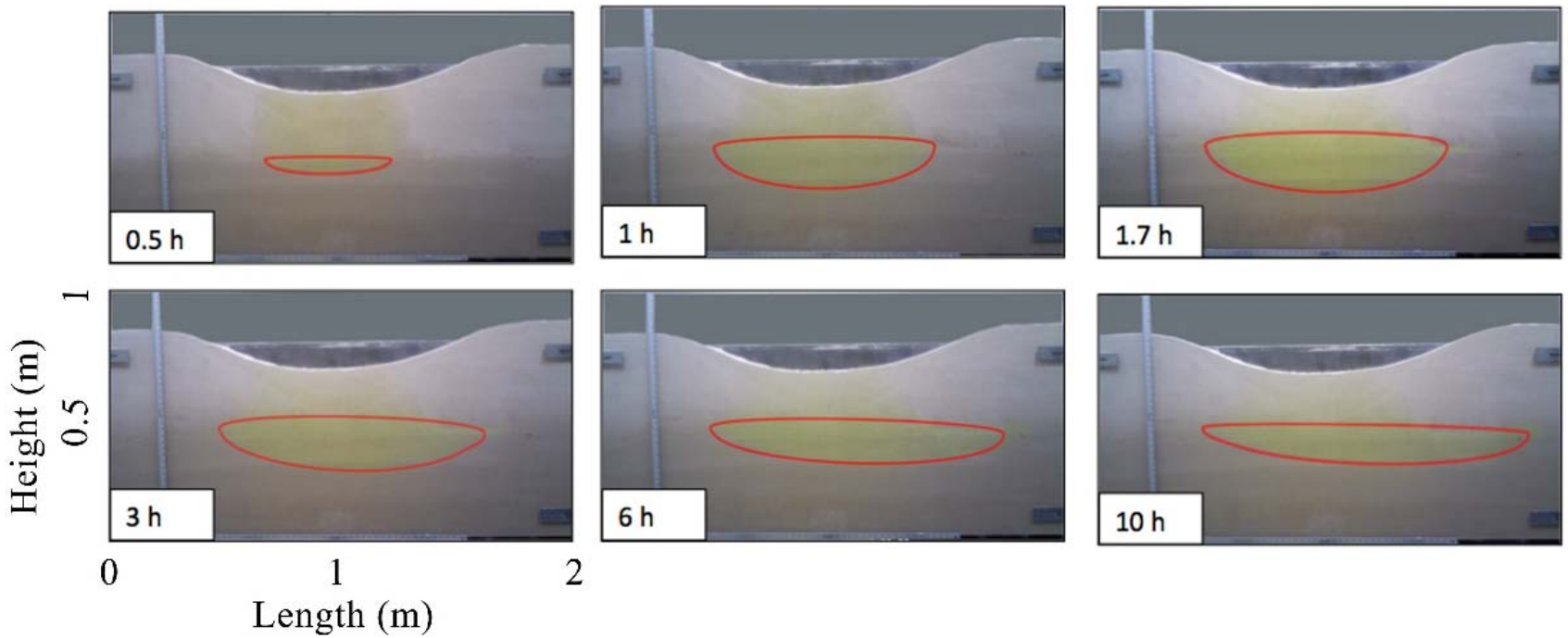

Figure 44. Physical model Simulation 2 shows IFL development and transient evolution.

Table 11. The initial recharge rate (R_i), time of recharge flux (T_q), time of observed maximum thickness (T_{max}), adjusted recharge (R_a) rates, and stress period times for the numerical model simulations.

Simulation	R_i (m/s)	T_q (s)	T_{max} (s)	R_a (m/s)	Stress Periods Starts (1, 2, 3) (s)
1	4.72×10^{-5}	1620	6480	3.33×10^{-5}	1620, 6480, 720,000
2	6.48×10^{-5}	1296	6120	4.72×10^{-5}	1296, 6120, 720,000
3	7.86×10^{-5}	1008	5400	6.67×10^{-5}	1008, 5400, 720,000

RESULTS

Model Calibration and Results

The numerical model successfully converged using the observational data from the three previously conducted physical model simulations and demonstrated IFL transient evolution (Figure 45). The numerical model calibration for each simulation was achieved through a parameter estimation tool (PEST) (Doherty, 2004) and a trial and error approach improving estimates of the hydraulic conductivity in the x and z directions while minimizing the error in head values. This value is referred to as the objective function (Φ). PEST adjusted the model parameters until the fit between the physical observations and numerical outputs was optimized to minimize the weighted least squares. The optimization procedure successfully estimated the hydraulic conductivities in the x and z directions (Table 12).

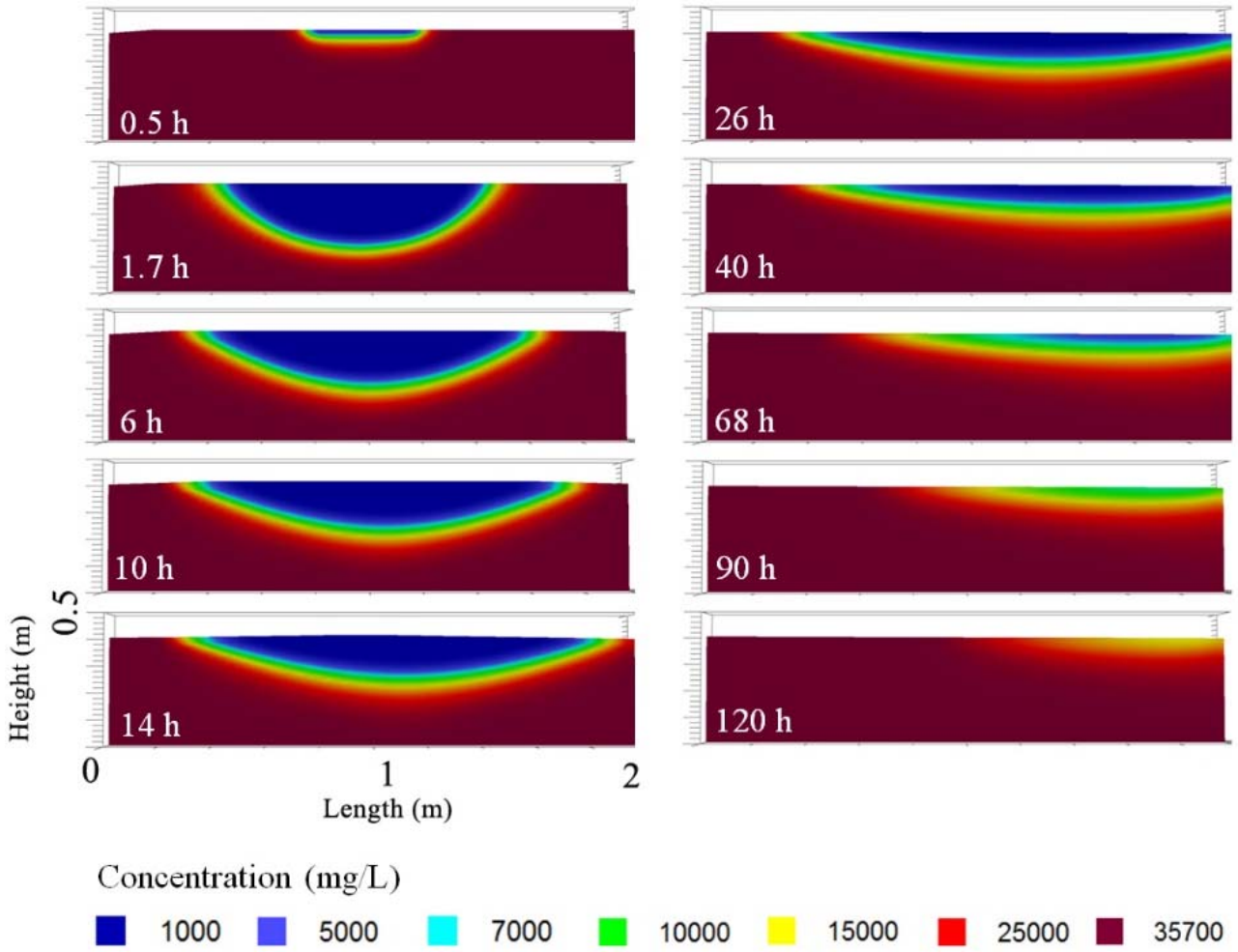

Figure 45. Numerical model Simulation 2 of IFL development and transient evolution. The dimensions of each cross-section match the numerical model domain of 2.0 m (L) × 0.5 m (H) × 0.10 m (W).

Table 12. The objective function (Φ), hydraulic conductivity estimates (Kx, Kz), and confidence intervals for the numerical simulations using the parameter estimation tool (PEST).

Run	Φ (m)	K_x (m/s)	K_z (m/s)	Confidence Interval for K_x (m/s)	Confidence Interval for K_z (m/s)
1	4.8×10^{-4}	7.6×10^{-4}	7.0×10^{-4}	7.6×10^{-4}–1.2×10^{-3}	2.5×10^{-5}–1.9×10^{-2}
2	5.5×10^{-3}	3.6×10^{-4}	4.3×10^{-4}	2.5×10^{-4}–5.3×10^{-4}	2.1×10^{-5}–8.5×10^{-3}
3	1.5×10^{-3}	4.3×10^{-4}	9.0×10^{-4}	5.3×10^{-4}–1.0×10^{-3}	5.8×10^{-5}–4.7×10^{-3}

Water Table Elevation Results

The comparison between the observed and simulated water table elevations is presented in Figure 46. Overall, the statistical values indicate accurate model simulation (Moriasi et al., 2007). The slope and y-intercept of the best-fit regression line indicate a slight overprediction of simulated water table elevations and a lag effect (m = 1.0477, b = −0.02). The coefficient of determination describes a strong degree of collinearity and a positive linear relationship between the simulated and measured data (R^2 = 0.89). The Nash–Sutcliffe efficiency (NSE) indicates a good fit between the observed and simulated data (NSE = 0.84). The root mean square error (RMSE) indicates a small error value appropriate for model evaluation (RMSE = 0.007). The percent bias (PBIAS) value suggests nearly zero model overestimation bias of water table elevation (PBIAS = −0.7).

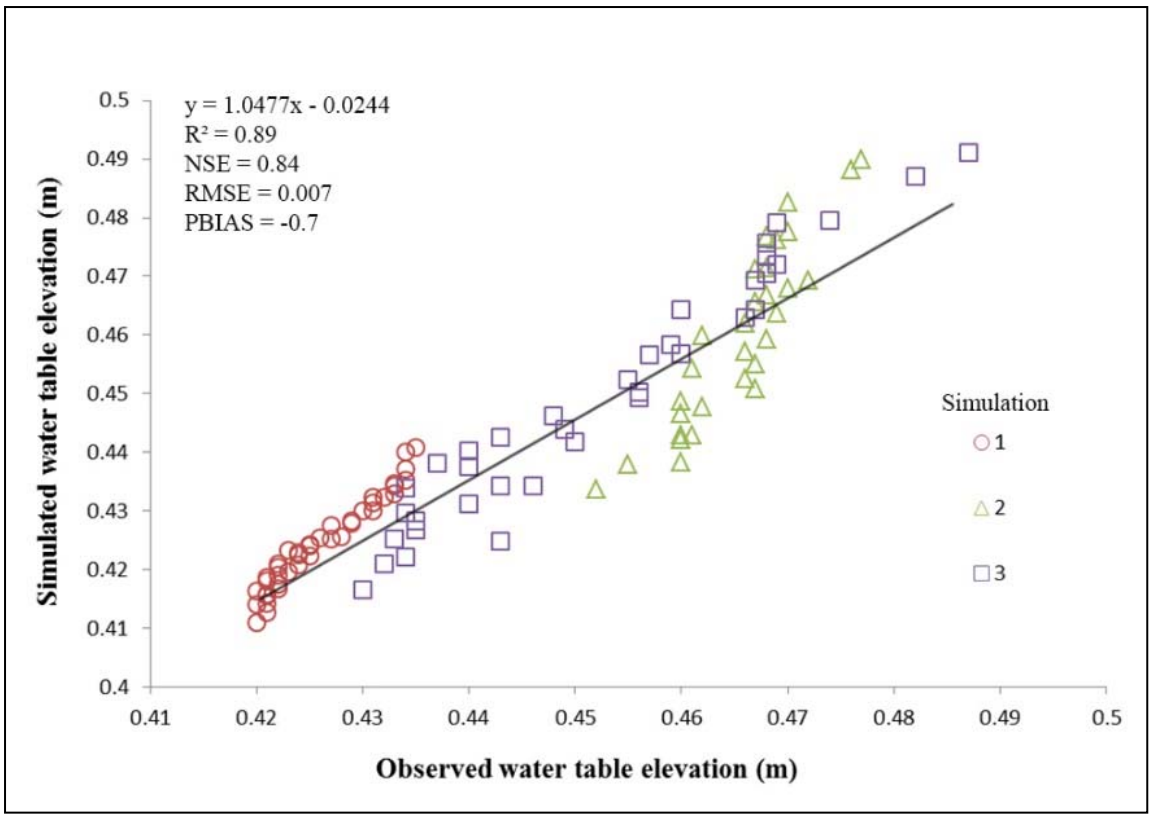

Figure 46. Simulated vs. observed water table elevation values.

Lens Geometry Results

The comparison between the observed and simulated IFL thicknesses and lengths is presented in Figure 47 and Figure 48. Overall, the statistical values indicate accurate model simulation for both geometric parameters (Moriasi et al., 2007). For the thicknesses and lengths, the slope and y-intercept of the best-fit regression line indicate a slight overprediction of simulated thicknesses and a slight to moderate lead effect (m = 1.0856, b = 0.0133) and (m = 1.0134, b = −0.0094), respectively. The coefficient of determination describes a strong degree of collinearity and a positive linear relationship between the simulated and measured data (R^2 = 0.94) and (R^2 = 0.85). The NSE indicated a good to moderate fit between the observed and simulated data (NSE = 0.65) and (NSE = 0.82). The RMSE indicates an error value appropriate for model evaluation (RMSE = 0.03) and (RMSE = 0.06). The PBIAS value suggests a slight to moderate model overestimation bias of IFL thickness (PBIAS = −16.3) and (PBIAS = −0.4). For lengths, Simulations 2 and 3 correlates more linearly; however, Simulation 1 deviates from the linear trend likely from a decrease in velocity during the physical model simulation from hydraulic conductivity variations due to the packing of the sand (Figure 47). A summary of these results is presented in Table 13.

Table 13. Summary of model evaluation statistics for IFL water table elevation, thickness, and length for Simulations 1, 2, and 3. The evaluation statistics are defined as a measure of fit (R^2), the Nash Sutcliffe Efficiency (NSE), root mean square error (RMSE), and percent bias (PBIAS).

Run	Slope-Intercept Form	R^2	NSE	RMSE	PBIAS
Water table elevation	y = 1.0477x – 0.0244	0.89	0.84	0.007	-0.7
Thickness	y = 1.0856x + 0.0133	0.94	0.65	0.03	-16.3
Length	y = 1.0134x – 0.0094	0.85	0.82	0.06	-0.4

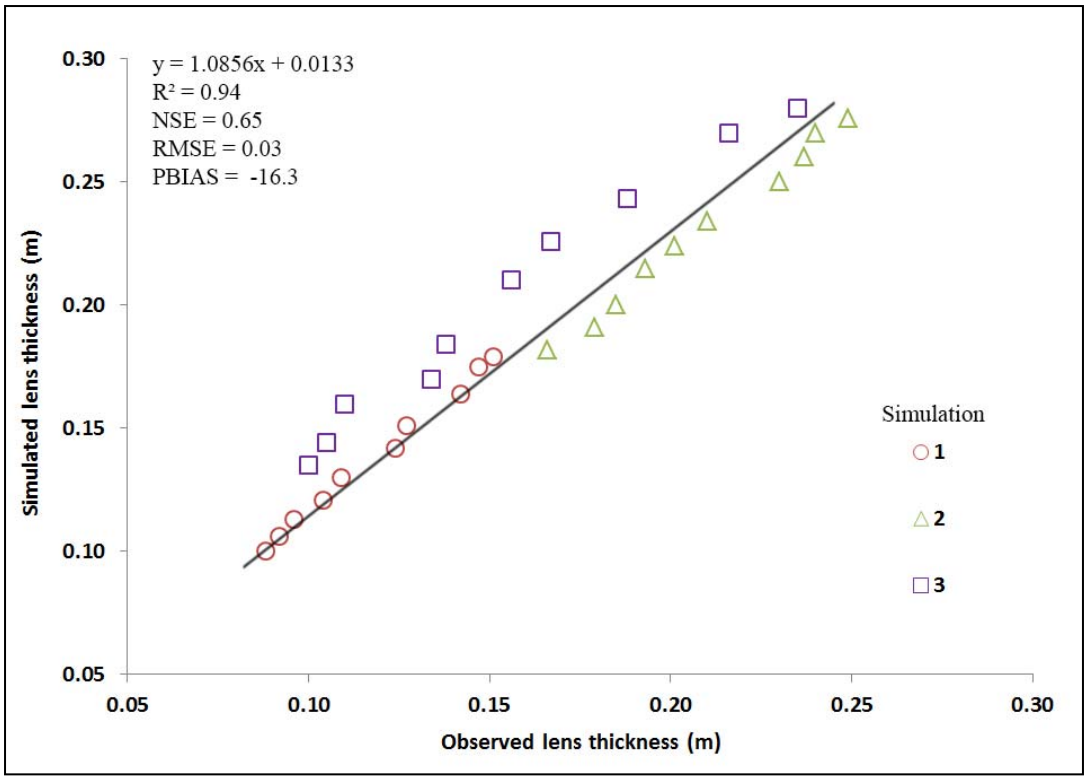

Figure 47. Simulated vs. observed IFL thicknesses.

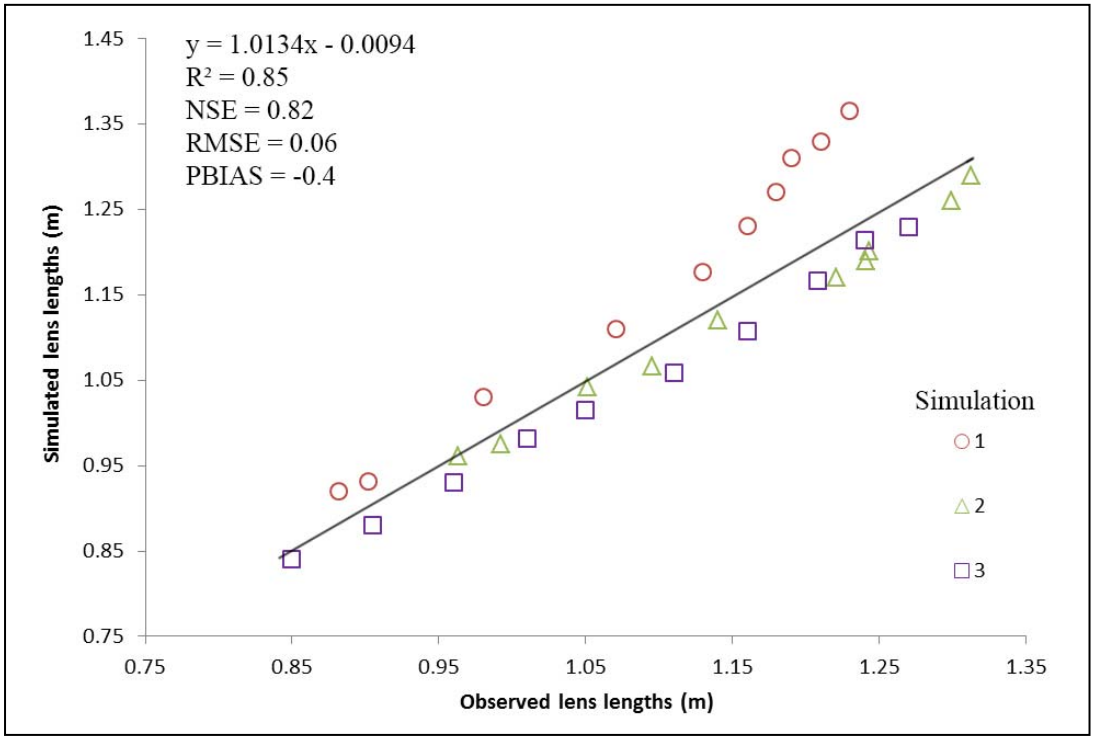

Figure 48. Simulated vs. observed IFL lengths.

Velocity Results

The average velocities for each simulation were calculated along a transect on the x-axis (v_x) from the center layer and column to the last column of the downgradient or right side of the domain (x = 1.0–2.0 m, z = 0.25 m) for each simulation before, during, and after the recharge stress period as shown in Table 14.

Table 14. Average groundwater velocity (v_x) measurements of the numerical model simulations before, during, and after the recharge stress event.

Run	v_x Before Recharge Stress Period (m/s)	v_x During Recharge Stress Period (m/s)	v_x After Recharge Stress Period (m/s)
1	6.88×10^{-6}	2.40×10^{-5}	7.04×10^{-6}
2	3.86×10^{-6}	6.99×10^{-5}	3.85×10^{-6}
3	5.64×10^{-6}	6.48×10^{-5}	4.84×10^{-6}

Degradation Results

The decrease of IFL thicknesses, referred to as IFL degradation, was compared between the physical and numerical simulations. As noted in the lens geometry results, the numerical model over-predicted the thicknesses of all three solutions for the duration of the simulation but consistently predicted the rate of decrease in thickness (Figure 49). The IFL was delineated by locations during the simulation, where the concertation values were less than 1000 mg/L. The changes in IFL thicknesses were compared between models with best fit exponential regression lines. IFL degradation was predicted for both the physical and numerical models by calculating the time required for the thicknesses to equal 0.01 m. A summary of the results is outlined in Table 15.

Table 15. Lens degradation results between the physical model and numerical model simulations. Units have been converted from seconds to hours.

Run	Physical Model Regression	Degradation Time (h)	Numerical Model Regression	Degradation Time (h)
1	$y = 1.699 \times 10^{-1} e^{-0.069x}$	41	$y = 2.023 \times 10^{-1} e^{-0.072x}$	42
2	$y = 2.697 \times 10^{-1} e^{-0.047x}$	70	$y = 3.017 \times 10^{-1} e^{-0.05x}$	68
3	$y = 2.597 \times 10^{-1} e^{-0.1x}$	33	$y = 3.185 \times 10^{-1} e^{-0.087x}$	40

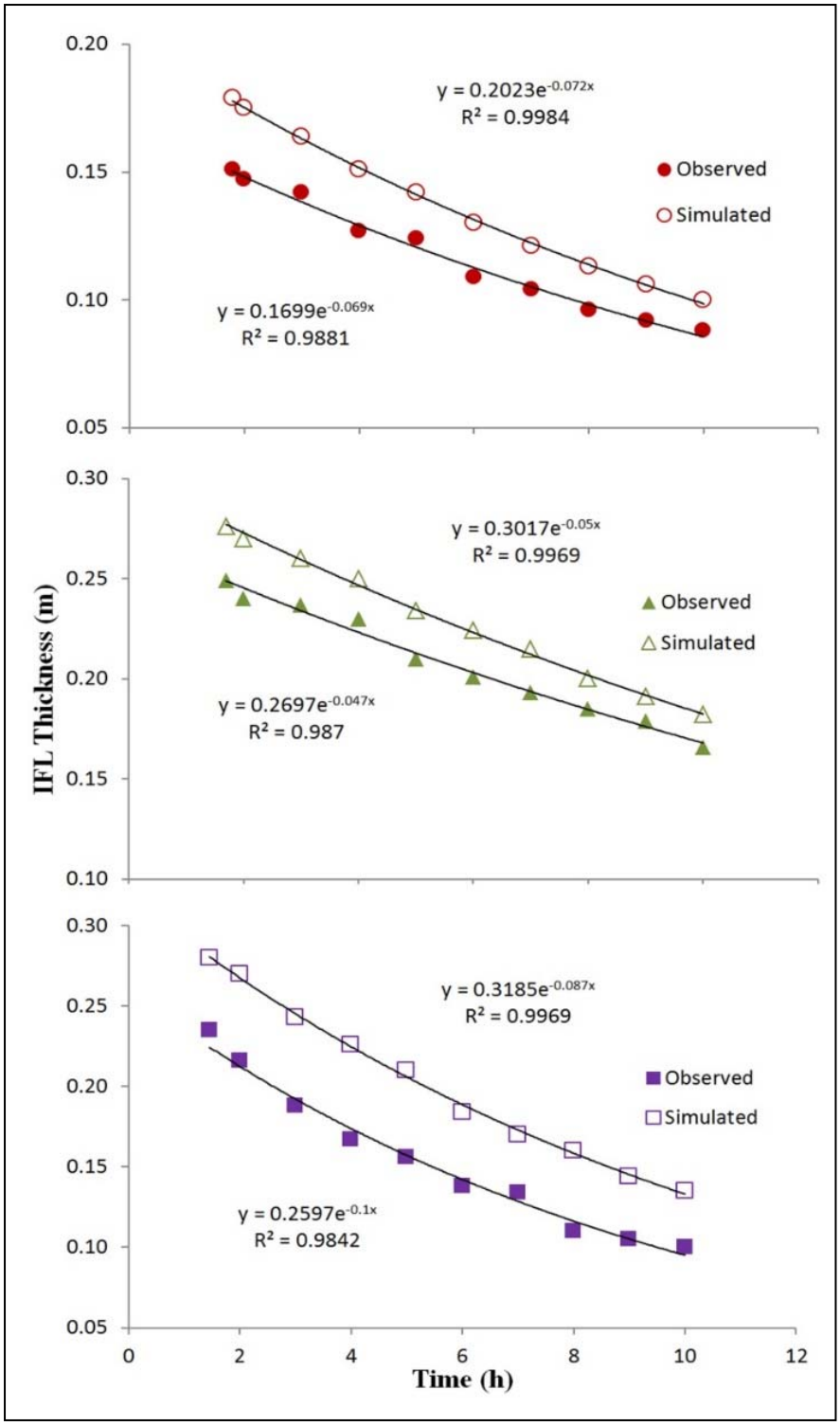

Figure 49 Observed vs. simulated thicknesses with best fit exponential regression lines to represent IFL degradation for Simulation 1 (red circles), Simulation 2 (green triangles), and Simulation 3 (purple squares).

DISCUSSION

The numerical model using the SEAWAT programming code successfully modeled the development and transient evolution of three IFLs produced with a physical laboratory model (Rotz and Milewski, 2019). Although SEAWAT does not model variable-saturated conditions, the adjusted recharge rates were sufficient to adequately simulate water table elevations, thicknesses, and lengths based on the physical laboratory model observations. In all cases, the model evaluation statistics indicated that the numerical model over-predicted thicknesses and lengths under the assumption that the error variance occurs within the simulated values.

The numerical model parameters of hydraulic conductivity were refined with the PEST calibration tool, which estimated hydraulic conductivities within an acceptable range for fine to medium unconsolidated, heterogeneous sand. The initial laboratory measurement of hydraulic conductivity at 0.0015 m/s likely did not consider the heterogeneity and anisotropy present in the physical model sand due to the systematic, horizontal packing of sand during the model setup. However, the statistical evaluations of the water table elevations, thicknesses, and lengths show that the numerical model adequately reproduced the magnitudes of the measured data.

The average velocities estimated by the numerical model aligned with velocities measured from the physical model, as well as the average velocities reported by Al-Weshah and Yihdego (2016) of 6.34×10^{-7}–2.85×10^{-6} m/s. The numerical model showed an increase in average velocity during the recharge stress period by an order of magnitude (10^{-5} m/s), which aligns with the range of recharge rates used in the physical and numerical model simulations 3.33×10^{-6}–6.67×10^{-6} m/s. Based on these values, freshwater recharge that entered the center of the Raudhatain depression is estimated to travel 4000 meters towards the periphery between 20 and 200 years, depending on the hydraulic conductivity. This estimate aligns with those by Yihdego and Al-

Weshah (2017) and Parsons Engineering and Construction Corporation (1961) who reported an inferred flow velocity between 11 and 245 m/year based on ^{14}C and ^{3}H age dating, as well as an estimated groundwater velocity of 20–90 m/year based on a hydraulic conductivity range of 40–80 m/day. Estimates such as these inform geochemical studies that aim to approximate IFL water age, such as the study by Kuldzhayev (1974), which determined the onset of freshwater accumulation of an IFL in the Karakum desert to be 3400 years. Investigations into the formation, geometry, and extent of freshwater lenses over long temporal scales are needed for inland and coastal environments to quantify the supply of drinking water and the effects of external changes such as precipitation and sea-level rise (Kwarteng et al., 2000; Al-Weshah and Yihdego, 2016), but also geomorphological (Holt et al., 2019) and anthropogenic impacts (Senay, 1977; Schneider and Kruse, 2006)

Errors from the measurements taken from the physical model simulations were likely produced from multiple sources. The water table elevation or top of the IFL was challenging to estimate due to the capillary fringe. Preferential flow paths or heterogeneities of hydraulic conductivity likely developed from the packing of the sand during the setup of the physical model simulations, which required careful consideration when determining IFL length. The numerical model did not account for these heterogeneities or water retained in the pore space of the unsaturated area, which likely further contributes to errors in the numerical simulations.

Physical and numerical models are helpful tools to understand the stochastic relationships for subsurface flow and transport in variable-density aquifers in naturally and artificially recharged aquifers (Trefry et al., 2011; van Ginkel et al., 2016). Numerical models such as SEAWAT and others (e.g., MODFLOW-SURFACT, SUTRA (Saturated-Unsaturated Transport)) allow for the incorporation of variable-density conditions and parameters such as recharge volume, recharge

location, concentration, temperature, multiple species, and other variables in terms of solute transport and subsurface flow. Although freshwater lens geometry, including transience, can be determined with these models, additional tools, and optimization approaches to automate the monitoring of lens geometry are needed to improve the understanding of IFL sustainability. Models should be developed to consider the freshwater extent in the vertical and horizontal directions to predict volume, location, and residence time. Numerical simulations that include concentration data may use PEST to improve model calibration, which in turn improves the position and shape of the lens. These advancements will be useful for studying the dependence of periodic recharge on IFL degradation for water resources management. Figure 50 shows a conceptual example of IFL sustainability after a second recharge pulse is applied during IFL degradation.

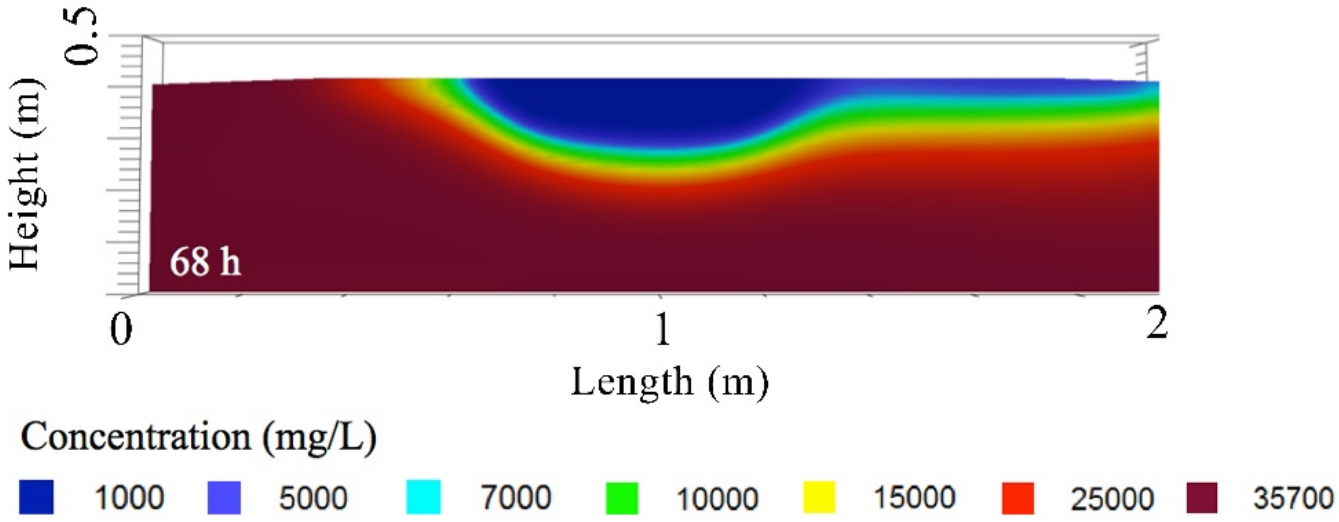

Figure 50. A second recharge pulse is applied to Simulation 2 to show the potential applications for IFL models that consider IFL transient evolution.

CONCLUSIONS

The purpose of this study was to create a conceptual framework for topographically induced IFL transient evolution using a numerical model and demonstrate the utility of IFL geometric analyses for resource management. We employed the SEAWAT programming code with Visual Modflow to simulate variable-density groundwater flow and solute transport within an inland setting based on observations made during physical laboratory model simulations (Rotz and Milewski, 2019). The numerical model was calibrated against the observed water table elevations measured in the laboratory by adjusting the values of hydraulic conductivity. The numerical model simulated IFL transient evolution and demonstrated the usefulness of predicting IFL geometry over time for water resource management.

As the demand for water resources in arid environments intensifies in conjunction with climate change, novel approaches for water resources development are needed (Al-Dousari et al., 2010; Becker et al., 2012; Sagintayev et al., 2012; Seyoum and Milewski, 2016, 2017). Desert communities have historically used inland and coastal freshwater lenses combined with ancient irrigation techniques (e.g., runoff harvesting, subsurface canals) for access to freshwater because the methods were uncomplicated and technologically inexpensive (Murray, 1955; Fleskens et al., 2007; Zonn, 2012). Similar systems have been identified within the deserts of the Middle East, Asia, Australia, South America, and Africa but have declined in use. A return to these systems with a focus on the interplay between meteoric recharge and the underlying saline groundwater offers development opportunities through modern and traditional methods to meet the growing demand for water resources in arid environments (Fleskens et al., 2007; Milewski et al., 2014a). This study provides a useful example for investigating IFL dynamics for the discovery of new resources (Milewski et al., 2014a), adjustment of pumping schemes (Senay, 1977), and artificial

recharge applications (van Ginkel et al., 2016). The SEAWAT programming code serves as an effective tool for investigating the complexity of IFL transient evolution over long temporal scales for the prediction of available water resources in drylands.

AUTHOR CONTRIBUTIONS

R.R., A.M., and T.R. conceptualized and designed this project. R.R. and A.M. acquired the financial support for this project leading to the manuscript. R.R. and A.M. developed the methodology. R.R. conducted the experiments, performed the formal analysis, and prepared the initial draft of the manuscript. A.M. provided the software and computing resources. A.M. and T.R. provided oversight and mentorship for the research activity. R.R., A.M., and T.R. critically reviewed and prepared the final draft of this manuscript.

FUNDING

This research was funded by the Society of Exploration Geophysicists Lynn and Gary Servos Groundwater Exploration Scholarship and the University of Georgia Department of Geology Gilles Allard Research Grant.

ACKNOWLEDGMENTS

The authors would like to thank the University of Georgia Water Resources and Remote Sensing Laboratory and John Dowd for assistance with the research, as well as the reviewers who invaluably helped with the improvement of this manuscript.

CONFLICTS OF INTEREST

The authors declare no conflict of interest.

CHAPTER 7

FLUVIAL INCISION AND TECTONIC UPLIFT ON MARS

INTRODUCTION

Evidence for water flowing on the surface of Mars is widespread in the form of fluvial landforms such as valley networks, outflow channels, deltas, gullies, and playa lakes (Baker et al., 1992). In specific terrains of Arabia Terra devoid of surficial fluvial features, extensive inverted and buried fluvial channels suggest the region underwent prolonged precipitation and runoff much like the highly dissected, Noachian surfaces below 60° latitude (Hynek et al., 2010; Davis et al., 2016). The majority of hydrologic activity is believed to have occurred around the Noachian/Hesperian transition (3.7 – 3.9 Ga) (Howard et al., 2005; Irwin et al., 2008). Extensive work has been done to constrain the timing of fluvial activity using crater counting techniques from satellite images of various resolutions, as well as invoking the principle of superposition to constrain the relative ages between fluvial activity, volcanism, and recent impact events (Mangold, 2012; Keske et al., 2015). While these approaches identify the timing of fluvial activity, the dates are merely a snapshot in time with a high degree of uncertainty (Hartmann, 2005) that cannot be used to determine flow duration, or how long water was flowing on the surface. However, we identified a location where a pair of valley networks appear to have codeveloped with a thrust fault, providing a novel opportunity to determine the local flow duration using quantitative tectonic techniques. This study presents the observations and analyses of a candidate location not only to determine the flow duration of valley networks in northern Arabia Terra, but also as a proof-of-

concept to determine the flow duration of fluvial landforms in other locations with similar settings on Mars (i.e., Ogygis Rupes and Hiddekel Rupes) (Klimczak et al., 2018).

Due to numerous meteorite impacts of northern Arabia Terra, few intact channels have been documented in the region (Hynek et al., 2010). One exception is a valley network located on the edge of a 400-km closed basin called Phison Patera (Davis et al., 2019). The valleys flow towards the basin (from SW to NE), but peculiarly, that direction trends in the opposite direction of tilt of the uplifted hanging wall block of a thrust fault, on which the valleys are located. This suggests the valley network incises the positive relief and terminates into the basin. This suggests the valley network, which is superimposed on the backslope of a thrust fault, incises the positive relief and terminates into the basin. This interplay of processes has been observed on Earth, including in Iran of the Shardar River and Shotori mountains (Walker et al., 2003), where the river has flowed during the presently active thrust-faulting (Torabi et al.). Further, studies into the fluvial incision of a thrust fault system can also be found in central Nepal (Lavé and Avouac, 2001), Papua New Guinea (Miller et al., 2012), Romania (Necea et al., 2013), Turkey (Westaway et al., 2009), and other places on Earth with past or present tectonic activity.

Thrust faulting on Earth occurs in both orogenic and intraplate tectonic settings, and thrust faulting on Mars is found to compare well with terrestrial intraplate faulting (Klimczak et al., 2018). Thrust faults accommodate shortening to produce positive-relief landforms, the largest of which are expressed as asymmetric ridge with thousands of meters of vertical relief and hundreds of kilometers in length (Twiss et al., 1992). The most pronounced landforms formed by thrust fault systems on Mars, commonly also termed wrinkle ridges or lobate scarps, are in the southern highlands, but also occur on the northern lowlands albeit less pronounced.

Fault structures are measured in three dimensions and the common parameters are length, displacement, throw, strike angle, dip angle, and their activity is measured with strain or slip rates. The relationship between throw, displacement, dip angle, and slip rate can be used to calculate the amount of time required for the vertical relief to occur (Twiss et al., 1992). On Mars, the positive relief features produced by thrust faults remain largely unaltered. This allows for the measurement of the structural relief, calculation of displacement for a set of likely fault dips, and under the assumption of intraplate fault slip rates allows us to estimate uplift duration.

Study Site

The study site (45°N, 28°E) is located on the western edge of the Phison Patera basin in the northern region of Arabia Terra (Figure 51). This is a cratered region that extends from the northern boundary at 45°N latitude to 0° latitude at the southern boundary and covers an area of 12,000,000 km^2. The terrain of Arabia Terra includes fragmented valley networks, debris-flow deposits, wrinkle ridges, and faulting (McGill, 2002). The elevation of the region is mostly below the planetary reference of 610.5 Pa (6.105 mbar) and relatively low for the highland terrane that appears to underlie it. Much of the older terrain of Arabia Terra (Early Noachian) has been eroded by fluvial activity during a high-intensity resurfacing event (Late Noachian), as well as the infilling of craters by volcanic activity (McGill, 2000). Arabia Terra borders the crustal dichotomy, which is a low elevation area defined by the Northern Lowlands region (Figure 51). Ancient shorelines are purported to occur along the border of Arabia Terra and the Northern Lowlands, which may have once been filled with an ocean (Webb, 2004). Younger, lowland deposits surround the northern region of Arabia Terra, which exhibits sharp-angled landforms that may have formed by faults and joints.

The Phison Patera basin is reported as a 400-km, highly modified impact crater and closed basin (Davis et al., 2019). Very little information about the basin exists in the literature. A thrust fault related landform borders the southwestern edge (Figure 52). The entire length of the ridge is 317 km and extends NW-SE from 44.61° E, 30.62° N from the northwest to 45.86° E, 26.96° N in the southeast. Several impact craters occur around the area and appear to be filled with sediment. The elevation is higher on the western side of the ridge and steeply drops in the basin on the eastern side of the ridge. The landform exhibits the typical morphological characteristics associated with thrust faulting. This includes a steeply sloping cliff that faces the uplifted block and a gentle slope located above the underlying fault. The elevation of the uplift block is highest on its eastern edge and decreases eastward. However, the general flow direction of the region is west to east (Figure 52). A pair of valley networks on the western side of the fault surface break incise the uplift block and terminate in the basin. From these observations, we hypothesize that the channel was active at least during the activity of the thrust fault related landform. The objectives of this study are to (1) characterize the coincidence of the fluvial incision of a thrust fault on Mars and (2) calculate the uplift duration as a proxy for flow duration at a candidate site in the northern Arabia region of Mars.

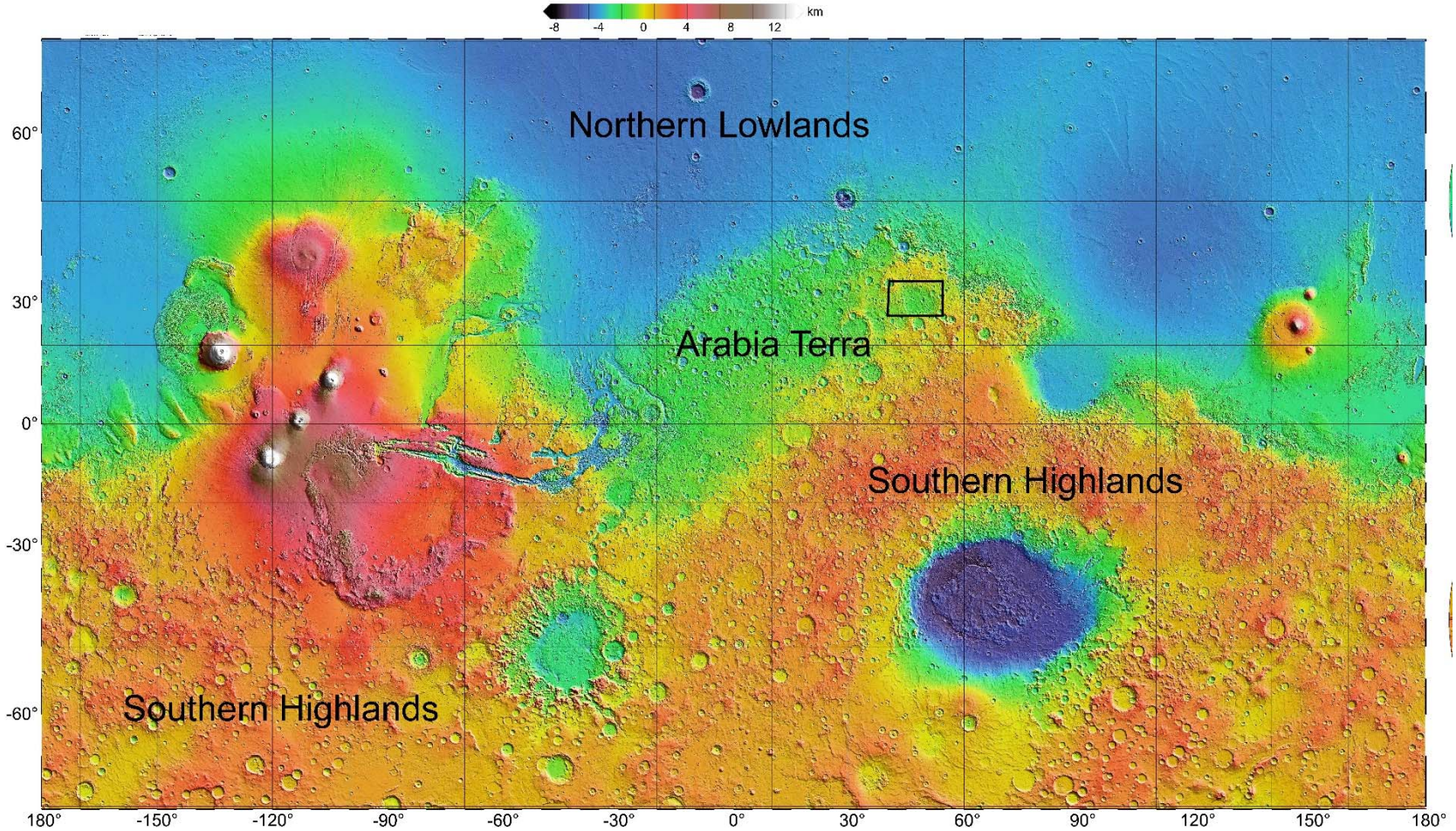

Figure 51. Global Map of Mars by the Mars Orbiter Laser Altimeter (MOLA). The black box surrounds Phison Patera and the study site within the northern region of Arabia Terra.

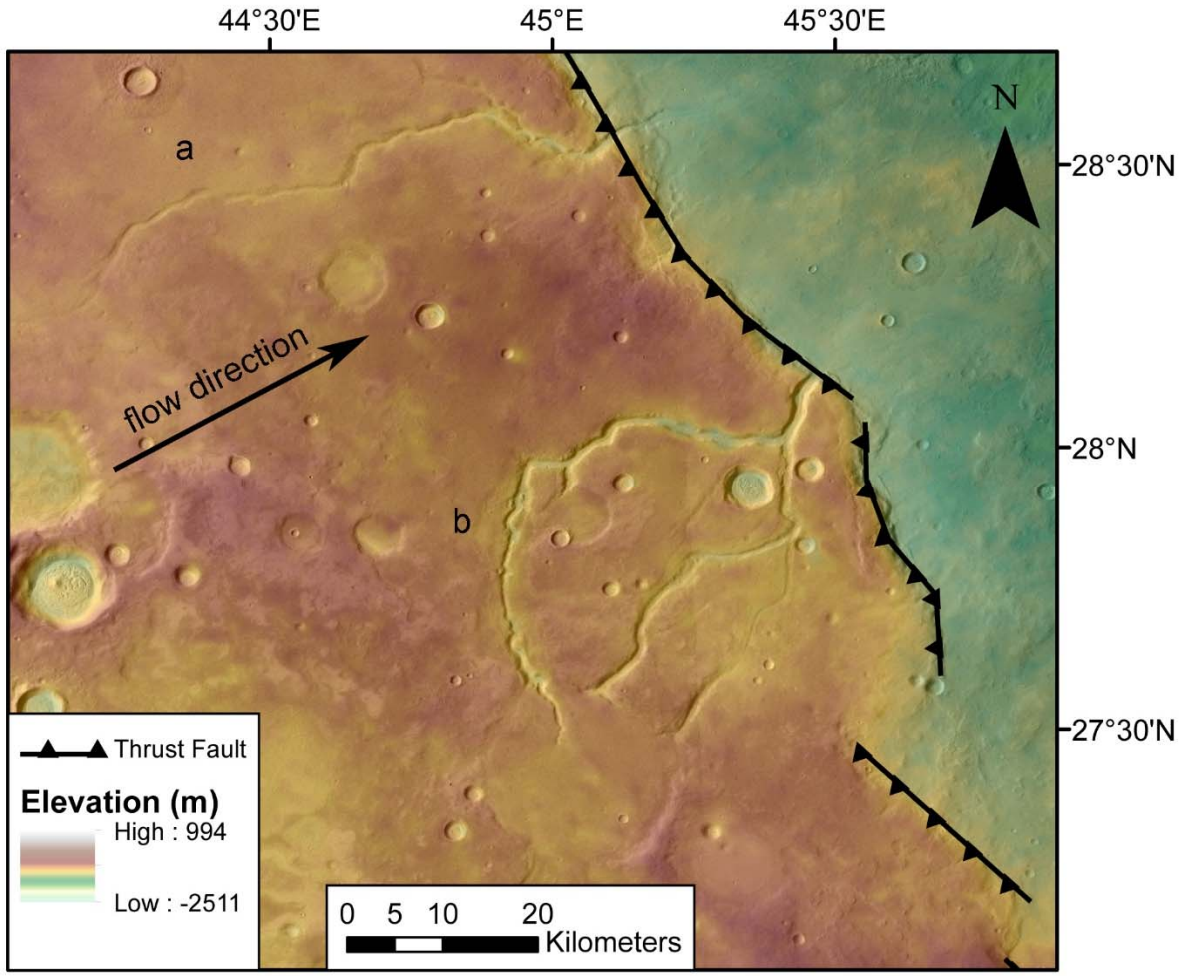

Figure 52. Two valley networks, one in the north (a), and one in the south (b) appear to have incised a thrust fault on the southwestern edge of the Phison Patera basin.

METHODOLOGY

Data Collection

Satellite remote sensing data were acquired from the Context Camera (CTX) of the Mars Reconnaissance Orbiter for mapping (resolution = 6 m) (Malin et al., 2007), and the High/Super Resolution Stereo Color Imager (HRSC) for the regional DEMs (resolution = 150 m) (Scholten et al., 2005) due to the paucity of CTX stereo pairs in the region. Images were mosaicked in ArcMap.

Measurements

Five elevation profiles for the area were generated in ArcMap to demonstrate that the ridge within the region of interest exhibits features consistent with thrust fault related landforms and to calculate the throw values, or amount of vertical displacement of the uplift block. Five transects were selected across the region that strike quasi-parallel to the valleys, as well as in between the valley networks in the north and south regions of the study area. High and low elevation values were selected at the location of the thrust fault landform for each profile to calculate the throw. The throw values from the five transects were used as inputs to calculate the fault displacement with a range of dip angle rates between 20° and 40° in 1° increments using the trigonometric relationship between throw, dip angle, and displacement as in Klimczak et al. (2018):

$$\sin a = \frac{t}{D} \tag{18}$$

where a is the dip angle, t (L) is throw, and D (L) is the fault displacement.

21 values of fault displacement were generated for each transect for a total of 105 values. These values were used as inputs to calculate the uplift duration time using a range of slip rates from 0.01 to 1 mm/yr (Schultz (2003) at 0.01 mm increments using the relationship between

displacement, slip rate, and uplift duration to provide a minimum and maximum duration for the calculated ranges:

$$T = \frac{D}{s} \tag{19}$$

where T is the duration of uplift (T), and *s* is the slip rate (L/T).

2100 values of uplift duration were generated for each transect for a total of 10,500 duration values. Statistical analyses were then performed using the R programming language.

RESULTS

Thrust Fault Measurements & Calculations

Results support the objectives of this study to characterize the coincidence of the fluvial incision of a thrust fault on Mars and calculate the uplift duration as a proxy for flow duration at a candidate site in the northern Arabia region of Mars. The elevation profiles of the five transects were generated to demonstrate features consistent with thrust fault related landforms. The high standing part of the thrust fault along Transect BC that declines back towards the southwest and counters the general flow direction (Figure 53). The throw values calculated from the five transects are shown in Figure 54 and summarized in Table 16.

Table 16. Values used from the elevation profiles of five transects to determine the throw (t) or vertical uplift values.

Transect	X-axis location for high value (m)	High value (m)	X-axis location for low value (m)	Low Value (m)	*t* (m)
A	60,255	-800	71,683	-1350	550
B	46,148	-761	60,678	-1431	670
BC	44,183	-622	73,988	-1442	820
C	59,202	-765	69,178	-1345	580
D	45,565	-912	51,145	-1307	395

The displacement values calculated from the five elevation profiles ranged from 614 meters for Transect D to 2,398 meters for Transect BC for a total of 105 values as shown in Figure 55. The uplift duration values calculated from the 105 displacement values ranged from 600,000 years for Transect D to 239,800,000 years for transect BC for a total of 10,500 values as shown in Figure 56. A summary of values is provided in Appendix D.

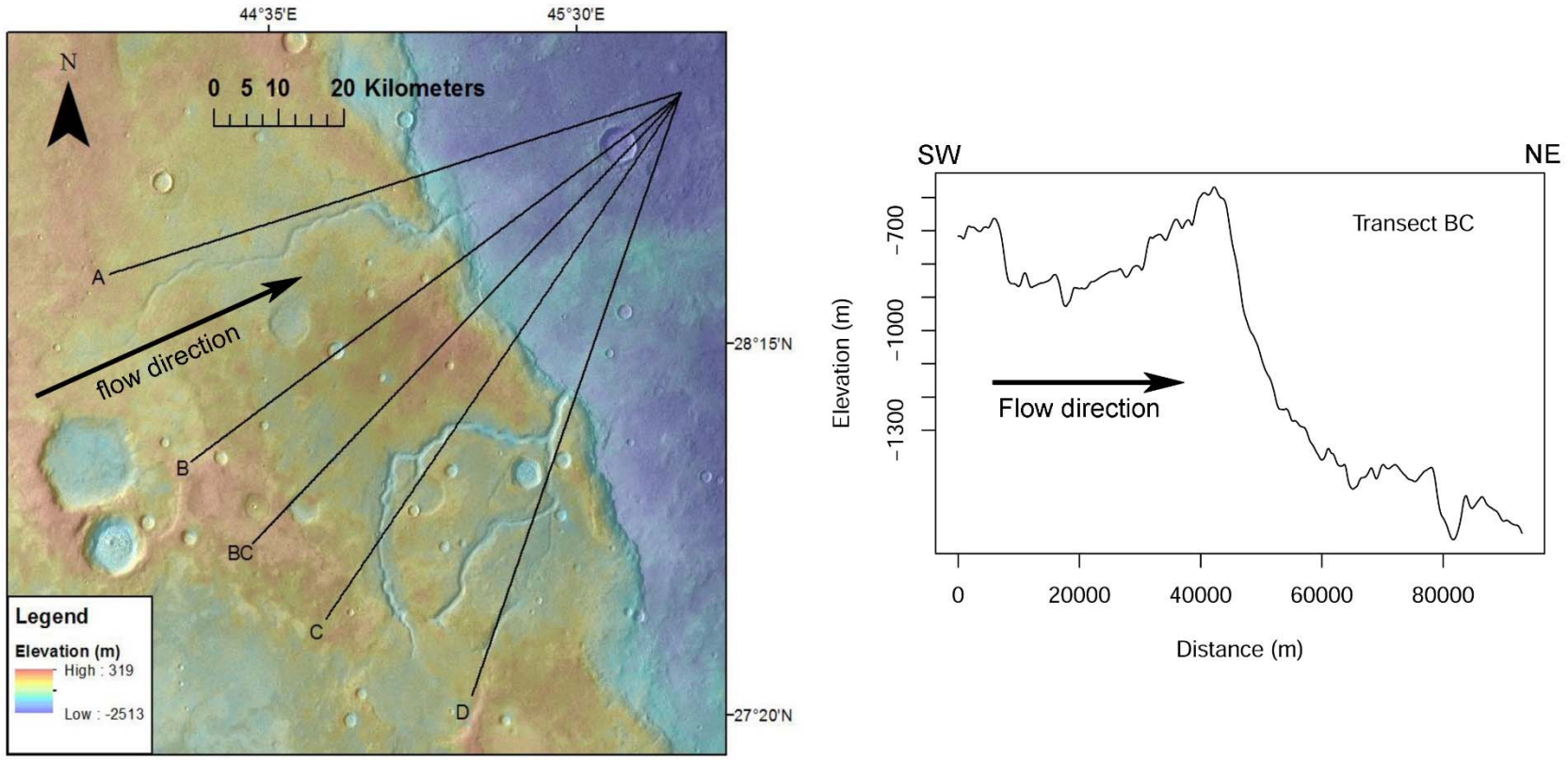

Figure 53. Figure with transects and general flow direction (towards the NW) (left), and the elevation profile of Transect BC in comparison to the uplift black of the thrust fault related landform sloping in the opposite direction (towards the SW) (right).

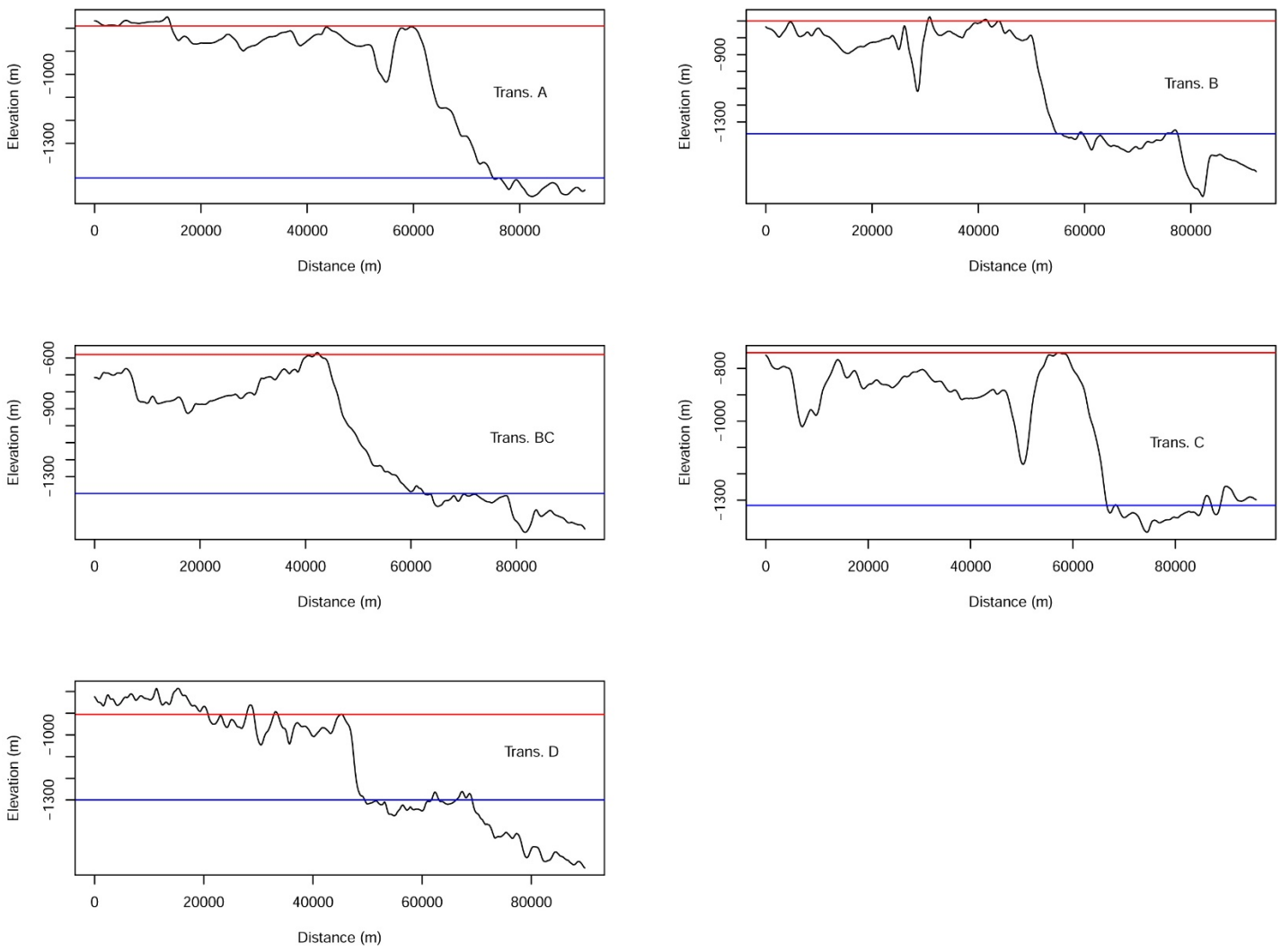

Figure 54. The elevation profiles for the five transects. The red line indicated the highest elevation value and the blue line indicates the lowest elevation value to calculate the throw.

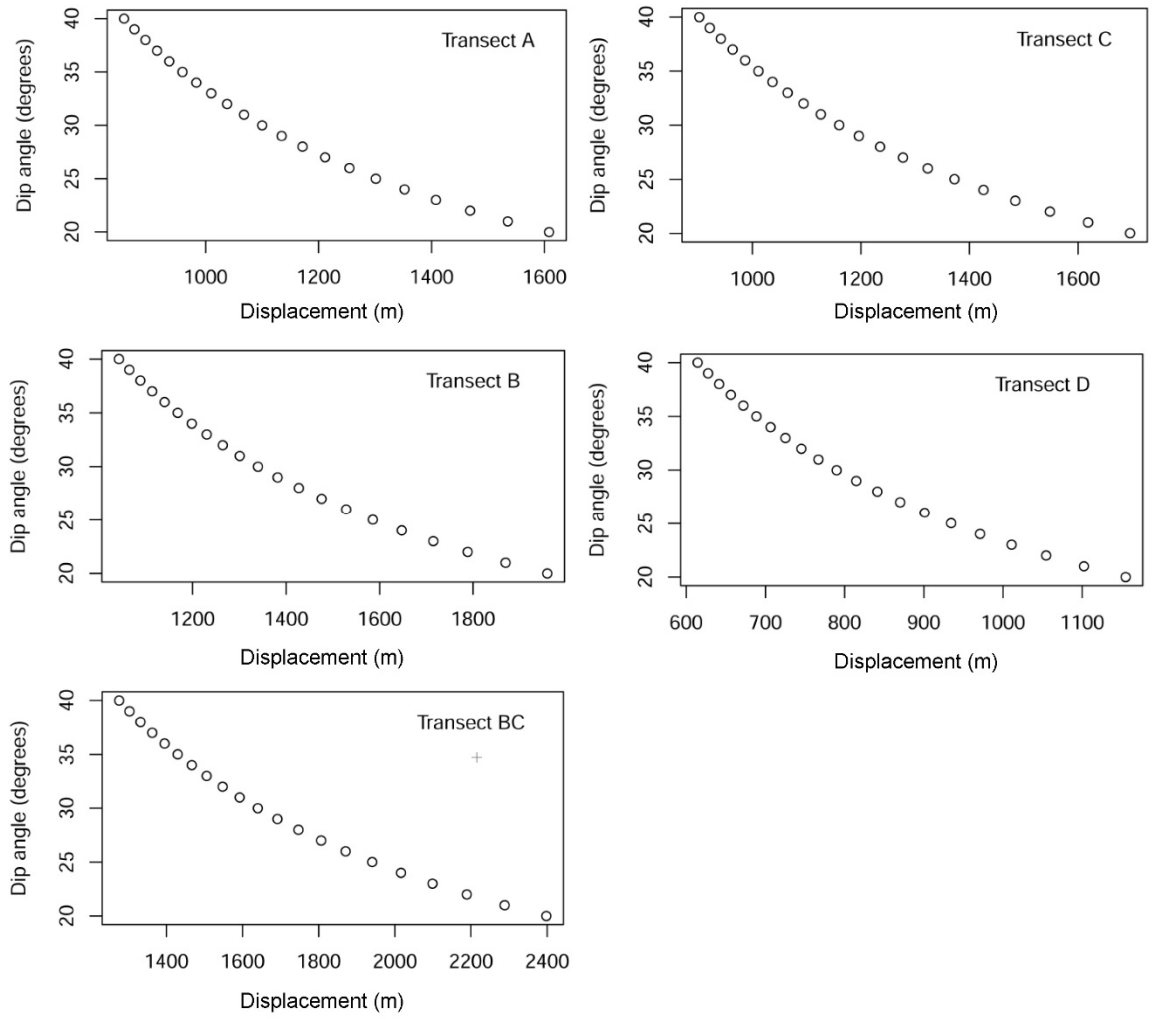

Figure 55. Displacement values as a function of dip angle by transect.

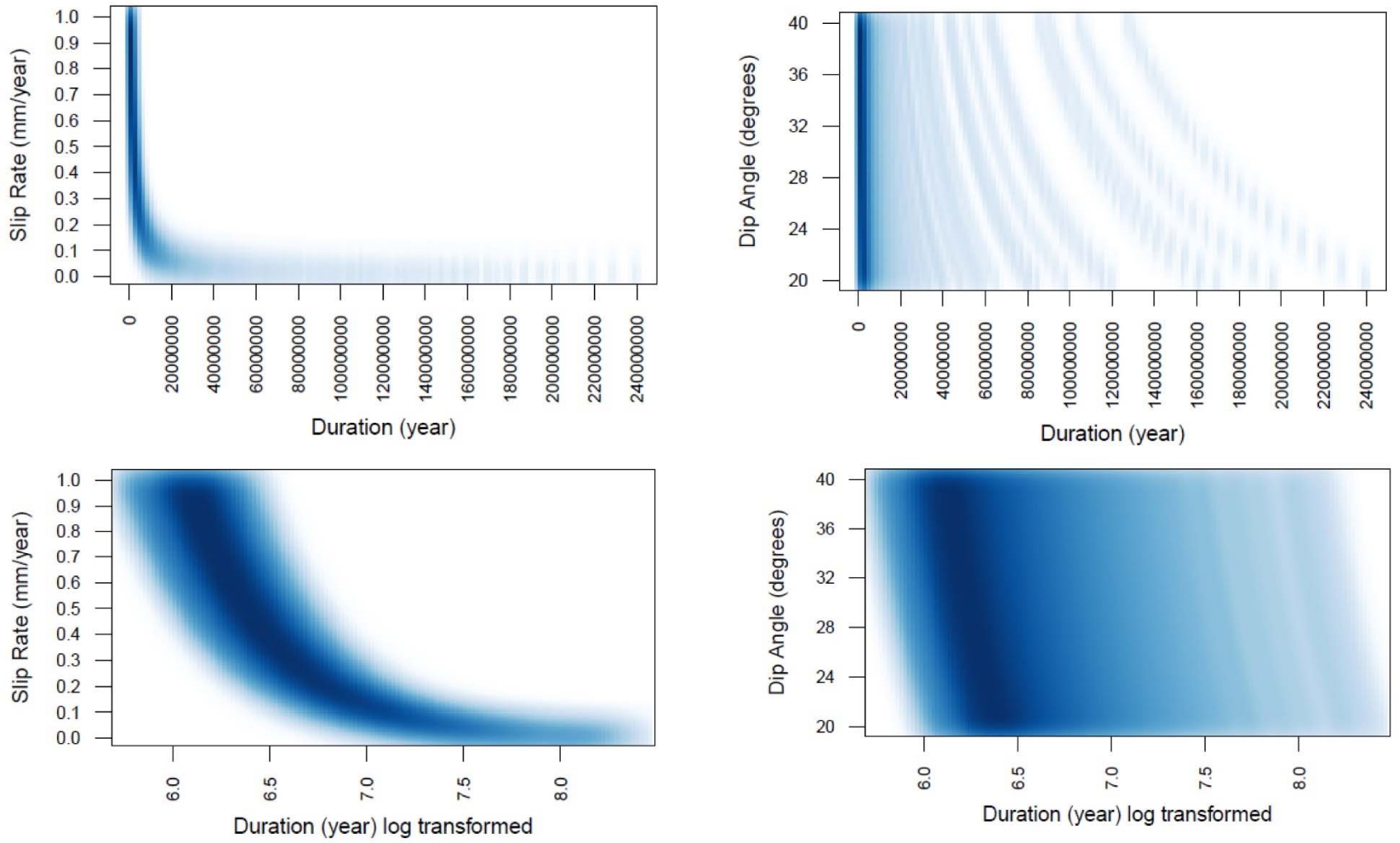

Figure 56. Density plots of uplift duration calculations for all elevation profile transects as a function of slip rate (left) and dip angle (right). The lower plots show the duration values log transformed.

Discussion & Conclusion

Results demonstrated how geomorphic and geologic indicators at zones of hydrologic flux can be used on Mars to understand the timing and flow of surface water on extraterrestrial settings like Mars. We analyzed a thrust fault related landform and a series of incising valley networks to calculate the throw, displacement, and uplift duration as a proxy for flow duration. A total of five elevation profile transects were examined within the study area. The profiles show features consistent with thrust fault related landforms, including the highest standing part declining backward against the direction of the current geographic trend.

Throw, or vertical uplift, values were calculated using DEMs and used as inputs to calculate the fault displacement and flow duration over a range of dip angles and slip rates appropriate for tectonics on Mars. The duration values calculated ranged from 614,510 to 239,751,961 years. Although this is a large range, the log transformed density plots (Figure 56) indicate the highest likelihood of flow duration between 625,000 and 725,000 years considering all values in the parameter space are equally unconstrained. These numbers align with a study by Hoke et al. (2011), which estimated the formation of valley networks in southern Arabia Terra occurred over 10^5-10^7 years using sediment transport models. Constraining the dip angle, as well as improved access to higher resolution DEMs, such as with CTX stereo pairs, will also further refine the ranges of values. A comparison of a CTX and HRSC DEM is included in

Appendix E and

Appendix F. This study serves as a useful proof-of-concept for detecting duration of water flow at locations with the co-occurrence of fluvial channels and fault systems and can be further used to constrain total water volumes as shown in

Appendix G. Its application to other such locations would allow to tightly constrain the duration of liquid water on the surface on Mars. The results from this approach help to define periods of hydrologic activity on Mars and major implications for understanding the Martian water cycle and the historical evolution of the climate.

CHAPTER 8

DISCUSSION & CONCLUSION

In drylands, water is hidden in the subsurface as groundwater, but traces are left on the surface as distinct features that point to past hydrologic movement. This paper presents three studies that investigate geomorphic and geologic indicators to understand the timing and flow of surface and subsurface water in drylands across scales.

Field methods, laboratory techniques, and remote sensing applications allowed for the observation of flooding in a playa lake (wet days = 237/6936; flood events > 58) of the Simpson Desert of Australia on a medium-time scale. Large gravels were identified at depths of 151 cm and 200 cm suggesting high-magnitude floods occurred in the past. Samples using OSL techniques have been submitted to determine the timing of those floods. Mineralogical results showed that the playa sediment contains evaporite and clay minerals not found in the dune adjacent to the sample site. Additional lithological, mineralogical, and chronological analysis of the downwind linear dunes is needed to further investigate the relationship between playa flooding and dune building.

Physical, numerical, and analytical modeling approaches allowed for the observation and prediction of fresh groundwater flowing atop a saline groundwater system in northern Kuwait. An analytical solution for freshwater lenses in oceanic variable-density settings was deemed invalid to model IFLs when compared to the formation of an inland freshwater lens with a physical model. A modified solution was created, and the physical model simulations were compared to a numerical model, which performed within acceptable statistical rates for hydrology models.

Velocities measured in the physical and numerical models were similar to values in the literature for the IFL of northern Kuwait suggesting the numerical method to be a useful to characterize and predict IFL formation and degradation in Kuwait and other drylands with similar settings.

On Mars, remote sensing and analytical techniques allow for the calculation of the timing (preliminary results = 600 ka-240 Myr) and flow (TBD) of surface water at the intersection of a channel and thrust fault in Arabia Terra, Mars on a long-time scale. The culmination of these results demonstrates the strength in approaching questions of geomorphological and hydrological significance through the lens of interdisciplinary and comparative geological research to expound on the topic of groundwater accumulation in drylands on planetary surfaces.

Gaps of Knowledge in Data Sparse Regions

Although these analyses occur in different deserts on Earth and beyond, there are few surfaces and subsurface processes that control topography, shape the landscape, and encourage groundwater storage. These are tectonic, hydrological, and erosional processes which in turn drive the biogeochemical processes and so on. The broad approach of using indicators of water in drylands is challenging because investigations must consider a breadth of theory, disciplines, techniques, and assumptions to produce reliable results and draw convincing conclusions. One may feel constrained by such a broad perspective to impose conclusions. The challenges of researching remote areas (e.g., Mars) over long time spans with little data produces high levels of uncertainly in models. However, the results help close gaps of knowledge within their respective fields. For example, the recent frequency of flooding in the playas of northern Australia (i.e., Lake Caroline) has never been documented. Reports relied on anecdotal "evidence" and weather station data from as far away as 100 km (Duguid, 2011). Advancements in remote sensing satellite technology, such as GPM, provide continuous, global, rainfall data for 19 years and counting.

However, GPM obtains rainfall data by proxy from measurements of atmospheric reflectivity and calibrates this data to precipitation gauges, which include inherent error (Huffman et al., 2015). The satellite-gauge combination model of GPM often underestimates rainfall in arid environments, of which high variability and few gauges occur (Milewski et al., 2015; Mahmoud et al., 2020). As a result, the measurement of rainfall and subsequent quantification of available water for recharge is also underestimated. It is likely that in both Australia and Kuwait, recharge volumes are larger than currently believed. In data-starved regions like drylands, approaches such as the analyses of topography and drainage densities are powerful tools to understand climate. This case was made by Milewski et al. (2014a) for annual runoff and recharge estimates for the IFLs of Kuwait (8×10^6 m^3), which was previously estimated for the entire country by Abdulrazzak (1994) and Kwarteng et al. (2000) at a much lower annual volume (2×10^6 m^3). Ancillary data, such as the visual confirmation of flooding as shown with Landsat, ASTER, Sentinel, and Rapid-Eye satellite images, provide ways to substantiate runoff and recharge estimates.

On Mars, Craddock and Howard (2002) purport the critical need for topographic analyses to support prolonged rainfall and runoff for an early, warm/wet Mars. Questions regarding available water for recharge is linked to its source (i.e., rainfall). When we look back in time, as is the case for Mars or the analyses of desert paleodrainage systems, geomorphic and geologic features may be the best indicators of past climate and hydrologic activity. As Professor Alexander Winchell writes in the book entitled *Comparative Geology*, "he cannot transport himself across the intervals of geologic eons, but he can gaze upon other works just entering upon states passed millions of years ago by our Earth…" In Arabia Terra and throughout Mars, we see evidence for aqueous activity on the surface. Most studies agree one or more punctuated periods of intense fluvial activity occurred during the Noachian period. Davis et al. (2019) estimate the chronology

of the Arabia Terra fluvial systems to have occurred between 3.9-3.7 Ga, whereas the first-order calculation of uplift duration proposed a flow duration of 600 ka-240 Myr. We do not know if the river flowed before and after uplift but offer a constrained period for the water budget and other studies related to tectonics, fluid, and slip rates (Personal conversation with Christian Klimczak, 2019).

Water Resources and Variable-Density Groundwater in Drylands

The most applicable study in this paper that addresses Earth's dryland water resource problems is the inland freshwater lens study. Here, we characterize the transient evolution of an IFL, as well as present a method to quantify the longevity of freshwater as it changes position and mixes with the underlying saline water. The physical, analytical, and numerical modeling of an IFL like the one beneath the Raudhatain Depression in Kuwait provided a means to observe and predict the lens longevity (20 – 200 years) after the initial formation without an additional recharge. These results are within the scale of a study done by Alrashidi and Bailey (2020) that estimate a reduction in lens thickness of 9-21% within 100 years (longevity = 500-1,100 years) with a 50% reduction in annual recharge (250,000 m^3).

Numerical modeling and calibration of head and concentration values are currently the best method to determine lens geometry and freshwater volume because the traditional analytical solutions for variable-density mounding assume a steady-state condition with no energy gradient (Baydon-Ghyben, 1898; Hantush, 1967; Vacher, 1988). Although the grade in drylands can be quite flat (e.g., Kuwait = 0.002), particularly in playas and basins, it is enough for IFLs to migrate downhill. The front edge of the lens smears and violates the lenticular shape of the geometric model. Further research is needed to establish automated models that numerically account for the geometry.

In Australia, we observed flooding within Lake Caroline, a zone of hydrologic flux that both discharges the upland throughflow but also recharges the GAB. Currently, water resource assessment does not account for any recharge entering the GAB from Lake Caroline (Smerdon et al., 2012). The presence of gypsum and halite in the sediment of Lake Caroline suggests the surficial aquifer may be brackish to saline. This is substantiated by hydrogeochemical studies in the western margin of the Western Eromanga Basin where GAB groundwater is predominantly Na-Cl-Ca-SO_4 (Habermehl, 1982). Also, salinity values over 100,000 mg/L have been detected in GAB bores in South Australia, but salinity data for Northern Territory are not available. Implications of the observations that Lake Caroline frequently floods in the winter months include the plausibility of an IFL beneath Lake Caroline that is sustained by meteoric recharge. Future research should examine this possibility. Pastoral, agricultural, mining, and inland populations may benefit as the demand for water resources is growing in this area.

Terrestrial Analogues

Deserts on Earth have much to offer in the way of analogue sites (West et al., 2010). The geomorphic and geologic indicators presented in this paper all make useful terrestrial analogues to investigate surface processes on Mars. For example, the dune fields and hematite-coated sediments in Australia are analogues of dunes (Bishop, 2001) and sediment (Kuhlman et al., 2001) on Mars, as well as linear dunes on Titan (Craddock et al., 2015). Flood plains (e.g., Todd River) and playas (e.g., Lake Eyre) in Australia are also of high utility for Mars analogues for their low-relief, unconfined, and fine-grained characteristics like flood-out areas on Mars. Other sites in Australia include impact craters (e.g., Henbury), inverted channels, (e.g., Painted Desert mesas), and saline bays (e.g., Hamelin Pool). Terrestrial analog sites are used to improve understanding of the processes on Earth to translate information from scientific missions to extraterrestrial bodies

The experimental approaches, instruments, and research methods presented in this paper are also used for terrestrial field campaigns for planetary research. For example, the in-situ sampling of playa sediments at Lake Caroline and the analysis using X-ray diffraction is similar to work done by the Mars Curiosity rover at Gale crater (Bish et al., 2013). Remote sensing maps (McEwen et al., 2007) used to identify geomorphic and geologic indicators are also used by scientists as reconnaissance for surface in-situ investigations as was done with the playa lake study at Lake Caroline. Extreme environments on Earth provide similar terrain conditions to perform in-situ and remote sensing investigations to examine the timing and duration of past hydrologic activity on Mars and other planetary surfaces.

Interdisciplinary Approaches

The experts and work put forth in this dissertation represent different branches of the geosciences. So rarely are they brought together to present results on the topic of water in deserts on Earth and Mars by such a diversified range of scientists. The term interdisciplinary studies may be defined as a process of addressing a topic that is too broad or complex to be dealt with by a single discipline (Klein and Newell, 1997). While the primary purpose of this study is to answer questions about the timing and flow of surface and subsurface waters in drylands on Earth and other planetary surfaces, work towards problems related to sediment supply for landforms and structural activity in deserts has also been addressed.

The advancement of interdisciplinary studies is believed to invigorate the capacities of analysis, problem-solving, communication, and synthesis for students across disciplines in both academic and real-life situations. Interdisciplinary research and the integration of techniques (e.g., fieldwork, laboratory, modeling, analytical, and remote sensing applications) create opportunities for students and faculty in the areas of curriculum development, shared facilities and

instrumentation, and interinstitutional alliances that strengthen the scientific community. We see this happening in many disciplines including aeolian and fluvial studies where they have historically been viewed as mutually exclusive. Bullard and Livingstone (2002) refer to this as the reductionist approach and highlight areas of future research that will advance these fields together. The same can be said for surface and groundwater, which are often identified as different compartments of the hydrologic cycle and managed separately. Barthel (2014) calls for discussions on how to integrate surface and groundwater research to move towards a more interdisciplinary approach for water resources in field studies, modeling, and regional management. Investigating the geomorphic and geologic indicators at zones of hydrologic flux in drylands on Earth and other planetary surfaces integrate disciplines to allow for work in different settings across scales.

Summary

The search for water resources in drylands is an important effort to support growing human populations and protect wildlife biodiversity. Also, as humans travel to extraterrestrial settings, water resources are needed to support manned-missions and the search for life. Scientists can use geomorphic and geologic indicators to identify zones of hydrologic flux in drylands on Earth, Mars, and other planetary surfaces. They may serve as indicators during reconnaissance missions for the identification of in-situ studies and terrestrial analogues for insight into planetary processes. The integrated application of field, laboratory, analytical, modeling, and remote sensing methods allows for the quantification of the timing and flow of surface and subsurface waters across scales. The broad and complex questions about water in drylands can be answered using an interdisciplinary approach, which enhances teaching and learning activities and creates hybrid teams within the scientific community. The work presented in this paper is important because it

demonstrates a multitude of locations, indicators, and methods to be used within the philosophical framework to answer questions of geomorphological and hydrological significance in drylands on Earth and extraterrestrial settings.

REFERENCES

Abdelkareem, M., Abdalla, F., Mohamed, S. Y., and El-Baz, F., 2020, Mapping paleohydrologic features in the arid areas of Saudi Arabia using remote-sensing data: Water, v. 12, no. 2, p. 417.

Abdulrazzak, M. J., 1994, Review and assessment of water resources in Gulf Cooperation Council countries: International Journal of Water Resources Development, v. 10, no. 1, p. 23-37.

Abotalib, A. Z., Sultan, M., and Elkadiri, R., 2016, Groundwater processes in Saharan Africa: Implications for landscape evolution in arid environments: Earth-science reviews, v. 156, p. 108-136.

Abouelmagd, A., Sultan, M., Sturchio, N. C., Soliman, F., Rashed, M., Ahmed, M., Kehew, A. E., Milewski, A., and Chouinard, K., 2014, Paleoclimate record in the Nubian sandstone aquifer, Sinai Peninsula, Egypt: Quaternary research, v. 81, no. 1, p. 158-167.

Al-Dousari, A., Milewski, A., Din, S. U., and Ahmed, M., 2010, Remote sensing inputs to SWAT model for groundwater recharge estimates in Kuwait: Advances in Natural and Applied Sciences, v. 4, no. 1, p. 71-77.

Al-Masrahy, M. A., and Mountney, N. P., 2015, A classification scheme for fluvial–aeolian system interaction in desert-margin settings: Aeolian Research, v. 17, p. 67-88.

Al-Rashed, M., and Sherif, M., 2000, Water Resources in the GCC Countries: An Overview: Water Resources Management, v. 14, no. 1, p. 59-75.

Al-Rukaibi, D., Abdullah, W., Al-Fares, R., and Hussain, M., 2017, Site suitability index (ssi) model to delineate and assess suitability of rainwater runoff basins in jal alzor heights, kuwait: Jordan Journal of Civil Engineering, v. 11, no. 3.

Al-Ruwaih, F., and Hadi, K., 2005, Water quality trends and management of fresh groundwater at Rawdhatain, Kuwait: Editorial Advisory Board, v. 11, no. 3, p. 423-437.

Al-Ruwaih, F., Sayed, S., and Al-Rashed, M., 1998, Geological controls on water quality in arid Kuwait: Journal of Arid Environments, v. 38, no. 2, p. 187-204.

Al-Sarawi, M., 1995, Surface geomorphology of Kuwait: GeoJournal, v. 35, no. 4, p. 493-503.

Al-Sulaimi, J., Khalaf, F. J., and Mukhopadhyay, A., 1997, Geomorphological analysis of paleo drainage systems and their environmental implications in the desert of Kuwait: Environmental Geology, v. 29, no. 1-2, p. 94-111.

Al-Sulaimi, J., and Mukhopadhyay, A., 2000, An overview of the surface and near-surface geology, geomorphology and natural resources of Kuwait: Earth-Science Reviews, v. 50, no. 3–4, p. 227-267.

Al-Sulaimi, J. S., and El-Rabaa, S. M., 1994, Morphological and morphostructural features of Kuwait: Geomorphology, v. 11, no. 2, p. 151-167.

Al-Weshah, R. A., and Yihdego, Y., 2016, Flow modelling of strategically vital freshwater aquifers in Kuwait: Environmental Earth Sciences, v. 75, no. 19, p. 1315.

Allison, G., Gee, G., and Tyler, S., 1994, Vadose-zone techniques for estimating groundwater recharge in arid and semiarid regions: Soil Science Society of America Journal, v. 58, no. 1, p. 6-14.

Alrashidi, M. S., and Bailey, R. T., 2020, Estimating groundwater recharge for a freshwater lens in an arid region: Formative and stability assessment: Hydrological Processes, v. 34, no. 4, p. 1063-1080.

Alsharhan, A. S., Rizk, Z. A., Nairn, A. E. M., Bakhit, D. W., and Alhajari, S. A., 2001a, Chapter 5 - Hydrogeochemistry, Hydrogeology of an Arid Region: The Arabian Gulf and Adjoining Areas: Amsterdam, Elsevier Science B.V., p. 101-124.

Alsharhan, A. S., Rizk, Z. A., Nairn, A. E. M., Bakhit, S. W., and Alhajari, S. A., 2001b, Chapter 1 - An introduction to water resources in the Arabian Peninsula, Hydrogeology of an Arid Region: The Arabian Gulf and Adjoining Areas: Amsterdam, Elsevier Science B.V., p. 1-6.

Anand, R., and De Broekert, P., 2005, Weathering history, landscape evolution and implications for exploration: Regolith Landscape Evolution Across Australia: A Compilation of Regolith Landscape Case Studies with Regolith Landscape Evolution Models, p. 2-40.

Anderson, E., 2013, Middle East: Geography and Geopolitics, Routledge.

Ansan, V., Mangold, N., Masson, P., Gailhardis, E., and Neukum, G., 2008, Topography of valley networks on Mars from Mars Express High Resolution Stereo Camera digital elevation models: Journal of Geophysical Research: Planets, v. 113, no. E7.

Ash, J., and Wasson, R., 1983, Vegetation and sand mobility in the Australian desert dunefield: Zeitschrift fur Geomorphologie, v. 45, no. Supp., p. 7-25.

Australian Bureau of Meteorology, 2020, Climate Data Online, Commonwealth of Australia.

Babiker, M., and Gudmundsson, A., 2004, The effects of dykes and faults on groundwater flow in an arid land: the Red Sea Hills, Sudan: Journal of Hydrology, v. 297, no. 1-4, p. 256-273.

Bagnold, R., 1941, 1941: The physics of blown sand and desert dunes. London: Methuen.

Baker, V., Carr, M. H., Gulick, V. C., Williams, C. R., and Marley, M. S., 1992, Channels and valley networks, Mars, University of Arizona Press, Space Science Series, p. 493-522.

Baker, V. R., 1982, The channels of Mars: Research supported by NASA, NSF, and Australian-American Educational Foundation Austin, TX, University of Texas Press, 1982. 204 p.

Baker, V. R., Hamilton, C. W., Burr, D. M., Gulick, V. C., Komatsu, G., Luo, W., Rice Jr, J. W., and Rodriguez, J., 2015, Fluvial geomorphology on Earth-like planetary surfaces: a review: Geomorphology, v. 245, p. 149-182.

Barrett, B., Heinson, G., Hatch, M., and Telfer, A., 2002, Geophysical methods in saline groundwater studies: locating perched water tables and fresh-water lenses: Exploration Geophysics, v. 33, no. 2, p. 115-121.

Barthel, R., 2014, HESS Opinions "Integration of groundwater and surface water research: an interdisciplinary problem?": Hydrol. Earth Syst. Sci., v. 18, no. 7, p. 2615-2628.

Baydon-Ghyben, 1898, Nota in verband met de voorgenomen putboring nabil Amsterdam'Tijdschr. K: Inst. Ing., The Hague, v. 27, p. 1888-1889.

Bear, J., 1979, Groundwater hydraulics, McGraw-Hill, New York.

Becker, D., Sultan, M., Milewski, A., Becker, R., Sauck, W., Soliman, F., Rashed, M., Ahmed, M., Yan, E., and Wagdy, A., 2012, Integrated solutions for hydrologic investigations in arid lands: Geosphere, v. 8, no. 6, p. 1588-1605.

Bergstrom, R., and Aten, R., 1965a, Natural recharge and localization of fresh ground water in Kuwait: Journal of Hydrology, v. 2, no. 3, p. 213-231.

Bergstrom, R. E., and Aten, R. E., 1965b, Natural recharge and localization of fresh ground water in Kuwait: Journal of Hydrology, v. 2, no. 3, p. 213-231.

Beutner, E. L., Gaebe, R. R., and Horton, R. E., 1940, Sprinkled-Plat Runoff-And Infiltration-Experiments On Arizona Desert-Soils: Eos, Transactions American Geophysical Union, v. 21, no. 2, p. 550-558.

Bhandary, H., Al-Senafy, M., and Marzouk, F., 2015, Usage of carbon isotopes in characterizing groundwater age, flow direction, flow velocity and recharge area: Procedia Environmental Sciences, v. 25, p. 28-35.

Bioregional Assessment Program, 2019, Classified depth to water table for the Great Artesian Basin: Bioregional Assessment Program, Canberra, Australia, http://data.bioregionalassessments.gov.au/dataset/6eabd9e1-0018-4314-bba4-87d5d1ebc8c3.

Bish, D. L., Blake, D., Vaniman, D., Chipera, S., Morris, R., Ming, D., Treiman, A., Sarrazin, P., Morrison, S., and Downs, R. T., 2013, X-ray diffraction results from Mars Science Laboratory: Mineralogy of Rocknest at Gale crater: science, v. 341, no. 6153, p. 1238932.

Bishop, M. A., 2001, Seasonal variation of crescentic dune morphology and morphometry, Strzelecki–Simpson Desert, Australia: Earth Surface Processes and Landforms: The Journal of the British Geomorphological Research Group, v. 26, no. 7, p. 783-791.

Bond, G., Kromer, B., Beer, J., Muscheler, R., Evans, M. N., Showers, W., Hoffmann, S., Lotti-Bond, R., Hajdas, I., and Bonani, G., 2001, Persistent solar influence on North Atlantic climate during the Holocene: science, v. 294, no. 5549, p. 2130-2136.

Bourke, M. C., Lancaster, N., Fenton, L. K., Parteli, E. J., Zimbelman, J. R., and Radebaugh, J., 2010, Extraterrestrial dunes: An introduction to the special issue on planetary dune systems: Geomorphology, v. 121, no. 1-2, p. 1-14.

Bouwer, H., 1962, Main content area Analyzing ground-water mounds by resistance network: Journal of irrigation and drainage engineering, v. 88, no. 3 pt 1, p. 15-26.

Brakenridge, G. R., 1978, Evidence for a Cold, Dry Full-Glacial Climate in the American Southwest: Quaternary Research, v. 9, no. 1, p. 22-40.

Bristow, C., Jones, B. G., Nanson, G., Hollands, C., Coleman, M., and Price, D., 2007, GPR surveys of vegetated linear dune stratigraphy in central Australia: Evidence for linear dune extension with vertical and lateral accretion: Geological Society of America Special Papers, v. 432, p. 19-33.

Brown, D. A., Campbell, K. S. W., and Crook, K. A. W., 1968, Chapter 11 - The Tertiary System, The Geological Evolution of Australia and New Zealand, Pergamon, p. 294-337.

Brown, G., and Brindley, G., 1980, X-ray diffraction procedures for clay mineral identification: Crystal structures of clay minerals and their X-ray identification, v. 5, p. 305-359.

Buckley, R., 1981, Soils and vegetation of central Australian sandridges III. Sandridge vegetation of the Simpson Desert: Australian Journal of Ecology, v. 6, no. 4, p. 405-422.

Bullard, J. E., and Livingstone, I., 2002, Interactions between aeolian and fluvial systems in dryland environments: Area, v. 34, no. 1, p. 8-16.

Caldwel, L. T., 1969, Groundwater Geology of Alluvial Fan Aquifers Located in the Western Third of the Gwydir River Valley, New South Wales, Australia: JAWRA Journal of the American Water Resources Association, v. 5, no. 3, p. 3-17.

Carol, E., Kruse, E., and Roig, A., 2010, Groundwater travel time in the freshwater lenses of Samborombón Bay, Argentina: Hydrological sciences journal, v. 55, no. 5, p. 754-762.

Carr, M. H., 1974, Tectonism and volcanism of the Tharsis region of Mars: Journal of Geophysical Research, v. 79, no. 26, p. 3943-3949.

Carr, M. H., 1986, Mars: A water-rich planet?: Icarus, v. 68, no. 2, p. 187-216.

Cellone, F., Tosi, L., and Carol, E., 2018, Estimating the freshwater-lens reserve in the coastal plain of the middle Río de la Plata Estuary (Argentina): Science of The Total Environment, v. 630, p. 357-366.

Cendón, D. I., Larsen, J. R., Jones, B. G., Nanson, G. C., Rickleman, D., Hankin, S. I., Pueyo, J. J., and Maroulis, J., 2010, Freshwater recharge into a shallow saline groundwater system, Cooper Creek floodplain, Queensland, Australia: Journal of Hydrology, v. 392, no. 3-4, p. 150-163.

CGIAR-CSI, 2009, CGIAR-CSI Global-Aridity and Global-PET Database, Washington, DC, https://cgiarcsi.community/data/global-aridity-and-pet-database/.

Chang, Y., Hu, B. X., Xu, Z., Li, X., Tong, J., Chen, L., Zhang, H., Miao, J., Liu, H., and Ma, Z., 2018, Numerical simulation of seawater intrusion to coastal aquifers and brine water/freshwater interaction in south coast of Laizhou Bay, China: Journal of Contaminant Hydrogelogy, v. 215, p. 1-10.

Chesnaux, R., and Allen, D., 2008, Groundwater travel times for unconfined island aquifers bounded by freshwater or seawater: Hydrogeology Journal, v. 16, no. 3, p. 437-445.

Chowdhury, A., Jha, M. K., and Chowdary, V. M., 2010, Delineation of groundwater recharge zones and identification of artificial recharge sites in West Medinipur district, West Bengal, using RS, GIS and MCDM techniques: Environmental Earth Sciences, v. 59, no. 6, p. 1209.

Christellis, G., Struckmeier, W., and Baumie, R., 2001, Groundwater in Namibia: an explanation to the hydroegeological map.

Christensen, P., Bandfield, J., Clark, R., Edgett, K., Hamilton, V., Hoefen, T., Kieffer, H., Kuzmin, R., Lane, M., and Malin, M., 2000, Detection of crystalline hematite mineralization on Mars by the Thermal Emission Spectrometer: Evidence for near-surface water: Journal of Geophysical Research: Planets, v. 105, no. E4, p. 9623-9642.

Christensen, P., Morris, R., Lane, M., Bandfield, J., and Malin, M., 2001, Global mapping of Martian hematite mineral deposits: Remnants of water-driven processes on early Mars: Journal of Geophysical Research: Planets, v. 106, no. E10, p. 23873-23885.

Cisneros, J., 2014, Morphologic and computational fluid dynamic analysis of sand dune-topographic obstacle interactions on Earth and Titan.

Clifford, S. M., 1993, A model for the hydrologic and climatic behavior of water on Mars: Journal of Geophysical Research: Planets, v. 98, no. E6, p. 10973-11016.

Cluff, C. B., 1990, Kuwait Water Harvesting System: Final Report: Water Resources Research Center, Water Resources Research Center, University of Arizona.

Cohen, T. J., Nanson, G. C., Jansen, J. D., Jones, B. G., Jacobs, Z., Treble, P., Price, D. M., May, J.-H., Smith, A. M., and Ayliffe, L. K., 2011, Continental aridification and the vanishing of Australia's megalakes: Geology, v. 39, no. 2, p. 167-170.

Cohen, T. J., Nanson, G. C., Larsen, J. R., Jones, B., Price, D. M., Coleman, M., and Pietsch, T., 2010, Late Quaternary aeolian and fluvial interactions on the Cooper Creek Fan and the association between linear and source-bordering dunes, Strzelecki Desert, Australia: Quaternary Science Reviews, v. 29, no. 3-4, p. 455-471.

Covino, T., 2017, Hydrologic connectivity as a framework for understanding biogeochemical flux through watersheds and along fluvial networks: Geomorphology, v. 277, p. 133-144.

Craddock, R. A., 2011, Aeolian processes on the terrestrial planets: Recent observations and future focus: Progress in Physical Geography, v. 36, no. 1, p. 110-124.

Craddock, R. A., 2012, Aeolian processes on the terrestrial planets: Recent observations and future focus: Progress in Physical Geography, v. 36, no. 1, p. 110-124.

Craddock, R. A., and Howard, A. D., 2002, The case for rainfall on a warm, wet early Mars: Journal of Geophysical Research: Planets, v. 107, no. E11.

Craddock, R. A., Hutchinson, M. F., and Stein, J. A., 2010, Topographic data reveal a buried fluvial landscape in the Simpson Desert, Australia: Australian Journal of Earth Sciences, v. 57, no. 1, p. 141-149.

Craddock, R. A., Tooth, S., Zimbelman, J. R., Wilson, S. A., Maxwell, T. A., and Kling, C., 2015, Temporal observations of a linear sand dune in the Simpson Desert, central Australia: Testing models for dune formation on planetary surfaces: Journal of Geophysical Research: Planets, v. 120, no. 10, p. 1736-1750.

Crespin, I., and Evans, P. R., 1962, Cretaceous Microfossils from the Hay River Area Northern Territory: Bureau of Mineral Resources, Geology, and Geophysics, Bureau of Mineral Resources, Geology, and Geophysics, Canberra, Australia.

Critchley, W., Siegert, K., Chapman, C., and Finket, M., 2013, Water harvesting: A manual for the design and construction of water harvesting schemes for plant production, Scientific Publishers.

Dagan, G., 1967, Linearized solutions of free-surface groundwater flow with uniform recharge: Journal of Geophysical Research, v. 72, no. 4, p. 1183-1193.

Dailey, D., Sauck, W., Sultan, M., Milewski, A., Ahmed, M., Laton, W., Elkadiri, R., Foster, J., Schmidt, C., and Al Harbi, T., 2015, Geophysical, remote sensing, GIS, and isotopic applications for a better understanding of the structural controls on groundwater flow in the Mojave Desert, California: Journal of Hydrology: Regional Studies, v. 3, p. 211-232.

Davidson, I., 1999, First People Becoming Australian: Anthropologie, v. 37, no. 2, p. 125-141.

Davis, J., Balme, M., Grindrod, P., Williams, R., and Gupta, S., 2016, Extensive Noachian fluvial systems in Arabia Terra: Implications for early Martian climate: Geology, v. 44, no. 10, p. 847-850.

Davis, J. M., Gupta, S., Balme, M., Grindrod, P. M., Fawdon, P., Dickeson, Z. I., and Williams, R. M. E., 2019, A Diverse Array of Fluvial Depositional Systems in Arabia Terra: Evidence for mid-Noachian to Early Hesperian Rivers on Mars: Journal of Geophysical Research: Planets, v. 124, no. 7, p. 1913-1934.

Din, S. U., Al Dousari, A., and Al Ghadban, A. N., 2007, Sustainable freshwater resources management in northern Kuwait—A remote sensing view from Raudatain basin: International journal of applied earth observation and geoinformation, v. 9, no. 1, p. 21-31.

Doherty, J., 2004, PEST model-independent parameter estimation user manual: Watermark Numerical Computing, Brisbane, Australia, v. 3338, p. 3349.

Dose, E. J., Stoeckl, L., Houben, G. J., Vacher, H. L., Vassolo, S., Dietrich, J., and Himmelsbach, T., 2014, Experiments and modeling of freshwater lenses in layered aquifers: Steady state interface geometry: Journal of Hydrology, v. 509, no. 0, p. 621-630.

Duguid, A., 2011, Wetlands of the Great Artesian Basin Water Control District (Northern Territory): Northern Territory Government Department of Natural Resources, Environment, the Arts and Sport, Northern Territory Government Department of Natural Resources, Environment, the Arts and Sport, Alice Springs.

Dupuit, J. E. J., 1863, Études théoriques et pratiques sur le mouvement des eaux dans les canaux découverts et à travers les terrains perméables., Paris, France, Librairie des Corps Impérial des Ponts et Chaussées et des Mines.

Eeman, S., Leijnse, A., Raats, P. A. C., and van der Zee, S. E. A. T. M., 2011, Analysis of the thickness of a freshwater lens and of the transition zone between this lens and upwelling saline water: Advances in Water Resources, v. 34, no. 2, p. 291-302.

Ehlmann, B. L., and Edwards, C. S., 2014, Mineralogy of the Martian surface: Annual Review of Earth and Planetary Sciences, v. 42, p. 291-315.

Ehtiat, M., Mousavi, S. J., and Srinivasan, R., 2018, Groundwater Modeling Under Variable Operating Conditions Using SWAT, MODFLOW and MT3DMS: a Catchment Scale Approach to Water Resources Management: Water Resources Management, p. 1-19.

El-Baz, F., Maingue, M., and Robinson, C., 2000, Fluvio-aeolian dynamics in the north-eastern Sahara: the relationship between fluvial/aeolian systems and ground-water concentration: Journal of Arid Environments, v. 44, no. 2, p. 173-183.

El-Ghani, M. M. A., Huerta-Martínez, F. M., Hongyan, L., and Qureshi, R., 2017, Plant responses to hyperarid desert environments, Springer.

El-Sayed, M., 1999, Sedimentological characteristics and morphology of the aeolian sand dunes in the eastern part of the UAE, a case study from Ar Rub'Al Khali: Sedimentary Geology, v. 123, no. 3-4, p. 219-238.

El-Baz, F., Breed, C., Grolier, M., and McCauley, J., 1979, Eolian features in the western desert of Egypt and some applications to Mars: Journal of Geophysical Research: Solid Earth, v. 84, no. B14, p. 8205-8221.

Ely, L. L., Enzel, Y., Baker, V. R., and Cayan, D. R., 1993, A 5000-year record of extreme floods and climate change in the southwestern United States: Science, v. 262, no. 5132, p. 410-412.

English, P., Spooner, N. A., Chappell, J., Questiaux, D. G., and Hill, N. G., 2001, Lake Lewis basin, central Australia: environmental evolution and OSL chronology: Quaternary International, v. 83-85, p. 81-101.

Exon, N. F., and Senior, B. R., 1976, The Cretaceous of the Eromanga and Surat Basins: Journal of Australian Geology and Geophysics, v. 1, p. 33-50.

Fadlelmawla, A., Hadi, K., Zouari, K., and Kulkarni, K., 2008, Hydrogeochemical investigations of recharge and subsequent salinization processes at Al-Raudhatain depression in Kuwait/Analyses hydrogéochimiques de la recharge et des processus associés de salinisation dans la dépression de Al-Raudhatain au Koweit: Hydrological sciences journal, v. 53, no. 1, p. 204-223.

Fairén, A. G., Dohm, J. M., Baker, V. R., de Pablo, M. A., Ruiz, J., Ferris, J. C., and Anderson, R. C., 2003, Episodic flood inundations of the northern plains of Mars: Icarus, v. 165, no. 1, p. 53-67.

Farr, A. M., Houghtalen, R., and McWhorter, D., 1990, Volume estimation of light nonaqueous phase liquids in porous media: Ground Water, v. 28, no. 1, p. 48-56.

Fetter, C., 1972, Position of the saline water interface beneath oceanic islands: Water Resources Research, v. 8, no. 5, p. 1307-1315.

Fetter, C. W., 1988, Applied hydrogeology, Columbus, Ohio, Merrill Publishing Company.

Field, J. P., Breshears, D. D., and Whicker, J. J., 2009, Toward a more holistic perspective of soil erosion: Why aeolian research needs to explicitly consider fluvial processes and interactions: Aeolian Research, v. 1, no. 1, p. 9-17.

Fitzsimmons, K. E., Bowler, J. M., Rhodes, E. J., and Magee, J. M., 2007, Relationships between desert dunes during the late Quaternary in the Lake Frome region, Strzelecki Desert, Australia: Journal of Quaternary Science, v. 22, no. 5, p. 549-558.

Fleskens, L., Ataev, A., Mamedov, B., and Spaan, W., 2007, Desert water harvesting from takyr surfaces: assessing the potential of traditional and experimental technologies in the Karakum: Land Degradation & Development, v. 18, no. 1, p. 17-39.

Folk, R. L., 1971, Longitudinal dunes of the northwestern edge of the Simpson Desert, Northern Territory, Australia, 1. Geomorphology and grain size relationships: Sedimentology, v. 16, no. 1-2, p. 5-54.

Folk, R. L., 1976, Reddening of desert sands; Simpson Desert, NT, Australia: Journal of Sedimentary Research, v. 46, no. 3, p. 604-615.

Foster, S., and Loucks, D. P., 2006, Non-renewable groundwater resources: United Nations Educational, Scientific and Cultural Organization (UNESCO), United Nations Educational, Scientific and Cultural Organization (UNESCO), Paris, France.

Freeze, R. A., 1969, The Mechanism of Natural Ground-Water Recharge and Discharge: 1. One-dimensional, Vertical, Unsteady, Unsaturated Flow above a Recharging or Discharging Ground-Water Flow System: Water Resources Research, v. 5, no. 1, p. 153-171.

Freeze, R. A., 1971, Three-Dimensional, Transient, Saturated-Unsaturated Flow in a Groundwater Basin: Water Resources Research, v. 7, no. 2, p. 347-366.

Freeze, R. A., 1979, Groundwater.

Fujioka, T., Chappell, J., Fifield, L. K., and Rhodes, E. J., 2009, Australian desert dune fields initiated with Pliocene–Pleistocene global climatic shift: Geology, v. 37, no. 1, p. 51-54.

Gee, G. W., and Hillel, D., 1988, Groundwater recharge in arid regions: review and critique of estimation methods: Hydrological Processes, v. 2, no. 3, p. 255-266.

Glover, R., 1959, The pattern of fresh-water flow in a coastal aquifer: Journal of Geophysical Research, v. 64, no. 4, p. 457-459.

Golombek, M., and Rapp, D., 1997, Size-frequency distributions of rocks on Mars and Earth analog sites: Implications for future landed missions: Journal of Geophysical Research: Planets, v. 102, no. E2, p. 4117-4129.

Goudie, A., 1991, Pans: Progress in Physical Geography, v. 15, no. 3, p. 221-237.

Goudie, A., Stokes, S., Livingstone, I., Bailiff, I., and Allison, R., 1993, Post-depositional modification of the linear sand ridges of the West Kimberley area of north-west Australia: Geographical Journal, p. 306-317.

Gough, D., 1981, Solar interior structure and luminosity variations, Physics of Solar Variations, Springer, p. 21-34.

Grasby, S., Bezys, R., and Beauchamp, B., 2009, Silica chimneys formed by low-temperature brine spring discharge: Astrobiology, v. 9, no. 10, p. 931-941.

Greeley, R., and Iversen, J. D., 1987, Wind as a geological process: on Earth, Mars, Venus and Titan, CUP Archive.

Greeley, R., and Spudis, P. D., 1981, Volcanism on Mars: Reviews of Geophysics, v. 19, no. 1, p. 13-41.

Greenville, A. C., Wardle, G. M., and Dickman, C. R., 2012, Extreme climatic events drive mammal irruptions: regression analysis of 100-year trends in desert rainfall and temperature: Ecology and evolution, v. 2, no. 11, p. 2645-2658.

Grott, M., Hauber, E., Werner, S. C., Kronberg, P., and Neukum, G., 2007, Mechanical modeling of thrust faults in the Thaumasia region, Mars, and implications for the Noachian heat flux: Icarus, v. 186, no. 2, p. 517-526.

Grotzinger, J. P., Arvidson, R. E., Bell, J. F., Calvin, W., Clark, B. C., Fike, D. A., Golombek, M., Greeley, R., Haldemann, A., Herkenhoff, K. E., Jolliff, B. L., Knoll, A. H., Malin, M., McLennan, S. M., Parker, T., Soderblom, L., Sohl-Dickstein, J. N., Squyres, S. W., Tosca, N. J., and Watters, W. A., 2005, Stratigraphy and sedimentology of a dry to wet eolian depositional system, Burns formation, Meridiani Planum, Mars: Earth and Planetary Science Letters, v. 240, no. 1, p. 11-72.

Gulick, V. C., 1998, Magmatic intrusions and a hydrothermal origin for fluvial valleys on Mars: Journal of Geophysical Research: Planets, v. 103, no. E8, p. 19365-19387.

Guo, W., and Langevin, C. D., 2002, User's guide to SEAWAT; a computer program for simulation of three-dimensional variable-density ground-water flow.

Habermehl, M. A., 1982, Investigations of the Geology and Hydrology of the Great Artesian Basin, 1878-1980, Bureau of Mineral Resources, Geology and Geophysics.

Hadi, K., and Al-Ruwaih, F., 2008, Geochemical Evolution of the Fresh Groundwater in Kuwait Desert.

Hansen, J., Sato, M., Russell, G., and Kharecha, P., 2013, Climate sensitivity, sea level and atmospheric carbon dioxide: Philosophical Transactions of the Royal Society A: Mathematical, Physical and Engineering Sciences, v. 371, no. 2001, p. 20120294.

Hantush, M. S., 1967, Growth and decay of groundwater-mounds in response to uniform percolation: Water Resources Research, v. 3, no. 1, p. 227-234.

Harbaugh, A. W., Banta, E. R., Hill, M. C., and McDonald, M. G., 2000, MODFLOW-2000, The U. S. Geological Survey Modular Ground-Water Model-User Guide to Modularization Concepts and the Ground-Water Flow Process: Open-file Report. U. S. Geological Survey, no. 92, p. 134.

Hartmann, W., 2005, Adventures (Arrrggghh!) in Crater Counting: Small Crater Controversies: LPI, p. 1427.

Hayes, A., Birch, S., Dietrich, W., Howard, A., Kirk, R., Poggiali, V., Mastrogiuseppe, M., Michaelides, R., Corlies, P., and Moore, J., 2017, Topographic constraints on the evolution and connectivity of Titan's lacustrine basins: Geophysical Research Letters, v. 44, no. 23.

Heggy, E., 2018, Probing groundwater in arid environments: challenges and opportunities south of the Mediterranean basin, Springer.

Henry, H. R., 1959, Salt intrusion into fresh-water aquifers: Journal of Geophysical Research, v. 64, no. 11, p. 1911-1919.

Henry, H. R., 1964, Interfaces between salt water and freshwater in coastal aquifers: US Geological Survey Water-Supply Paper, p. C35-70.

Herzberg, A., 1901, Die Wasserversorgung einiger Nordseebäder, v. 44, p. 815-819; 842-844.

Hesp, P., Hyde, R., Hesp, V., and Zhengyu, Q., 1989, Longitudinal dunes can move sideways: Earth Surface Processes and Landforms, v. 14, no. 5, p. 447-451.

Hesse, P. P., and Simpson, R. L., 2006, Variable vegetation cover and episodic sand movement on longitudinal desert sand dunes: Geomorphology, v. 81, no. 3-4, p. 276-291.

Hesse, P. P., Telfer, M. W., and Farebrother, W., 2017, Complexity confers stability: Climate variability, vegetation response and sand transport on longitudinal sand dunes in Australia's deserts: Aeolian Research, v. 25, p. 45-61.

Himida, I. H., 1981, Groundwater in Kuwait and the Environmental Factors Affecting its Quality: Studies in Environmental Science, v. 17, p. 121-124.

Hoekstra, T. W., and Shachak, M., 1999, Arid lands management: toward ecological sustainability, University of Illinois Press.

Hoffman, P. F., Kaufman, A. J., Halverson, G. P., and Schrag, D. P., 1998, A Neoproterozoic snowball earth: science, v. 281, no. 5381, p. 1342-1346.

Hoke, M. R., Hynek, B. M., and Tucker, G. E., 2011, Formation timescales of large Martian valley networks: Earth and Planetary Science Letters, v. 312, no. 1-2, p. 1-12.

Hollands, C. B., Nanson, G. C., Jones, B. G., Bristow, C. S., Price, D. M., and Pietsch, T. J., 2006, Aeolian–fluvial interaction: evidence for Late Quaternary channel change and wind-rift linear dune formation in the northwestern Simpson Desert, Australia: Quaternary Science Reviews, v. 25, no. 1, p. 142-162.

Holt, T., Greskowiak, J., Seibert, S. L., and Massmann, G., 2019, Modeling the Evolution of a Freshwater Lens under Highly Dynamic Conditions on a Currently Developing Barrier Island: Geofluids, v. 2019, p. 15.

Holzbecher, E. O., 1998, Modeling density-driven flow in porous media: principles, numerics, software, Springer Science & Business Media.

Hooke, R. L., 1967, Processes on arid-region alluvial fans: The Journal of Geology, v. 75, no. 4, p. 438-460.

Horton, R. E., 1933, The role of infiltration in the hydrologic cycle: Eos, Transactions American Geophysical Union, v. 14, no. 1, p. 446-460.

Horvath, D. G., and Andrews-Hanna, J. C., 2017, Reconstructing the past climate at Gale crater, Mars, from hydrological modeling of late-stage lakes: Geophysical Research Letters, v. 44, no. 16, p. 8196-8204.

Houben, G., Noell, U., Vassolo, S., Grissemann, C., Geyh, M., Stadler, S., Dose, E. J., and Vera, S., 2014, The freshwater lens of Benjamín Aceval, Chaco, Paraguay: a terrestrial analogue of an oceanic island lens: Hydrogeology journal, v. 22, no. 8, p. 1935-1952.

Howard, A. D., Moore, J. M., and Irwin III, R. P., 2005, An intense terminal epoch of widespread fluvial activity on early Mars: 1. Valley network incision and associated deposits: Journal of Geophysical Research: Planets, v. 110, no. E12.

Howe, G. M., Reed, L. J., Ball, J. T., Fisher, G. E., and Lassow, G. B., 1968, Classification of world desert areas: Travelers Research Center, Inc., Travelers Research Center, Inc., Hartford, Connecticut.

Hubbert, M. K., 1940, The Theory of Ground-Water Motion: The Journal of Geology, v. 48, no. 8, Part 1, p. 785-944.

Huffman, G. J., Bolvin, D. T., Braithwaite, D., Hsu, K., Joyce, R., Xie, P., and Yoo, S.-H., 2015, NASA global precipitation measurement (GPM) integrated multi-satellite retrievals for GPM (IMERG): Algorithm Theoretical Basis Document (ATBD) Version, v. 4, p. 26.

Huntley, D. J., Godfrey-Smith, D. I., and Thewalt, M. L., 1985, Optical dating of sediments: Nature, v. 313, no. 5998, p. 105.

Hynek, B. M., Beach, M., and Hoke, M. R., 2010, Updated global map of Martian valley networks and implications for climate and hydrologic processes: Journal of Geophysical Research: Planets, v. 115, no. E9.

Ingersoll, R. V., 1988, Tectonics of sedimentary basins: GSA Bulletin, v. 100, no. 11, p. 1704-1719.

Irwin, R. P., Howard, A. D., and Craddock, R. A., 2008, Fluvial valley networks on Mars: River confluences, tributaries and the fluvial network, p. 419.

Irwin, R. P., Howard, A. D., Craddock, R. A., and Moore, J. M., 2005, An intense terminal epoch of widespread fluvial activity on early Mars: 2. Increased runoff and paleolake development: Journal of Geophysical Research: Planets, v. 110, no. E12.

Jacob, C. E., 1943, Correlation of ground-water levels and precipitation on Long Island, New York: Eos, Transactions American Geophysical Union, v. 24, no. 2, p. 564-573.

James, W. P., Chakka, K. B., and Masciangliolí, P. A., 1996, Control of Natural Brine Springs in Brazos River Basin Part I:: Recovery System 1: JAWRA Journal of the American Water Resources Association, v. 32, no. 3, p. 475-484.

Jayawickreme, D. H., Santoni, C. S., Kim, J. H., Jobbágy, E. G., and Jackson, R. B., 2011, Changes in hydrology and salinity accompanying a century of agricultural conversion in Argentina: Ecological Applications, v. 21, no. 7, p. 2367-2379.

Jenny, H., and Smith, G. D., 1935, Colloid chemical aspects of clay pan formation in soil profiles: Soil Science, v. 39, no. 5, p. 377-390.

Johnsen, S. J., Dahl-Jensen, D., Gundestrup, N., Steffensen, J. P., Clausen, H. B., Miller, H., Masson-Delmotte, V., Sveinbjörnsdottir, A. E., and White, J., 2001, Oxygen isotope and palaeotemperature records from six Greenland ice-core stations: Camp Century, Dye-3, GRIP, GISP2, Renland and NorthGRIP: Journal of Quaternary Science: Published for the Quaternary Research Association, v. 16, no. 4, p. 299-307.

Kacimov, A., and Obnosov, Y. V., 2019, Analytic solutions for fresh groundwater lenses floating on saline water under desert dunes: The Kunin-Van Der Veer legacy revisited: Journal of Hydrology, v. 574, p. 733-743.

Kalma, J. D., and Franks, S. W., 2003, Rainfall in arid and semi-arid regions, Understanding water in a dry environment, CRC Press, p. 31-80.

Keske, A. L., Hamilton, C. W., McEwen, A. S., and Daubar, I. J., 2015, Episodes of fluvial and volcanic activity in Mangala Valles, Mars: Icarus, v. 245, p. 333-347.

King, D., 1960, The sand ridge deserts of South Australia and related aeolian landforms of the Quaternary arid cycles: Transactions of the Royal Society of South Australia, v. 83, p. 99-108.

Klein, J. T., and Newell, W. H., 1997, Advancing interdisciplinary studies: Handbook of the undergraduate curriculum: A comprehensive guide to purposes, structures, practices, and change, p. 393-415.

Klimczak, C., Kling, C. L., and Byrne, P. K., Growth and Structural Style of Thrust Systems on Mars, *in* Proceedings European Planetary Science Congress2018, Volume 12.

Knauth, L. P., and Lowe, D. R., 1978, Oxygen isotope geochemistry of cherts from the Onverwacht Group (3.4 billion years), Transvaal, South Africa, with implications for secular variations in the isotopic composition of cherts: Earth and Planetary Science Letters, v. 41, no. 2, p. 209-222.

Knighton, D., 1998, Fluvial forms and processes: a new perspective, Routledge.

Konikow, L. F., Akhavan, M., Langevin, C., Michael, H., and Sawyer, A., 2013, Seawater circulation in sediments driven by interactions between seabed topography and fluid density: Water Resources Research, v. 49, no. 3, p. 1386-1399.

Koohafkan, P., and Stewart, B. A., 2008, Drylands, people and land use: Food and Agriculture Organization, Food and Agriculture Organization.

Kottek, M., Grieser, J., Beck, C., Rudolf, B., and Rubel, F., 2006, World map of the Köppen-Geiger climate classification updated: Meteorologische Zeitschrift, v. 15, no. 3, p. 259-263.

Kuhlman, K., Marshall, J., Evans, N., and Luttge, A., 2001, Australian red dune sand: A potential Martian regolith analog: Lunar and Planetary Institute, v. 1101, Lunar and Planetary Institute, Houston, TX

Kuldzhayev, N. K., 1974, Origin of the Yaskhan freshwater lens in Karakumy: International Geology Review, v. 16, no. 3, p. 247-254.

Kunin, V., 1968, The Study of Local Waters in Deserts of the USSR: Soviet Geography v. 9, no. 6, p. 469-488.

Kwarteng, A. Y., Viswanathan, M. N., Al-Senafy, M. N., and Rashid, T., 2000, Formation of fresh ground-water lenses in northern Kuwait: Journal of Arid Environments, v. 46, no. 2, p. 137-155.

Laattoe, T., Werner, A. D., Woods, J. A., and Cartwright, I., 2017, Terrestrial freshwater lenses: Unexplored subterranean oases: Journal of Hydrology, v. 553, p. 501-507.

Lancaster, I. N., 1978, The pans of the southern Kalahari, Botswana: Geographical Journal, p. 81-98.

Lancaster, J., Lancaster, N., and Seely, M. K., 1984, Climate of the central Namib Desert: Madoqua, v. 14, no. 1, p. 5-61.

Lancaster, N., 1982, Linear dunes: Progress in Physical Geography, v. 6, no. 4, p. 475-504.

Lancaster, N., 1986, Grain-size characteristics of linear dunes in the southwestern Kalahari: Journal of Sedimentary Research, v. 56, no. 3, p. 395-400.

Lancaster, N., 2006, Linear dunes on Titan: Science, v. 312, no. 5774, p. 702-703.

Langevin, C. D., Shoemaker, W. B., and Guo, W., 2003, MODFLOW-2000, the U.S. Geological Survey Modular Ground-Water Model--Documentation of the SEAWAT-2000 Version with the Variable-Density Flow Process (VDF) and the Integrated MT3DMS Transport Process (IMT), 2003-426.

Langevin, C. D., Thorne Jr, D. T., Dausman, A. M., Sukop, M. C., and Guo, W., 2008, SEAWAT version 4: a computer program for simulation of multi-species solute and heat transport: Geological Survey (US), 2328-7055, Geological Survey (US).

Langford, R. P., 1989, Fluvial-aeolian interactions: Part I, modern systems: Sedimentology, v. 36, no. 6, p. 1023-1035.

Lavé, J., and Avouac, J., 2001, Fluvial incision and tectonic uplift across the Himalayas of central Nepal: Journal of Geophysical Research: Solid Earth, v. 106, no. B11, p. 26561-26591.

Le, P. V., and Kumar, P., 2014, Power law scaling of topographic depressions and their hydrologic connectivity: Geophysical Research Letters, v. 41, no. 5, p. 1553-1559.

Lee, P., and Thomas, P. C., 1995, Longitudinal dunes on Mars: Relation to current wind regimes: Journal of Geophysical Research: Planets, v. 100, no. E3, p. 5381-5395.

Lewis, F. M., and Walker, G. R., 2002, Assessing the potential for significant and episodic recharge in southwestern Australia using rainfall data: Hydrogeology Journal, v. 10, no. 1, p. 229-237.

Lezzaik, K., and Milewski, A., 2018, A quantitative assessment of groundwater resources in the Middle East and North Africa region: Hydrogeology Journal, v. 26, no. 1, p. 251-266.

Lezzaik, K., Milewski, A., and Mullen, J., 2018, The groundwater risk index: Development and application in the Middle East and North Africa region: Science of The Total Environment, v. 628-629, p. 1149-1164.

Li, G., 2011, World atlas of oil and gas basins, John Wiley & Sons.

Li, K., Bai, Z., and Zhang, H., 2015, Community succession of bacteria and eukaryotes in dune ecosystems of Gurbantünggüt Desert, Northwest China: Extremophiles, v. 19, no. 1, p. 171-181.

Lian, O. B., 2007, LUMINESCENCE DATING | Optically-Stimulated Luminescence A2 - Elias, Scott A, Encyclopedia of Quaternary Science: Oxford, Elsevier, p. 1491-1505.

Liu, B., and Coulthard, T. J., 2015, Mapping the interactions between rivers and sand dunes: Implications for fluvial and aeolian geomorphology: Geomorphology, v. 231, p. 246-257.

Livingstone, I., Bristow, C., Bryant, R. G., Bullard, J., White, K., Wiggs, G. F., Baas, A. C., Bateman, M. D., and Thomas, D. S., 2010, The Namib Sand Sea digital database of aeolian dunes and key forcing variables: Aeolian Research, v. 2, no. 2-3, p. 93-104.

Lorenz, R. D., Mitchell, K. L., Kirk, R. L., Hayes, A. G., Aharonson, O., Zebker, H. A., Paillou, P., Radebaugh, J., Lunine, J. I., Janssen, M. A., Wall, S. D., Lopes, R. M., Stiles, B., Ostro, S., Mitri, G., and Stofan, E. R., 2008, Titan's inventory of organic surface materials: Geophysical Research Letters, v. 35, no. 2.

Maasland, M., 1959, Water table fluctuations induced by intermittent recharge: Journal of Geophysical Research, v. 64, no. 5, p. 549-559.

Maclay, R., and Small, T., 1983, Hydrostratigraphic subdivisions and fault barriers of the Edwards aquifer, south-central Texas, USA: Journal of Hydrology, v. 61, no. 1-3, p. 127-146.

Macumber, P. G., 2003, Lenses, plumes and wedges in the Sultanate of Oman: a challenge for groundwater management, Developments in Water Science, Volume 50, Elsevier, p. 349-370.

Madigan, C. T., 1946, Crossing the Dead Heart, Georgian House.

Magee, J. W., 2009, Palaeovalley groundwater resources in arid and semi-arid Australia: A literature review, Geoscience Australia.

Magee, J. W., Bowler, J. M., Miller, G. H., and Williams, D. L. G., 1995, Stratigraphy, sedimentology, chronology and palaeohydrology of Quaternary lacustrine deposits at Madigan Gulf, Lake Eyre, South Australia: Palaeogeography, Palaeoclimatology, Palaeoecology, v. 13, p. 3-42.

Mahmoud, M., Mohammed, S., Hamouda, M., and Mohamed, M., Temporal assessment of the GPM satellite rainfall products across extremely arid regions, *in* Proceedings E3S Web of Conferences2020, Volume 167, EDP Sciences, p. 02001.

Malin, M. C., Bell, J. F., Cantor, B. A., Caplinger, M. A., Calvin, W. M., Clancy, R. T., Edgett, K. S., Edwards, L., Haberle, R. M., and James, P. B., 2007, Context camera investigation on board the Mars Reconnaissance Orbiter: Journal of Geophysical Research: Planets, v. 112, no. E5.

Mangold, N., 2012, Fluvial landforms on fresh impact ejecta on Mars: Planetary and Space Science, v. 62, no. 1, p. 69-85.

Marcella, M. P., and Eltahir, E. A., 2008, The hydroclimatology of Kuwait: explaining the variability of rainfall at seasonal and interannual time scales: Journal of hydrometeorology, v. 9, no. 5, p. 1095-1105.

Matsubara, Y., Howard, A. D., and Gochenour, J. P., 2013, Hydrology of early Mars: Valley network incision: Journal of Geophysical Research: Planets, v. 118, no. 6, p. 1365-1387.

McEwen, A. S., Eliason, E. M., Bergstrom, J. W., Bridges, N. T., Hansen, C. J., Delamere, W. A., Grant, J. A., Gulick, V. C., Herkenhoff, K. E., and Keszthelyi, L., 2007, Mars reconnaissance orbiter's high resolution imaging science experiment (HiRISE): Journal of Geophysical Research: Planets, v. 112, no. E5.

McGill, G. E., 2000, Crustal history of north central Arabia Terra, Mars: Journal of Geophysical Research: Planets, v. 105, no. E3, p. 6945-6959.

McGill, G. E., 2002, Geologic map transecting the highland/lowland boundary zone, Arabia Terra, Mars; quadrangles 30332, 35332, 40332, and 45332: US Geological Survey, US Geological Survey.

Meigs, P., 1953, World distribution of arid and semi-arid homoclimates: Reviews of research on arid zone hydrology. Paris, UNESCO.

Meinzer, O. E., 1923, Outline of ground-water hydrology: US Geological Survey Water Supply Paper, v. 494, p. 5.

Milewski, A., Elkadiri, R., and Durham, M., 2015, Assessment and comparison of TMPA satellite precipitation products in varying climatic and topographic regimes in Morocco: Remote Sensing, v. 7, no. 5, p. 5697-5717.

Milewski, A., Sultan, M., Al-Dousari, A., and Yan, E., 2014a, Geologic and hydrologic settings for development of freshwater lenses in arid lands: Hydrological Processes, v. 28, no. 7, p. 3185-3194.

Milewski, A., Sultan, M., Al-Dousari, A., and Yan, E., 2014b, Geologic and hydrologic settings for development of freshwater lenses in arid lands: Hydrological processes, v. 28, no. 7, p. 3185-3194.

Miller, S. R., Baldwin, S. L., and Fitzgerald, P. G., 2012, Transient fluvial incision and active surface uplift in the Woodlark Rift of eastern Papua New Guinea: Lithosphere, v. 4, no. 2, p. 131-149.

Milton, D. I., 1968, Geology of the Arabian Peninsula; Kuwait: United States, U. S. Geological Survey : Reston, VA, United States.

Mond, A., and Yeates, A. N., 1973, Progress Report on Geological Mapping of the Northwestern Part of the Eromanga Basin, Northern Territory: Bureau of Mineral Resources, Geology, and Geophysics, v. 47, Bureau of Mineral Resources, Geology, and Geophysics, Canberra, Australia.

Moriasi, D. N., Arnold, J. G., Van Liew, M. W., Bingner, R. L., Harmel, R. D., and Veith, T. L., 2007, Model evaluation guidelines for systematic quantification of accuracy in watershed simulations: Transactions of the ASABE, v. 50, no. 3, p. 885-900.

Moscardelli, L., Dooley, T., Dunlap, D., Jackson, M., and Wood, L., 2012, Deep-water polygonal fault systems as terrestrial analogs for large-scale Martian polygonal terrains: GSA Today, v. 22, no. 8, p. 4-9.

Murray, G. W., 1955, Water from the desert: some ancient Egyptian achievements: The Geographical Journal, v. 121, no. 2, p. 171-181.

Nativ, R., 2004, Can the desert bloom? Lessons learned from the Israeli case: Groundwater, v. 42, no. 5, p. 651-657.

Neal, J. T., 1975, Playas and dried lakes, Dowden, Hutchinson & Ross.

Necea, D., Fielitz, W., Kadereit, A., Andriessen, P., and Dinu, C., 2013, Middle Pleistocene to Holocene fluvial terrace development and uplift-driven valley incision in the SE Carpathians, Romania: Tectonophysics, v. 602, p. 332-354.

Northern Territory Government of Australia, 2018, Hay River, Northern Territory: Northern Territory Geological Survey, scale 1:250 000.

Oberlander, P. L., 1989, Fluid Density and Gravitational Variations in Deep Boreholes and Their Effect on Fluid Potential: Groundwater, v. 27, no. 3, p. 341-350.

Omar, S., 1982, Artificial recharge into the Kuwait Group at Ar-Rawdhatain: M. Sc. Thesis, Loughborough University of Technology. Water quality trends and management of fresh groundwater 437.

Ostrovsky, V. N., 2007, Comparative analysis of groundwater formation in arid and super-arid deserts (with examples from Central Asia and Northeastern Arabian Peninsula): Hydrogeology Journal, v. 15, no. 4, p. 759-771.

Palumbo, A. M., Head, J. W., and Wordsworth, R. D., 2018, Late Noachian Icy Highlands climate model: Exploring the possibility of transient melting and fluvial/lacustrine activity through peak annual and seasonal temperatures: Icarus, v. 300, p. 261-286.

Parson's Corporation, L. A. C., 1961, Fresh ground-water resources, Rawdatain area, Kuwait : final report, Los Angeles, The Parson's Corporation

Parsons Engineering and Construction Corporation, 1961, Ground-water resources of Kuwait, Los Angeles, California.

Pell, S., Chivas, A., and Williams, I., 1999, Great Victoria Desert: development and sand provenance: Australian Journal of Earth Sciences, v. 46, no. 2, p. 289-299.

Pell, S. D., Chivas, A. R., and Williams, I. S., 2000, The Simpson, Strzelecki and Tirari Deserts: development and sand provenance: Sedimentary Geology, v. 130, no. 1, p. 107-130.

Penman, H. L., Natural evaporation from open water, bare soil and grass, *in* Proceedings Proc. R. Soc. Lond. A1948, Volume 193, The Royal Society, p. 120-145.

Pennink, J. M. K., 1915, Groundwater Stroombanen (Flowpaths): Stadsdrukkery Amsterdam.

Petit, J.-R., Jouzel, J., Raynaud, D., Barkov, N. I., Barnola, J.-M., Basile, I., Bender, M., Chappellaz, J., Davis, M., and Delaygue, G., 1999, Climate and atmospheric history of the past 420,000 years from the Vostok ice core, Antarctica: Nature, v. 399, no. 6735, p. 429.

Phelps, G., and Rohrer, K., 1987, Hydrogeology in the area of a freshwater lens in the Floridan aquifer system, northeast Seminole County, Florida.

Pieri, D. C., 1979, Geomorphology of Martian valleys.

Plunkett, I., 2020, Water in Aboriginal Art – the Centre of Life: Perth, Western Australia, Japingka Aboriginal Art.

Pollack, J. B., Kasting, J. F., Richardson, S. M., and Poliakoff, K., 1987, The case for a wet, warm climate on early Mars: Icarus, v. 71, no. 2, p. 203-224.

Poppe, L., Eliason, A., Fredericks, J., Rendigs, R., Blackwood, D., and Polloni, C., 2000, Grain size analysis of marine sediments: methodology and data processing: US Geological Survey East Coast sediment analysis: procedures, database, and georeferenced displays. US Geological Survey Open File Report 00-358. .

Pourghasemi, H. R., Sadhasivam, N., Yousefi, S., Tavangar, S., Nazarlou, H. G., and Santosh, M., 2020, Using machine learning algorithms to map the groundwater recharge potential zones: Journal of Environmental Management, v. 265, p. 110525.

Qahman, K., and Larabi, A., 2006, Evaluation and numerical modeling of seawater intrusion in the Gaza aquifer (Palestine): Hydrogeology Journal, v. 14, no. 5, p. 713-728.

Ramirez, R. M., and Craddock, R. A., 2018, The geological and climatological case for a warmer and wetter early Mars: Nature Geoscience, v. 11, no. 4, p. 230.

Randall, D., 2015, An introduction to the global circulation of the atmosphere, Princeton University Press.

Reeves Jr, C., 1966, Pluvial lake basins of West Texas: The Journal of Geology, v. 74, no. 3, p. 269-291.

Reid, I., and Frostick, L., 1997, Channel form, flows and sediments in deserts. Arid Zone Geomorphology: Process, Form and Change in Drylands, Thomas, DSG, John Wiley and Sons.

Rizk, Z., and Alsharhan, A., 2003, Water resources in the United Arab Emirates, 245-264 p.:

Robinson, B. W., and Al Ruwaih, F., 1985, The stable-isotopic composition of water and sulfate from the raudhatain and Umm Al Aish freshwater fields, Kuwait: Chemical Geology: Isotope Geoscience section, v. 58, no. 1-2, p. 129-136.

Rodriguez-Flores, J. L., Fakhro, K., Agosto-Perez, F., Ramstetter, M. D., Arbiza, L., Vincent, T. L., Robay, A., Malek, J. A., Suhre, K., and Chouchane, L., 2016, Indigenous Arabs are descendants of the earliest split from ancient Eurasian populations: Genome research, v. 26, no. 2, p. 151-162.

Rotz, R. R., and Milewski, A. M., 2019, Physical modeling of inland freshwater lens formation and evolution in drylands: Hydrogeology Journal, v. 27, no. 5, p. 1597-1610.

Royal Geographical Society, 1929, Proceedings of the Royal Geographical Society of Australasia : South Australian Branch: Royal Geographical Society of Australasia (South Australian Branch), v. 30, Royal Geographical Society of Australasia (South Australian Branch), Adelaide.

Royer, D. L., Berner, R. A., and Beerling, D. J., 2001, Phanerozoic atmospheric CO2 change: evaluating geochemical and paleobiological approaches: Earth-Science Reviews, v. 54, no. 4, p. 349-392.

Rubin, D. M., 1990, Lateral migration of linear dunes in the Strzelecki desert, Australia: Earth Surface Processes and Landforms, v. 15, no. 1, p. 1-14.

Rubin, D. M., and Hunter, R. E., 1985, Why deposits of longitudinal dunes are rarely recognized in the geologic record: Sedimentology, v. 32, no. 1, p. 147-157.

Sagintayev, Z., Sultan, M., Khan, S., Khan, S., Mahmood, K., Yan, E., Milewski, A., and Marsala, P., 2012, A remote sensing contribution to hydrologic modelling in arid and inaccessible watersheds, Pishin Lora basin, Pakistan: Hydrological Processes, v. 26, no. 1, p. 85-99.

Saleh, A., Al-Ruwaih, F., and Shehata, M., 1999, Hydrogeochemical processes operating within the main aquifers of Kuwait: Journal of Arid Environments, v. 42, no. 3, p. 195-209.

Salese, F., Pondrelli, M., Neeseman, A., Schmidt, G., and Ori, G. G., 2019, Geological evidence of planet-wide groundwater system on Mars: Journal of Geophysical Research: Planets, v. 124, no. 2, p. 374-395.

Scanlon, B. R., Keese, K. E., Flint, A. L., Flint, L. E., Gaye, C. B., Edmunds, W. M., and Simmers, I., 2006, Global synthesis of groundwater recharge in semiarid and arid regions: Hydrological Processes: An International Journal, v. 20, no. 15, p. 3335-3370.

Schneider, J. C., and Kruse, S. E., 2006, Assessing selected natural and anthropogenic impacts on freshwater lens morphology on small barrier Islands: Dog Island and St. George Island, Florida, USA: Hydrogeology Journal, v. 14, no. 1, p. 131-145.

Scholten, F., Gwinner, K., Roatsch, T., Matz, K.-D., Wählisch, M., Giese, B., Oberst, J., Jaumann, R., and Neukum, G., 2005, Mars Express HRSC data processing–Methods and operational aspects: Photogrammetric Engineering & Remote Sensing, v. 71, no. 10, p. 1143-1152.

Schroth, M., Istok, J., Ahearn, S., and Selker, J., 1995, Geometry and position of light nonaqueous-phase liquid lenses in water-wetted porous media: Journal of Contaminant Hydrology, v. 19, no. 4, p. 269-287.

Schultz, R. A., 2003, Seismotectonics of the Amenthes Rupes thrust fault population, Mars: Geophysical research letters, v. 30, no. 6.

Senay, Y., 1977, Groundwater resources and artificial recharge in Rawdhatain water field, 35, Ministry of Electricity and Water, Kuwait City, Kuwait.

Senger, R. K., and Fogg, G. E., 1990, Stream functions and equivalent freshwater heads for modeling regional flow of variable-density groundwater: 1. Review of theory and verification: Water Resources Research, v. 26, no. 9, p. 2089-2096.

Servant, M., 1973, Le Cénozoïque supérieur du Bassin du Tchad: Sé-quences continentales et variations climatiques: These d'Etudes, Paris.

Seyoum, W. M., and Milewski, A. M., 2016, Monitoring and comparison of terrestrial water storage changes in the northern high plains using GRACE and in-situ based integrated hydrologic model estimates: Advances in Water Resources, v. 94, p. 31-44.

Seyoum, W. M., and Milewski, A. M., 2017, Improved methods for estimating local terrestrial water dynamics from GRACE in the Northern High Plains: Advances in water resources, v. 110, p. 279-290.

Shanafield, M., Papageorgiou, A. W., and Arkwright, J. W., 2019, A visual approach to demonstrate groundwater flow processes: Hydrological Processes, v. 33, no. 25, p. 3236-3238.

Shanan, L., 2000, Runoff, erosion, and the sustainability of ancient irrigation systems in the Central Negev desert: IAHS PUBLICATION, p. 75-106.

Sharon, D., 1981, The distribution in space of local rainfall in the Namib Desert: Journal of Climatology, v. 1, no. 1, p. 69-75.

Shevchenko, N., 1963, Large freshwater lenses in the deserts of Turkmenistan: Freshwater lenses in a desert (in Russian). Academy of Sciences of the USSR, Moscow, p. 24-94.

Smedley, R. K., 2018, Telling the time with dust, sand and rocks: Elements: An International Magazine of Mineralogy, Geochemistry, and Petrology, v. 14, no. 1, p. 9-14.

Smerdon, B., Ransley, T., Radke, B., and Kellett, J., 2012, Water resource assessment for the Great Artesian Basin. A report to the Australian government from the CSIRO Great Artesian Basin water resource assessment, CSIRO Water for a Healthy Country Flagship, Australia, p. 3.

Squyres, S. W., and Carr, M. H., 1986, Geomorphic evidence for the distribution of ground ice on Mars: Science, v. 231, no. 4735, p. 249-252.

Stephen, J., 2005, Aridity Indexes, *in* Oliver, J. E., ed., Encyclopedia of World Climatology: Dordrecht, Springer Netherlands, p. 89-94.

Stoeckl, L., and Houben, G., 2012, Flow dynamics and age stratification of freshwater lenses: Experiments and modeling: Journal of Hydrology, v. 458–459, no. 0, p. 9-15.

Stoeckl, L., Walther, M., and Graf, T., 2016, A new numerical benchmark of a freshwater lens: Water Resources Research, v. 52, no. 4, p. 2474-2489.

Stone, R. O., 1967, A desert glossary: Earth-Science Reviews, v. 3, p. 211-268.

Sturt, C., 1849, Expedition into Central Australia, London, United Kingdom, Library of Alexandria.

Stuyfzand, P. J., and Bruggeman, G., Analytical approximations for freshwater lenses in coastal dunes, *in* Proceedings Proc. 13th Salt Water Intrusion Meeting (SWIM), Cagliari, Italy1994, p. 15-33.

Sultan, M., Ahmed, M., Sturchio, N., Yan, E., Milewski, A., Becker, R., Wahr, J., Becker, D., and Chouinard, K., 2013, Assessment of the Vulnerabilities of the Nubian Sandstone Fossil Aquifer,North Africa, Volume 5, p. 311-333.

Sultan, M., Sturchio, N., Al Sefry, S., Milewski, A., Becker, R., Nasr, I., and Sagintayev, Z., 2008a, Geochemical, isotopic, and remote sensing constraints on the origin and evolution of the Rub Al Khali aquifer system, Arabian Peninsula: Journal of Hydrology, v. 356, no. 1, p. 70-83.

Sultan, M., Wagdy, A., Manocha, N., Sauck, W., Gelil, K. A., Youssef, A., Becker, R., Milewski, A., El Alfy, Z., and Jones, C., 2008b, An integrated approach for identifying aquifers in transcurrent fault systems: The Najd shear system of the Arabian Nubian shield: Journal of Hydrology, v. 349, no. 3-4, p. 475-488.

Sultan, M., Yan, E., Sturchio, N., Wagdy, A., Gelil, K. A., Becker, R., Manocha, N., and Milewski, A., 2007, Natural discharge: A key to sustainable utilization of fossil groundwater: Journal of Hydrology, v. 335, no. 1-2, p. 25-36.

Suppiah, R., 1992, The Australian summer monsoon: a review: Progress in Physical Geography, v. 16, no. 3, p. 283-318.

Szymkiewicz, A., Gumuła-Kawęcka, A., Šimůnek, J., Leterme, B., Beegum, S., Jaworska-Szulc, B., Pruszkowska-Caceres, M., Gorczewska-Langner, W., Angulo-Jaramillo, R., and Jacques, D., 2018, Simulations of freshwater lens recharge and salt/freshwater interfaces using the HYDRUS and SWI2 packages for MODFLOW: Journal of Hydrology and Hydromechanics, v. 66, no. 2, p. 246-256.

Tanaka, K., Skinner, J., Dohm, J., Irwin, R., Kolb, E., Fortezzo, C., Platz, T., Michael, G., and Hare, T., 2014, Geologic map of Mars, Scientific Investigations Map 3292: US Geol. Sur., do i, v. 10.

Teller, J. T., and Lancaster, N., 1986, Lacustrine sediments at Narabeb in the central Namib Desert, Namibia: Palaeogeography, Palaeoclimatology, Palaeoecology, v. 56, no. 3, p. 177-195.

Thornthwaite, C. W., 1948, An Approach toward a Rational Classification of Climate: Geographical Review, v. 38, no. 1, p. 55-94.

Torabi, M., Fattahi1, 2, M., and Ghassemi, M. R., The link between water supply and earthquake in Iran.

Toussaint, S., Sullivan, P., and Yu, S., 2005, Water Ways in Aboriginal Australia: An Interconnected Analysis: Anthropological Forum, v. 15, no. 1, p. 61-74.

Trefry, M. G., McLaughlin, D., Lester, D. R., Metcalfe, G., Johnston, C. D., and Ord, A., 2011, Stochastic relationships for periodic responses in randomly heterogeneous aquifers: Water Resources Research, v. 47, no. 8.

Treiman, A. H., 2008, Ancient groundwater flow in the Valles Marineris on Mars inferred from fault trace ridges: Nature Geoscience, v. 1, no. 3, p. 181-183.

Tsoar, H., 1989, Linear dunes; forms and formation: Progress in Physical Geography, v. 13, no. 4, p. 507-528.

Tsoar, H., Moller, J., and Nickling, W., 1986, The role of vegetation in the formation of linear sand dunes: Boston, p. 75-95.

Turbet, M., Forget, F., Head, J. W., and Wordsworth, R., 2017, 3D modelling of the climatic impact of outflow channel formation events on early Mars: Icarus, v. 288, p. 10-36.

Tweed, S. O., Leblanc, M., Webb, J. A., and Lubczynski, M. W., 2007, Remote sensing and GIS for mapping groundwater recharge and discharge areas in salinity prone catchments, southeastern Australia: Hydrogeology Journal, v. 15, no. 1, p. 75-96.

Twidale, C., and Milnes, A., 1983, Aspects of the distribution and disintegration of siliceous duricrusts in arid Australia: Geol. Mijnbouw, v. 62, p. 373-382.

Twidale, C. R., 1972, Evolution of Sand Dunes in the Simpson Desert, Central Australia: Transactions of the Institute of British Geographers, no. 56, p. 77-109.

Twiss, R. J., Twiss, R. J., and Moores, E. M., 1992, Structural geology, Macmillan.

UN-ESCWA, B., 2013, Inventory of shared water resources in Western Asia: Chapter 6 Jordan River Basin. United Nations Economic and Social Commission for Western Asia: Federal Institute for Geosciences and Natural Resources, Beirut.

USDA-NRCS, 2007, Chapter 7 Hydrologic Soil Groups: US Department of Agriculture, Natural Resources Conservation Service, US Department of Agriculture, Natural Resources Conservation Service, Washington, DC.

Vacher, H., 1988, Dupuit-Ghyben-Herzberg analysis of strip-island lenses: Geological Society of America Bulletin, v. 100, no. 4, p. 580-591.

Van Der Veer, P., 1977, Analytical solution for steady interface flow in a coastal aquifer involving a phreatic surface with precipitation: Journal of Hydrology, v. 34, no. 1, p. 1-11.

van Ginkel, M., des Tombe, B., Olsthoorn, T., and Bakker, M., 2016, Small-Scale ASR Between Flow Barriers in a Saline Aquifer: Groundwater, v. 54, no. 6, p. 840-850.

Van Weert, F., and van der Gun, J., 2012, Saline and brackish groundwater at shallow and intermediate depths: genesis and world-wide occurrence: 39th International Association of Hydrologists, Niagara Falls: International Association of Hydrologists.

Vincent, P., 2008, Saudi Arabia: an environmental overview, CRC Press.

Walker, R., Jackson, J., and Baker, C., 2003, Surface expression of thrust faulting in eastern Iran: source parameters and surface deformation of the 1978 Tabas and 1968 Ferdows earthquake sequences: Geophysical Journal International, v. 152, no. 3, p. 749-765.

Wasson, R., Smith, G., and Agrawal, D., 1984, Late Quaternary sediments, minerals, and inferred geochemical history of Didwana Lake, Thar Desert, India: Palaeogeography, Palaeoclimatology, Palaeoecology, v. 46, no. 4, p. 345-372.

Webb, V. E., 2004, Putative shorelines in northern Arabia Terra, Mars: Journal of Geophysical Research: Planets, v. 109, no. E9.

Webster, P. J., and Yang, S., 1992, Monsoon and ENSO: Selectively interactive systems: Quarterly Journal of the Royal Meteorological Society, v. 118, no. 507, p. 877-926.

Welsh, W. D., and Doherty, J., Great Artesian Basin groundwater modelling, *in* Proceedings 29th Hydrology and Water Resources Symposium: Water Capital, 20-23 February 2005, Rydges Lakeside, Canberra2005, Engineers Australia, p. 177.

Werner, A. D., Kawachi, A., and Laattoe, T., 2016, Plausibility of freshwater lenses adjacent to gaining rivers: Validation by laboratory experimentation: Water Resources Research, v. 52, no. 11, p. 8487-8499.

Werner, A. D., and Laattoe, T., 2016a, Terrestrial freshwater lenses in stable riverine settings: Occurrence and controlling factors: Water Resources Research.

Werner, A. D., and Laattoe, T., 2016b, Terrestrial freshwater lenses in stable riverine settings: Occurrence and controlling factors: Water Resources Research, v. 52, p. 3654– 3662.

West, M. D., Clarke, J. D., Thomas, M., Pain, C. F., and Walter, M. R., 2010, The geology of Australian Mars analogue sites: Planetary and Space Science, v. 58, no. 4, p. 447-458.

Westaway, R., Guillou, H., Seyrek, A., Demir, T., Bridgland, D., Scaillet, S., and Beck, A., 2009, Late Cenozoic surface uplift, basaltic volcanism, and incision by the River Tigris around Diyarbakır, SE Turkey: International Journal of Earth Sciences, v. 98, no. 3, p. 601-625.

Wharton Jr, R., McKay, C., Mancinelli, R., and Simmons Jr, G., 1989, Early Martian environments: the Antarctic and other terrestrial analogs: Advances in Space Research, v. 9, no. 6, p. 147-153.

Wiedemann, A., 1971, Vegetation studies in the Simpson Desert, NT: Australian Journal of Botany, v. 19, no. 1, p. 99-124.

Wierzchos, J., Ascaso, C., and McKay, C. P., 2006, Endolithic cyanobacteria in halite rocks from the hyperarid core of the Atacama Desert: Astrobiology, v. 6, no. 3, p. 415-422.

Williams, D. R., 2020, Chronology of Mars Exploration, Lunar and Planetary Science, Volume 2020: Houston, Texas.

Williams, M., 2014, Climate change in deserts, Cambridge University Press.

Williford, K. H., Farley, K. A., Stack, K. M., Allwood, A. C., Beaty, D., Beegle, L. W., Bhartia, R., Brown, A. J., de la Torre Juarez, M., and Hamran, S.-E., 2018, The NASA Mars 2020 rover mission and the search for extraterrestrial life, From Habitability to Life on Mars, Elsevier, p. 275-308.

Wopfner, H., and Twidale, C., 2001, Australian desert dunes: wind rift or depositional origin?: Australian Journal of Earth Sciences, v. 48, no. 2, p. 239-244.

Wordsworth, R. D., Kerber, L., Pierrehumbert, R. T., Forget, F., and Head, J. W., 2015, Comparison of "warm and wet" and "cold and icy" scenarios for early Mars in a 3-D climate model: Journal of Geophysical Research: Planets, v. 120, no. 6, p. 1201-1219.

Yihdego, Y., and Al-Weshah, R. A., 2017, Engineering and environmental remediation scenarios due to leakage from the Gulf War oil spill using 3-D numerical contaminant modellings: Applied Water Science, v. 7, no. 7, p. 3707-3718.

Yizhaq, H., Ashkenazy, Y., and Tsoar, H., 2009, Sand dune dynamics and climate change: A modeling approach: Journal of Geophysical Research: Earth Surface, v. 114, no. F1.

Young, M. E., Macumber, P. G., Watts, M. D., and Al-Toqy, N., 2004, Electromagnetic detection of deep freshwater lenses in a hyper-arid limestone terrain: Journal of Applied Geophysics, v. 57, no. 1, p. 43-61.

Zhao, J., Wen, Z., Shu, L., Zhen, L., Zhou, C., and Liu, L., 2009, A laboratory model of the evolution of an island freshwater lens: IAHS-AISH Publication, v. 330, p. 154-161.

Zheng, C., and Wang, P. P., 1999, MT3DMS: a modular three-dimensional multispecies transport model for simulation of advection, dispersion, and chemical reactions of contaminants in groundwater systems; documentation and user's guide: US Army Corps of Engineers Engineer Research and Development Center, US Army Corps of Engineers Engineer Research and Development Center, Washington, DC.

Zonn, I. S., 2012, Water resources of Turkmenistan, The Turkmen Lake Altyn Asyr and Water Resources in Turkmenistan, Springer, p. 59-68.

APPENDIX A

Hourly wind data for Alice Springs from 1/1/2009-12/31/2015.

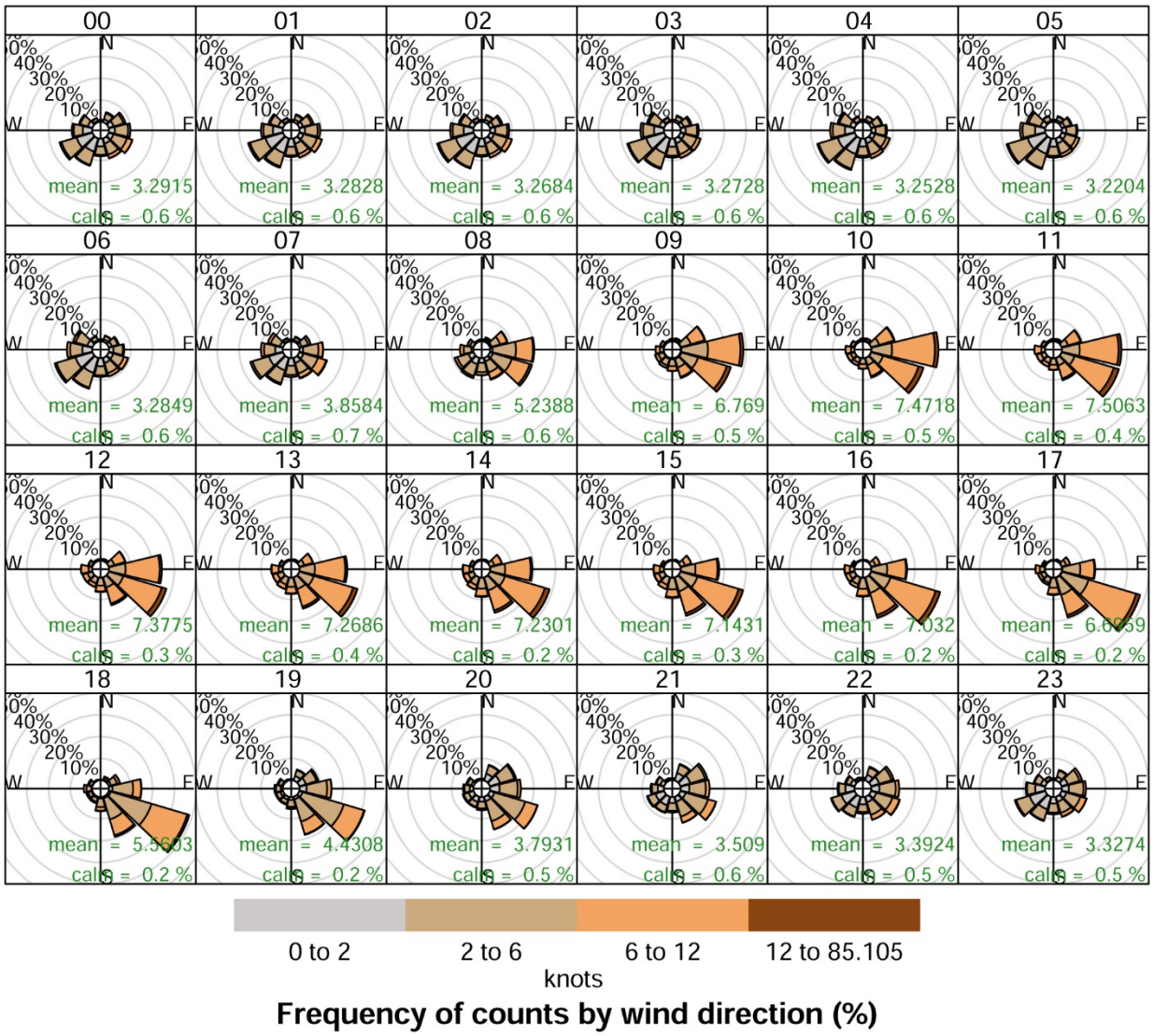

APPENDIX B

Seasonal wind data of Alice Springs from 1/1/2009 -12/31/2015.

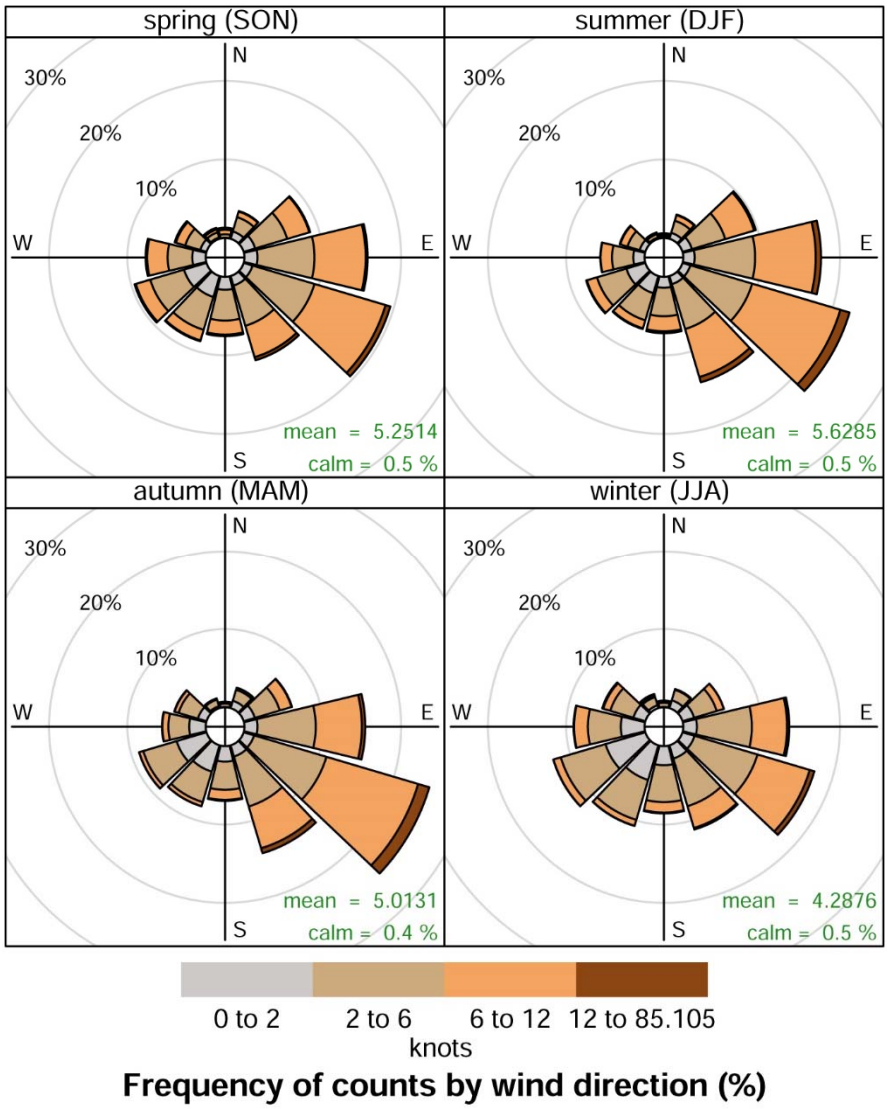

APPENDIX C

Yearly wind data of Alice Springs from 1/1/2009-12/31/2015.

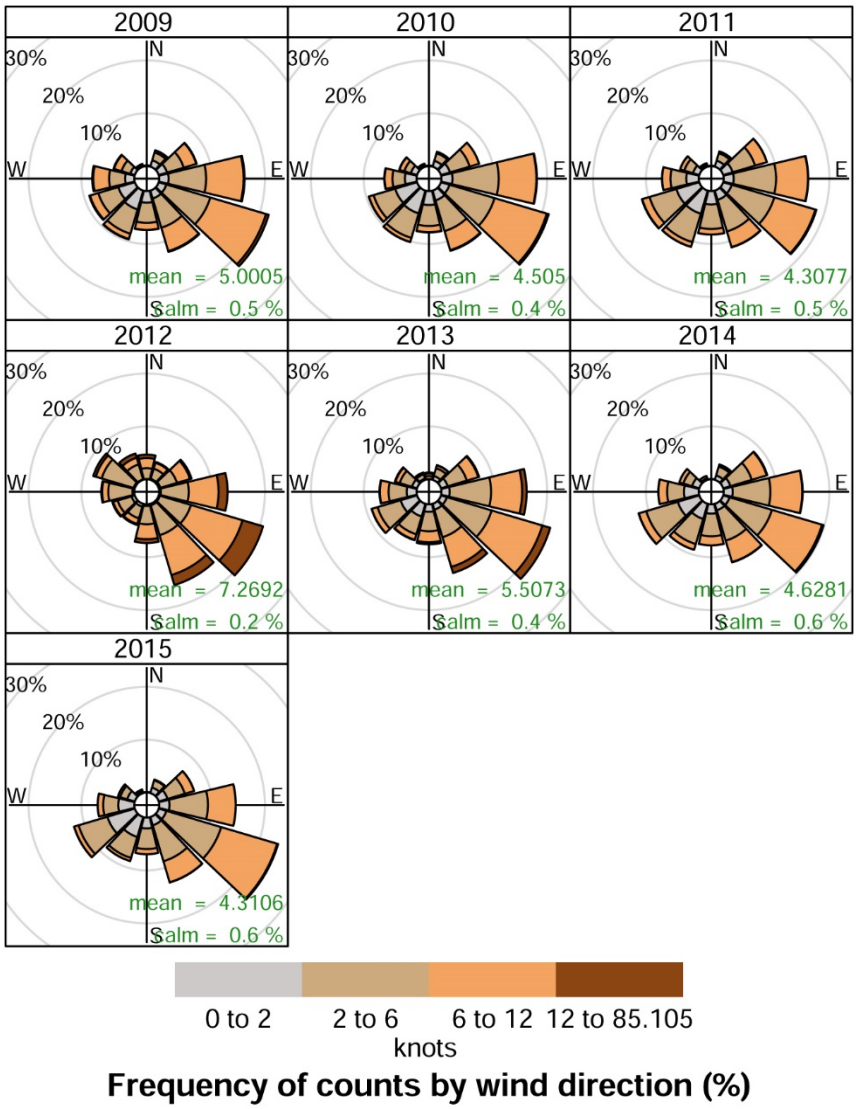

APPENDIX D

Shortened range of throw (t), dip angle (α), slip rate (s), displacement (D_{max}), and uplift duration (T) are shown in the below table from the HRSC DEMs. Uplift duration is rounded to the nearest 100,000 years.

Transect	***t* (m)**	**(α)**	***s* (mm/yr)**	**D_{max} (m)**	***T* (yr)**
A	550	20	0.01	1608	160,800,000
		30		1100	110,000,000
		40		856	85,600,000
		20	1	1608	1,600,000
		30		1100	1,100,000
		40		856	900,000
B	670	20	0.01	1959	195,900,000
		30		1340	134,000,000
		40		1042	104,200,000
		20	1	1959	2,000,000
		30		1340	1,300,000
		40		1042	1,000,000
BC	820	20	0.01	2398	239,800,000
		30		1640	164,000,000
		40		1276	127,600,000
		20	1	2398	2,400,000
		30		1640	1,600,000
		40		1276	1,300,000
C	580	20	0.01	1696	169,600,000
		30		1160	116,000,000
		40		902	90,200,000
		20	1	1696	1,700,000
		30		1160	1,200,000
		40		902	900,000
D	395	20	0.01	1155	115,500,000
		30		790	79,000,000
		40		615	61,500,000
		20	1	1155	1,200,000
		30		790	800,000
		40		615	600,000

APPENDIX E

The CTX DEM in the grey-scale is superimposed over the HRSC DEM showing the paucity of CTX coverage in this area.

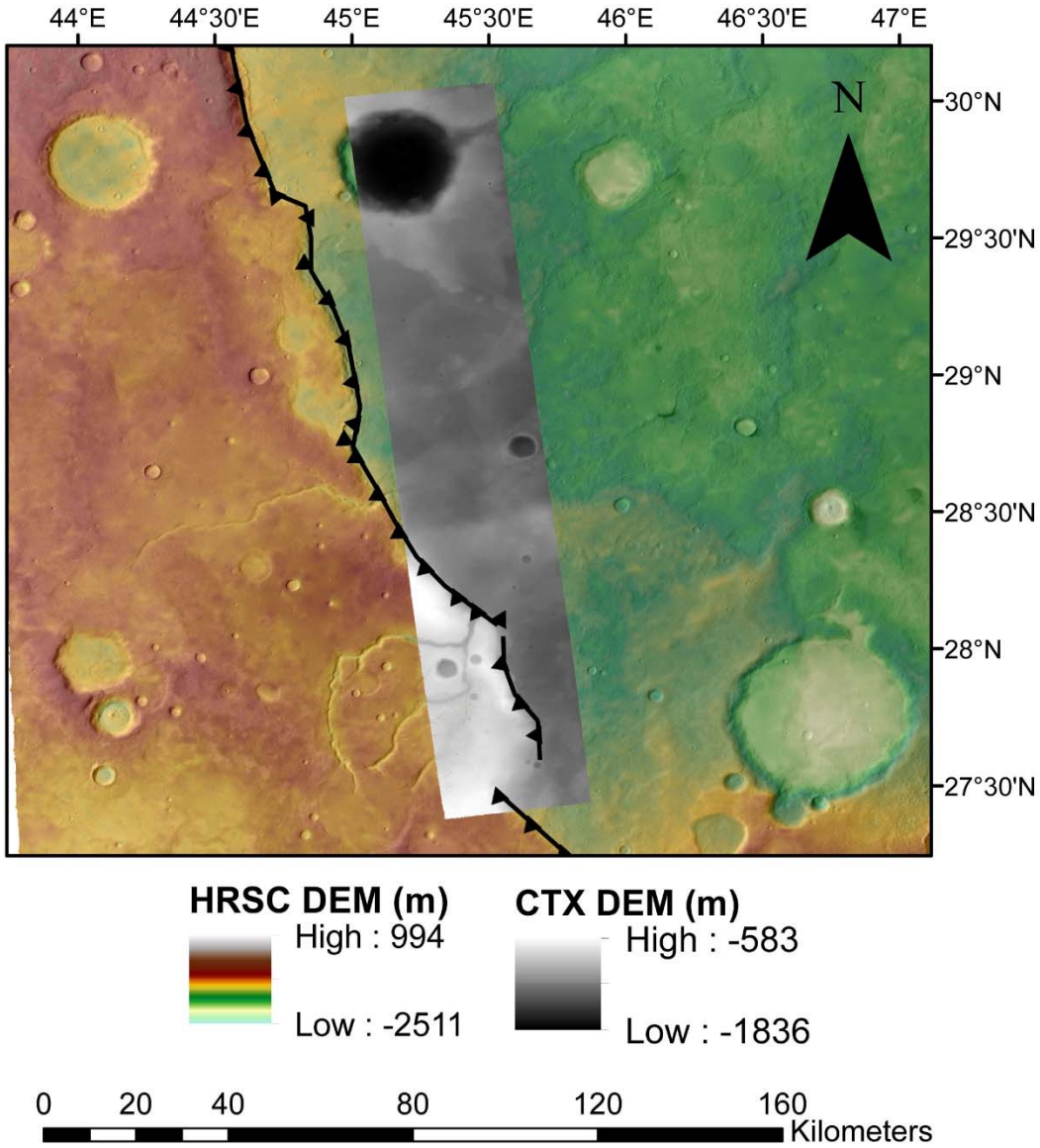

APPENDIX F

The CTX DEM with the transects in overlapping areas to the transects, and (right) the elevation profiles with selected highest elevation (red line) and lowest elevation (blue line) values to calculate uplift duration. Throw (t), dip angle (α), slip rate (s), displacement (D_{max}), and uplift duration (T) are shown in the below table from the CTX DEM. Uplift duration is rounded to the nearest 100,000 years.

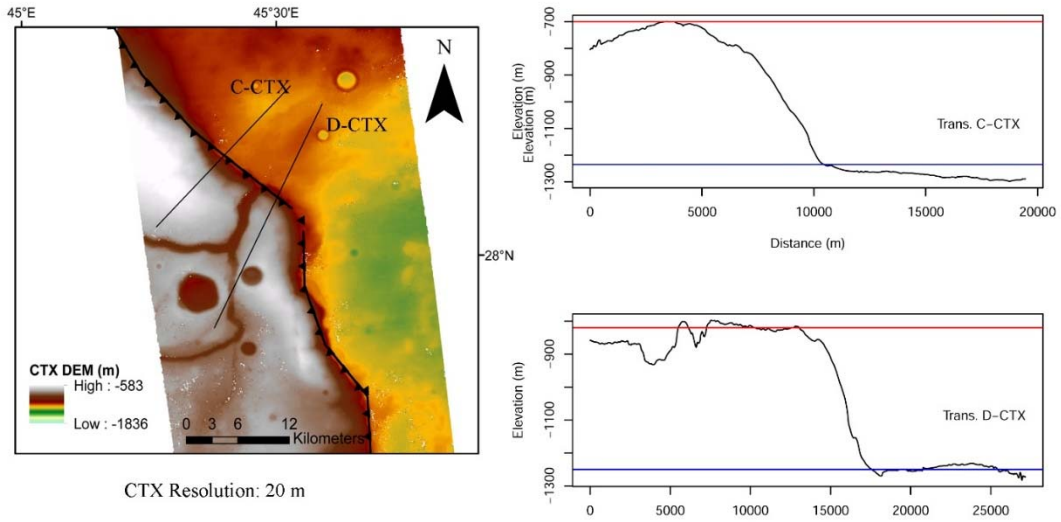

Transect	t (m)	(α)	s (mm/yr)	D_{max} (m)	T (yr)
C-CTX	640	20	0.01	1564	156,500,000
		30		1070	107,000,000
		40		832	83,300,000
		20	1	1564	1,600,000
		30		1070	1,100,000
		40		832	900,000
D-CTX	525	20	0.01	1257	125,800,000
		30		860	86,000,000
		40		669	66,900,000
		20	1	1257	1,300,000
		30		860	900,000
		40		669	700,000

APPENDIX G

(Left) Interpolated 3D lines of channel a south (top), channel b north (middle), and channel b south (bottom), and (right) longitudinal profiles and slopes with HRSC data. The red line indicated the selected highest elevation and blue line as the lowest elevation. The dotted line indicates the highest and lowest x-coordinates for the slope calculation.